Crystallography Reports, Vol. 47, No. 1, 2002, pp. 1–16. Translated from Kristallografiya, Vol. 47, No. 1, 2002, pp. 7–23.

DIFFRACTION AND SCATTERING OF X-RAY AND SYNCHROTRON RADIATION

Statistical Theory of Dynamical Diffraction of Mössbauer Radiation

V. L. Nosik

Shubnikov Institute of Crystallography, Russian Academy of Sciences, Leninskiĭ pr. 59, Moscow, 117333 Russia

Received July 27, 2000; in final form, April 4, 2001

Abstract—The statistical theory of dynamical diffraction of Mössbauer radiation providing the account for the mutual influence of coherent and elastic diffusion scattering has been considered. The sources of elastic and inelastic diffuse scattering for a hematite crystal are analyzed. The theoretical results are compared with the resonance nuclear scattering data obtained in the experiments performed at the Photon Factory in Tsukuba, Japan.

INTRODUCTION

Soon after the discovery of the Mössbauer effect in 1958, the process of diffraction of Mössbauer radiation from crystals with resonance nuclei was studied in detail for both ideal single crystals [1, 2] and polycrystals [3]. The coherence of Mössbauer radiation as well as the interference of the resonance and electron scattering were established. It was also shown that the effects of dynamical diffraction (the anomalous transmission in the Laue diffraction, the total external reflection in the Bragg diffraction, etc.) should be studied on perfect crystals purposefully enriched with a resonance isotope. Thus, the suppression of inelastic channels of nuclear reactions was studied on almost perfect isotope-enriched lead [4], iron [5], $FeBO_3$ [6], and hematite [7] crystals.

Recently, the widespread use of powerful synchrotron-radiation (SR) sources considerably increased the interest in studying time-delayed signals of nuclear radiation. The short (0.2 ns) SR pulses separated by considerable time intervals (1–2 ns) provide the unique possibility of separating the "fast" (elastic) electron and the "slow" (resonance) nuclear Mössbauer-radiation (MR) response of the crystal.

Moreover, the polarization characteristics and the high SR intensity allow unique experiments to be conducted for pure nuclear scattering (yttrium-iron garnets [8], iron borate [9], hematite [10]) and interference of electron and nuclear scattering in hematite [11]. At present, the theory and practice of the use of coherent nucleus scattering are studied quite well [12–16].

Because of a very narrow width of nuclear levels, the MR experiments require the use of specific crystals–monochromators with a high energy resolution necessary for diminishing the contribution from electron scattering and the special protection from vibrations. The high MR sensitivity to the magnetic structure and various dynamical excitations (phonons, structural phase transitions, diffusion, and relaxation) and its high intensity open new possibilities for conducting experiments on the diffuse scattering of Mössbauer radiation and require the construction of a corresponding theory.

An important notion for further consideration is coherence (in application to both the electromagnetic field of the incident beam and the field inside the crystal) and an ensemble of atoms in the crystal. Because of the high monochromaticity of Mössbauer radiation, the coherence length l of the train of electromagnetic waves generated by an individual nucleus in the emission of a quantum is determined by the lifetime of the excited state ($\tau \approx \Gamma^{-1}$) and, for Co^{57}, is equal in vacuum to $l = c\tau = 30$ m, i.e., has a value considerably exceeding the coherence length for the X-ray radiation from conventional sources ($\Gamma_x \approx 1$ eV) with the same wavelength ($l_x = 0.3$ μm). The synchrotron radiation used in experiments has an intermediate coherence length determined mainly by the energy resolution of the monochromator used.

In crystals, the radiation is scattered by a set of atoms forming a coherent ensemble if all the nuclei have the same scattering amplitude and are arranged strictly periodically. However, in actual fact, it is not the case and one has to single out a certain coherently scattering volume ξ, which can be either larger or smaller than the coherent volume of the electromagnetic field ($\sim\Gamma_c$). In the final analysis, Γ_c is determined by the dielectric constant of the medium [17], which makes its calculation under diffraction conditions even more complicated. Any deviations from the strict periodicity in the arrangement of identical atoms give rise to diffuse scattering with the intensity also dependent on the volume in which it occurs.

Moreover, in Bragg (reflection) diffraction, the key parameter can be the penetration depth of the field into the crystal, which coincides with the extinction length Λ if the radiation is incident at the Bragg angle,

whereas far from this angle, it coincides with the absorption length μ_a^{-1}.

It should be emphasized that the region in which diffuse waves are formed can also be finite. Thus, in the case of thermal diffuse scattering (TDS), the largest contribution comes from acoustic phonons having the maximum wavelength in the given crystal, so that, in this case, the whole crystal can be considered as a scattering volume. However, one of the most attractive concepts of the microscopic theory of phase transitions attribute these transitions to instability of some optical oscillations, whose excitation frequency decreases anomalously with the approach to the transitions temperature $\omega_0 = |T - T_c|^{1/2}$ [18]. The condensation of "soft" phonons makes the lattice rearrangement energetically favorable and, in this case, the volume of the restructured region increases proportionally to ω_0^{-1}.

In the final analysis, the relationship of the distances at which the coherent and incoherent waves are formed determines the contribution of the coherent and diffuse scattering into the total diffraction intensity.

At present, attempts are being made to construct a consistent statistical theory of dynamical diffraction which would describe the interaction between the coherently and diffusely scattered radiations. It was established that the corrections for diffuse scattering in the analysis of the structure and properties of real crystals can considerably distort the ideal diffraction pattern by imposing a certain basic limit on the accuracy of the diffraction experiment. A high coherence of Mössbauer radiation would allow one to approach this limit, although this would require that very complicated experiments be conducted.

Below, we make an attempt to construct a theory of statistical diffraction of Mössbauer radiation for a well-known hematite crystal such that it would consistently take into account incoherent elastic scattering (i.e., scattering occurring without a change in the frequency of the scattered radiation) and its effect on the coherent component. We also analyze inelastic-scattering channels (phonons, magnons, and critical fluctuations), which can make a considerable contribution to the intensity of diffuse scattering.

We deliberately limit our consideration to a hematite crystal, because it allows us to compare our results with the data of the well-known diffraction experiments made on imperfect crystals with a complex magnetic structure.

SOURCES OF DIFFUSE SCATTERING

Consider possible sources of diffuse scattering of Mössbauer radiation. Incoherent (diffuse) scattering can be defined as a process in which some information about the phase shift during scattering from individual nuclei is lost.

Considering MR diffraction, one has to distinguish between elastic and inelastic scattering. In elastic scattering, a quantum is scattered in a random way, but its energy remains constant and it can experience resonance scattering and participate in dynamical diffraction. In inelastic scattering, e.g., by phonons, a quantum acquires an additional energy ($\hbar\omega_s \approx 10^{-3}$ eV), which excludes its participation in dynamical scattering. This consideration of the incoherent part of the diffraction field of Mössbauer radiation drastically differs from consideration in the case of X-rays [19].

Elastic Incoherent Processes

Spin incoherence. A nucleus of an isotope in the ground state possesses a total angular momentum $\mathbf{J} = \hbar\mathbf{I}_g$, where $\mathbf{I}_g$ is the nuclear spin $\boldsymbol{\mu} = g\mu_n\mathbf{I}_g$. The projection of the magnetic moment onto the chosen quantization axis can have $2I_g + 1$ values

$$m_I = -I_g, -I_g + 1, \ldots, I_g. \tag{1}$$

Since the nuclear magneton

$$\mu_n = \frac{e\hbar}{m_n c} \tag{2}$$

is a thousand times less than the Bohr magneton μ_B, the magnetic order in the system of nuclear spins can be attained either in strong magnetic fields or at very low temperatures (0.1 K). Since the Mössbauer line is very narrow even in a relatively weak field of the atomic moment, only the nuclei with definite moment projections can experience nuclear resonance. Statistically, the number of such nuclei equals

$$w_m = (1/Z)\exp(-\beta m_I M) \approx 1/(2I_g + 1),$$
$$Z = \sum_{m_I} \exp(-\beta m_I M), \quad \beta^{-1} = kT. \tag{3}$$

Thus, for the Fe^{57} isotope ($I_g = 1/2$), only a half of the nuclei experience resonance coherent scattering.

Isotopic incoherence. The natural content of the resonance isotope is low (2.2%). Similar to binary solid solutions [20], the replacement of Fe^{56} by Fe^{57} in a hematite crystal results in small displacements of neighboring atoms and changes the energy of their interaction leaving the symmetry of the crystal lattice unchanged.

The isotope-enriched crystals grown from melt [21] with the *c*-axis being normal to their surface had the thickness $T = 0.4$ mm and the surface area 5×10 mm^2. The detailed X-ray study of the crystals [21, 22] showed that they were slightly bent (with the curvature radius 8–64 m) and had growth sectors (domains).

The statistically complete description of any system suggests the knowledge of all the moments of the polarizability distribution. We restrict our consideration only

to the first two moments—the average polarizability and its dispersion for "magnetic reflections" with the diffraction vector $\mathbf{g} = (h, h, h)$, where $h = 2n + 1$. The polarizability of the hematite crystal per unit cell with the arbitrarily distributed isotopes is determined by the expression (see Appendix 1)

$$\hat{\chi}(\mathbf{k}_\alpha - \mathbf{k}_\beta) = (1/N)\sum_{j=1}^{N} \exp(i(\mathbf{k}_\alpha - \mathbf{k}_\beta)\mathbf{x}_k)\hat{c}_{jk}\chi^k_{\alpha\beta}, \quad (4)$$

where $\mathbf{x}_k = \mathbf{R}_j + \mathbf{r}_{jk}$, $\mathbf{R}_j$ is the position of the jth unit cell in the crystal, N is the total number of unit cells, and $\mathbf{r}_{jk}$ is the position of the kth atom in the jth unit cell ($k = 1$–4). The σ-polarized SR radiation, scattering is determined by the following four transitions:

$$\chi^k_{\alpha\beta} = g_0\sum_{l=1}^{4} P^k_{\alpha\beta}\exp(-M_k)C_1^2(m_g, \Delta m_l)/(\Delta E_l + i). \quad (5)$$

The operators $\hat{c}_{jk}$ are defined in such a way that

$$\hat{c}_{jk} = 1, \quad (6)$$

if the kth position in the jth unit cell is occupied by the isotope Fe^{57} and the projection of the moment m_I is fixed, and $\hat{c}_{jk} = 0$, if the position is occupied by Fe^{56} or if the nucleus has a different projection of the magnetic moment.

Averaging over the ensemble of all the atoms participating in diffraction yields the following expression for polarizability per unit cell:

$$\langle\chi(\mathbf{k}_\alpha - \mathbf{k}_\beta)\rangle = (c/2)\sum_{\mathbf{g}}\chi^{57}_{10}\delta(\mathbf{k}_\alpha - \mathbf{k}_\beta - \mathbf{g}), \quad (7)$$

where χ^{57}_{10} is the magnetic susceptibility of the crystal consisting only of resonance isotopes, whereas the summation is performed over the set of diffraction vectors g of the crystal.

By definition, polarizability dispersion of the crystal is

$$\begin{aligned}\Omega(k_\alpha - k_\beta) &= \langle\hat{\chi}(k_\alpha - k_\beta)\hat{\chi}(k_\alpha - k_\beta)\rangle \\ &\quad - \langle\hat{\chi}(k_\alpha - k_\beta)\rangle\langle\hat{\chi}(k_\alpha - k_\beta)\rangle \\ &= (1/N^2)\sum_{k=1}^{N}\sum_{k'=1}^{N}\exp(ig(x_k - x_{k'}) \\ &\times\chi^k_{\alpha\beta}\chi^{k'}_{\alpha\beta}(\delta_{k,k'}(c/2)(1-c/2) + (c/2)(1-\delta_{k,k'})G_{kk'}),\end{aligned} \quad (8)$$

where $G_{kk'}$ is the conditional probability to encounter one Fe^{57} atom in the position k' if the other Fe^{57} atom is in the positions k. Assuming that the isotopes are uniformly distributed over the crystal ($G_{kk'} = 0$), we can conclude that the polarizability dispersion is almost N times lower than the squared average polarizability for the reflection with the diffraction vector $\mathbf{g}$:

$$\Omega(\mathbf{k}_\alpha - \mathbf{k}_\beta) = (1/N)(\chi^{57}(\mathbf{k}_\alpha - \mathbf{k}_\beta))^2(c/2)(1-c/2). \quad (9)$$

The latter expression provides no information on the crystal structure because, when deriving this expression, we took into account only the spin and isotopic incoherencies.

Even if one considers not the total number N of the unit cells but only the number of the unit cells which are illuminated by the SR source with the cross section 0.9×4 mm^2 [21], $N_r = 1.6 \times 10^{19}$, Equations (7) and (9) cannot give the equivalent contributions to the intensity. With the deviation of the incident radiation from the Bragg angle, the contribution from the coherent scattering rapidly decreases, which reverses the situation. For the hypothetical formation of clusters of Fe^{57} atoms, the contribution to diffuse scattering caused by isotopic incoherence can considerably increase.

Obviously, the polarizability dispersion (9) attains its maximum in the most isotope-enriched specimens ($c = 1$).

Formation of magnetic domains. The small width of the Mössbauer line determines its high sensitivity to fluctuations of the magnetic moment of atoms, $\mathbf{M} = \mathbf{M}_0 + \delta\mathbf{M}$. If $\delta\mathbf{M}$ is of an order of 1T,

$$\delta M = \frac{\Gamma}{\mu_n} \approx 10^{-7}, \quad (10)$$

the atom becomes "invisible" for a coherent beam tuned to the energy $E = \hbar\omega - \mu_n M_0$.

Figure 1 shows the rhombohedral unit cell of a hematite crystal, the position of the magnetic moments of atoms in the hexagonal magnetic structure above and below the temperature of the Morin transition (T_M = 253 K) [23], and the diffraction geometry. At room temperature, the magnetic moments in the neighboring layers (e.g., $\mathbf{M}_B$ and $\mathbf{M}_A$) are not exactly collinear but are rotated by a small angle (10^{-4} rad) with respect to the ideal position $\mathbf{M}_0$ in the plane normal to the c-axis (the unit vector $\mathbf{n}$),

$$\mathbf{m}(0) = d[\mathbf{n}, \mathbf{M}_B], \quad (11)$$

which changes the magnetic symmetry of the system (the d-constant).

The experimental data [21, 22] relate to the case where the domain structure of the specimen is destroyed by a 1 kG magnetic field applied either parallel to the diffraction plane $\mathbf{H}_\parallel$ (along the c-axis) or normally to it, $\mathbf{H}_\perp$. In the field $\mathbf{H}_\parallel$, the peak intensity of the (777) reflection was higher by a factor of 1.5 than the intensity in the field $\mathbf{H}_\perp$.

In terms of crystallography, the three directions of the atomic magnetic moment ($\mu_{Fe}(4.3\text{ K}) = 4.9\mu_B$) in the hexagonal structure in Fig. 1b are equivalent, and

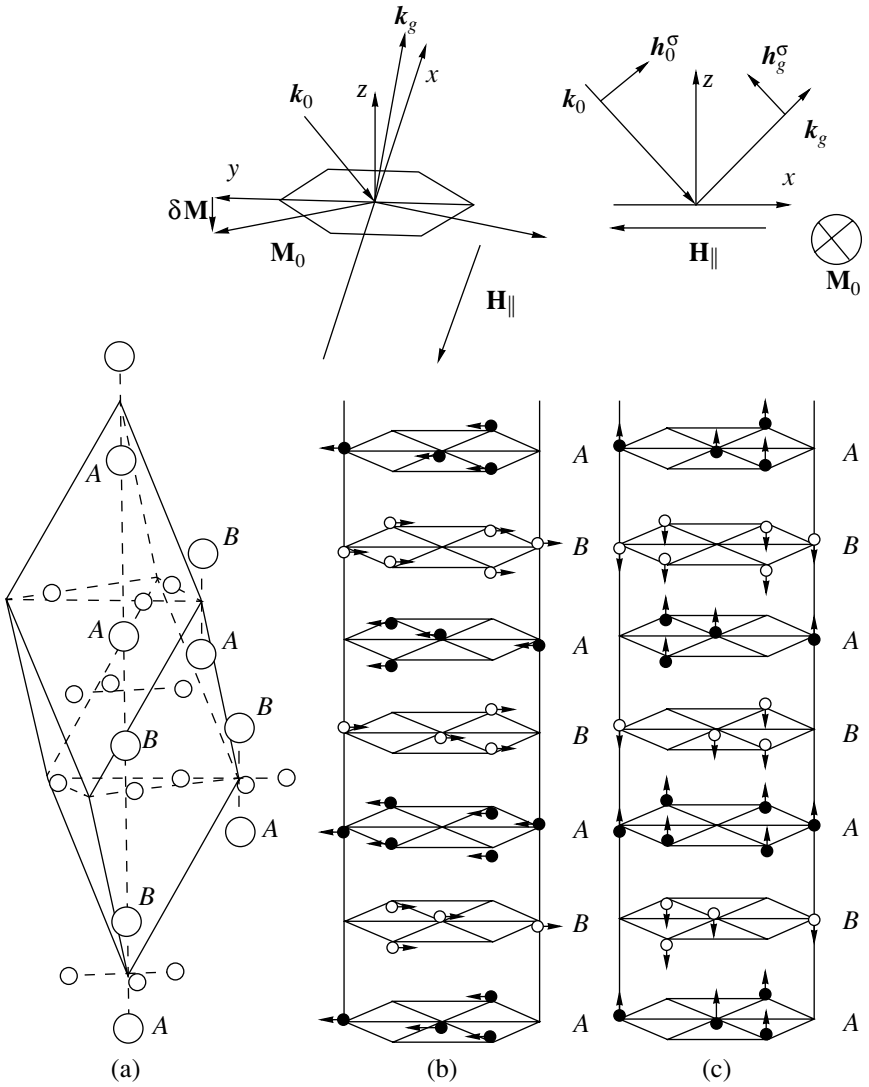

Fig. 1. (a) Unit cell of a rhombohedral α-Fe_2O_3 crystal and (b, c) positions of magnetic moments in the hexagonal structure at the temperature (b) above and (c) below T_N [23].

the crystal has three domains of approximately equal volumes. Now, direct the *z*-axis along the *c*-axis and the axes lying in the (111) plane in such a way that

$$\mathbf{M}_1 = \mu_{Fe}(0, 1, 0), \quad \mathbf{M}_{2,3} = \mu_{Fe}(1/2, \pm\sqrt{3}/2, 0). \quad (12)$$

And, apply the magnetic field **H** to an antiferromagnetic crystal. The magnetic fields acting onto the magnetic moments in the neighboring layers,

$$\mathbf{H}_{B,A} = \mathbf{H} - N_{BA}\mathbf{M}_{A,B} \quad (13)$$

rotate the moments in such a way that

$$[\mathbf{M}_{B,A}, \mathbf{H}_{B,A}] = 0. \quad (14)$$

Simultaneously, the average moment also slightly changes [24]. As a result, the magnetic moment of the atoms in the external field is rotated so that

$$\mathbf{M} = \mathbf{M}_0 + (1/N_{B,A})\left(\mathbf{H} - \frac{\mathbf{M}_0}{\mathbf{M}_0^2}(\mathbf{M}_0\mathbf{H})\right),$$
$$N_{BA} = 6kT_N/[Ng^2\mu_B^2 S(S+1)], \quad (15)$$

where *N* is the number of the magnetic moments per unit volume. If the magnetic field is normal to the (111) plane, the atoms in all the three domains possess the same energy

$$\delta E_i = \mathbf{M}_i\mathbf{H}_\parallel = 0, \quad (16)$$

and, thus, preserve their volumes unchanged.

If the magnetic field lies in the (111) plane, the nuclei inside one of the domains have the minimum Zeeman energy, and, therefore, this domain has a larger

volume than the other two

$$W_1 = \exp(-\beta \mathbf{M}_1 \mathbf{H}_\perp)/Z. \quad (17)$$

At a certain value of $\mathbf{H}_c$, almost all the magnetic moments rotate normally to the applied field. Nevertheless, even in this case, some part of the crystal volume V_d cannot participate in the nuclear resonance because of thermal vibrations

$$\rho = (V_d/V) \approx \sum_{i=2,3} \exp(-\beta(\mathbf{M}_i - \mathbf{M}_1)\mathbf{H}_\perp). \quad (18)$$

With a further increase in the magnetic-field intensity, the moments are aligned along the external field in accordance with formula (15).

Taking into account the random nature of the small-domain distribution with respect to the incident beam, one can state that the larger part of the crystal scatters the Mössbauer radiation coherently,

$$\langle \chi(\mathbf{k}_\alpha - \mathbf{k}_\beta) \rangle = (1-\rho) \sum_g \chi_g^{57} \delta(\mathbf{k}_\alpha - \mathbf{k}_\beta - \mathbf{g}), \quad (19)$$

whereas its smaller part contributes to the polarizability dispersion

$$\Omega_d = (\rho \chi^{id}(\mathbf{k}_\alpha - \mathbf{k}_\beta))^2. \quad (20)$$

It should also be remarked that an increase in the peak intensity of the magnetic (777) reflection by a factor of 1.5 because of rotation of the external field from $\mathbf{H}_\perp$ to $\mathbf{H}_\parallel$ observed in [21, 22] can be associated with an increase in the number of dynamical reflections. If all the magnetic domains in the $\mathbf{H}_\perp$ field have the same Zeeman energy and only one region of the total external reflection, then, in the case of $\mathbf{H}_\parallel$ field, some additional reflections appear at other values of the resonance energy.

Inelastic Incoherent Processes

Scattering with participation of phonons. As has already been indicated, if an X-ray quantum absorbs one or several phonons with an energy of 10^{-3} eV, it continues participating in diffraction (the linewidth is of the order of 1 eV), whereas the Mössbauer quantum upon such an absorption event cannot be scattered by nuclei any more. Therefore, the thermal diffuse scattering can be considered within the Born approximation.

If the field of the diffracted wave inside the crystal can be considered as a sum of plane (Bloch) waves (see Appendix 2),

$$E_g(z) = \exp(i\mathbf{g}\mathbf{r}) \sum_{i=1}^{4} a_g^i \exp(iq_i z), \quad (21)$$

the cross section of scattering of one of the Bloch waves with the pulse $\mathbf{p}$ within the unit solid angle into the plane wave with the pulse $\mathbf{p}'$ has the form

$$\frac{d\sigma}{d\Omega} = \frac{\omega^2}{4\pi^2\hbar^2} |\chi(\mathbf{p} - \mathbf{p}')|^2. \quad (22)$$

With due regard for crystal-lattice vibrations, the component of the crystal polarizability corresponding to diffuse scattering has the form [25, 26] (see Appendix 2)

$$F \sum_{nf} \frac{(\exp(i\mathbf{k}_0\mathbf{u}_j))_{0n} (\exp(-i\mathbf{k}_g\mathbf{u}_j))_{nf}}{\hbar\omega - E_{s0} - E_n + i\Gamma/2}, \quad (23)$$

where $\hbar\omega$ is the photon energy, E_{s0} is the resonance energy, E_n is the energy of the nth intermediate phonon state, f is the state of the phonon system upon one scattering event, and F is a certain constant.

Scattering of Mössbauer radiation occurs in two stages—absorption of an electromagnetic quantum with the wave vector $\mathbf{k}_0$ and emission of the quantum $\mathbf{k}_g$ after a certain time interval ($\tau = \hbar/\Gamma$) considerably exceeding the period of the characteristic phonon vibrations. Therefore, averaging over the states n and f is performed separately and yields a factor in the form of the sum of the Lamb–Mössbauer factors ($M_j = M(\mathbf{k}_0) + M(\mathbf{k}_g)$) for the coherent scattering

$$\exp(-M(\mathbf{k}_{0,g})) = (\exp(i\mathbf{k}_{0,g}\mathbf{u}_j))_{00}, \quad (24)$$

and not the Debye–Waller factor $W(\mathbf{k}_0 - \mathbf{k}_g)$ as in the case of X-ray diffraction. Limiting the consideration to the single-phonon processes, we can reduce Eq. (23) to the form

$$F\left(\sum_n \frac{(\exp(i\mathbf{k}_0\mathbf{u}_j))_{0n} \exp(-M(\mathbf{k}_g))}{\hbar\omega - E_{s0} - E_n + i\Gamma/2} + \sum_f \frac{\exp(-M(\mathbf{k}_0))(\exp(-i\mathbf{k}_g\mathbf{u}_j))_{0f}}{\hbar\omega - E_{s0} + i\Gamma/2} \right). \quad (25)$$

Write the operator of the phonon displacement in the secondary-quantization formalism,

$$\mathbf{u}_j = \sum_{\alpha,q} \sqrt{\frac{\hbar}{2MN\omega_\alpha(q)}} \mathrm{Re}(\hat{a}\mathbf{e}_\alpha(\mathbf{q}) \exp(i\mathbf{q}\mathbf{r}_j - \omega_\alpha(\mathbf{q}))), \quad (26)$$

where N is the number of the unit cells, and $\mathbf{e}_\alpha(\mathbf{q})$ and $\omega_\alpha(\mathbf{q})$ are the unit vector of the displacement and the frequency of the phonon with the wave vector $\mathbf{q}$ of the branch α, respectively. Hereafter, the complex-conjugated values are denoted by c.c.

Then the matrix element in (22) takes the form [27]

$$|\chi(\mathbf{p}-\mathbf{p}')|_{\pm}^2 \approx |F|^2 \exp(-M_j) \times \frac{kT(2\pi)^3}{2MN}\sum_{\alpha,q}\sum_{g}\frac{1}{\omega_\alpha^2(\mathbf{q})}\left(1+\frac{1}{\omega_\alpha^2(\mathbf{q})}\right) \times |(\mathbf{p}-\mathbf{p}')\mathbf{e}_\alpha|^2 \delta(\mathbf{p}-\mathbf{p}'+\mathbf{q}_\alpha+\mathbf{g}). \quad (27)$$

The major contribution to the last expression comes from acoustic phonons ($\omega_\alpha = c_\alpha q$), which results in a certain divergence of the cross section of thermal diffuse scattering q^{-2} (or even q^{-4}) with an approach to the Bragg angle.

Spin fluctuations. As is shown in Appendix 1, the polarization coefficient in the expression for crystal polarizability in the scattering of the wave with magnetic-field direction $\mathbf{h}_\alpha$ into the wave with $\mathbf{h}_\beta$ has the form

$$P_{\alpha\beta}^j = (\mathbf{h}_\alpha \mathbf{u}_j)(\mathbf{h}_\beta \mathbf{u}_j), \quad (28)$$

where $\mathbf{u}_j$ is the direction of the external field (atomic moment) at the jth nucleus. Obviously, under the effect of thermal fluctuations, the atomic moments preserve their directions only on average. These fluctuations can conveniently be described using the spin-wave (magnon) formalism. Within the framework of the harmonic approximation, the Hamiltonian of an antiferromagnetic crystal is the sum of the contributions from two magnetic sublattices

$$\mathcal{H} = \sum_q \hbar\omega_q a_q^\dagger a_q + \Omega_q b_q^\dagger b_q, \quad (29)$$

where $a_q^\dagger$ and a_q are the creation and the annihilation operators of a spin wave, respectively. For a hematite crystal in an external magnetic field $\mathbf{H}_\parallel$ ($T < T_N$), the spectrum of elementary magnetic excitations is determined by the expressions [28]:

$$\omega_q^2 = \omega^2(H) + v^2q^2, \quad \Omega_q^2 = \Omega^2(H) + v^2q^2, \quad (30)$$

$$\omega^2(H) = g^2(H(H+H_D)+2H_{ex}H_n) + gH_{ex}\omega_{ph}, \quad \Omega^2(H) = g^2H_aH_{ex} + \omega^2(H), \quad (31)$$

where H_a is the field of crystallographic anisotropy (2–3 kOe), H_{ex} is the field of the antiferromagnetic exchange between the sublattices (300 kOe), H_D is the Dzyaloshinski field, and H_n and ω_{ph} are provided by weak interactions between electrons and nuclear spins and phonons. It should be emphasized that even at $H = 0$ and $T = 0$, the violation of the axial symmetry of the magnetic subsystem results in a gap in the energy spectrum. In this case, the correlation function of a spin [29] relating the projections of spins at the sites j and $j + R$ is given by the following expression (the spectrally disordered system):

$$\Delta = \langle S_j^z S_{j+R}^z\rangle - S_0^2 \approx -(2S_0/N)\sum_q \langle a_g a_q^\dagger\rangle \exp(i\mathbf{qR}). \quad (32)$$

According to the Bose statistics, the average squared amplitude at high temperatures is

$$\langle a_g a_q^\dagger\rangle = kT/\hbar\omega_q. \quad (33)$$

Substituting expressions (30), (31), and (33) into definition (32) and performing integration over $\mathbf{q}$, we arrive at

$$\Delta = \frac{2S_0}{N\hbar}\sum_q \frac{kT}{\omega^2(H)+v^2q^2}\exp(i\mathbf{qR}) \sim \frac{c}{R}\exp(-R/\xi), \quad (34)$$

where ξ is the dimension of the region of spin ordering

$$\xi_1 = \omega(H)/v, \quad \xi_2 = \Omega(H)/v, \quad (35)$$

with each of the branches of spin excitations (analogues of the branches of the optical and acoustic vibrations) having its own region of ordering. The numerical evaluation of the parameter ξ_1 yields the value of 100–200 $a \approx$ 500–1000 Å.

Incoherent scattering from an ensemble of spin waves determines the following angular dependence of diffuse scattering in the vicinity of the reflection ($\mathbf{k}' = \mathbf{k}_g + \mathbf{q}$):

$$I_{\text{spin}}^{\text{dif}}(q) = I(0)\sum_{i=1,2}\frac{1}{1+\xi_i^2q^2}, \quad (36)$$

This dependence is essentially different from the dependence of q^{-2} for scattering from phonons and can give rise to the appearance of the diffuse-scattering "pedestal" considered below.

It should be indicated that similar effects can also be caused by the existence of nuclear spin waves [30], whose collective motion arises due to hyperfine interactions of nuclear and electron spins (the Sulla–Nakamura indirect exchange interaction).

Fluctuations in the Vicinity of a Phase Transition

With an approach to the phase-transition temperature, the spin system starts forming some ordered regions, whose further increase gives rise to the formation of a new long-range order. In general, diffuse scattering from these regions in the vicinity of the phase transition is elastic, although some phonons also take part in the formation of clusters of ordered spins.

Formally, we are interested in the spin correlation at the neighboring sites. In the quasichemical approximation (the generalized Curie–Weiss theory of the average field) [29, 31], the correlation length in the vicinity of the transition can be obtained in a form similar to (34), i.e.,

$$\xi = \left(\frac{T_C}{3(T_C - T/\mathcal{M})}\right)^{1/2} a, \quad \mathcal{M} = 1 - (M/M_0)^2, \quad (37)$$

where M is the average value of the magnetic moment (equal to zero at $T > T_C$ and to M_0 at $T = 0$) and a is the lattice constant. For a hematite crystal at room temperature, $T - T_N \approx 40$ K. The latter expression yields the correlation length equal to several interatomic distances.

The number of articles dedicated to order–disorder transition in the vicinity of the phase transition temperature T_C in magnetic crystals is among the largest in physics of condensed state. The appropriately chosen theoretical model and such methods as the cluster technique (the Bethe method [32]), the graph theory (Cayley's trees [33]), and the renorm-group methods [34], etc.) allow the extraction of valuable information about disorder in the spin system. The experiments on diffuse scattering of Mössbauer radiation can also provide the determination of such data.

DYNAMICAL DIFFRACTION OF MÖSSBAUER RADIATION

Let the z-axis be directed along the surface normal (the c-axis) of the hematite crystal whose direction coincides with the diffraction vector $\mathbf{g} = (hhh)$. The incident radiation passed through a crystal–monochromator can be approximated by a plane wave deviating for $\delta\theta$ from the exact Bragg angle.

In the general case of Mössbauer-radiation diffraction, the σ- and π-polarizations strongly interact [13–15]. However, in some occasions, this definition is quite profitable because the SR radiation is strongly polarized and, therefore, the use of the appropriate diffraction geometry (see Appendix 1) allows one to assume that the radiation is scattered without the change of its polarization.

Under the conditions of dynamical diffraction, the wave field with a known (σ) polarization can be represented as the sum

$$E(r) = E_0(r)\exp(i\mathbf{k}_0\mathbf{r}) + E_g(r)\exp(i\mathbf{k}_g\mathbf{r}), \quad (38)$$

where $E_{0,g}$ and $\mathbf{k}_{0,g}$ are the amplitude and the wave vector of the transmitted and diffracted waves, respectively.

Usually, the wave field in crystals with large-scale distortions is considered in terms of the Takagi–Taupin equations [35–37]:

$$\frac{dE_0}{dz} = i\hat{\sigma}_{00}E_0 + i\hat{\sigma}_{01}E_g,$$
$$\frac{dE_g}{dz} = i(\hat{\sigma}_{11} + \eta)E_0 + i\hat{\sigma}_{10}E_g. \quad (39)$$

For symmetric diffraction, we have

$$\hat{\sigma}_{\alpha\beta} = \frac{\pi\hat{\chi}(\mathbf{k}_\alpha - \mathbf{k}_\beta)}{\lambda\gamma_0}, \quad \eta = \frac{2\pi\sin(2\theta_0)}{\lambda\gamma_g}(\theta - \theta_0), \quad (40)$$

where $\chi_{0,g}$ are the Fourier-components of polarizability, $\gamma_{0,g}$ are the cosines of the angles formed by the inner normal and the vector $\mathbf{k}_0$, and λ is the wavelength of the incident radiation.

Coherent wave field. With due regard for incoherent processes, the amplitude of each wave equals the sum of the coherent and diffuse components

$$E_{0,g} = E^c_{0,g} + \delta E_{0,g}. \quad (41)$$

The same is true for crystal polarizability,

$$\hat{\sigma}_{ij} = \sigma_{ij} + \delta\sigma_{ij}. \quad (42)$$

It should be emphasized that in MR diffraction, the parameter σ_{00} also becomes a fluctuating quantity. However, we shall consider it to be a constant quantity because the diffraction scattering is determined mainly by the nondiagonal components $\sigma_{01,10}$; moreover, these effects were considered in detail in the description of the transmission of electromagnetic waves in a disordered media—the Earth's atmosphere [38].

Once the Takagi–Taupin equations [35, 36] are averaged with due regard for two moments of the polarizability distribution (the average value and dispersion Ω), we arrive at the following system of equations for the determination of coherent amplitudes:

$$-i\sigma_{00}E^c_0 + dE^c_0/dz = i\sigma_{01}E^c_g - \beta\sigma^2 L_0(z),$$
$$-i\Delta_{11}E^c_g + dE^c_g/dz = i\sigma_{10}E^c_0 - \beta\sigma^2 L_g(z), \quad (43)$$

where

$$L_0(z) = \int_0^z dz' \exp(i\Delta_{11}(z - z'))E^c_0(z'),$$
$$L_g(z) = \int_0^z dz' \exp(-i\sigma_{00}(z - z'))E^c_g(z'), \quad (44)$$
$$\beta = \frac{\pi^2}{(\lambda\gamma_0)^2\sigma^2}\Omega, \quad \sigma^2 = \sigma_{10}\sigma_{01}, \quad \Delta_{11} = \eta + \sigma_{11}.$$

The rigorous solution of system (43) with the use of the Laplace transform is considered in Appendix 2. The analysis of this solution shows that the wave field inside

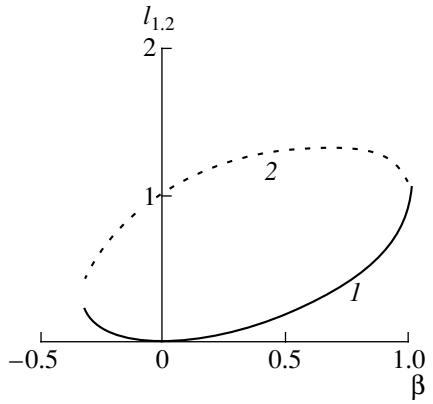

Fig. 2. Parameters (*1*) l_1 and (*2*) l_2 as functions of polarizability dispersion β.

the crystal consists of four Bloch waves with different refractive and absorption indices [see Eqs. (21)].

Two strong Bloch waves can be described with the use of the solution for an ideal crystal with the renormalized value of the crystal polarizability

$$\sigma^2 \longrightarrow \alpha_2\sigma^2, \quad \lim_{\beta \to 0} \alpha_2 = 1, \tag{45}$$

whereas two new Bloch waves are characterized by polarizability vanishing at $\beta \longrightarrow 0$, where

$$\alpha_{2,1} = (1/2)\{1 + 2\beta \pm \sqrt{(1 + 2\beta)^2 - 4\beta^2}\}. \tag{46}$$

The dependence of the refractive index for a split line can be analyzed only by numerical methods, because the crystal polarizability (both real and imaginary parts) is strongly dependent on the quantum energy. The calculation shows that with an increase of the parameter β, the peak value of the refractive index decreases, whereas the width of the rocking curve increases proportionally to $\sqrt{|\alpha_2|}$ (Fig. 2).

Generally speaking, the effect of disorder in the arrangement of isotopes on the coherent wave field is relatively weak, but it manifests itself in the diffraction-peak structure.

Figure 3 shows the refractive index $|R|^2$ as a function of the angular deviation η and the energy of an incident photon for the symmetric nuclear (777) reflection of hematite.

At present, the experiments on the scattering of Mössbauer radiation are performed at a number of synchrotron-radiation sources. Because of the time structure of the synchrotron radiation, the record of the diffraction signal within the interval between the synchrotron-radiation pulses allows one to separate the instantaneous electron response (the Rayleigh scattering) and the nuclear radiation which is generated within microseconds. One such method was being developed for a number of years for the NE3 station at the Accumulation Ring (AR) of the Photon Factory, Tsukuba, (Japan) [10, 20, 21, 39, 40]. At a Mössbauer station, an important role is played by X-ray optics used to reduce the contribution of electron scattering to the total recorded signal. In particular, the AR source is equipped with an asymmetric channel-cut monochromator with asymmetric (12, 2, 2) and (4, 2, 2) reflections, which can reduce the beam energy-width down to 6.7 meV.

However, even this energy resolution is insufficient for excitation of one of the hyperfine (Zeeman) nuclear transitions in the available magnetic fields. Thus, at the synchrotron-radiation pulse duration $\tau = 0.2$ ns [10, 21, 22], all the split levels are equally excited (the beam energy-width is $\Delta E = \hbar/2\tau \sim 10^{-5}$ eV).

Figure 4 shows the experimental rocking curves corresponding to the nuclear magnetic (777) reflection for natural and isotope-enriched ($c = 0.022$ and $c = 0.95$, respectively) hematite crystals [10, 21, 22, 39, 40]. It is seen that diffraction from the crystal with low isotope concentration is characterized by a broad halo caused by diffuse scattering and a rather low peak value. The rocking-curve width is almost the same as for diffraction from the isotope-enriched crystals. This indicates that the specimen experiences strong diffuse scattering whose intensity increases proportionally to coherent-scattering intensity, whereas the angular characteristics change only slightly. Indeed, in the absence of diffuse scattering, both the width and the height of the peak should increase proportionally to the isotope concentration (the average structure factor).

It should be emphasized that the total scattering intensity of both diffuse and coherent scattering for the isotope-enriched crystal ($c = 0.95$) dramatically decreases with the deviation from the Bragg condition by about 10 angular seconds (the inflection point).

For comparison, Figure 5 shows the calculated curves of the coherent-intensity distribution obtained by the conventional method (Fig. 5a) and with the invocation of the statistical theory [Fig. 5b, (777) reflection, $\beta = 0.1$ in arbitrary units]. The curves were obtained by integrating the intensity over the energy in the vicinity of the resonance at the crystal thickness $T = 10\lambda/g_0$. It is seen that the statistical calculation yields a broader rocking curve with a certain characteristic anomaly in the center.

Diffuse wave field. The experimentally observed quantities are the intensities of the diffracted, I_g, and transmitted, I_0, waves which both have coherent and diffuse components. The equations for determining the coherent component have already been derived. Those for determining the intensities of diffuse waves can be obtained as the differences between the averaged and coherent waves:

$$\langle I_n \rangle = I_n^c + I_n^d, \quad \langle \delta E_n^* \delta E_n \rangle = \langle I_n \rangle - I_n^c,$$
$$I_n^c = \langle E_n^* \rangle \langle E_n \rangle, \quad n = 0, g. \tag{47}$$

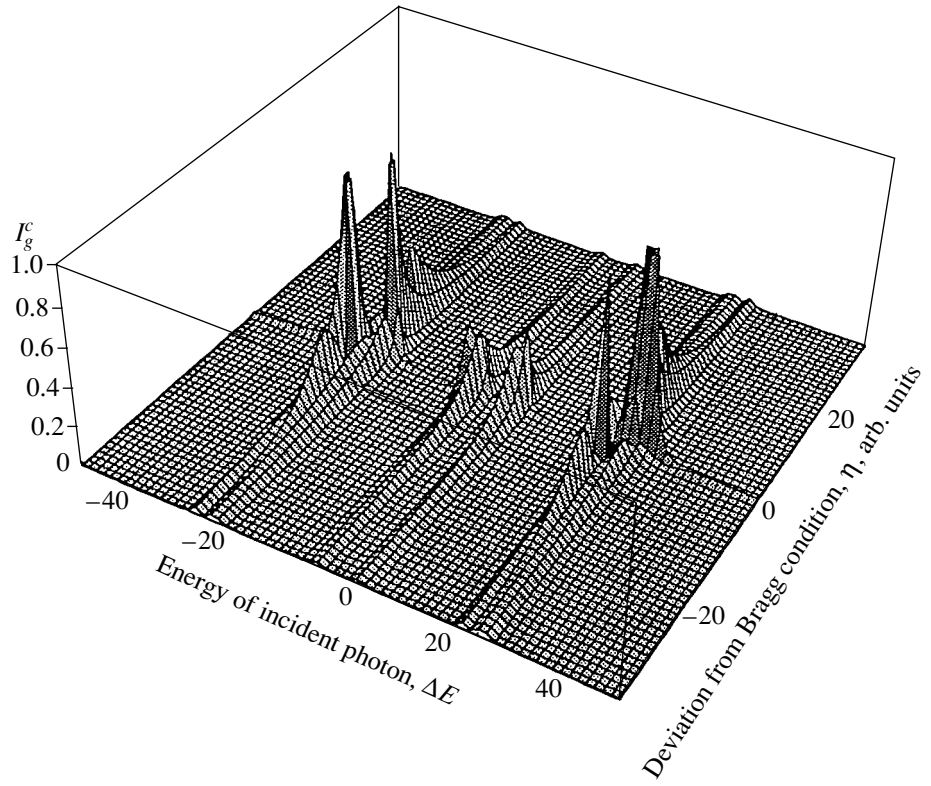

Fig. 3. The calculated reflection coefficient (coherent part) as a function of the angular deviation η and the energy of an incident photon; (777) reflection.

Using initial Takagi–Taupin Eqs. (39) and their averaged variant, Eqs. (43), one can also derive differential equations for the total and the coherent intensities,

$$\frac{d\langle I_n\rangle}{dz} = \mathrm{Re}\left(\left\langle E_n^* \frac{dE_n}{dz}\right\rangle\right),$$
$$\frac{dI_n^c}{dz} = \mathrm{Re}\left(E_n^{c*}\frac{dE_n^c}{dz}\right). \quad (48)$$

Omitting here the transformations made, we perform averaging, and subtract the coherent component from the total system of equations to arrive at the following diffuse wave intensities:

$$\frac{dI_0^d}{dz} = \mathrm{Re}\Big(i\sigma_{00}I_0^d + i\sigma_{01}\langle\delta E_0^*(z)\delta E_g(z)\rangle + \beta\sigma^2 L_0(z)E_0^{c*}(z)\Big),$$
$$\frac{dI_g^d}{dz} = \mathrm{Re}\Big(i\Delta_{11}I_g^d + i\sigma_{10}\langle\delta E_g^*(z)\delta E_0(z)\rangle + \beta\sigma^2 L_g(z)E_g^*(z)\Big). \quad (49)$$

In (49), we omitted both terms proportional to the odd products of the fluctuation component of polarizabilities and wave fields,

$$\langle\delta E_{0,g}^*\sigma_{01,10}\rangle = \langle E_{0,g}^c\delta\sigma_{01,10}\rangle = 0, \quad (50)$$

and also the terms proportional to

$$\langle\delta E_{0,g}^*\delta\sigma_{01,10}\rangle = \langle\delta E_{0,g}^c\delta E_{0,g}^c\delta\sigma_{01,10}\rangle = 0. \quad (51)$$

Using the well-known approximation from [35, 36], we can represent the contribution from the averaged

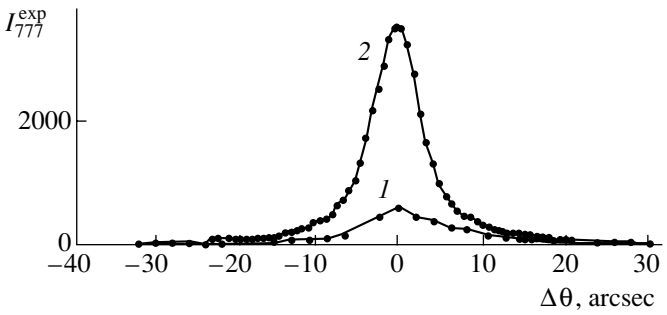

Fig. 4. Experimental rocking curves for the nuclear (777) reflection for (*1*) the crystal with the natural isotope concentration (c = 0.022) and (*2*) the isotope-enriched (c = 0.95) crystal; magnification ×40.

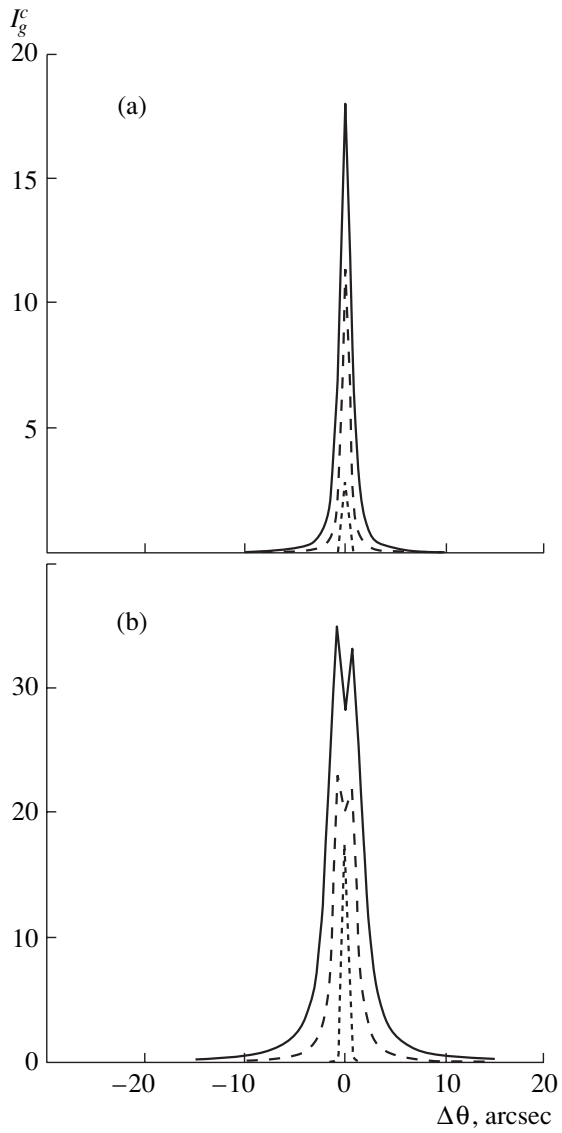

Fig. 5. Calculated rocking curves for the coherent intensity; (777) reflection: (a) calculation by the conventional method, (b) calculation by the statistical theory ($\beta = 0.1$); dashed line is obtained at the isotope concentration $c = 0.022$ (magnification ×40), solid line is obtained at the isotope concentration $c = 0.95$.

product of the fluctuations of the diffracted and transmitted waves in the form

$$\begin{aligned} &\mathrm{Re}(i\sigma_{01}\langle\delta E_0^*(z)\delta E_g(z)\rangle) \\ &\approx -2\,\mathrm{Re}(\sigma^2)\Gamma_c I_0^d + 2|\sigma_{01}|^2\Gamma_c I_g^d, \\ &\mathrm{Re}(i\sigma_{10}\langle\delta E_g^*(z)\delta E_0(z)\rangle) \\ &\approx -2\,\mathrm{Re}(\sigma^2)\Gamma_c I_g^d + 2|\sigma_{10}|^2\Gamma_c I_0^d. \end{aligned} \tag{52}$$

In fact, the latter expressions introduce into consideration the correlation length of the electromagnetic field under conditions of the dynamical diffraction, Γ_c.

It should be remembered that these expressions are not rigorous.

In accordance with the fluctuation–dissipative theorem, the fluctuations of the vector potential (the calibration $A_0 = \phi = 0$) are determined by the following expression [17]

$$\langle A_i(\mathbf{r}_1)A_j(\mathbf{r}_2)\rangle(\omega, \mathbf{k}) = -\coth\left(\frac{\hbar\omega}{kT}\right)\mathrm{Im}(D_{ij}^R(\omega, \mathbf{k})), \tag{53}$$

where $D_{ij}^R(\omega, \mathbf{k})$ is the Fourier-component of the delayed Green's function determined from the system of equations in which the statistical characteristics of the medium are expressed via the dielectric constant $\epsilon_{il}(\omega, \mathbf{r})$,

$$\begin{aligned} &\left\{\frac{\partial^2}{\partial x_i \partial x_l} - \delta_{il}\Delta - \frac{\omega^2}{c^2}\epsilon_{il}(\omega, r)\right\}D_{lk}^R(\omega, \mathbf{r}, \mathbf{r}') \\ &\quad = -4\pi\hbar\delta_{ik}\delta(\mathbf{r} - \mathbf{r}'). \end{aligned} \tag{54}$$

Thus, the problem of determining the statistical characteristics of the field is self-consistent. For dynamical diffraction, one of such self-consistent solutions was obtained in [41]. In the first approximation, it reduces to (52). For simplicity, we limit ourselves to the consideration of only this approximation.

Finally, the system of equations for determining the intensities of diffuse waves takes the form

$$\begin{aligned} \frac{dI_0^d}{dz} &= -\mu_0 I_0^d + \varphi_{0g} I_g^d + G_0(z), \\ \frac{dI_g^d}{dz} &= -\mu_g I_g^d + \varphi_{g0} I_0^d + G_g(z), \end{aligned} \tag{55}$$

where the following notation was introduced:

$$\begin{aligned} G_{0,g}(z) &= \mathrm{Re}(\beta\sigma^2 L_{0,g}(z)E_{0,g}^{c*}(z)), \\ \mu_{0,g} &= 2\,\mathrm{Im}(\sigma_{11,00}) + 2\,\mathrm{Re}(\sigma^2)\Gamma_c, \\ \varphi_{g0,0g} &= 2|\sigma_{10,01}|^2\Gamma_c. \end{aligned} \tag{56}$$

The correlation length of the electromagnetic field Γ_c determines the volume of the region inside which the field fluctuations are correlated. Under diffraction conditions, it is natural to assume [36] that Γ_c has the same order of magnitude as the extinction length, because any deviation of the transmitted beam would also affect, sooner or later, the diffracted beam and vice versa.

As follows from the above consideration, this parameter is introduced phenomenologically rather than calculated, because it is related to both coherence and wave characteristics of the incident radiation and to the parameters of the scattering medium.

In Bragg diffraction, the mutual scattering of transmitted and diffracted diffuse waves can be ignored [42–44]. Then

$$\frac{dI_g^d}{dz} = -\mu_g I_g^d + G_g(z). \quad (57)$$

The physical sense of Eq. (57) reduces to the competition of the two processes—transformation of coherent waves into diffuse ones at the expense of the fluctuations in polarizability ($G_g(z)$), which act as a source, and absorption, which either efficiently removes the radiation quanta from the diffuse beam or, at $\mu_g < 0$, adds the quanta to it.

The intensity of the diffuse component at the entrance surface of the crystal is obtained from (57) in the form

$$I_g^d(0) = -\int_0^T dz' \exp(\mu_g z') G_g(z'). \quad (58)$$

The analytical expressions for the coherent amplitudes of transmitted and diffracted waves are derived in Appendix 2. Substituting these expressions into (58), we have

$$G_g(z) = \mathrm{Re}\left(\sum_{k=1}^{4}\sum_{j=1}^{4}\rho_g^{kj}[\exp(i\{q_j - q_k^*\}z) - \exp(i\{q_j + \sigma_{00}^*\}z)\right), \quad (59)$$

where

$$\rho_g^{kj} = \beta\sigma^2 E_0^2(0)\frac{\xi_k^*\xi_j}{i(\sigma_{00} - q_k^*)}\psi_g^j\psi_g^{k*}. \quad (60)$$

Ignoring rapidly oscillating terms, we can represent the diffuse-wave intensity in the form

$$I_g^d = \mathrm{Re}\left(\sum_{k=1}^{4}\sum_{j=1}^{4}\rho_g^{kj}\left[\frac{1}{i(q_j - q_k^*) + \mu_g} - \frac{1}{i(q_j + \sigma_{00}^*) + \mu_g}\right]\right), \quad (61)$$

where q_k is the wave vector of the Bloch wave. The intensities of elastically scattered diffuse waves are directly proportional to the incident-wave intensity. In the absence of the polarizability dispersion ($\beta = 0$), it tends to zero.

Figure 6 shows the calculated rocking curves of the diffuse (Fig. 6a) and the diffuse and coherent (Fig. 6b) components in the vicinity of the (777) reflection for crystals with different isotope concentrations, $c = 0.022$ (dashed line) and $c = 0.95$ (solid line) at the polarizability dispersion β equal 0.1. The curves were obtained by integrating intensities over the energy in the vicinity of the resonance at the crystal thickness $T = 10\lambda/g_0$. The allowance for polarizability dispersion reduced the coherent component and led to the formation of the diffuse-scattering pedestal.

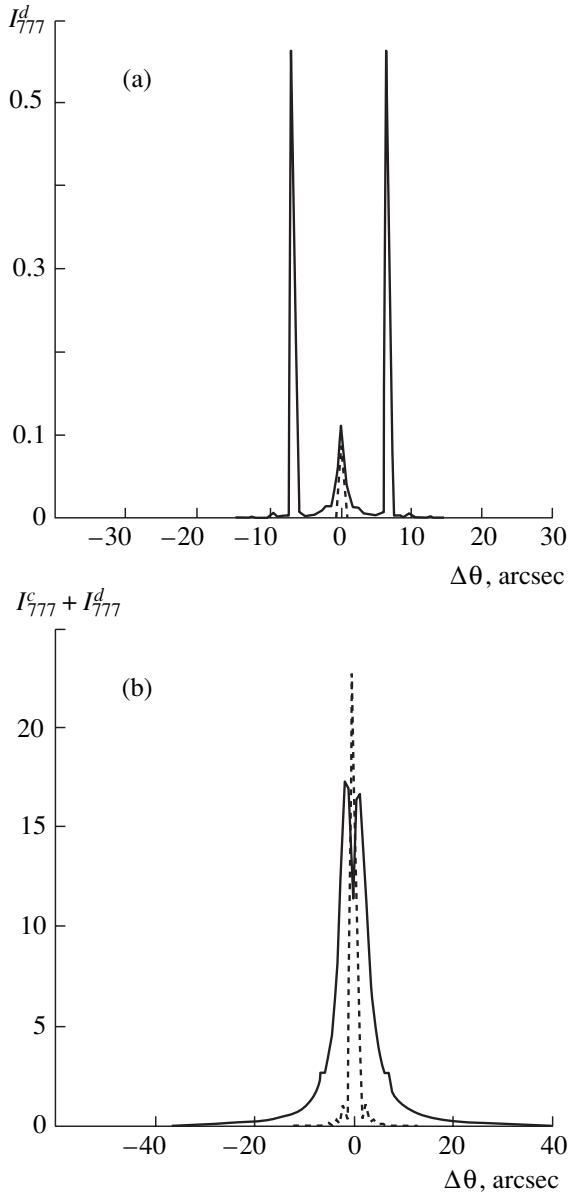

Fig. 6. Calculated rocking curves for hematite crystal; (777) reflection: (a) diffuse scattering, (b) diffuse and coherent scattering; dashed line is obtained at the isotope concentration $c = 0.022$ (magnification ×40) and solid line, at the isotope concentration $c = 0.95$.

We used the correlation-length value

$$\Gamma_c = 0.1\frac{\lambda\gamma_0}{\pi g_0}.$$

The remaining parameters are indicated in Appendix 1. Obviously, the diffuse-scattering plateau on the

Table 1. Polarization factors in scattering occurring without the change of polarization

σσ transition	$\Delta m = 0$	$\Delta m = \pm 1$
$2P_{00}$	D^2	D^2
$2P_{11}$	D^2	$-D^2$
$2P_{10}$	$-D^2$	$\cos2\theta - D^2 \pm iM\,u_z\sin2\theta$
$2P_{01}$	$-D^2$	$\cos2\theta - D^2 \mp iM\,u_z\sin2\theta$

Table 2. Polarization factors in scattering occurring with the change of polarization

σπ transition	$\Delta m = 0$	$\Delta m = \pm 1$
$2P_{00}$	$-Du_z$	$-Du_z \pm i\,\delta M\sin\theta$
$2P_{11}$	Du_z	$-Du_z \pm i\,\sin\theta\delta M$
$2P_{10}$	Du_z	$Du_z \pm i\,\sin\theta\delta M$
$2P_{01}$	$-Du_z$	$-Du_z \mp i\,\delta M\sin\theta$

Note: θ is the Bragg angle; $D = \cos\theta\delta M$.

Table 3. Polarizability of crystal as a function of the reflection index

Reflection	$\Phi_{00,\,11}$	$\Phi_{10,\,01}$
h is even	1	$\cos(6\pi uh)\cos2\theta$
h is odd	1	$\mp i\cos(6\pi uh)\sin2\theta$

Table 4. Parameters of hyperfine levels

m_e, m_g	Δm	δE, neV	$C_1^2(1/2, 1, 3/2; m_g, \Delta m_l)$
3/2, 1/2	1	419	$\frac{3}{12}$
1/2, −1/2	1	−63	$\frac{1}{12}$
−1/2, 1/2	−1	63	$\frac{1}{12}$
−3/2, −1/2	−1	419	$\frac{3}{12}$

Note: The energy width of the levels is $\Gamma_0 = 17$ meV.

experimental curve in Fig. 4 can be explained by the dramatic increase of the elastic diffuse scattering under certain deviations from the Bragg angle.

How to explain this anomaly in diffuse scattering? Consider again initial differential equation (57). Under conditions of the dynamical diffraction, the coherent electromagnetic field penetrates the crystal for a depth of the order of the extinction length. With the deviation from the Bragg angle, the penetration depth first increases, then becomes equal to

$$\mu_g = 2q_k'', \quad k = 1\text{–}4 \tag{62}$$

and, finally, exceeds the crystal depth at which diffuse waves can be formed $L = \mu_g^{-1}$. Such an increase in the volume within which diffuse waves are formed increases, in turn, the diffuse intensity. However, with the deviation from the Bragg angle, the intensity of the coherent wave drastically decreases, thus compensating the pronounced anomaly in diffuse scattering with an increase in the deviation from the Bragg condition.

In this experiment, we did not separate the elastically and the inelastically diffusely scattered waves, so that it was impossible to distinguish between the described increase in the peak of elastic diffuse scattering and scattering by spin waves or fluctuations in the vicinity of the phase transition.

As the calculations show, the change in the correlation length Γ_c results in the change of the height and the shift of the diffuse peak, which can be used for determining Γ_c.

CONCLUSION

In recent decades, the interest in diffuse scattering of X-rays has considerably increased. The development of the experimental diffraction methods has stimulated the widespread use of powerful sources of synchrotron radiation, whose high intensity provided the detection of weak diffuse signals. Considerable progress has also been achieved in the development of the statistical theory of diffraction in crystals with low defect concentrations and its experimental verification.

The study of the characteristics of diffuse scattering of the Mössbauer radiation under the conditions of dynamical diffraction provides valuable information about the sources of both elastic (domain structure, isotopic and spin incoherence order fluctuation) and inelastic (phonon and spin waves) diffusely scattered radiation.

The time structure of the synchrotron-radiation beams allows the experimental study of the decay of nuclear excitations in crystals and separation of the delayed nuclear radiation and the fast electron response. In terms of materials science, one of the important problems is the separation of the coherent and diffuse (elastic and inelastic) components [35, 36]. In principle, the elastic and inelastic components can be separated with the use of a Mössbauer crystal–analyzer tuned to a certain energy. The separation of the coherent and elastic diffuse components can be made only by numerical methods on the basis of a certain concrete model. The theory developed above allows the consistent analysis of the mutual effect of elastically scattered diffuse and coherent waves.

Also, this theory helps one to determine the correlation length of electromagnetic fields Γ_c from the diffuse

scattering data. It seems that further studies along these lines would allow better understanding of the nature of the fluctuations in the electromagnetic field inside crystals in nuclear and electron scattering.

ACKNOWLEDGMENTS

I should like to express my gratitude to M. Ando, K. Kohra, J. Zhao, and X.W. Zhang for their continuous interest in my work and useful discussions, for supplying me with the experimental data used in this article, and for the possibility to perform some studies at the Photon Factory in Tsukuba, Japan.

APPENDIX 1

Mössbauer Polarizability of Hematite Crystal

A hematite crystals (α-Fe_2O_3) is rhombohedral (sp. gr. D_{3d}^6 ($R\bar{3}c$)), with two molecules in the unit cell and the lattice parameters $a_0 = 5.4243$ Å, $\alpha = 55.17°$, $V_c = 100.5$ Å^3 (Fig. 1).

The coordinates of four Fe^{+3} ions (*A*, *B*, *C*, and *D*) can be represented in the a_0 units with the positional parameter $u = 0.355$ as

$$A\colon (-u, -u, -u), \quad B\colon \left(u - \frac{1}{2}, u - \frac{1}{2}, u - \frac{1}{2}\right),$$
$$C\colon \left(\frac{1}{2} - u, \frac{1}{2} - u, \frac{1}{2} - u\right), \quad D\colon (u, u, u). \tag{1.1}$$

As was indicated above, we limited our consideration to the nuclear part of crystal polarizability. Let a photon with the wave vector $\mathbf{k}_\alpha$ and the unit vectors of the electric, $\mathbf{e}_\alpha$, and magnetic, $\mathbf{h}_\alpha$, fields be transformed due to scattering into the state with the indices β ($\alpha, \beta = 0, g$). The unit vectors of these fields are related by the transversality condition

$$\mathbf{h}_\alpha = [\mathbf{e}_\alpha, \mathbf{k}_\alpha]/K. \tag{1.2}$$

Taking into account hyperfine splitting, the nuclear component of susceptibility can be written as the sum taken over several transitions between the levels of the ground and excited states of a nucleus with different values of the projections of the magnetic moment. Taking into account only the magnetic-dipole transitions, the incident radiation with the σ polarization can be written as

$$\chi(\mathbf{k}_\alpha - \mathbf{k}_\beta) = cg_0 \sum_{l=1}^{4} \sum_j \exp\{i(\mathbf{k}_\alpha - \mathbf{k}_\beta)\mathbf{r}_j\} P_{\alpha\beta}^j$$
$$\times \exp(-M_j) \frac{1}{\Delta E_l + i} C_1^2(I_g, l, I_e; m_g, \Delta m_l), \tag{1.3}$$

where M_j is the Lamb–Mössbauer factor for the *j*th atom of the unit cell, C_1 is the Clebsch–Gordon coefficient, I_g and I_e are the moments of the ground and the excited nuclear states, respectively, m_g and Δm_l are the projections of the moment onto the quantization axis in the ground state and its change upon transition, and α is the internal-conversion coefficient ($\alpha^{57} = 9$). Thus we have

$$g_0 = -\frac{3\lambda^3}{4\pi^2 V_c} \frac{1}{2I_g + 1} \frac{1}{1 + \alpha}, \quad \Delta E_l = \delta E_l/\Gamma. \tag{1.4}$$

where $P_{\alpha\beta}^j$ is the nuclear polarization factor dependent on the direction of unit magnetic vectors of the incident and scattered radiation, $\mathbf{h}_\alpha$ and $\mathbf{h}_\beta$, and the direction of the magnetic field at the nucleus of the *j*th atoms, $\mathbf{u}_j$,

$$P_{\alpha\beta}^j = (\mathbf{h}_\alpha \mathbf{u}_j)(\mathbf{h}_\beta \mathbf{u}_j). \tag{1.5}$$

There are three temperature intervals within which a hematite crystal possesses different magnetic structures. Above the Neél temperature ($T_N = 948$ K), all the magnetic moments of hematite are completely disordered due to thermal vibrations (the paramagnetic structure).

In the temperature range $T_M < T < T_N$, where T_M is the temperature of the Morin transition ($T_M = 253$ K), the spins of iron atoms in the positions *A* ($\mathbf{M}_1$) and *B* ($\mathbf{M}_2 \approx -\mathbf{M}_1$) are directed almost opposite to each other, which results in the formation in the bulk of a weak ferromagnetic moment (0.4 G cm^3 g^{-1}) normal to the main spin direction in the (111) plane (Fig. 1).

Below the temperature of the Morin transition ($T < T_M$), the spins are aligned in the direction of the *c*-axis of the crystal, and hematite becomes antiferromagnetic.

In the experiments described in [10, 21, 22], a weak magnetic field $\mathbf{H}_\parallel$, was applied to the specimen parallel to the diffraction plane (normally to the *c*-axis) (Fig. 1)

$$\mathbf{H}_\parallel = (-H, 0, 0), \tag{1.6}$$

which resulted in the transition of the specimen to the single-domain state and the alignment of most of the magnetic moments, $\mathbf{M}_i$, of atoms normally to the applied field $\mathbf{H}_\parallel$

$$\mathbf{M}_{B,A} = (-\delta M, \pm M, 0), \quad M \approx M_0 - \frac{1}{2M_0}(\delta M)^2. \tag{1.7}$$

To study of the influence of spin fluctuations, we took into account a weak ferromagnetic moment of the crystal volume directed along the field, despite the fact that its numerical value was very low, $\delta M/M_0 \approx 10^{-4}$.

Depending on the difference between the projections of the moments in the ground and excited states

(Δm), several variants are possible:

$$\mathbf{u}_l(\Delta m = 0) = \mathbf{u}_z,$$
$$\mathbf{u}_l(\Delta m = \pm 1) = \mp\frac{1}{\sqrt{2}}(\mathbf{u}_x \pm i\mathbf{u}_y), \quad (1.8)$$

where ($\mathbf{u}_x$, $\mathbf{u}_y$, $\mathbf{u}_z$) is the right-hand set of the unit vectors in the system of coordinates in which the vector $\mathbf{u}_z$ is parallel to **M**. Performing some obvious transformations, we can readily obtain

$$P_{\alpha\beta}(\Delta m = 0) = (\mathbf{h}_\alpha \mathbf{u}_z)(\mathbf{h}_\beta \mathbf{u}_z),$$
$$P_{\alpha\beta}(\Delta m = \pm 1) \quad (1.9)$$
$$= (1/2)\{(\mathbf{h}_\alpha \mathbf{h}_\beta) - (\mathbf{h}_\alpha \mathbf{u}_z)(\mathbf{h}_\beta \mathbf{u}_z) \mp i([\mathbf{h}_\alpha, \mathbf{h}_\beta]\mathbf{u}_z)\}.$$

It is convenient to consider the σ and π polarizations of the incident radiation separately,

$$\mathbf{h}^{\sigma}_{0,g} = (\pm\cos\theta, 0, \sin\theta), \quad \mathbf{h}^{\pi}_{0,g} = (0, -1, 0). \quad (1.10)$$

Substituting the above expressions into definition (1.9), we arrive at $P_{\alpha\beta}$ for individual transitions.

Diffraction of the incident σ-polarized radiation proceeds mainly without the change of polarization (Table 1), whereas the scattering channel changes the polarization $\sigma \longrightarrow \pi$ and can be considered with the invocation of the perturbation theory because of the smallness of δM (Table 2).

If the incident radiation is σ-polarized, the main process is the diffraction scattering without the change of the polarization, whereas the scattering channel changes the polarization, $\sigma \longrightarrow \pi$, which can be considered according to the perturbation theory (because of the smallness of δM). Moreover, in scattering with $\sigma \longrightarrow \sigma$, one has to take into account only four transitions, these with $\Delta m = \pm 1$.

Kinematical scattering with the change of polarization, $\sigma \longrightarrow \pi$, reduces the number of coherent quanta participating in dynamical diffraction. Taking into account the smallness of the corresponding polarizability component of the crystal, one can ignore a possible inverse transition of the quantum, $\pi \longrightarrow \sigma$. Using the expansion of the coherent beams in Bloch waves (see Appendix 2),

$$E^c_{0,g} = \sum_{l=1}^{4} a^l_{0,g} \exp(i\mathbf{k}_l \mathbf{r}), \quad \mathbf{k}_l = q_l z + \mathbf{k}_{0,g},$$

we obtain for the cross section of the kinematical elastic scattering along the direction $\mathbf{k}'$

$$\frac{d\sigma(k')}{d\Omega} \sim (1/N)\left|\sum_{l=1}^{4}(\chi^{\sigma\pi}_{01}(\mathbf{k}-\mathbf{k}')a_0 + \chi^{\sigma\pi}_{11}(\mathbf{k}-\mathbf{k}')a_1)\sum_j \exp(i(\mathbf{k}-\mathbf{k}')\mathbf{x}_j)\right|^2.$$

Usually, the final formulas are simplified by tending the final limits of summation over the unit cell number j to infinity. Let the region of the crystal providing diffraction be finite ($N_1 \times N_2 \times N_3$), then the maximum of the kinematical scattering is of finite width

$$\delta k_m = \frac{\pi}{4N_m},$$

because

$$F(\mathbf{k}-\mathbf{k}') = \prod_{m=1}^{3}\left|\sum_{x_m=0}^{N_m}\exp(i(\mathbf{k}_m - \mathbf{k}'_m)\mathbf{x}_m)\right|^2$$
$$= \prod_{m=1}^{3}\frac{\sin^2((N_m+1)(k_m - k'_m)/2)}{\sin^2((k_m - k'_m)/2)}.$$

Because of the complicated variation of the coherent-wave amplitudes with the deviation from the Bragg angle, the resulting width of such kinematical peak can exceed the width of the dynamical rocking curve. Thus, the formation of a diffuse-scattering pedestal can additionally be caused by scattering with the change of polarization.

For the reflections $\mathbf{g} = (h, h, h)$ in the hematite crystal, the summation for scattering with $\sigma \longrightarrow \sigma$ over all the iron atoms yields (without the allowance for weak ferromagnetism)

$$\chi_{\alpha\beta} = 2cg_0\frac{1}{\Delta E_l + i}C_1^2(I_g, l, I_e, m_g, \Delta m_l)\Phi^l_{\alpha\beta},$$
$$\Phi^l_{\alpha\beta} = \cos(6\pi uh)P^{n,l}_{\alpha\beta}(u_z) \quad (1.11)$$
$$+ \cos(6\pi uh - 3\pi h)P^{n,l}_{\alpha\beta}(-u_z).$$

The values of coefficients $\Phi^l_{\alpha\beta}$ are listed in Table 3.

In the case under consideration, the internal magnetic field splits the nuclear transition at the energy E = 14.413 keV into four symmetric levels with the deviations $E_l = E + \delta E_l$ whose parameters are indicated in Table 4.

APPENDIX 2

Coherent Wave Field. Exact Solutions

Now, apply the Laplace transform [45] to system (43) of Takagi equations for coherent waves. The use of the conventional transformation rules

$$\frac{dE^c_{0,g}(z)}{dz} \Rightarrow se_{0,g}(s) - E_{0,g}(0),$$
$$\exp(i\Delta_{11}z)E^c_{0,g}(z) \Rightarrow (s + i\Delta_{11})e^c_{0,g}(s), \quad (2.1)$$
$$\int_0^z dz' g(z') \Rightarrow g(s)/s$$

reduces the integro-differential system of the Takagi equations to the algebraic system of equations for the Laplace transforms

$$\begin{aligned} A_{00}e_0^c(s) - i\sigma_{10}e_g^c(s) &= E_0(0), \\ -i\sigma_{01}e_0^c(s) + A_{gg}e_g^c(s) &= E_g(0), \end{aligned} \tag{2.2}$$

where

$$\begin{aligned} A_{00}(s) &= -i\sigma_{00} + s + \beta\sigma^2\frac{1}{s - i\Delta_{11}}, \\ A_{gg}(s) &= -i\Delta_{11} + s + \beta\sigma^2\frac{1}{s - i\sigma_{00}}. \end{aligned} \tag{2.3}$$

The solution to the latter system of equations has the form

$$\begin{aligned} e_0^c(s) &= \frac{1}{\mathrm{Det}}\{i\sigma_{10}E_g(0) + A_{gg}E_0(0)\}, \\ e_g^c(s) &= \frac{1}{\mathrm{Det}}\{i\sigma_{01}E_0(0) + A_{00}E_g(0)\}, \end{aligned} \tag{2.4}$$

where

$$\begin{aligned} \mathrm{Det} &= A_{gg}A_{00} + \sigma_{10}\sigma_{01} = \frac{D(s)}{l(s)}, \\ l(s) &= (s - i\sigma_{00})(s - i\Delta_{11}), \\ D(s) &= (l + \beta\sigma^2)^2 + \sigma^2 l, \quad \sigma^2 = \sigma_{10}\sigma_{01}. \end{aligned} \tag{2.5}$$

The zeroes of the function Det(s) determine four points of the pole s_k of the function $e_{0,g}$. In other words, the solution obtained consists of four waves (k = 1–4),

$$D(s_k) = 0. \tag{2.6}$$

The function $D(s)$ can be represented as

$$\begin{aligned} D(s) &= (l - l_1)(l - l_2) = \prod_{j=1}^{4}(s - s_j), \\ s_j &= iq_j. \end{aligned} \tag{2.7}$$

For symmetric diffraction, the positions of the pole points are determined by the wave vectors of Bloch waves in the crystal

$$\begin{aligned} q^s_{1,2} &= \eta/2 \pm \sqrt{(\eta/2 - \sigma_{00})^2 - l_1^2}, \\ q^s_{3,4} &= \eta/2 \pm \sqrt{(\eta/2 - \sigma_{00})^2 - l_2^2}, \end{aligned} \tag{2.8}$$

where the constants $l_{1,2}$ correspond to new values of the crystal polarizability,

$$\begin{aligned} l^2_{1,2} &= \alpha_{1,2}\sigma^2, \\ \alpha_{1,2} &= 1/2\{1 + 2\beta \mp \sqrt{(1 + 2\beta)^2 - 4\beta^2}\}. \end{aligned} \tag{2.9}$$

Figure 2 shows the dependence of the parameter $\sqrt{\alpha_{1,2}}$ (dashed and solid lines) on polarizability dispersion β. If the β values are low, the contribution of weak reflections

$$l_1 \approx 3\beta^2\sigma^2$$

can be ignored in comparison with strong ones whose polarizabilities are close to the polarizability of an ideal crystal,

$$l_2 \approx \sigma^2(1 + 2\beta).$$

Now, return to the calculation of the coherent-wave amplitudes using known Laplace transforms (2.5). According to the well-known rules considered in [45], the initial function is equal to

$$\frac{F(s)}{D(s)} \Rightarrow \sum_{k=1}^{4}\frac{F(s_k)}{D_k}\exp(s_k z), \quad z > 0, \tag{2.10}$$

where s_k are the points of the pole determined by (2.7),

$$D_k = \prod_{j=1,\, j\neq k}^{4}(s_k - s_j). \tag{2.11}$$

One can readily see that the poles of the expression A_{00} are compensated with the corresponding parts of the expression for D. Performing the necessary transformations, we obtain

$$\begin{aligned} E_g^c(z) &= \sum_{k=1}^{4}\xi_k\exp(iq_k z)\{E_g(0)A_{00}(s_k) + i\sigma_{01}E_0(0)\}, \\ E_0^c(z) &= \sum_{k=1}^{4}\xi_k\exp(iq_k z)\{i\sigma_{10}E_g(0) + A_{gg}(s_k)E_0(0)\}, \end{aligned} \tag{2.12}$$

where

$$\begin{aligned} \xi_k &= \frac{l(s_k)}{D_k}, \quad \xi_{2,1} = \pm\frac{il_1}{Q_1 L}, \quad \xi_{3,4} = \pm\frac{il_2}{Q_2 L}, \\ Q_{1,2} &= q_1^s - q_2^s = 2\sqrt{(\eta/2 - \sigma_{00})^2 - l_{1,2}}, \\ L &= l_1 - l_2 = |\sigma^2|\sqrt{(1 + 2\beta)^2 - 4\beta^2}. \end{aligned}$$

For Laue diffraction, the diffracted-wave amplitude at the entrance surface of the crystal equals zero, $E_g(0) = 0$. Thus, we have

$$E_g^c(z) = i\sigma_{01}E_0(0)\sum_{k=1}^{4}\xi_k\exp(iq_k z).$$

For Bragg diffraction, the boundary conditions should be satisfied at the exit surface of the crystal,

$$E_g^c(T) = 0,$$

whence the diffracted-wave amplitude at the entrance

surface of the crystal is determined by the expression

$$E_g(0) = RE_0(0),$$
$$R = -i\frac{\sigma_{01}\sum_{k=1}^{4}\xi_k \exp(iq_kT)}{\sum_{k=1}^{4}\xi_k A_{00}(s_k)\exp(iq_kT)}, \quad (2.13)$$

where R is the reflection coefficient.

To calculate the diffuse intensities, we have to use not only the reflection coefficient, but also the coherent wave field inside the crystal. Substituting the reflection coefficient R into Eqs. (2.4), we obtain

$$E^c_{0,g}(z) = E_0(0)\sum_{k=1}^{4}\xi_k \exp(iq_kz)\psi^k_{0,g}, \quad (2.14)$$

where

$$\psi^k_0 = i\sigma_{10}R + A_{gg}(q_k), \quad \psi^k_g = i\sigma_{0g} + A_{00}(q_k)R. \quad (2.15)$$

REFERENCES

1. A. M. Afanas'ev and Yu. Kagan, Zh. Éksp. Teor. Fiz. **48**, 327 (1965) [Sov. Phys. JETP **21**, 215 (1965)].
2. J. P. Hannon and G. T. Trammell, Phys. Rev. **169**, 315 (1968).
3. P. I. Black and P. B. Moon, Nature **188**, 488 (1960).
4. V. K. Voĭtovetskiĭ, I. L. Korsunskiĭ, A. I. Novikov, *et al.*, Pis'ma Zh. Éksp. Teor. Fiz. **11**, 149 (1970) [JETP Lett. **11**, 91 (1970)].
5. G. V. Smirnov, N. I. Semeshkina, V. V. Sklyarevskiĭ, *et al.*, Zh. Éksp. Teor. Fiz. **71**, 2214 (1976) [Sov. Phys. JETP **44**, 1167 (1976)].
6. U. Burck, G. V. Smirnov, R. L. Mössbauer, *et al.*, J. Phys. C **11**, 2305 (1978).
7. G. V. Smirnov, V. V. Sklyarevskii, A. A. Artem'ev, *et al.*, Phys. Lett. A **32A**, 532 (1970).
8. U. Burck, R. L. Mössbauer, E. Gerdau, *et al.*, Phys. Rev. Lett. **59**, 355 (1987).
9. R. Ruffer, E. Gerdau, H. D. Rutter, *et al.*, Phys. Rev. Lett. **63**, 2677 (1989).
10. S. Kikuta, Y. Yoda, Y. Hasegawa, *et al.*, Hyperfine Interact. **71**, 1491 (1992).
11. J. B. Hastings, D. P. Siddons, G. Faigel, *et al.*, Phys. Rev. Lett. **63**, 2252 (1989).
12. D. C. Champeney, Rep. Prog. Phys. **42** (6), 1017 (1979).
13. V. A. Belyakov, *Diffraction Optics of Periodic Media with Complicated Structure* (Nauka, Moscow, 1988; Springer-Verlag, New York, 1992).
14. M. A. Andreeva and R. N. Kuz'min, *Mössbauer Gamma-Ray Optics* (Mosk. Gos. Univ., Moscow, 1982).
15. *Resonant Anomalous X-ray Scattering*, Ed. by G. Materlik *et al.* (North-Holland, Amsterdam, 1994), Part VI.
16. V. A. Belyakov and R. N. Kuz'min, *Mössbauer Diffraction* (Znanie, Moscow, 1979), News in Life, Science, Technology, Series Physics, No. 1.
17. E. M. Lifshitz and L. P. Pitaevskiĭ, *Course of Theoretical Physics*, Vol. 5: *Statistical Physics* (Fizmatlit, Moscow, 2000; Pergamon, New York, 1980), Part 2.
18. R. Blinc and B. Zéks, *Soft Modes in Ferroelectrics and Antiferroelectrics* (North-Holland, Amsterdam, 1974; Mir, Moscow, 1975).
19. S. A. Grigoryan, M. V. Kovalchuk, and V. L. Nosik, Poverkhnost **8**, 5 (1999).
20. P. Bardhan and J. B. Cohen, Acta Crystallogr., Sect. A: Cryst. Phys., Diffr., Theor. Gen. Crystallogr. **32**, 597 (1976).
21. C. K. Suzuki, H. Ohno, H. Takei, *et al.*, Rev. Sci. Instrum. **63**, 1206 (1992).
22. C. K. Suzuki, H. Takei, F. Sakai, *et al.*, Jpn. J. Appl. Phys. **32**, 3900 (1993).
23. G. E. Bacon, *Neutron Diffraction* (Clarendon, Oxford, 1955; Inostrannaya Literatura, Moscow, 1967).
24. *Problems in Solid State Physics*, Ed. by H. J. Goldsmid (Academic, New York, 1968; Nauka, Moscow, 1976).
25. A. M. Afanas'ev and Yu. Kagan, Acta Crystallogr., Sect. A: Cryst. Phys., Diffr., Theor. Gen. Crystallogr. **24**, 164 (1967).
26. A. M. Afanas'ev and Yu. Kagan, Zh. Éksp. Teor. Fiz. **52**, 191 (1967) [Sov. Phys. JETP **25**, 124 (1967)].
27. A. S. Davydov, *Theory of Atomic Nucleus* (Fizmatlit, Moscow, 1958).
28. V. S. L'vov, *Nonlinear Spin Waves* (Nauka, Moscow, 1987).
29. J. M. Ziman, *Models of Disorder: the Theoretical Physics of Homogeneously Disordered Systems* (Cambridge Univ. Press, Cambridge, 1979; Mir, Moscow, 1982).
30. V. A. Tulin, Fiz. Nizk. Temp. **5**, 965 (1979) [Sov. J. Low Temp. Phys. **5**, 455 (1979)].
31. R. H. Brout, *Phase Transitions* (Benjamin, New York, 1965; Mir, Moscow, 1967).
32. H. A. Bethe, Proc. R. Soc. London, Ser. A **216**, 45 (1935).
33. *Graph Theory and Theoretical Physics*, Ed. by F. Harary (Academic, London, 1967).
34. L. P. Kadanoff, in *Phase Transitions and Critical Phenomena*, Ed. by C. Domb and M. S. Green (Academic, London, 1976), Vol. 5a, p. 1.
35. N. Kato, Z. Naturforsch. A **28**, 604 (1973).
36. N. Kato, Acta Crystallogr., Sect. A: Cryst. Phys., Diffr., Theor. Gen. Crystallogr. **36**, 763 (1980).
37. N. Kato, Acta Crystallogr., Sect. A: Cryst. Phys., Diffr., Theor. Gen. Crystallogr. **36**, 770 (1980).
38. J. W. Goodman, *Statistical Optics* (Wiley, New York, 1985).
39. J. Zhao, *Study of Nuclear-Resonant Bragg Scattering from Synthetic 2.2% and 95% Fe57* Hematite Single Crystal PhD Thesis (Tsukuba, 1996).
40. S. Yamamoto, X. W. Zhang, H. Kitamura, *et al.*, J. Appl. Phys. **74**, 500 (1993).
41. A. M. Polyakov, F. N. Chukhovskii, and D. I. Piskunov, Zh. Éksp. Teor. Fiz. **99** (2), 589 (1991) [Sov. Phys. JETP **72**, 330 (1991)].
42. P. H. Dederichs, Phys. Rev. B **1**, 1306 (1970).
43. V. I. Punegov, Fiz. Tverd. Tela (Leningrad) **33** (1), 234 (1991) [Sov. Phys. Solid State **33**, 136 (1991)].
44. V. A. Bushuev, Fiz. Tverd. Tela (Leningrad) **31** (11), 70 (1989) [Sov. Phys. Solid State **31**, 1877 (1989)].
45. G. A. Korn and T. M. Korn, *Mathematical Handbook for Scientists and Engineers* (McGraw-Hill, New York, 1961; Nauka, Moscow, 1973).

Translated by L. Man

Crystallography Reports, Vol. 47, No. 1, 2002, pp. 101–105. Translated from Kristallografiya, Vol. 47, No. 1, 2002, pp. 108–113.

REAL STRUCTURE OF CRYSTALS

Irradiation-Induced Diffusion in Tracks of Swift Ions

V. N. Peregudov and V. M. Manichev

Russian Research Centre Kurchatov Institute, pl. Kurchatova 1, Moscow, 123182 Russia

e-mail: vlad@dni.polyn.kiae.su

Received February 22, 2001

Abstract—Radiation-induced diffusion in tracks of swift ions caused by excitation of electrons and resulting in the formation of dilatations has been considered. The expressions for the longitudinal and radial atomic displacements are derived as well as those for the diagonal components of the strain tensor. The atomic-density distribution in the vicinity of a track is obtained in terms of the parameters of the three-dimensional energy distribution in an excited electron gas. The results obtained theoretically are compared with the known experimental data. The suggested approach provides the evaluation of the time of formation of track dilatations, the mobility of the atoms in the target irradiated with swift ions, and the energy losses for formation of wirelike dilatations in the tracks. It is shown that the ion irradiation of semiconductor crystals can be used for obtaining one-dimensional quantum objects. © *2002 MAIK "Nauka/Interperiodica".*

The interaction of high-energy ions with matter is accompanied by a considerable energy release into the electron subsystem of the target, which occurs in the narrow region along the track axis. This process gives rise to such phenomena as anomalous defect formation [1, 2], alloy amorphization [3, 4], the so-called anisotropic expansion at low temperatures, and creep along the directions normal to the ion beam [5–8]. A number of theoretical studies are also devoted to the models of thermal spike [9–12], Coulomb explosion [13–15], soft phonon modes [16], modification of structure [17], and the local electric field excited by δ-electrons in tracks [18]. The wide use of semiconductor crystals as detectors of high-energy ions stimulated the studies of their degradation and, thus, also of all the accompanying physical processes in the tracks. The characteristic features of defect formation in silicon crystals irradiated with 5.6-GeV Xe-ions and 0.21-GeV Kr-ions were studied by the method of double-crystal X-ray diffractometry [19]. The experimental data obtained show that the atomic density in the Kr-ion tracks decreases by about 10%, which is indicated by the appearance of the second maximum on the dependence of the interplanar spacing Δd on crystal depth at high irradiation doses. This effect is attributed to ions that hit the "old" tracks and whose track length exceeds the conventional value by 10%. The modern methods of structural diagnostics based on the triple-crystal X-ray diffractometry allows one to single out diffuse scattering the study in detail the specific features of dilatations in the swift-ion tracks. These data show that it is possible to create one-dimensional quantum objects by irradiating semiconductor crystals with swift ions. The detailed review of the research and application of low-dimensional quantum systems [20] is focused on the systems based on the semiconductor heterostructures. The recent advances in the study of heterostructures and their use in laser technology stimulate the search for new alternative methods of obtaining low-dimensional quantum systems. The irradiation of semiconductor crystals with high-energy ions can be considered as a method for obtaining one-dimensional quantum wires formed due to mutual repulsion of atomic chains between which the track axis is located. The energy released by swift ions is spent mainly for the excitation of an electron gas with a high value of the pressure gradient which can exceed the shear modulus and give rise to an irreversible plastic deformation of the lattice in a narrow region along the track axis.

Below, we suggest a mechanism of formation of track dilatations based on the diffusion of target atoms caused by the pressure gradient of the electron gas excited in the track region. The pressure of the electron gas is determined by the spatial distribution of the energy density of excited electrons. In the case of the azimuthal symmetry, the electron-gas pressure $P(z, r, t)$ is a function of time t and the longitudinal and radial coordinates, z and r. This corresponds to the case where the electron distribution is independent of the electron-momentum direction. If the relaxation time of an electron momentum τ_p is much less than the time of the energy relaxation τ, the target atoms, which cannot be displaced for too short a time $\tau_p \approx 10^{-16}$–10^{-15} s, can be displaced for the longer time τ. The considerable ionization of target atoms in the track region provides their sufficient mobility b within the relaxation time. Let the origin of the reference system be located on the irradiated surface and the z-axis be directed along the direction of the velocity of an impinging ion. Then the equation for the averaged displacement velocities of target atoms $\mathbf{v}(z, r)$ in a homogeneous isotropic medium has the form

$$n_0\mathbf{v} = -b\,\mathrm{grad}\,P(z, r, t), \quad (1)$$

where n_0 is the atomic density of the medium. It follows from Eq. (1) that the displacement of an atom depends on the degree of the spatial inhomogeneity of the electron-energy distribution. Equation (1) shows that, similar to the velocity field $\mathbf{v}(z, r)$, the displacement field $\mathbf{u}(z, r)$ is also determined by the change in the local shape of the isoenergetic surface at each point of the track during relaxation. Consider the case where the spatial shape of the isoenergetic surfaces is preserved for rather a long time interval $\tau_p < t < \tau_r$. Then, the radial dispersion of the spatial electron-energy distribution $P(z, r, t)$ varies noticeably only within the time of the electron–electron collisions determined by the diffusion coefficient of electrons $\chi_e \approx v_e l_{tr} \le 1$ cm^2/s. Therefore, the spatial broadening of the distribution $P(z, r, t)$ with the characteristic radius $r_0 \approx 1$–2 nm can occur within the time $\tau_r \ge 10^{-14}$ s. It is also assumed that the time-of-flight of an impinging ion is much shorter than the relaxation time τ and that $P(z, r, t)$ decreases by the exponential law $P(z, r, t) = p(z, r)\exp(-t/\tau)$ within the time interval $\tau_p < t < \tau_r$. Then, Equation (1) gives the displacement $\mathbf{u}$ determined by

$$n_0\mathbf{u} = -\tau b \operatorname{grad} p(z, r). \qquad (2)$$

Now, consider the effect of the spatial shape of the electron-energy distribution $p(z, r)$ on the character of deformations. Within the framework of this approach, the constant mobility b of atoms is assumed to be "switched-on" within the time interval when the target atoms are ionized. Then the displacement field $\mathbf{u}(z, r)$ becomes similar to the velocity field, and the target atoms are displaced along the normal $\mathbf{n}(z, r)$ to the isoenergetic surface passing through the given point

$$u(z, r) = -\frac{\tau b}{n_0}\frac{dp}{ds}, \qquad (3)$$

where $s = [r^2 + (z - z_0)^2]^{1/2}$ is the distance from the point (z, r) to the track axis along the normal $\mathbf{n}(z, r)$, whereas z_0 is determined by the intersection of this normal with the track axis. The ionized atoms displaced for the time of electron relaxation τ participate in the recombination with electrons and fix their positions because of a drastic decrease in their mobility. The spatial electron-energy distribution formed upon the relaxation of an electron momentum has the form

$$p(z, r) = \frac{\varepsilon_e}{\pi\gamma L r_0^2} f(z/L)\exp\left[-\frac{g(z/L)r^2}{r_0^2}\right], \qquad (4)$$

where L is the path of an impinging ion, r_0 is the characteristic entrance radius of the isoenergetic surface, and ε_e is the energy transferred by an ion for the excitation of the electron gas. The functions $f(x)$ and $g(x)$ determine the variation of the height and the width of the Gaussian distribution along the track axis, where $x - z/L$, $\gamma = \int_0^\infty dx f(x)/g(x)$ is the normalization factor. The functions $f(x)$ and $g(x)$ should satisfy the condition following from the definition of the stopping power of an electron, $S_e(z)$. The radial integral

$$2\pi\int_0^\infty p(z, r) r dr = \frac{\varepsilon_e}{\gamma L}\frac{f(z/L)}{g(z/L)} = \frac{\varepsilon_e}{\gamma L}F(z/L) \qquad (5)$$

should behave as the function $S_e(z)$ possessing the maximum at the depth, where the velocity of an impinging ion is approximately equal to the velocity of electrons in the target atoms.

Each point with the coordinates (z, r) is projected onto the point z_0 on the track axis

$$z_0 = z - \frac{r_0^2}{2Lg(x)}\left(g'(x)\frac{r^2}{r_0^2} - \frac{f'(x)}{f(x)}\right), \qquad (6)$$

where $x = z/L$. As follows from Eq. (6), the point on the track axis $(z, 0)$ is projected onto the point $z_0 = z - R_c$, where $R_c = (r_0^2/2Lg)|f'(x)|/f(x)$ is the curvature radius of the isoenergetic surface at the point of its intersection with the track axis and z_0 is the focal point.

Taking into account the explicit form of the pressure given by Eq. (4), Equation (3) yields the following displacement of an atom at the point (z, r) in the vicinity of the track

$$u(z, r) = \frac{2\tau b}{n_0 r_0^2} p(z, r) s(z, r) g(z/L), \qquad (7)$$

where $s(z, r)$ is the distance from the point (z, r) to the point z_0.

As follows from Eq. (7), the maximum displacement should be observed at a distance $r \approx r_0/\sqrt{g(z/L)}$ from the track axis, where the energy distribution given by Eq. (4) has the maximum derivative. At shorter distances from the track axis, the displacement decreases because of the smallness of $s(z, r)$, whereas at longer distances, the decrease is caused by the smallness of $p(z, r)$.

The radial $u_r(z, r)$ and the longitudinal $u_z(z, r)$ displacement components are determined by the direction of the normal at the point (z, r) and are

$$u_r(z, r) = \frac{u}{s}r, \quad u_z(z, r) = \frac{u}{s}(z - z_0). \qquad (8)$$

According to Eq. (8), the atomic displacements along the track axis have only the longitudinal components, determined only by the change in the height of the Gaussian distribution given by Eq. (4)

$$u_r(z, 0) = 0, \quad u_z(z, 0) = \frac{\tau b \varepsilon_e}{n_0 \Omega_0 L} f'(z/L), \qquad (9)$$

where $\Omega_0 = \pi\gamma r_0^2 L$ is the conventional volume of the track. The existence of the maximum of the function $f(x)$ results in the displacement of atoms toward the irradiated surface of the crystal in the initial part of the track and in the displacement into the crystal bulk in the end part of the track. Equation (9) shows that the function $f(x)$ should rapidly decrease at $z \geq L$. The atomic displacements in the vicinity of the track given by Eqs. (8) result in the formation of a rarefied region with $n < n_0$ in the vicinity of the track axis and of a "compressed" region with $n > n_0$ at the track periphery. The spatial density distribution $n(z, r)$ is determined by the diagonal components of the strain tensor $u_{ik}(z, r)$ as

$$n(z, r) = n_0(1 + Spu_{ik})^{-1}. \quad (10)$$

The diagonal components have the form

$$u_{rr} = \frac{\partial u_r}{\partial r} = \frac{u}{s}\left(1 - 2g\frac{r^2}{r_0^2}\right), \quad u_{\varphi\varphi} = \frac{u_r}{r} = \frac{u}{s},$$

$$u_{zz} = \frac{\partial u_z}{\partial z} = \frac{u}{s}\frac{r_0^2}{2L^2} \quad (11)$$

$$\times\left[\left(\frac{g'}{g}\frac{r^2}{r_0^2} - \frac{f'}{fg}\right)\left(\frac{g'}{g} + \frac{f'}{f} - g'\frac{r^2}{r_0^2}\right) + \left(\frac{g'}{g}\right)'\frac{r^2}{r_0^2} - \left(\frac{f'}{fg}\right)'\right].$$

The factor $r_0^2/2L^2$ makes the longitudinal component u_{zz} much less than u_{rr} and $u_{\varphi\varphi}$ along the whole track length except for its end. At the distances of the order of r_0 from the track end, the longitudinal and the radial components of the strain tensor are of the same order of magnitude. The common factor u/s is determined by Eq. (7). Equation $Spu_{ik} = 0$ defines the boundary surface separating the rarefied and the compressed regions. The smallness of u_{zz} (the track end is ignored) results in the following simple form of the boundary surface

$$r^2 \simeq \frac{r_0^2}{g(z/L)}. \quad (12)$$

The allowance for u_{zz} leads to a more rigorous equation of the boundary surface in the vicinity of the track end

$$r^2 \simeq \frac{r_0^2}{g}\left[1 + \frac{\lambda}{g}\left[\left(\frac{g'}{g}\right)^2 - \frac{F''}{F}\right]\right], \quad (13)$$

which also includes an additional term proportional to the small parameter $\lambda = r_0^2/4L^2$. The atomic displacements give rise to the formation of a surface, where the atomic density n attains the maximum value, whereas Spu_{ik}, the minimum value. The equation of such a surface can readily be obtained. Ignoring the longitudinal component u_{zz} of the strain tensor, we arrive at the expression for the radius of the maximum-density surface

$$r_m^2 \simeq \frac{2r_0^2}{g(z/L)}. \quad (14)$$

Comparing Eqs. (12) and (14), we see that the radius of the maximum-density surface along almost the whole track is larger by a factor of $\sqrt{2}$ than the radius of the boundary surface. However, Equation (14) for the maximum-density surface becomes invalid at the track end, where the longitudinal and the radial components of the strain tensor become comparable. The rigorous equation of the maximum-density surface $r = \varphi(z)$ can be obtained by solving the nonlinear differential equation $\varphi' = -(\partial n/\partial z)/(\partial n/\partial r)$, where the coordinate r should be replaced by $\varphi(z)$. The points of the intersection of the boundary and the maximum-density surfaces with the z-axis are determined by the equations $f'' = fg/\lambda$ and $(fg)'' = 2fg^2/\lambda$, respectively.

In order to compare the results obtained with the known experimental data on experimentally measured interplanar spacing $\langle\Delta d\rangle$ averaged over the radial coordinate obtained by the X-ray diffractometry method, one has, first, to derive the equation for the averaged value of the longitudinal component of the strain tensor given by Eq. (11),

$$\frac{\langle\Delta d\rangle}{d} \sim \int_0^\infty \frac{\partial u_z}{\partial z} \times 2\pi r\,dr \sim \frac{f}{g}\left[\frac{g''}{g} - \frac{f''}{f} + 2\frac{f'g'}{fg} - 2\left(\frac{g'}{g}\right)^2\right].$$

Taking into account Eq. (5), we arrive at $\langle\Delta d\rangle/d \sim -F''(z/L)$. Proceeding from the fact that the function $F(z/L)$ should behave as the stopping power $S_e(z)$, we assume that the function $F(x)$ should have a deflection point at the depth where the Bethe–Bloch deceleration mechanism is changed for the Firsov mechanism. This deflection point corresponds to the sign reversal of $\langle\Delta d\rangle$. The second deflection point on $\langle\Delta d\rangle$ is provided by a falling tail of the spatial distribution of excited electrons at $z \geq L$. Between the above two deflection points on $F(x)$, there is a dilatation region, where $\langle\Delta d\rangle > 0$. Outside this region, the atomic planes parallel to the irradiated surface become closer to one another and $\langle\Delta d\rangle < 0$. The $\langle\Delta d\rangle$ values measured during the low-dose irradiation with 210-MeV Kr-ions (see curve 1 in Fig. 1 in [19]) show the existence of the region with $\langle\Delta d\rangle > 0$. However, outside this region, the lattice compression is insignificant and, therefore, it could not be recorded in [19], where the authors made the conclusion that a 10% decrease in the density in the Kr-tracks occurred because of the appearance of the second maximum of $\langle\Delta d\rangle$ at high irradiation doses. In fact, this maximum corresponds to ions that hit "old" tracks and whose track length thus increases by 10% of the conventional value. In accordance with Eqs. (10) and (11),

the atomic density along the track axis varies according to the following equation:

$$n(z, 0) = n_0\left[1 + \frac{4\varepsilon_e\tau b}{n_0\Omega_0 r_0^2} fg\left(1 - \lambda\frac{f''}{fg}\right)\right]^{-1}. \quad (15)$$

The above equation allows the detailed analysis of the experimental data. The atomic density attains the maximum value on the maximum-density surface described by Eq. (14) quite satisfactorily everywhere except for the end of the track

$$n(z, r_m) \simeq n_0\left[1 - \frac{4\varepsilon_e\tau b}{e^2 n_0\Omega_0 r_0^2} fg\left[1 - \frac{\lambda}{g}\left[\frac{g''}{g} - \frac{f''}{f} - 3\left(\frac{g'}{g}\right)^2 + 4\frac{f'g'}{fg}\right]\right]\right]^{-1}. \quad (16)$$

Equation (16) shows that the characteristic value of the maximum density is lower by the factor of e^2 than the rarefaction value in Eq. (15), where $e \simeq 2.718$. Therefore, the experimental data obtained in [19] had no maximum due to ions that are in the maximum-density region because of high irradiation doses. According to our estimates, this maximum should be very weak in comparison with the maximum provided by the rarefied regions. Equation (15) allows one to evaluate the relaxation time τ from the experimental data [19] on the rarefaction value in the track, $(\Delta n/n_0)_{\exp} \approx 0.1$ in a silicon single crystal irradiated with 210-MeV-Kr-ions. Taking into account that the mobility of the target atoms is $b \cong \tau/M$ (where M is the mass of a target atom), we obtain

$$\tau = \sqrt{\frac{\gamma\pi n_0 r_0^4 LM}{4\varepsilon_e fg}\left(\frac{\Delta n}{n_0}\right)_{\exp}} \approx 2.6\times 10^{-14}\ \text{s} \quad (17)$$

at the following parameters: $\varepsilon_e = 100$ MeV, $n_0 = 5\times 10^{22}$ m^3, $r_0 = 1$ nm, $L = 30$ μm, $M = 28m_n \cong 4.67\times 10^{-23}$ g, and $\gamma \approx fg \approx 1$. The above expression takes into account that the minimum in Eq. (15) is attained in the vicinity of the maximum stopping power of an electron, where $f''(z/L) \cong 0$. Then, we can also obtain that the mobility of silicon atoms in the track equals $b \approx 5.6\times 10^8$ s/g. In accordance with Eq. (7), the maximum displacement equals $u \approx 0.02$ nm. This corresponds to the displacement velocity $v = u/\tau \approx 10^5$ cm/s, i.e., the value which is in good agreement with the velocity determined from the initial Eqs. (1) and (4)

$$v = b\frac{\sqrt{2}\varepsilon_e}{\pi\sqrt{e}n_0 r_0^3 L} \approx 1.6\times 10^5\ \text{cm/s}.$$

Despite the fact that we consider irradiation of a homogeneous isotropic medium, the comparison of the data obtained with the experimental data on an irradiated silicon single crystal [19] yields quite reasonable b- and τ-values. This indicates that the model based on the measurement of residual strains suggested here provides reliable data on the displacement field in the swift-ion tracks.

The energy losses of the electron gas for medium deformation in the vicinity of the track can be estimated by the formula

$$\varepsilon_d(z, r) \cong \int_0^\infty F(t)v(t)dt \cong \frac{\varepsilon_e f(z/L)}{2n_0\Omega_0}\left(\frac{\Delta n}{n_0}\right)_{\exp}\frac{r^2}{r_0^2}\exp\left(-2\frac{r^2}{r_0^2}\right). \quad (18)$$

Thus, the losses of a swift ion for medium deformation integrated over the track volume are equal to

$$E_d = n_0\int_\Omega \varepsilon_d(z, r)\times 2\pi r dr dz \cong \frac{\varepsilon_e}{8}\left(\frac{\Delta n}{n_0}\right)_{\exp}$$

and, with due regard for the 10% strain in silicon irradiated with 210-MeV Kr ions, is one-eightieth of the energy of the electron gas excited by an impinging ion. In accordance with expression (18), the maximum stress arising at $r \cong r_0/\sqrt{2}$ is

$$\varepsilon_d^{\max}\left(\frac{r^2}{r_0^2} = \frac{1}{2}\right) \cong \varepsilon\frac{S_e}{4en_0\Omega_0}\left(\frac{\Delta n}{n_0}\right)_{\exp}.$$

For a silicon irradiated with 210-MeV Kr ions at $r_0 \cong 0.5$ nm, we obtain the maximum stress $\varepsilon_d^{\max} \cong 1.3\times 10^{10}$ nm^{-2}, which can be higher than the value of the shear modulus $G \cong 10^{10}$ nm^{-2}, thus indicating, that deformation of the irradiated specimen in the narrow region along the track axis is of plastic rather than of elastic nature and, thus, gives rise to nucleation of dislocations and specific track dilatations. The allowance for the elasticity and friction forces in Eq. (1) results in a more general equation for atoms of the medium under electron-gas pressure

$$n_0 d\rho/dt = b\left(-\frac{dp}{ds}\exp(-t/\tau) - M\omega_0^2\rho - M\kappa d\rho/dt\right), \quad (19)$$

where ρ is the displacement of the atom in the medium with the coordinates (z, r), ω_0 is the natural frequency of atomic vibrations in the irradiated medium, κ is the coefficient of the motion deceleration in the medium, which is determined by its viscosity, and $-(dp/ds)\exp(-t/\tau)$ is the force of the electron-gas pressure. If $\beta = (\omega_0\tau)^2/(1 + \kappa\tau)$ is of the order of unity, Equa-

tion (19) yields the following atomic displacement at the point (z, r)

$$\rho(z, r, t) = u(z, r)(\exp(-\beta t/\tau) - \exp(-t/\tau))/(1 + \kappa\tau - \omega_0^2\tau^2).$$

The above equation describes the aperiodic vibrations of an atom and its return to the initial position $\rho = 0$ if the stress $\varepsilon_d(z, r)$ corresponding to the displacement $\rho(z, r, t)$ does not exceed the value of the shear modulus G. If $\beta \ll 1$ (the situation considered in this article), the energy of the δ-electrons is transferred to atoms of the medium so quickly that the elasticity and the friction forces do not have enough time to bring the atoms into their initial positions. As a result, the deformation starts exceeding the shear modulus and, thus, becomes irreversible.

In conclusion, it should be indicated that it would be very useful to perform X-ray small-angle scattering experiments on track dilatations in order to refine the model parameters. Such measurements are sensitive to radial deformations and, thus, can complement the diffractometric data providing information mainly on longitudinal deformations. The X-ray diffractometric measurements of radial deformations performed in the asymmetric geometries are also possible, but these experiments are associated with some additional experimental difficulties. The refinement of the model parameters with the invocation of the experimental methods of the structural diagnostics would allow a more correct description of the interactions between δ-electrons and target atoms and also the evaluation of the effect of the changed structural characteristics in crystals irradiated with swift ions. The formation of wire-like dilatations in semiconductor crystals irradiated with high-energy ions allows the creation of one-dimensional quantum objects. The track dilatations with the transverse dimension of the order of $r_0 \cong 0.5$ nm should give rise to additional quasistationary electron levels with energies of the order of $\varepsilon \cong 3$ eV and a width of $\Delta\varepsilon \cong /\tau \cong 0.025$ eV. As a result, the irradiated crystals would acquire anomalous electrophysical properties inherent in the one-dimensional electron gas in quantum wires.

ACKNOWLEDGMENTS

This study was supported by the Russian Foundation for Basic Research, project no. 00-02-17693.

REFERENCES

1. A. Dunlop and D. Lesueur, Radiat. Eff. Defects Solids **126**, 132 (1993).
2. A. Iwase and T. Iwata, Nucl. Instrum. Methods Phys. Res. B **90**, 332 (1994).
3. A. Benyagoub and L. Thome, Phys. Rev. B **38**, 10205 (1988).
4. A. Audouard, E. Balanzad, S. Bouffard, *et al.*, Phys. Rev. Lett. **65**, 875 (1990).
5. S. Klaumunzer, C. Li, and G. Schumacher, Appl. Phys. Lett. **51**, 97 (1987).
6. S. Klaumunzer, C. Li, S. Loffler, *et al.*, Radiat. Eff. Defects Solids **108**, 131 (1989).
7. A. I. Ryazanov, A. E. Volkov, and S. Klaumunzer, Phys. Rev. B **51**, 12107 (1995).
8. H. Trinkaus and A. I. Ryazanov, Phys. Rev. Lett. **74**, 5072 (1995).
9. M. I. Kaganov, I. M. Lifshitz, and L. V. Tanatarov, Zh. Éksp. Teor. Fiz. **31**, 232 (1956) [Sov. Phys. JETP **4**, 173 (1957)].
10. I. M. Lifshitz, M. I. Kaganov, and L. V. Tanatarov, At. Énerg. **6**, 391 (1959).
11. T. Talemonde, C. Dufour, and E. Paumier, Phys. Rev. B **46**, 14362 (1992).
12. K. Yasui, Nucl. Instrum. Methods Phys. Res. B **90**, 409 (1994).
13. R. L. Fleuscher, P. B. Price, and R. M. Walker, J. Appl. Phys. **36**, 3645 (1965).
14. S. Klaumunzer, Ming Dong Hou, and G. Schumacher, Phys. Rev. Lett. **57**, 850 (1986).
15. D. Lesueur and A. Dunlop, Radiat. Eff. Defects Solids **126**, 163 (1993).
16. A. Dunlop, P. Legrand, D. Lesueur, *et al.*, Europhys. Lett. **15**, 765 (1991).
17. A. E. Volkov and V. A. Borodin, in *High-Current Electronics and Modification of Materials*, Ed. by D. Vaisburg (Tomsk, 2000), Vol. 1, p. 231.
18. E. V. Metelkin and A. I. Ryazanov, Zh. Éksp. Teor. Fiz. **117**, 420 (2000) [JETP **90**, 370 (2000)].
19. A. R. Chelyadinskiĭ, V. S. Varichenko, and A. M. Zaĭtsev, Fiz. Tverd. Tela (St. Petersburg) **40**, 1627 (1998) [Phys. Solid State **40**, 1478 (1998)].
20. Zh. I. Alferov, Fiz. Tekh. Poluprovodn. (St. Petersburg) **32**, 3 (1998) [Semiconductors **32**, 1 (1998)].

Translated by L. Man

Crystallography Reports, Vol. 47, No. 1, 2002, pp. 106–110. Translated from Kristallografiya, Vol. 47, No. 1, 2002, pp. 114–118.

REAL STRUCTURE OF CRYSTALS

Specific Features of Oxygen Dissolution in Refractory Metals in Gas-Phase Deposition

V. P. Kobyakov and V. I. Ponomarev

Institute of Structural Macrokinetics and Problems of Materials Science, Russian Academy of Sciences, Chernogolovka, Moscow oblast, 142432 Russia

Received January 20, 2000; in final form, February 28, 2001

Abstract—The phase composition of niobium specimens obtained by crystallization from the gaseous chloride–hydrogen mixture with regular addition of oxygen has been studied by the method of X-ray phase analysis. It is established that the oxygen-containing niobium contains a solid solution of oxygen in niobium monoxide. The specific feature of the phases revealed is an unusually pronounced deformation of the crystal lattice (with an increase in the oxygen content in the specimen, the lattice parameter increases by 0.5–0.6%). It is concluded that oxygen possesses elevated solubility in niobium and that during their gas-phase crystallization oxygen is present in niobium monoxide in a "superstoichiometric" concentration. The results obtained are compared with the known data on oxygen-enriched tungsten and chromium also obtained by various modifications of gas-phase technology. © *2002 MAIK "Nauka/Interperiodica".*

INTRODUCTION

Oxygen-containing niobium (ON) is a promising material for preparing electrodes for thermionic converters. Its use in the manufacturing of anodes considerably improves the output anode characteristic [1, 2]. The preparation of oxygen-containing niobium by crystallization from the gas phase was first reported in [3]. In particular, it was indicated that gas-phase ON also contains a certain unknown oxide responsible for a number of ON properties never observed in pure niobium—high values of microhardness and the work function of electron and the ability to evolve oxygen during heating in vacuum. Below, we consider the structural aspects of oxygen-containing niobium obtained by the gas-phase method and compare its structure with the structures of other oxygen-containing refractory metals obtained from the gas phase.

EXPERIMENTAL

Similar to [3], the specimens of oxygen-containing niobium were prepared by the method of gas-phase deposition from the gaseous chloride–hydrogen mixture with a regular addition of oxygen at the growth rate of about 0.1 mg cm^{-2} s^{-1} and the temperature of 1350 ± 10 K. To remove the residual stresses, the specimens were subjected to 1-h-annealing in a $(5–8) \times 10^{-5}$ Pa vacuum at 1400 K. The oxygen content in the specimens was measured by the neutron-activation methods according to the reaction $O^{16}(n, p)N^{14}$ [4]. The phase composition of the specimens was studied on a computer-controlled automated DRON-3M diffractometer (CuK_α radiation). The analysis was performed with the use of the Powder Diffraction File (PDF2) database.

RESULTS AND DISCUSSION

The oxygen-containing niobium specimens were 0.5–0.6-mm-thick rough layers on 17 × 17 × 3-mm-large molybdenum substrates. The crystallites with shining faces forming the rough surface were up to 1 mm in length and were misoriented within 20 angular degrees. The diffraction patterns revealed the well-developed texture with the [100] axis. It was established that the successive polishing-away of the layers of oxygen-containing niobium did not change the texture, which considerably hindered the analysis of the diffraction patterns because the variation of the mutual orientation of the specimen and an incident X-ray beam changed the relative intensities of diffraction reflections. Moreover, polishing also changed the relative ratio of phases in the specimen. To average the results, we rotated the specimen and obtained several diffraction patterns from the same regions of the specimen. This provided better reproducibility of the reflections which lay within the 2θ angles from 0.02 to 0.03 angular degrees.

The results of the X-ray study of ON obtained by the gas-phase deposition listed in Table 1 show that the ON specimens consisted of two phases—pure niobium (sp. gr. *Im*3*m*) and niobium monoxide (sp. gr. *Fm*3*m*). Table 1 also lists the reflections from Nb and NbO taken from the PDF2 Data File which were also observed in textured specimens. These are usually the most intense reflections. The presence of niobium monoxide in the ON specimens is quite consistent with the known data, of which the most reliable ones [7] provide the interpretation of the mechanism of niobium monoxide crystallization on the niobium surface.

1063-7745/02/4701-0106$22.00

Table 1. Structural parameters of oxygen-containing niobium specimens

ON19 with 1.90 wt % O		N12 with 1.24 wt % O		KN75 with 0.75 wt % O		Nb 34–370, (JCPDS)			NbO 15–535, (JCPDS)		
d, nm	*I**	*d*, nm	*I*	*d*, nm	*I*	*d*, nm	*I*	*hkl*	*d*, nm	*I*	*hkl*
0.2987	2								0.2946	50	110
0.2361	86	0.2358	16	0.2350	100	0.2336	100	110			
0.2109	4								0.2095	100	200
0.1658	100			0.1659	43	0.1652	18	200			
		0.1497	2						0.1484	100	220
0.1354	18	0.1352	100	0.1354	20	0.1348	28	211			
0.1177	4	0.1178	3	0.1171	8	0.1168	8	220	0.1167	20	320
0.1048	13	0.1048	66	0.1047	12	0.1045	11	310			
				0.0959	4	0.0953	3	222			
				0.0956	4		–	–	0.0941	100	420
0.0889	4	0.0885	30	0.0884	13	0.0883	13	321			
0.0887	4	0.0864	3						0.0859	100	422
				0.0831	6	0.0826	2	400	0.0825	50	510
0.0828	14			0.0828	5				0.0810	100	

* Intensity.

Table 2. Lattice parameters of the phases in the specimens

Phase composition of the specimens and the lattice parameters according to PDF2	Specimens					
	ON19		ON12		ON75	
	a, nm	$\Delta a/a_0$, %	*a*, nm	$\Delta a/a_0$, %	*a*, nm	$\Delta a/a_0$, %
Nb (a_0 = 0.33034 nm)	0.33242	+0.63	0.33212	+0.54	0.33172	+0.42
NbO (a_0 = 0.42040 nm)	0.42104	+0.15	0.42274	+0.56	0.42004	–0.09

In accordance with [7], the interaction of oxygen with the (110) niobium surface results in surface reconstruction accompanied by the "lowering" of oxygen atoms and formation of the rows of niobium atoms protruding from the surface, i.e., the formation of the surface structure with the same arrangement of atoms as on the (110)NbO surface. The unit-cell dimensions of this structure (0.286 × 0.436 nm) differ by not more than 3.8% from the unit-cell dimensions of the (110)NbO face (0.297 × 0.420 nm) in both directions. Further growth of the NbO film proceeds on this initial matrix.

Table 1 shows that diffraction reflections of both niobium and niobium monoxide are displaced from their positions. Using a special program written for a personal computer, we determined the lattice parameters of the identified phases within an error of ±0.0003 nm (figure and Table 2). According to [8–10], the formation of the α-solid solution of oxygen in niobium is accompanied by the deformation of the niobium lattice with the lattice parameter linearly increasing with the oxygen concentration within its solubility limits. As was shown in [8] (these data seem to be the first reliable data to the effect), the homogeneous solid solutions obtained by diffusion-induced saturation of the compacted niobium with oxygen in vacuum at low partial oxygen pressure could be quenched without the precipitation of niobium monoxide only if oxygen is present in niobium in the concentration not exceeding 4.1 at. % (0.75 wt %). The lattice parameter corresponding to this composition is *a* = 0.3311 nm. The specimens obtained in [8] by melting the niobium with an oxide-containing alloy were two-phase specimens (with NbO the second phase) with 2.60–3.76 wt % O. The lattice parameter of such specimens was independent of oxygen concentration and, when being quenched from the 1300–1400 K, varied within 0.3311–0.3313 nm. In [9, 10], the ON specimens were prepared by the method of diffuse saturation of compacted niobium with oxygen in vacuum for considerable periods of time. As a result, homogeneous specimens were obtained with a lattice parameter up to 0.3317 nm and the oxygen concentration in the solid solution of oxygen in niobium about 4.3 at. % (0.77 wt %). The results

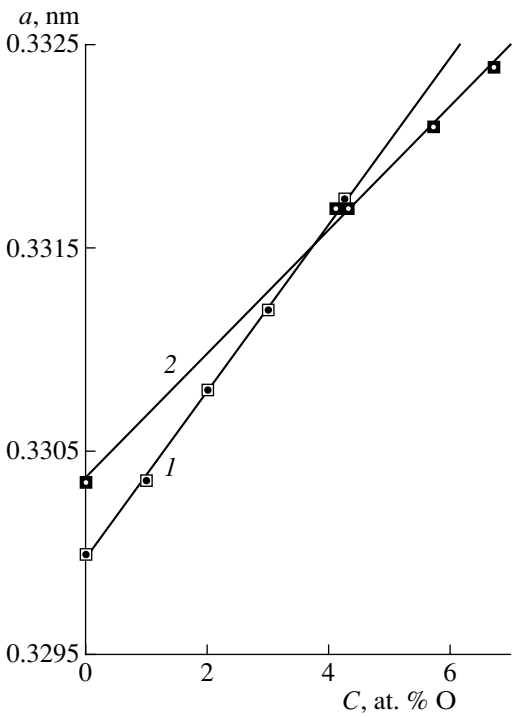

Lattice parameter of the solid solution of oxygen in niobium: (*1*) according to [9, 10]; (*2*) by the experimental points with due regard for the value a_0 for "oxygen-free" niobium (34-370 PDF2 card).

obtained in [9] and [10] are well consistent (curve *1* in figure at the oxygen content 0.00–4.3 at. %).

As is seen from Table 2, the ON75 specimen consists of two phases, although in accordance with [8–10], it should be located in the solid-solution region. The lattice parameter of this specimen slightly exceeds that for the ON specimens studied in [9, 10]. We did not aim to prepare homogeneous specimens with an extremely high concentration of dissolved oxygen; moreover, our experimental conditions did not allow rapid quenching of the specimens. Thus, we could expect the partial decomposition of the solid solution with the segregation of the oxide phase, however, according to our estimates, the degree of such decomposition was rather low. It should also be indicated that the lattice parameter of the oxide phase in the ON75 specimen was close to the "normal value" of the NbO lattice parameter (Table 2). Specimens ON12 and ON19 with higher oxygen content considerably differed from the KN75 specimen. First of all, their lattices were considerably distorted. If one assumes that oxygen solubility in niobium in these specimens is very high and the dependence $a = f$(C, at. % O) is still linear, then the lattice parameters measured from the plots in figure (a = 0.33212 and a = 0.33242 nm) correspond to 5.7 at. % (1.04 wt %) and 6.7 at. % (1.22 wt %) of dissolved oxygen. The neutron–activation analysis showed 1.24 and 1.90 wt % of oxygen in these specimens. The difference seems to be associated with oxygen in the specimens present in the form of the oxide phase. Then the ON12 specimen contains 1.4, and the ON19 specimen, 4.6 wt % of the oxide recalculated for stoichiometric NbO. Figure shows that the experimental data (curve *2*) extrapolated to the "zero" lattice parameter of niobium are somewhat higher than in [9, 10] (curve *1*). Our results better fit the straight line at the first of two known a_0 values for oxygen-free niobium—a_0 = 0.33034 nm (card 34-370 PDF2) and a_0 = 0.33066 nm (card 35-789 PDF2). It should be indicated that the value a_0 [9, 10] considerably differs from the above values taken from the PDF2 data base. We believe that the scatter in the a_0 values for oxygen-free niobium is explained by the real degree of "freedom of oxygen." The figure shows that at high oxygen concentration, our experimental points are lower than those of the extrapolated dependence obtained by data [9, 10]. One can assume that the small slope of curve *2* is associated with the insufficient and noncontrollable cooling rate of the specimens in our study. At the same time, bearing in mind the error in our measured lattice parameter (±0.00015 nm), the discrepancies revealed should be recognized as insignificant.

Another difference between the ON19 and ON12 specimens, on the one hand, and the ON75 specimen, on the other, is that the oxide phase in these specimens shows considerable displacement of the X-ray diffraction reflections (Tables 1 and 2). The strain of the NbO lattice in the ON12 specimen is $\Delta a/a_0 = 0.56\%$. Similar observations were also made in [5, 6], where this effect determined from the data of secondary-ion mass-spectrometry, X-ray phase analysis, and X-ray diffraction analysis was attributed to the formation of metastable "superstoichiometric" niobium monoxide $NbO_{1.2}$ formed only in gas-phase deposition of niobium with the simultaneous incorporation of oxygen into the lattice (as was also observed in the present study). For ON specimens obtained by different methods (e.g., diffusion-induced saturation of the compact niobium with oxygen in vacuum or melting of niobium with oxide-containing alloy), no excessive lattice deformation was revealed, whereas the oxygen concentration in oxide corresponded to the stoichiometric composition $NbO_{0.95}$–NbO [3, 5, 6]. Under the assumption that the KN19 and KN12 specimens contain the metastable $NbO_{1.2}$ oxide, its content would not exceed 1.2 and 4.0 wt %, whence it follows that the total increase in oxygen content in niobium is not necessarily accompanied by its uniform distribution between the solid solution and the precipitated oxide. Here, the main part seems to be played by the technological parameters of the specimen preparation, e.g., a cooling rate. The cause of such a behavior of oxygen dissolution in niobium should be explained by the configuration of the outer $4d^45s^1$ electrons in niobium atoms [11] having half-filled and even vacant *d*-orbitals. Some vacancies are filled due to electron interactions between the framework niobium atoms [12–14]. At the temperature

of gas-phase deposition of a niobium layer, the remaining half-filled *d*- and *p*-orbitals of oxygen atoms become hybridized, which results in a slightly higher solubility of oxygen in niobium than in diffusion-induced saturation of niobium with oxygen [6]. The lone pairs of *p*-electrons of oxygen and vacant *d*-orbitals of niobium form the donor–acceptor bonds and formation of superstoichiometric NbO_{1+x} oxide. It was indicated [5, 6] that the above reasoning is valid only for ON specimens formed due to oxygen incorporation into the niobium layer from the gas phase.

It is interesting to compare the results obtained for the niobium grown from the gas phase with the analogous data obtained for other *d*-transition bcc metals not dissolving oxygen, and, in particular, with the data on tungsten deposited from the gaseous chloride phase with addition of oxygen [15]. Oxygen solubility in conventional tungsten is negligibly low—about 0.06 at. % (0.005 wt %) at 2000 K [16]. In accordance with [15], the outer electron shell of tungsten has the configuration $5d^5 6s^1$ because of the "fall" of one *s*-electron onto the closest *d*-shell in the transition from an isolated atom to the crystal (for comparison, the outer electron shell of molybdenum is $4d^5 5s^1$ and that of chromium, $3d^5 4s^1$ [11]). In all these cases, there are no vacant *d*-orbitals, and, thus, oxygen cannot be dissolved in these metals. The revealed oxygen traces are associated with lattice defects.

It was revealed [15] that the tungsten layer obtained from the gaseous chloride phase can incorporate up to 10^{-1} wt % oxygen. The maximum change in the lattice parameter did not exceed 0.01%, which is close to the measurement error. The electron microscopy studies revealed no inclusions in the specimen either. Taking into account these data and the indirect proof given in [15], we concluded that oxygen is incorporated into the bulk of the tungsten crystal. This effect was explained by the formation of the adsorption tungsten suboxide W_3O on the crystallization front which, in the course of tungsten-layer deposition, is *buried* in the deposit bulk. The formation of pure surface W_3O suboxide results from the surface reconstruction of the tungsten substrate at the initial stage of its interaction with oxygen [17]. Thus, the use of the chloride gas-phase technology [15] provided the dissolution of oxygen even in the metal where the oxygen constitutionally cannot be dissolved.

Chromium films prepared by the method of vacuum condensation on the glass substrates were studied in [18]. Similar to tungsten, chromium atoms contain no vacant *d*-orbitals, i.e., constitutionally cannot dissolve oxygen. Nevertheless, it was shown that with an increase of the partial oxygen pressure in the range from 10^{-5} to 10^{-3} Pa, the oxygen content in the chromium deposit linearly increases from the trace amounts up to about 32 at. % (8 wt %), i.e., up to the complete transformation of the sputtered chromium into the Cr_2O_3 oxide. The lattice parameter of chromium increased up to $a = 0.2895$ nm, which corresponded to the $\Delta a/a_0 = 38\%$ lattice strain. The diffraction patterns from chromium films deposited under elevated partial oxygen pressure were characterized by high background intensity in comparison with the background intensity from the films deposited in high vacuum. It is believed [18] that the high background intensity can be explained by the presence of chromium oxide either in the amorphous or ultradispersed state, since the X-ray diffraction patterns from the films obtained at $p(O_2) > 7 \times 10^{-4}$ Pa showed the reflections due to Cr_2O_3, whose intensity increased with an increase of $p(O_2)$.

These results [18] seem to be very interesting because, with an increase in oxygen content dissolved in chromium, the diffraction reflections are displaced, i.e., oxygen is dissolved in the metal where, constitutionally, it should not be dissolved. One can assume that, similar to the case of tungsten, the mechanism of formation of surface compounds and their "burial" is the same.

The above comparison led us to the conclusion that the incorporation of nonequilibrium oxygen into the lattice of refractory bcc metals is possible only if the metal bulk is formed in the presence of oxygen and simultaneous adsorption of metal and oxygen atoms from the gas phase onto the growth surface. This condition is satisfied if one uses the gas-phase methods, because only these methods allow one to obtain the nonequilibrium metastable products. If the well-established collective of metal atoms interacts with oxygen, the equilibrium conditions for the synthesis are met and the reaction yields the products corresponding to the equilibrium phase diagrams. Each metal–oxygen system has its own individual features and its own limits of oxygen adsorption, which are determined not only by the outer electron shells of metal atoms but also by the differences in the methods used for preparing metal layers.

REFERENCES

1. I. G. Gverdtsiteli, I. L. Korobova, R. Ya. Kucherov, *et al.*, Zh. Tekh. Fiz. **46** (3), 544 (1976) [Sov. Phys. Tech. Phys. **21**, 312 (1976)].
2. V. P. Kobyakov and A. G. Kalandarishvili, Zh. Tekh. Fiz. **68** (8), 131 (1998) [Tech. Phys. **43**, 997 (1998)].
3. B. Ya. Dynkina, V. P. Kobyakov, S. P. Mitrofanova, *et al.*, Izv. Akad. Nauk SSSR, Met., No. 4, 114 (1986).
4. V. P. Kobyakov, N. E. Menabde, A. M. Sirenko, *et al.*, Poverkhnost, No. 2, 145 (1987).
5. V. P. Kobyakov and V. N. Taranovskaya, in *Proceedings of the 2nd Branch Conference Nuclear Power Engineering in Space. Physics of Thermionic Converters, Sukhumi, 1992*, p. 369.
6. V. P. Kobyakov and V. N. Taranovskaya, Kristallografiya **44** (6), 1017 (1999) [Crystallogr. Rep. **44**, 948 (1999)].
7. B. M. Zykov, D. S. Ikonnikov, and V. K. Tskhakaya, Fiz. Tverd. Tela (Leningrad) **17** (12), 3562 (1975) [Sov. Phys. Solid State **17**, 2322 (1975)].

8. A. U. Seybolt, Trans. AIME **200**, 774 (1954).
9. E. Gebhardt and R. Rothenbacher, Z. Metallkd. **54** (8), 443 (1963).
10. A. K. Volkov, É. A. Goritskaya, I. N. Kidin, *et al.*, Fiz. Met. Metalloved. **29** (5), 957 (1970).
11. T. I. Krasovitskaya, *Electronic Structures of Atoms and Chemical Bonding* (Prosveshchenie, Moscow, 1980).
12. V. K. Grigorovich and E. N. Sheftel', *Dispersion Hardening of Refractory Metals* (Nauka, Moscow, 1980).
13. V. K. Grigorovich and K. V. Grigorovich, in *Alloys of Refractory and Less-Common Metals for High-Temperature Works* (Nauka, Moscow, 1984), p. 23.
14. B. M. Zykov and A. M. Sabel'nikov, Poverkhnost, No. 10, 61 (1988).
15. V. P. Kobyakov and S. A. Zaslavskiĭ, Vysokochist. Veshchestva, No. 5, 75 (1989).
16. Yu. V. Levinskiĭ, *Metal–Gas Phase Diagrams* (Metallurgiya, Moscow, 1975).
17. B. M. Zykov, V. P. Kobyakov, and Yu. I. Nardaya, Vysokochist. Veshchestva, No. 1, 71 (1991).
18. V. S. Kogan, Yu. E. Semenenko, A. L. Seryugin, *et al.*, Metallofizika **2** (6), 86 (1980).

Translated by L. Man

Crystallography Reports, Vol. 47, No. 1, 2002, pp. 111–116. Translated from Kristallografiya, Vol. 47, No. 1, 2002, pp. 119–124.

REAL STRUCTURE OF CRYSTALS

Effect of Inhomogeneity on the Formation of Regular Domain Structures in $LiNbO_3$ Crystal

A. A. Blistanov, V. V. Antipov, O. M. Kugaenko, and G. S. Mikhaĭlova

Moscow State Institute of Steel and Alloys, Leninskiĭ pr. 4, Moscow, 117936 Russia

e-mail: zak_konst@mtu-net.ru

Received March 14, 2000; in final form, July 5, 2001

Abstract—The conditions necessary for the formation of regular domain structures in lithium niobate crystals used for quasi-synchronous non-linear optical transformations of laser radiation have been considered. The analysis of the mechanism and the kinetics of domain formation during thermoelectric repolarization showed that the true thickness of domain boundaries characterized by the combination of the faces of some simple forms of a crystal depends on both angles between the directions of the vectors of the temperature gradient and the spontaneous-polarization and on the homogeneity of the initial crystal. *© 2002 MAIK "Nauka/Interperiodica".*

INTRODUCTION

The synthesis of ferroelectric crystals with regular domain structures allows the creation of new crystalline elements for nonlinear optics. In particular, $LiNbO_3$ crystals with a regular domain structure were used for manufacturing electrooptical modulators for nonpolarized radiations [1, 2]. The design of nonlinear-optical devices based on quasi-synchronous interactions in both bulk crystals [3, 4] and elements of integrated optics [5, 6] is under way.

METHODS OF FORMATION OF REGULAR DOMAIN STRUCTURES

There are several methods for the formation of regular domain structures of which the main are:

—Formation of domain structures during crystal growth [5, 6] (regular domain structures with a period up to several microns). The shortcoming of the method is the fact that the shape and the orientation of the domain boundaries are determined by the shape and the orientation of the crystallization front, whereas the domain size is determined by the parameters of the growth process (such as temperature oscillations, conditions of formation of growth striation, etc.), which considerably restrict the possibilities of the method;

—Scanning of a crystal by an electron beam [7, 8], which provides the domains with high reproducibility of the structural parameters and a distance between the walls up to several microns, which makes this method very promising for obtaining regular domain structures characterized by nonlinear–optical interactions and doubling of the laser-radiation frequency under the conditions of quasiphase matching in second-harmonic generation. This method can be used to create domain structures only in relatively thin (up to tens of microns) surface layers;

—Formation of regular domain structure by pulling a crystal through the temperature zone with the temperature gradient under the simultaneous action onto the crystals of sign-alternating electric field (the so-called postgrowth thermoelectric treatment) [9, 10]. In its essence, the method reduces to the motion of a crystal in a temperature field (Fig. 1) varying from $T > T_C$ to

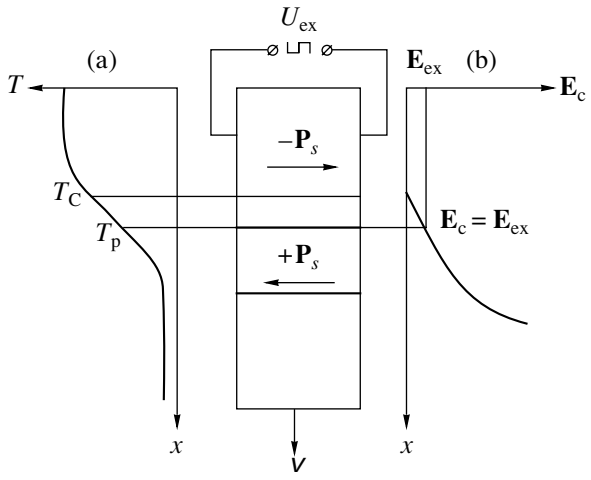

Fig. 1. Scheme of the repolarization process during formation of a regular domain structure by the method of postgrowth thermoelectric treatment of the crystal: (a) the temperature field in the repolarization zone and (b) the dependence of the coercive field E_c on temperature, where x is the coordinate along the direction of crystal motion and v is the velocity of this motion; U_{ex} is the variable potential difference changing the sign depending on the time t and inducing a sign-alternating field $\mathbf{E}_{ex}$ in the crystal; and T_C and T_p are the Curie and repolarization temperatures, respectively.

1063-7745/02/4701-0111$22.00 © 2002 MAIK "Nauka/Interperiodica"

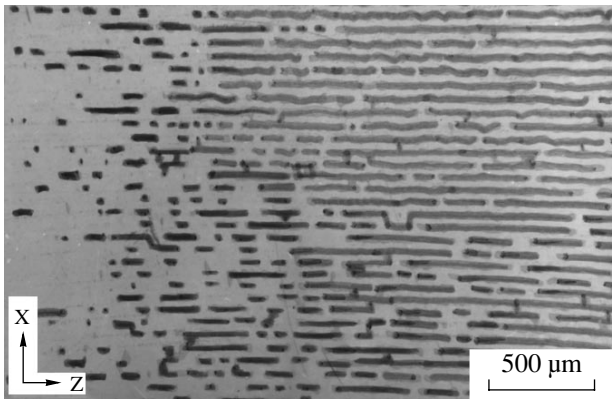

Fig. 2. Growth of domains from the electrode by merge of microdomains formed in the crystal bulk. The period of the domain structure is 35 μm.

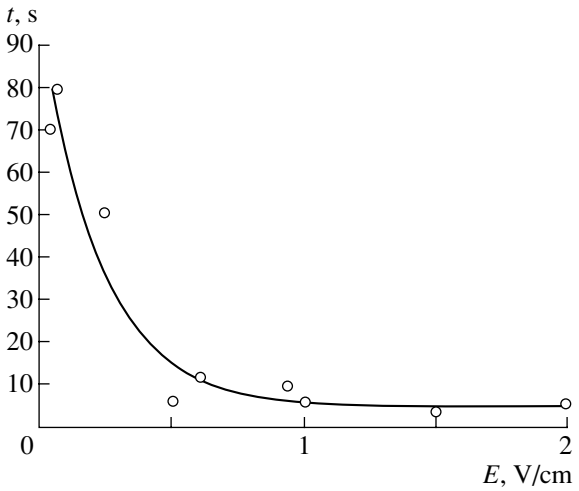

Fig. 3. Time of domain growth as a function of the intensity of the applied electric field.

$T < T_C$ (where T_C is the Curie temperature). The applied electric field results in crystal polarization ($+\mathbf{P}_s$) in the region where $T < T_C$. If prior to the field switching-on, the crystal polarization had the opposite sign ($-\mathbf{P}_s$), then, at $T = T_C$ a domain boundary is formed, which is shifted to low temperatures until the moment when the external field ($\mathbf{E}_{ext}$) would become equal to the coercive field ($\mathbf{E}_c$), increasing with a decrease in the temperature. In other words, the domain boundary stops in the temperature zone slightly lower than T_C. This temperature can be called the repolarization temperature, T_p. The repolarization process proceeds in two stages—(i) the initial nucleation of wedgelike domains in the near-electrode region and (ii) growth of microdomains from the sites of their nucleation into the crystal depth with the subsequent side intergrowth. The initial nucleation and growth of domains usually proceed from the electrode whose sign determines the direction of polarization $\mathbf{P}_s$ of a newly formed domain but can also occur in those regions of the crystal bulk (Fig. 2) where either local overstresses or reduced T_p caused by the presence of defects or concentration inhomogeneity are observed. The domain nucleation with the opposite polarization starts at a certain threshold field intensity at the given temperature. The rate of domain growth at T close to T_C increases, whereas the time of domains growth decreases with the electric-field intensity by the logarithmic law (Fig. 3).

With the motion of a crystal to the low-temperature region, the domain boundary is moved together with the crystal. The switching of polarity $\mathbf{E}_{ex}$ repeats the repolarization process, and a new domain boundary is formed at a distance $d = vt$ (where t is the time of the action of the field of the given polarity and v is the velocity of the crystal motion). The periodic (with the period t) repolarization of the external field results in the formation of a regular domain structure with a set domain size.

The thermoelectric treatment provides the formation of a regular domain structure with any preset orientation of domain boundaries relative to the crystallographic axes in bulk crystals with rather high domain-size reproducibility over the whole crystal volume. Such structures are used to design the diffraction electro-optical modulators of unpolarized laser radiation. Unfortunately this method cannot be used to obtain polydomain crystals with a period less than 20–225 μm. Such structures cannot be used for the implementation of quasi-synchronous nonlinear optical interactions of the optical beams in the generation of radiation harmonics of semiconductor or Nd-containing lasers, because the coherent length of the interaction for lithium niobate crystals attains several microns.

Among several alternative methods of formation of regular domain structures in lithium niobate crystals, only the thermoelectric treatment allows one to obtain volume elements with the maximum effective interaction length and the minimum domain period limited to several tens of microns. The problem of reducing the domain period can be solved based on the analysis of the kinetics of domain repolarization in an applied external electric field, the laws of growth of the domain boundaries, and their interaction with the defects of the crystal structure.

DIFFUSION OF DOMAIN BOUNDARIES DURING FORMATION OF REGULAR DOMAIN STRUCTURE

The minimum domain size in a regular domain structure is determined by the deviation of the domain boundaries from the ideal plane. Obviously, if the domain boundary is rough and is characterized by the roughness parameter Δ (here the term roughness has the same sense as in the characterization of the outer-surface roughness, i.e., Δ is the deviation of the relief height of the domain boundary from the middle line of

the profile *S* (Fig. 4), then the distance *d* between two adjacent boundaries cannot be less than Δ, otherwise the boundaries would merge together at the sites of their contacts and the regular domain structure would disintegrate into individual segments with opposite signs of spontaneous polarization.

If a regular domain structure is obtained by the method of postgrowth electrothermal treatment, the shape of the domain boundaries depends on the homogeneity of the applied electric field and the shape of the repolarization-temperature (T_p) isotherm in the region of domain nucleation. The creation of regular domain structures in a homogeneous electric field of a flat capacitor (except for the region of the edge effects, with the varying density of the force lines) provides such conditions that the shape of the domain boundaries is determined by the thermal-field isotherm and the homogeneity of the crystal.

The profile of the thermal-field isotherm in the region of domain nucleation is determined by the design of the thermal unit and can be close to a flat one. The minimum temperature of domain repolarization depends not only on the intensity of the electric field, but also on the composition and the structural perfection of the crystal. Therefore, even for an ideally planar thermal-field isotherm in a real (inhomogeneous) crystal, it is impossible to create ideally planar domain boundaries.

The shape and the roughness of a domain boundary depend on several factors related directly to the crystal properties. One of the reasons for the appearance of the parameter Δ determining the true thickness of the domain boundary is an increase in the domain-wall energy because of ion charges during the formation of a regular domain structure under conditions where **k** and $\mathbf{P}_s$ form an angle $\alpha \neq 90°$ (where $\mathbf{k} = \mathbf{n}/d$ is the spatial-periodicity vector, **n** is the normal to the domain boundary, and *d* is the domain size). This can occur if $\mathbf{P}_s$ and grad *T* form an angle different from 90°. The domain walls which arise during the cooling of grown crystals as a broken zigzaglike surface are formed by the planes among which the most often encountered ones are those of a rhombohedron, $\{10\bar{1}2\}$. The same effect is also observed in the formation of domain boundaries by the method of thermoelectric treatment under the condition that either $\mathbf{P}_s \parallel \mathrm{grad}\,T$ or $\mathbf{P}_s$ and grad *T* form an angle smaller than 90°.

This effect can be explained by the fact that with a decrease of the angle α formed by $\mathbf{P}_s$ and **k** (an increase of the angle between $\mathbf{P}_s$ and the domain wall), a polarizing charge $\rho_s = |\mathbf{P}_s|\cos\alpha$ is formed on the domain wall. Then, the corresponding field at the domain boundary becomes equal to

$$|\mathbf{E}_s| = \frac{|P_s|}{\varepsilon\varepsilon_0}\cos\alpha. \qquad (1)$$

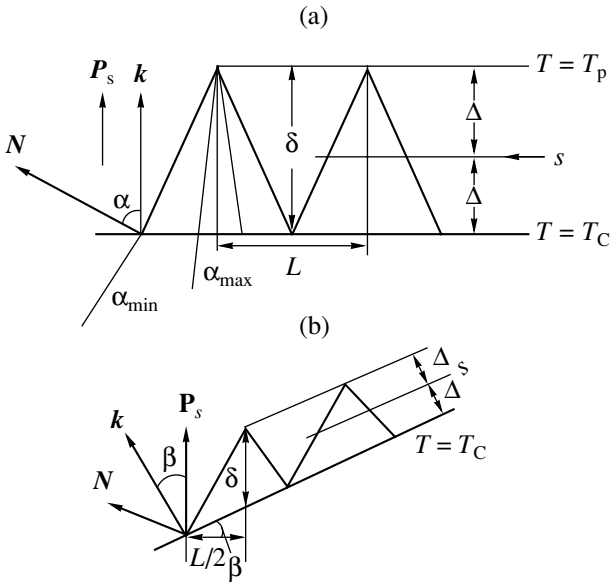

Fig. 4. Schematic domain boundary at (a) $\mathbf{k} \parallel \mathbf{P}_s$ (*s* is the average position of the domain boundary); (b) at **k** forming an angle β with $\mathbf{P}_s$.

This field is partly compensated with free charges of density $\rho = \int_0^t \sigma|\mathbf{E}|dt$, where *t* is the time of the action of the external electric field of the given polarization (the moment $t = 0$ corresponds to the beginning of the repolarization cycle), σ is electrical conductivity, and $|\mathbf{E}|$ is the strength of an uncompensated electric field of the domain boundary. As a result, the following electric field arises in the vicinity of the domain boundary

$$|\mathbf{E}| = \frac{1}{\varepsilon\varepsilon_0}\left(|\mathbf{P}_s|\cos\alpha - \int_0^t \sigma|\mathbf{E}|dt\right). \qquad (2)$$

The change of $|\mathbf{E}|$ with time is determined by the Maxwell relaxation $|\mathbf{E}| = |\mathbf{E}_0|\exp\left(-\frac{t}{\tau}\right)$, where $\tau = \frac{\varepsilon\varepsilon_0}{\sigma}$.

Thus, we have

$$|\mathbf{E}| = \frac{1}{\varepsilon\varepsilon_0}\left[|\mathbf{P}_s|\cos\alpha - |\mathbf{E}_0|\sigma\tau\int_0^t \exp(-t/\tau)dt\right] \qquad (3)$$

$$= \frac{|\mathbf{P}_s|}{\varepsilon\varepsilon_0}\cos\alpha + |\mathbf{E}_0|[\exp(-t/\tau) - 1],$$

$$\cos\alpha = \varepsilon\varepsilon_0\frac{|\mathbf{E}| + |\mathbf{E}_0|[1 - \exp(-t/\tau)]}{|\mathbf{P}_s|}. \qquad (4)$$

The field $|\mathbf{E}|$ and the external field $|\mathbf{E}_{ex}|$ move the domain boundary if the difference $|\mathbf{E}_{ex}| - |\mathbf{E}|$ exceeds the coercive field $|\mathbf{E}_c|$.

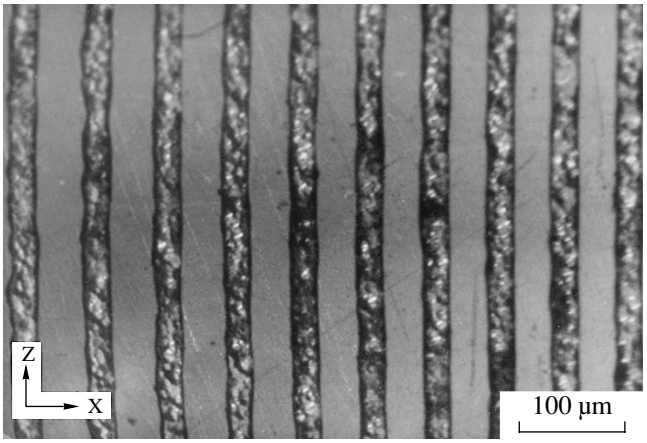

Fig. 5. Domain boundaries at $\mathbf{k} \perp \mathbf{P}_s$. The period of the domain structure equals 60 μm.

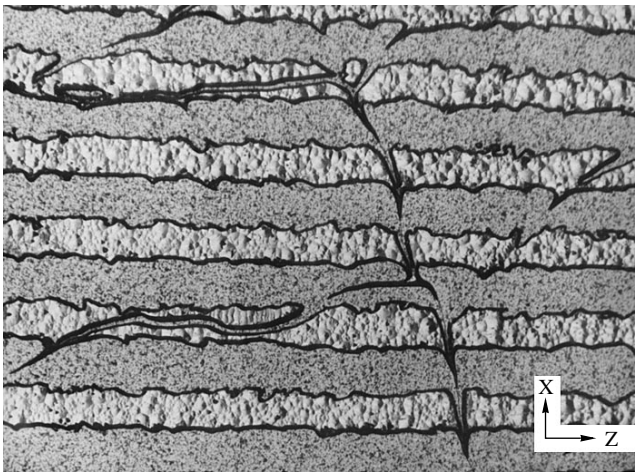

Fig. 6. Intersection of domain boundaries by block boundaries revealed by etching. The period of the domain structure equals 80 μm.

At the end of the repolarization cycle at $t = T$ (where t is the time of the action of the field of the given polarity), the domain boundary is fixed in the position where the uncompensated field of ion charges is equal to

$$|\mathbf{E}| = |\mathbf{E}_{ex}| - |\mathbf{E}_c| = \frac{|\mathbf{P}_s|}{\varepsilon\varepsilon_0}\cos\alpha_{min} + |\mathbf{E}_0|[\exp(-T/\tau) - 1]. \quad (5)$$

Here $|\mathbf{E}_0|$ is the field of coupled charges at $t = 0$, i.e., in the absence of any compensation with free charges, which, according to (1), is equal to

$$|\mathbf{E}_0| = |\mathbf{E}_s|_{max} = \frac{|\mathbf{P}_s|}{\varepsilon\varepsilon_0}\cos\alpha_{max}. \quad (6)$$

Thus, the angle formed by the domain-boundary normal N and $\mathbf{P}_s$ (Fig. 4a) at the moment t can be defined as

$$\cos\alpha_{min} = \frac{|\mathbf{E}_{ex}| - |\mathbf{E}_c|}{|\mathbf{E}_s|} + [\exp(-T/\tau) - 1]\cos\alpha_{max}. \quad (7)$$

If relaxation proceeds so fast that $T \gg \tau$, then $\cos\alpha_{min} = \dfrac{|\mathbf{E}_{ex}| - |\mathbf{E}_c|}{|\mathbf{E}_s|}$.

TRUE THICKNESS OF DOMAIN BOUNDARIES AS A FUNCTION OF CRYSTAL HOMOGENEITY AND THE TEMPERATURE GRADIENT IN THE REPOLARIZATION ZONE

The formation of a domain boundary in lithium niobate starts with the nucleation of needle-like domains with length determined by the condition $|\mathbf{E}_{ex}| = |\mathbf{E}_c|$. The angles between the domain-boundary normals and $\mathbf{P}_s$ are equal to ($\pm\alpha_{max}$). The subsequent growth of domains in the polar and the side directions results in the transformation of the needles into the pyramidal formations with an increase of α up to α_{min} (Fig. 4). At the distance L between the nucleus centers, the height of these pyramids is $\delta = \dfrac{L}{2}\tan\alpha_{min}$ (Fig. 4a), which corresponds to the double roughness parameter of the boundary and can be considered as the true thickness of the domain boundary if the normal $\mathbf{k}$ to the average position of the domain boundary forms an angle of $\beta = 0$ with $\mathbf{P}_s$. A domain boundary is the superposition of such pyramids (Fig. 4c) with their number being equal to the number of nuclei and their height being directed along the polar axis.

The true thickness of the domain boundary at $\beta \neq 0$ (Fig. 4b) is

$$2\Delta = \delta\cos\beta. \quad (8)$$

As follows from Fig. 4, the true thickness of the domain boundary decreases with the approach of T_C to T_p, in other words, with an increase of grad$T$ in the repolarization zone.

Expression (4) describes the monotonic dependence $\alpha(E)$, whereas, in actual fact, the angle α often corresponds to an angle formed by the faces of the simple forms. For lithium niobate, such a simple form is the $\{10\bar{1}2\}$-rhombohedron. This signifies that the electrostatic energy of the domain boundary cannot depend on α monotonically and forms the minima at the sites where the domain boundary coincides with the simple-form faces. In other words, one can state that the coercive force depends on α and that this dependence has the maxima at the sites where the position of the domain boundary coincides with the faces of some simple forms.

If the regular domain structures are formed under the conditions such that grad$T \perp \mathbf{P}_s$, the domain walls are parallel to the polar direction; no charges can be

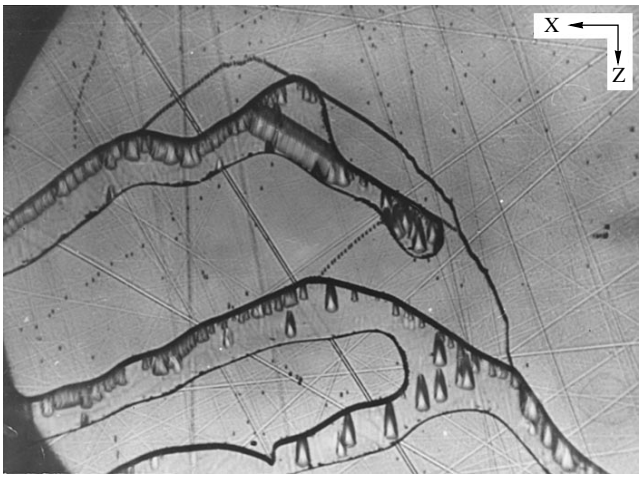

Fig. 7. Localization of domains of opposite signs at dislocation pile-ups revealed by selective etching. The period of the domain structure equals 65 μm.

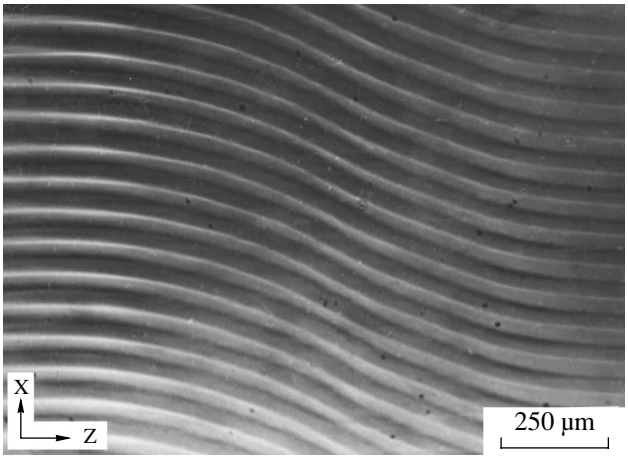

Fig. 8. Intersection of the concentration inhomogeneity by domain boundaries in the striation band. The period of the domain structure equals 35 μm.

formed on these walls and, therefore, no kinks can be formed either. The domain walls are flattened and the domain boundary becomes smoother and thinner (Fig. 5).

There are some other reasons resulting in the distortion of the flat shape of the domain boundary which are associated with crystal inhomogeneity. The correlation between the domain-boundary positions and the profile of the Curie-temperature isotherm in the crystal bulk depends on the constancy of the composition and the structural perfection of the crystal. It was established that composition inhomogeneities affect the Curie temperature and that the interaction of the domain boundaries with the structure defects results in domain pinning on growth layers and block boundaries.

Figure 6 illustrates the distortion of domain boundaries by block boundaries in $LiNbO_3$ crystals during the formation of a regular domain structure under the conditions $\mathrm{grad}\,T \perp \mathbf{P}_s$. It is seen that the block boundaries are "dragged" by the domain walls into the region of higher temperatures. This can be explained by an increase of the Curie temperature in the region of the block boundaries due to an increase of the concentrations of impurities and point defects in these regions. Knowing the value of $\mathrm{grad}T$ in the repolarization region and the distance D of the domain-wall deviation caused by the block boundary (or the growth stria), one can evaluate the change in the Curie temperature in the vicinity of the structural defect as $\Delta T_c = D\,\mathrm{grad}\,T$. On the other hand, the ratio $D = \Delta T_k/\mathrm{grad}\,T$ signifies that the domain-boundary distortions from the flat shape can be reduced by increasing the temperature gradient in the repolarization zone. Thus, the block boundaries pin the domain walls. Repolarization is also hindered by pile-ups of dislocations which leave some regions where the domains have the opposite sign in a newly formed domain (Fig. 7).

Another example of the effect of crystal inhomogeneity on the position of domain boundaries is the domain curvature in the region of concentration inhomogeneities caused by growth stria (Fig. 8). This curvature can be explained by the influence of the composition on the Curie temperature. A chemical inhomogeneity of doped crystals (e.g., $LiNbO_3$:Mg) and, as a result, the variation in T_C result in disintegration of domains into individual islands, even at such distances between the walls and the models of regular domain-structure formation at which the formation of a regular domain structure in pure and homogeneous crystals occurs in the steady-state mode.

An electric field sufficient for the formation of a regular domain structure by zone repolarization has upper and the lower limits. It seems that the more intense the polarizing field, the easier the formation of the regular domain structure and the higher the domain-wall qual-

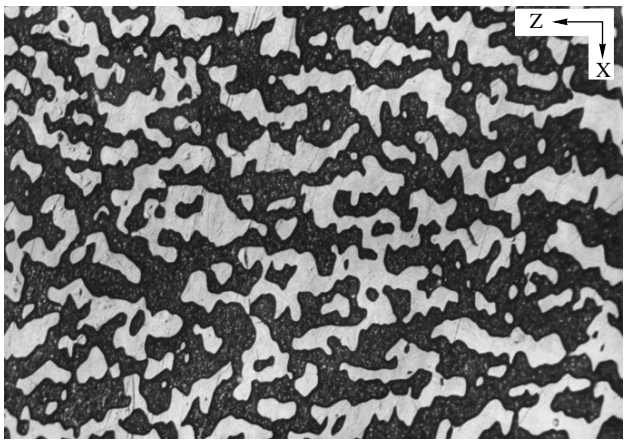

Fig. 9. Formation of domain islands at low intensity of the repolarizing field ($\mathbf{E}_{ex}$ = 0.25 V/cm).

ity. However, in actual fact, an increase in the polarizing-field intensity increases the conductivity, which, at high temperatures, results in an increase of the defect concentration in the crystal because of electrolysis. Therefore, it is desirable that repolarization occur in the vicinity of the lower field limit, $\mathbf{E}_l$. The value of $\mathbf{E}_l$ is determined by the fact that a decrease in $\mathbf{E}$ below $\mathbf{E}_l$ results in the disintegration of domains into individual islands (Fig. 9). The existence of the lower limit of the field intensity in the formation of a regular domain structure is explained by the fact that, at low values of the applied electric field, the rates of formation of wedgelike domains and their growth into the crystal bulk are too low to provide the complete filling with domains of the crystal region within which the repolarization boundary moved within the time of the application of a positive or a negative electric field.

CONCLUSION

The minimum distance between the domain boundaries that can be obtained by creating a regular domain structure by repolarization of a crystal moving in the temperature field with a temperature gradient depends on the variation in the roughness heights of the domain boundary, which are, in fact, a set of wedgelike protrusions along the normal $\mathbf{k}$ to the boundary. The value of the roughness parameter Δ is determined by the true width of the domain boundary dependent on the angle formed by $\mathbf{k}$ and $\mathbf{P}_s$ and the crystal homogeneity. The size of the domains can be reduced by increasing the homogeneity of the crystals used for the formation of regular domain structures and by an increase in the temperature gradient in the repolarization zone.

REFERENCES

1. A. A. Blistanov, V. L. Kopa-Ovdienko, V. L. Naumov, *et al.*, Kvantovaya Élektron. (Moscow) **15**, 986 (1988).
2. A. N. Baryshnikov, A. A. Blistanov, V. L. Kopa-Ovdienko, *et al.*, Kvantovaya Élektron. (Moscow) **16**, 164 (1989).
3. D. H. Jundt, G. A. Magel, M. M. Fejer, *et al.*, J. Opt. Soc. Am. **181**, 614 (1991).
4. D. H. Jundt, G. A. Magel, M. M. Fejer, *et al.*, Appl. Phys. Lett. **59**, 2657 (1991).
5. Y. Ishigame, T. Suhara, and H. Nishihara, Opt. Lett. **16**, 375 (1991).
6. K. Ymamoto, K. Mizuuchi, and T. Taniuchi, J. Opt. Soc. Am. **181**, 616 (1991).
7. J. Chen, Q. Zou, J. F. Hong, *et al.*, J. Appl. Phys. **66**, 336 (1989).
8. S. V. Tkachev, D. N. Frantsev, and D. V. Roshchupkin, Izv. Vyssh. Uchebn. Zaved., Mater. Élektron. Tekh., No. 2, 40 (1999).
9. V. V. Antipov, A. A. Blistanov, N. G. Sorokin, *et al.*, Kristallografiya **30**, 2534 (1985) [Sov. Phys. Crystallogr. **30**, 428 (1985)].
10. N. G. Sorokin, V. V. Antipov, and A. A. Blistanov, Ferroelectrics **167**, 267 (1995).

Translated by L. Man

Crystallography Reports, Vol. 47, No. 1, 2002, pp. 117–119. Translated from Kristallografiya, Vol. 47, No. 1, 2002, pp. 125–127.

PHYSICAL PROPERTIES OF CRYSTALS

Simulation of Transport Properties of α-$AgI_{1-x}Cl_x$ ($0 < x < 0.25$) by the Molecular Dynamics Method

A. K. Ivanov-Shitz, B. Yu. Mazniker, and E. S. Povolotskaya

Shubnikov Institute of Crystallography, Russian Academy of Sciences, Leninskiĭ pr. 59, Moscow, 117333 Russia

e-mail: ivanov@ns.crys.ras.ru

Received January 16, 2001

Abstract—The transport characteristics of the α-$AgI_{1-x}Cl_x$ solid solutions have been calculated by the molecular dynamics method. It is established that the diffusion coefficient of cations decreases with an increase in the concentration of chlorine atoms, which agrees with the well-known experimental data on the behavior of ionic conductivity. © *2002 MAIK "Nauka/Interperiodica".*

As is well known, the high-temperature α-phase of silver iodide possesses high ionic conductivity [1] and, because of its rather simple crystal structure, is used as a model system in the studies of ionic-transport processes in solids in studies by various methods including the computer simulation. In a row of quasibinary systems AgI–AgX, where X = Br, Cl [1–6], and AgI–MI (M = Cu, Cs) [7–10], the α-AgI-based solid solutions exist in a rather wide concentration and temperature ranges. The concentration dependences of ionic conductivity (σ_i) of α-$AgI_{1-x}Cl_x$ ($0 < x < 0.25$) solid solutions [6] indicate the reduction of electrical conductivity of the material with an increase in chlorine concentration in the specimen. (In a low-temperature β-$AgI_{1-x}Cl_x$ phase, conductivity increases with an increase of x [6] because the introduction of chloride ions into the silver iodide matrix results in a higher concentration of Frenkel defects [11].)

Recently, we calculated the diffusion coefficient of Ag^+ in copper-doped silver iodide [12] and established that the variations in the mobile cationic subsystem deteriorate the transport characteristics of the solid solutions. Below, we describe the study of the effect of substitutions in the rigid anionic sublattice on diffusion of silver cations in the AgI–AgCl system performed by the molecular dynamics (MD) method.

The computations were made by the specially modified program suggested earlier in [13] for studying the bulk properties of solid electrolytes. The atomic motion was calculated by the fifth-order predictor–corrector algorithm, whereas electrostatic interactions were calculated by the Ewald method. Simulation was made for a system consisting of 256 ions, i.e., the pixel consisted of 64 unit cells including 128 anions and 128 cations. The anions formed a body-centered cubic lattice, whereas two cations were randomly located in the centers of the cube faces of the unit cell. The iodine and chlorine atoms in the anionic positions were randomly placed.

The first Born–Mayer–Huggins interaction potential was used in the form

$$V_{i,j} = \frac{z_i z_j e^2}{r} + \frac{H_{ij}}{r^{n_{ij}}} - \frac{P_{ij}}{r^4} - \frac{W_{ij}}{r^6},$$

where r is the interionic distance, z_i is the effective charge of the ith ion, the parameters H_{ij} and n_{ij} enter the term which describes the repulsion energy caused by the overlap of electron shells, and $P_{ij} = 0.5(\alpha_i z_i^2 + \alpha_j z_j^2)$ is the parameter of the dipole–dipole interaction (α_i is the electron polarizability of the ith ion and W_{ij} is the parameter entering the term provided by the van der Waals interaction).

The concrete parameters of the interparticle potential were taken from [11] and are listed in Table 1.

The effective anion charge was taken to be equal to $z(I^-) = -0.6e$, $z(Cl^-) = -0.7e$, and the charge of the silver cations was chosen based on the condition of the electrical neutrality of the crystal [14, 15]. The electron polari-

Table 1. Parameters of ion interactions

Type of the $i-j$ pair	n_{ij}	H_{ij}^*	W_{ij}^*
$Ag^+ - Ag^+$	11	0.014804	0.0
$Ag^+ - I^-$	9	114.64	0.0
$Ag^+ - Cl^-$	11	127.645	0.0
$I^- - I^-$	7	446.64	6.9832
$I^- - Cl^-$	7	266.317	2.11074
$Cl^- - Cl^-$	11	17152.23	2.11074

* In e^2/Å units (14.39 eV).

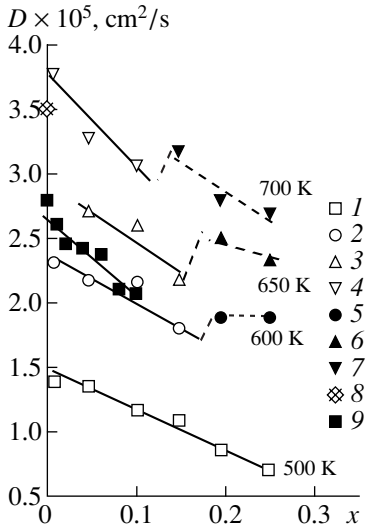

Concentration dependences of the diffusion coefficients of silver cations in $AgI_{1-x}Cl_x$ solid solutions. (*1–4*) Solid phase, (*5–7*) melt, (*8*) AgI at 700 K (experiment [18]), (*9*) calculated from the electrical conductivity data at 500 K [6].

zabilities were $\alpha_{Ag} = 0$, $\alpha_I = 6.52 \times 10^{-3}$, and $\alpha_{Cl} = 3.45 \times 10^{-3}$ mm^3 [11]; the pixel size equal to $a = 0.5062$ nm was determined from the experimental data for AgI [16, 17].

The time step 5×10^{-15} s provided the stability of the total energy of the system within an accuracy of 0.2%. The particle velocities at the initial moment were assumed to be zero; then, using the thermalization mechanism [13], the system temperature was brought to the set level. The characteristics of the simulated crystal were determined from the data of about 10^4 iterations.

The MD computations provided the determination of the coefficient of particle self-diffusion from the analysis of the root-mean square deviations of ions ($r_k^2(t)$) in accordance with the relationship

$$\lim\{r_k^2(t)\} = 6D_k t + B_k, \quad t \longrightarrow \infty,$$

where D_k is the diffusion coefficient of a *k*-type particle and B_k is the Debye–Waller factor.

Table 2. Heiven coefficient H_R for the α-AgI phase

T, K	H_R^*	H_R^{**}
433	0.69	0.67
623	0.69	0.59
813	0.82	0.56

* Experimental [18, 19].
** Calculated [20].

The analysis of the root-mean square deviations of silver cations and iodide and chloride anions indicate that only silver cations participate in the translational motions in the high-temperature α-phase, whereas the iodide and chloride anions vibrate about their equilibrium positions. The good agreement of the calculated (for the composition α-$AgI_{0.992}Cl_{0.008}$) and the experimental (for pure α-AgI [18]) diffusion coefficients at 700 K (Fig. 1) confirms the validity of the chosen interaction potential.

The figure shows the concentration dependences of the diffusion coefficient D_{Ag} of silver cations. A decrease of D_{Ag} with an increase of the chlorine concentration in the solid solutions is observed at all the temperatures (Figure, points *1–4*). The decrease of conductivity in the α-$Ag_{1-x}Cu_xI$ solid solution in the range of weak nonstoichiometry of α-$Ag_{1-x}Cu_xI$ (in the vicinity of $x < 0.1$) was first observed by Ihara *et al.* [6]. For comparison, the figure also shows the experimental data on the diffusion coefficients of cations at 500 K calculated from the experimentally measured conductivities by the Nernst–Einstein ratio

$$D_\sigma = \frac{\sigma kT}{n(ze)^2},$$

where *n* is the number of the charge carriers (*ze*). The Heiven ratio $H_R = D/D_\sigma$ is about 0.58 for all the compositions at 500 K, which agrees with the Heiven coefficients determined experimentally for α-AgI [18, 19] and calculated by the Monte–Carlo method [20] (Table 2). Since $H_R < 1$ in the whole temperature range studied, this indicates the cooperative character of the motion. Okasaki [21], considering the "caterpillar" mechanism of the motion, obtained a correlation coefficient equal to 0.5–0.66, which is close to the experimentally determined value $H_R = 0.58$.

The activation energy of diffusion is $E_D = 0.14 \pm 0.01$ eV for all the solid solutions studied and is close to the value $E_D \approx 0.15$ eV for the nonstoichiometric α-$Ag_{1-x}Cu_xI$ phases with substitutions in the cationic sublattice [12].

The analysis of the $r_k^2(t)$ curves shows that the crystals of the composition α-$AgI_{1-x}Cl_x$ melt at lower temperatures than the crystals of pure silver iodide. As is seen from the figure (points *5–7*), upon crystal melting, *D* sightly increases, whereas, for pure silver iodide, the value of electrical conductivity in the melt is slightly lower than in the solid phase [19].

The MD computations lead to some assumptions about the phase diagram of the AgI–AgCl system in the range of α-phase existence (still not studied) based on the data on solid-solution melting. It seems that the phase diagram of the AgI–AgCl system differs from the phase diagram of the similar AgI–AgBr system [2], because with an increase in the temperature the stability range of the α-$AgI_{1-x}Cl_x$ phase decreases.

As follows from the above consideration, silver diffusion in α-$AgI_{1-x}Cl_x$ solid solutions decreases with an increase in the Cl^- concentration, which indicates the existence of some optimum relationships between the dimensions of the mobile particles and conductivity channels in crystalline solid electrolytes [22]. It can also be assumed that with an increase in the chloride ion concentration (the ionic radius of chlorine r_{Cl} = 0.181 is less than the iodine radius r = 0.216 nm), the parameter of the solid solutions decreases in accordance with Vegard's law and therefore the "free volume" available for diffusion of cations also decreases, which would have resulted in lower conductivity. However, our studies showed that a decrease in the lattice parameter practically does not affect the transport characteristics. The analysis of the structural characteristics of α-AgI based on the EXAFS data [23, 24] allowed us to establish that the most favorable path of Ag^+ transport is provided by the transition from the tetrahedral position via the trigonal one to another tetrahedral position and overcoming the potential barrier of 0.04–0.07 eV. The theoretical consideration within the stochastic model [25] indicates the pronounced dependence of ion mobility on the shape of the potential relief along which the particles move. In other words, even at the same value of the potential barrier, the mobilities and, therefore, also the diffusion of silver ions are different, because the particles move along different reliefs with different geometric and force characteristics of I and Cl atoms. Thus, the conclusion made in [12] regarding strongly correlated cation motion in α-AgI-based solid solutions has been confirmed once again.

ACKNOWLEDGMENTS

This study was supported by the Russian Foundation for Basic Research, project no. 99-03-32726 and the NWO grant no. 047-007-008 (the Netherlands).

REFERENCES

1. A. K. Ivanov-Shitz and I. V. Murin, *Solid State Ionics* (Sankt-Peterb. Gos. Univ., St. Petersburg, 2000).
2. R. M. Biefeld, R. T. Johnson, Jr., and M. M. Karnowsky, J. Electrochem. Soc. **126** (5), 818 (1979).
3. K. Shahi and J. B. Wagner, Jr., Phys. Rev. B **23** (12), 6417 (1981).
4. H. B. Takahashi, S. Tamaki, and S. Harada, Solid State Ionics **14** (2), 107 (1984).
5. H. Takahashi and S. Tamaki, Solid State Ionics **15** (1), 43 (1985).
6. S. Ihara, Y. Warita, and K. Suzuki, Phys. Status Solidi A **86** (2), 729 (1984).
7. J. Nölting, Ber. Bunsenges. Phys. Chem. **68** (10), 932 (1964).
8. J. C. Bazán and J. A. Schmidt, J. Appl. Electrochem. **6**, 411 (1976).
9. J. A. Schmidt, R. E. Fornari, and J. C. Bazán, Electrochim. Acta **24**, 1131 (1979).
10. M. Kusakabe, Y. Shirakawa, S. Tamaki, and Y. Ito, J. Phys. Soc. Jpn. **64** (1), 170 (1995).
11. S. Ihara and K. Suzuki, Phys. Status Solidi B **131** (1), 97 (1985).
12. A. K. Ivanov-Shitz, B. Yu. Mazniker, and E. S. Povolotskaya, Kristallografiya **46** (2), 336 (2001) [Crystallogr. Rep. **46**, 292 (2001)].
13. A. K. Ivanov-Shitz, A. S. Bukhshtab, and S. Kh. Aĭt'yan, Fiz. Tverd. Tela (Leningrad) **32** (5), 1360 (1990) [Sov. Phys. Solid State **32**, 795 (1990)].
14. F. Shimojo and M. Kobayashi, J. Phys. Soc. Jpn. **60** (11), 3725 (1991).
15. A. Fukumoto and A. Ueda, Solid State Ionics **3/4**, 115 (1981).
16. K. Ihata and H. Okazaki, J. Phys.: Condens. Matter **9**, 1477 (1997).
17. R. J. Cava, F. Reidinger, and B. J. Wuensch, Solid State Commun. **24**, 411 (1977).
18. A. Kvist and R. Tärneberg, Z. Naturforsch. A **25**, 257 (1970).
19. A. Kvist and A.-M. Josefson, Z. Naturforsch. A **23**, 625 (1968).
20. F. Tachibana and H. Okazaki, Solid State Ionics **23**, 219 (1987).
21. H. Okazaki, J. Phys. Soc. Jpn. **23** (2), 355 (1967).
22. *Physics of Superionic Conductors*, Ed. by M. B. Salamon (Springer-Verlag, New York, 1979; Zinatne, Riga, E. M. Iolin, Ed., 1982).
23. T. M. Hayes and J. B. Boyce, Phys. Rev. B **21**, 2513 (1980).
24. A. Yoshiasa, F. Kanamuru, and K. Koto, Solid State Ionics **27**, 275 (1988).
25. W. Dieterich, I. Peschel, and W. R. Schneider, Z. Phys. B **27**, 177 (1977).

Translated by L. Man

Crystallography Reports, Vol. 47, No. 1, 2002, pp. 120–123. Translated from Kristallografiya, Vol. 47, No. 1, 2002, pp. 128–132.

PHYSICAL PROPERTIES OF CRYSTALS

Effect of Nonstoichiometry and Technological Impurities on the Structural Properties and Absorption of $Y_3F_5O_{12}$ Crystals in the IR Range

I. D. Lomako and A. G. Dutov

Institute of Solid-State and Semiconductor Physics, National Academy of Sciences of Belarus, ul. Brovki 17, Minsk, 220071 Belarus

Received January 18, 2001; in final form, March 3, 2001

Abstract—Complex studies of the optical and structural properties and the elemental composition of a series of yttrium iron garnets (YIG) grown from flux have been performed with due regard for the crystallographic orientation of the platelets. It has been established that the presence of Mn, Ba, and V microimpurity ions at a level of a few thousandths of a percent can play a stabilizing role in the synthesis of perfect crystals with the garnet structure. The criterion of the quality of the grown crystals is formulated as the ratio of the total number of Y and Fe cations to the number of oxygen anions (in wt %). © *2002 MAIK "Nauka/Interperiodica".*

INTRODUCTION

The crystals of yttrium iron garnets (YIG) of a rather high quality are characterized by high values of optical transparence, specific Faraday rotation in the IR range, and excellent microwave parameters [1, 2]. Despite the enormous number of publications on the properties and nonstoichiometry of crystals with the garnet structure, these characteristics were always considered ignoring the crystallographic orientation of the specimens.

It is well known that, according to the phase diagram [3], growth of YIG crystals from flux results in a slight deficit of oxygen ions in the structure. It is usually believed that the oxygen deficit is compensated with the formation of Fe^{2+} ions providing the neutrality of the YIG molecule [4, 5]. The estimation of the probability of intrinsic-defect formation in YIG crystals showed that the formation of anion vacancies accompanied by the change of the charge of some Fe-ions occupying the octahedral positions is energetically advantageous [4]. The garnet structure is the most appropriate for the arrangement of various types of cations with variable valences and concentrations in three sublattices of the structure.

EXPERIMENTAL

We studied YIG crystals grown from flux based on the PbO–PBF_2–B_2O3 systems in both statistical and dynamical modes. The relative concentration of Mn ions and the weight ratio of the main cations, Y/Fe, were determined by neutron–activation analysis and X-ray photoelectron spectroscopy. The photoelectron spectra were recorded on an ES 2401 electron spectrometer in a 10^{-6} Pa vacuum with the use of the K_α magnesium line at the energy of 1253 eV. The concentration of Ba-ions replacing Y-ions in the dodecahedral sublattice is determined by the method of X-ray radiometric analysis with the use of an Am^{241} excitation source. The characteristics of the YIG specimens studied, their orientation, lattice parameters, the Ba/Y ratio (hereafter indicated in wt %), and other impurities revealed in the crystals are indicated in table. To study the anisotropy of defect distribution in YIG crystals, the specimens were cut in the shape of 1.6–2.5 mm-thick platelets parallel to the (110), (111), and (100) planes. The X-ray diffraction patterns were obtained on a DRON-3 diffractometer (Fe K_α radiation) with the accuracy in the lattice parameter determination being $\pm 2 \times 10^{-3}$ Å. The transmission spectra of the YIG specimens including two unoriented specimens, 32-NO and 45-NO, were recorded on a Beckman spectrometer in the unpolarized light in the range 1000–2000 nm at 293 K. The absorption coefficient a was calculated by the standard formula with due regard for the reflection coefficient R and the refractive index $n = 2.3$, namely:

$$\alpha = d^{-1}\ln\{(1 - R)^2/(2I/I_0) + [(1 - R)^2/(2I/I_0) + R^2]^{1/2}\},$$

$$R = (n - 1)^2/(n + 1)^2,$$

where d is the platelet thickness in cm and I_0 and I are the intensities of the incident and the transmitted light, respectively.

RESULTS AND DISCUSSION

The garnet structure is cubic with eight $\{C_3\}[A_2](D_3)O_{12}$ formula units in the unit cell (the curved and square brackets and the parentheses indicate the positions of cations with the dodecahedral, octahedral, and tetrahedral coordination relative to oxygen, respectively).

1063-7745/02/4701-0120$22.00 © 2002 MAIK "Nauka/Interperiodica"

The quality of the grown YIG crystals was determined from the absorption coefficient α at the wavelength λ = 1300 nm and the lattice parameter *a*. The fluctuations of the growth rates with time give rise to oscillations in impurity concentrations in the crystal and, thus, determine the zonal or striation structure [6]. The zonal inhomogeneity in the impurity distribution results in the formation of dislocation sources, internal stresses, and other crystal defects. It was concluded [7] that the growth rates of the (211)- and (110)-type faces in the crystal with the garnet structure are almost twice as low as the growth rate of the (111) face. We observed different variants of incorporation of Ba-ions for each orientation and their different effect on the specimen transparence. With a four-time increase in the Ba concentration in the (111) oriented platelets, the *a* value decreases from 23.5 to 17 cm^{-1} (curve *2* in Fig. 1), whereas an increase of the number of Ba ions by an order of magnitude in the (110)-oriented specimens, gives rise to an increase of *a* from 0.4 to 13.2 cm^{-1} (curve *1* in Fig. 1).

The barium concentration (wt %) with respect to yttrium ions is indicated in Table 1. It is seen that the concentration of Ba-ions in the growth pyramid on the (110) face considerably differs from the expected value for the habit-forming face, which favors the formation of crystals with rather perfect crystal structure (specimens 7, 43, 52, and 41) and high transparence ($\alpha \approx$ 5 cm^{-1}). Curve *3* in Fig. 1 corresponds to specimens with rather high concentrations of Ba-ions and other inclusions, which often interact with one another (specimens 41, 3, 32-NO, 45-NO, and 22-Bi). The different run of the curves for the (110)- and (111)-orientated crystals leads to the conclusion that the Ba/Y ratio influences the *a*-parameter by different mechanisms. It is possible that the reticular density of cations in the octahedral and dodecahedral positions produces an important effect, which is much more pronounced for the (110) faces than for the (100) and (111) faces [8, 9].

In addition to Ba ions, the YIG crystals also contain some other impurities, e.g., Mn and Sm ions with valences varying from 2 to 4. For (110)- and (111)-oriented platelets with the Ba and Mn impurities, we observed the following: in the specimens with minimum Ba-concentration, the concentration of Mn ions was higher (specimens 7 and V-3); in other words, the maximum concentration of one impurity corresponds to the minimum concentration of the other impurity. At first glance, this correlation is rather surprising, because the Ba- and Mn-ions replacing the Fe-ions occupy different sites in the crystal lattice (Ba occupies the dodecahedral sites and Mn, the octahedral ones). Therefore, these impurities do not compete with one another. One possible explanations of this fact is the incorporation of a large divalent Mn-ion into the dodecahedral sublattice. In this case, the Mn-ion starts competing with Ba- or Pb-ions. The established fact shows that Ba-and Mn-impurities mutually enhance their effect on the concentration of optically-active defect centers in YIG.

Characteristics of YIG crystals studied

Specimen	Orientation	α, cm^{-1}	*a*, Å	Ba/Y, wt %	Other impurities
30	110	24.6	12.374	0.165	Mn
50	110	13.2	12.374	0.243	–
51	110	10.0	12.372	–	
22-Bi	110	5.60	12.390	1.556	Sm, Mn, Bi
32-HO	HO	7.20	–	1.62	V, Pb
52	110	5.15	12.377	0.95	Sm, V, Pb, Bi
50"	110	6.91	12.374	1.40	–
43	110	3.60	12.371	0.08	–
41	110	1.27	12.377	0.90	Sm, Mn
7	110	0.40	12.370	0.023	Sm, Mn, Pb, Bi
V-3	111	23.5	12.375	0.08	Mn, Pb
V-1	111	20.7	12.365	0.16	Mn, Pb
III-6	111	17.3	12.363	0.73	Mn, Pb
46	111	10.2	12.370	–	
34	111	6.16	–	2.10	
42	111	0.90	12.376	0.58	
VI-4	100	23.5	12.378	0.32	Mn
3	100	2.33	12.375	0.083	Sm, Mn
31	100	2.19	12.365	0.06	

Figure 2 shows the dependence Y/Fe = f[ln(Ba/Y)] demonstrating the different character of incorporation of Ba ions into the (100)- and (111)-oriented specimens of the garnet structure. Possibly, at a relative low growth rate of the (110) face, the Ba-ions, both at low and high concentrations, are incorporated into the structure in a more uniform way, which explains the slight change in the Y/Fe ratio (by 0.91–0.96) for this orientation accompanied by the change of Ba-concentration from 0.023 to 0.90 for pure (without impurities) crystals and up to 1.556 for Bi-substituted YIG crystals. The high growth rate of the (111) face provides the incorporation of a noticeable number of Ba-ions (curve *2* in Fig. 2) distributed more uniformly than in the first case, which explains the considerable range of the Y/Fe variation (0.86–0.97). The most pronounced scatter (0.83–1.089) in the Y/Fe ratio is observed for the (100)-oriented plates. The corresponding curve is not shown in Fig. 2 because there were only three plates of this type. The nonmonotonic character of the Y/Fe variation for differently oriented plates seems to be the consequence of the growth anisotropy which could be estimated only qualitatively—it was minimal for the (110)-oriented plates, intermediate for the (111)-oriented ones, and maximal for the (100)-oriented specimens.

It should be emphasized that neither the Y/Fe ratio nor the lattice parameter can be used as reliable criteria

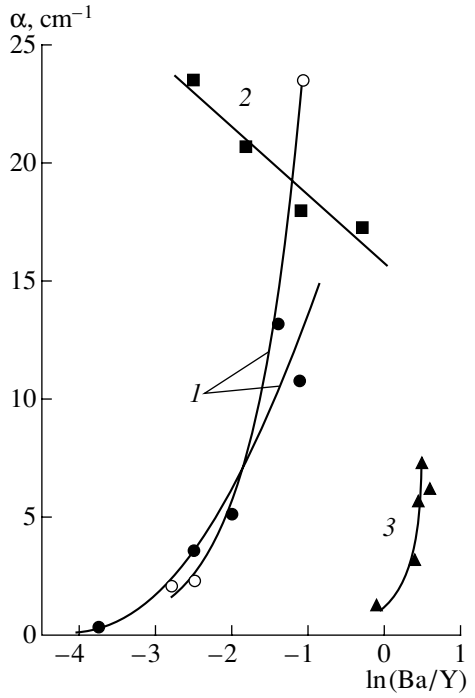

Fig. 1. Dependence of α on ln(Ba/Y) at the wavelength λ = 1300 nm for differently oriented YIG specimens: (*1*) (110)-orientation (filled circles), (100)-orientation (open circles); (*2*) (111)-orientation; and (*3*) NO-specimens and specimens with high impurity concentrations.

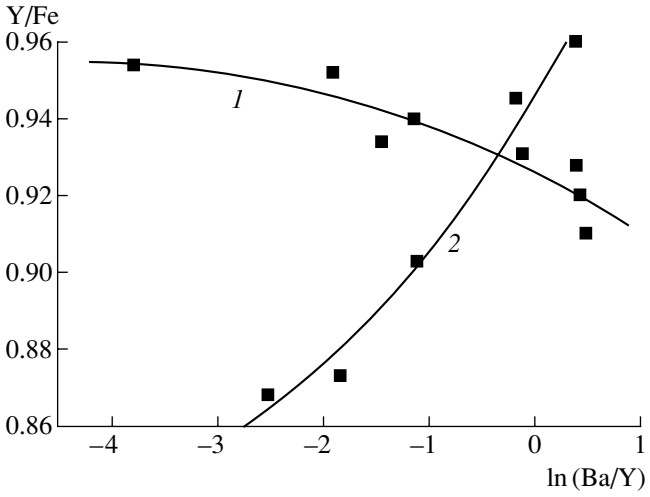

Fig. 2. The Y/Fe ratio as a function of ln(Ba/Y) for differently oriented YIG specimens: (*1*) (110) and (*2*) (111) orientations.

for evaluating the degree of perfection of YIG single crystals, which can be illustrated by the following examples. Specimen 30 with the (110) orientation has the Y/Fe ratio close to that for the stoichiometric composition; still, it was not sufficient for relating it to the best specimens of the series studied, because the total number of cations was small and the plate had poor transparency ($\alpha = 24.6$ cm^{-1}) despite the "good" lattice parameter ($a = 12.374$ Å). Specimen 3 with the (100) orientation had the Y/Fe ratio equal to 1.089, i.e., far from the ideal value (0.954), but its absorption coefficient was lower by an order of magnitude than this coefficient for specimen 30, whereas the lattice parameter almost equals the lattice parameters of the "best" YIG crystals. Table 1 from [10] yields more such examples. Continuing the discussion to the effect [2, 11], we would like to state that neither the lattice parameter nor the Y/Fe ratio can serve as an unambioguous criterion for evaluating the quality of multicomponent crystals with the garnet structure.

The study of 18 differently oriented YIG specimens allowed us to formulate the criterion for evaluating their quality—it is the ratio of the total number of Y-and Fe-cations to the number of O anions. The oxygen content in the specimens was calculated as the difference between the weight of the specimen and the weight of the total number of cations. The use of this method is quite justified because the crystal density and the structure constants differ only insignificantly. The dependence $\alpha = f((Y + Fe)/O)$ for the specimens studied is described by a parabola with the points of this parabola corresponding to specimens of different degrees of perfection. The best YIG specimens with a composition close to stoichiometric [$S = (Y + Fe)/O \sim 2.84$] are characterized by low α-values, well-balanced concentrations of Ba-, Mn-, Pb-, and Bi-impurities, and the clearly pronounced minimum [10]. This minimum on the dependence $\alpha = f(S)$ for specimens 41, 42, 44, 7, 3, and 31 leads to the conclusion that the crystals possess the highest perfection among all the crystals studied.

The competing effect of different impurities on the α-value is clearly seen on the specimen having a pronounced concentration of Sm and a low concentration of Ba-ions (specimens 52 and 3) and *vice versa* (specimens 42 and 32-NO), which is also well seen from Fig. 3 (curve *1*). Specimen 41 has only a small number of Ba- and Sm- ions and is highly transparent ($\alpha = 1.3$ cm^{-1}). The YIG specimens without Sm-ions have a high concentration of Ba-ions (specimen 32-NO). The preferable location of Sm-ions in the dodecahedral sublattice is partly provided by the fact that the ionic radius of Sm is less than that of Ba ($r_{Sm} < r_{Ba}$), moreover, the effective coefficient of the distribution of a three-charged Sm-ion equals 1.1. Another variant of interaction is observed at the simultaneous incorporation of V- and Ba-ions into the lattice (Fig. 3, curve *2*). Figure 3 presents the results of the analysis of the X-ray photoelectron spectroscopy data for the opposite surfaces of 2.5-mm-thick specimen 52 with $\alpha = 5.15$ cm^{-1}): one surface of the specimen has only the Sm-impurities, whereas the other surface has low concentrations of Ba-, V-, Pb-, and Bi-impurities. Thus, the Sm-ions dominate in the competition for the dodecahedral positions with Ba-, Pb-, and Bi-ions. It should be indicated that X-ray photoelectron analysis was made for one surface of seven YIG specimens and for both surfaces

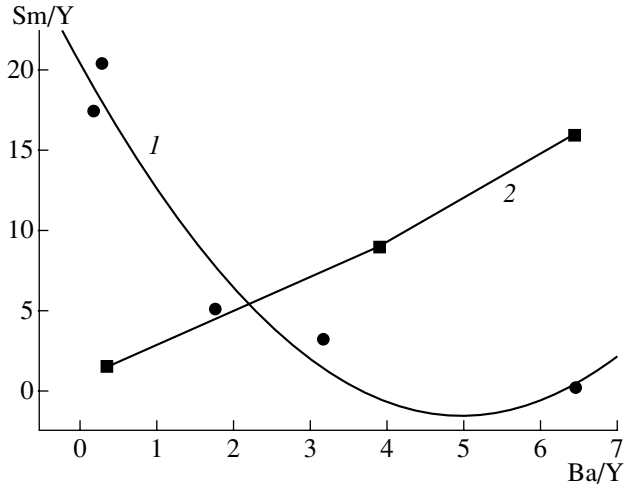

Fig. 3. Dependence of (*1*) Sm/Y and (*2*) V/Fe ratios on ln(Ba/Y).

only of specimen 52; the results of the X-ray radiometric analysis for both sides of the specimens were averaged and the Ba/Y column of Table 1 gives only this averaged value.

The concentrations in wt % were determined by energy dispersive analysis (EDA) for both the main elements (Y, Fe, and O) and for the technological impurities (Ba, Mn, Pb) for five YIG specimens of different qualities. The EDA analysis was made on a large surface area of the specimen (8 mm in diameter) and also on six to eight small (180×240-μm) areas. The fluctuations in the concentration of the main components and the Y/Fe ratio increase almost linearly with the reduction of the specimen transparency. At an arbitrary choice of the studied surface regions, the Y concentration in a poor-quality specimen V-3 varied within 3.5 wt %, the variation in the Fe concentration was slightly less (~2 wt %). The inhomogeneities in the Mn distribution are seen from the fact that they were detected only within one or two regions of the YIG platelet. The variations in the Ba concentration in different regions of the YIG specimens were of a more smooth character.

The best specimens with $\alpha < 1$ cm^{-1} showed the presence of Sm-, Mn-, Ba-, Pb-, and Bi-microimpurities, with the first two having the valence varying from two to four, which is of great importance for leveling the electric neutrality of a garnet molecule in the case where a certain part of divalent Ba-and Pb-ions are incorporated into the dodecahedral sublattice.

CONCLUSIONS

The complex studies of the optical and structural properties and the elemental composition of YIG crystals studied with due regard for their crystallographic orientation lead to the following conclusions.

The impurity-free YIG crystals (within the accuracy of the methods used) have a considerable absorption coefficient (10–12 cm^{-1} (specimens 46 and 51)). As was indicated earlier [9], the Y/Fe ratio ranging within 0.023–0.58 wt % results in the minimum α-values for three orientations of the YIG crystals. This can be associated with the suppression of dislocation generation due to incorporation of Ba-ions into the garnet structure.

The presence of Sm-, Mn-, Ba-, and V-microimpurities (at a level of several thousandths of a percent) can play the stabilizing role in the formation of a perfect YIG structure.

An increase of the Ba concentration in the (110)-oriented YIG platelets results in a higher absorption coefficient, whereas, for the (111)-oriented platelets, in a lower α value. It is established that the incorporation of impurities is of a competing nature for the following pairs of ions: Mn–Ba and Sm–Ba. Quite a different situation is observed for the incorporation of V-ions instead of Fe-ions in the sublattice.

The quality criterion for the series of the specimens studied has been formulated. The YIG quality is determined by the ratio of the total number of Y- and Fe-cations (Y + Fe) to the number of O-anions (in our case, expressed in wt %).

REFERENCES

1. D. L. Wood and J. P. Remeika, J. Appl. Phys. **38**, 1038 (1967).
2. A. A. Kaminskii, E. A. Belokonova, A. V. Butashin, *et al.*, Izv. Akad. Nauk SSSR, Neorg. Mater. **22**, 1061 (1986).
3. H. J. van Hook, J. Am. Ceram. Soc. **44**, 208 (1961).
4. H. Donnerberg and C. R. A. Catlow, J. Phys.: Condens. Matter **5** (18), 2947 (1993).
5. Yu. B. Rozenfeld and S. R. Rotman, Phys. Status Solidi A **139**, 249 (1993).
6. A. A. Chernov, in *Modern Crystallography*, Vol. 3: *Crystal Growth*, Ed. by B. K. Vainshtein, A. A. Chernov, and L. A. Shuvalov (Nauka, Moscow, 1980; Springer-Verlag, Berlin, 1984), Chap. 1.
7. A. H. Bobeck, Bell Lab. Rec. **48**, 163 (1970).
8. G. M. Kuz'micheva, B. V. Mukhin, and E. G. Khomutova, Neorg. Mater. **29**, 89 (1993).
9. I. D. Lomako, T. V. Smirnova, A. N. Igumentsev, and A. A. Mel'nikov, Zh. Prikl. Spektrosk. **63** (4), 667 (1996).
10. I. D. Lomako, A. G. Dutov, and A. N. Igumentsev, Zh. Prikl. Spektrosk. **67** (2), 217 (2000).
11. Yu. P. Vorob'ev, O. Yu. Goncharov, and V. B. Fetisov, Neorg. Mater. **35** (5), 632 (1999).

Translated by L. Man

Crystallography Reports, Vol. 47, No. 1, 2002, pp. 124–129. Translated from Kristallografiya, Vol. 47, No. 1, 2002, pp. 133–139.

PHYSICAL PROPERTIES OF CRYSTALS

Anomalies Induced by Refraction-Surface Configuration in Phonon Spectra of a Piezoelectric Plate

S. V. Tarasenko

Donetsk Physicotechnical Institute, National Academy of Sciences of Ukraine, ul. Rosy Lyuksemburg 74, Donetsk, 340114 Ukraine

e-mail: tarasen@host.dipt.donetsk.ua

Received June 16, 1999; in final form, February 7, 2001

Abstract—The conditions for existence of the regions with a local negative curvatures on the refraction surface of the bulk elastic oscillations and formation of anomalies, which are absent in the model of an infinite crystal and in piezoelectric plates with the convex refraction surface, have been determined for a cubic piezoelectric plate with two metallized surfaces. *© 2002 MAIK "Nauka/Interperiodica".*

INTRODUCTION

The existence of an additional oscillation, which cannot be classified as an intrinsic oscillation of the system and is formed only in the presence of a bulk elastic wave incident onto the surface of a piezoelectric crystal, is one of the most typical characteristics of phonon dynamics of finite piezoelectric crystals [1] and is associated with the effect of a quasistatic electromagnetic field. If such an additional oscillation is localized at the crystal surface, the so-called accompanying surface oscillation, its allowance is very important for the analysis of the nature of the interaction between the piezoelectrically active acoustic waves and the crystal surface. The analysis of the reflection (refraction) conditions of elastic waves along the boundary of a piezoelectric crystal showed that, in terms of the elastic field structure, one can distinguish qualitatively different types of accompanying surface oscillations. The existence of the accompanying surface oscillations of the first type does not make the spatial structure of the elastic field of a transverse piezoelectrically active wave more complicated in comparison with that in a nonpiezoelectric crystal: the field of elastic displacements remains one-component. The presence of the accompanying surface oscillation of the second type gives rise to the formation of an elastic field of a piezoelectrically active acoustic *SH*-wave of an additional partial oscillation in the spatial structure of the elastic field. The character of the reflection (refraction) of an elastic wave at the boundary of the piezoelectric crystals in these cases is qualitatively different. For a first-type accompanying surface oscillation, the curve formed due to the intersection of the refraction surface by the sagittal plane is convex, and all the reflected (refracted) waves belong to different branches of the phonon spectra. For the second type of the accompanying surface oscillation, the analogous curve can have both "parabolic" (the regions with the zero curvature) and "concave" points (i.e., the regions having negative Gaussian curvature). In particular, in terms of reflection (refraction) of a bulk elastic wave at the crystal boundary, the existence of such a region can give rise to the disappearance of the second-type accompanying surface oscillation and the formation, along with the normal reflected wave, also of an additional bulk elastic wave with the same polarization (the so-called effect of multibeam reflection (refraction) of the waves without the change of the branch) [1]. Naturally, the local geometry of the wave-vector surface for normal bulk oscillations of the type under consideration in an infinite crystal should also be reflected in the structure of their spectrum, because the spatial distribution of the amplitude of the bulk oscillations results from the interference of the incident and the bulk waves reflected from the specimen boundaries.

An additional argument confirming the essential influence of the refraction-surface configuration on the structure of the spectrum of the bulk elastic oscillations is the fact that the presence on the slowness surface of the region with negative Gaussian curvature is a sufficient condition for the formation of the generalized shear surface acoustic wave (SAW) propagating in the vicinity of the mechanically free surface of a piezoelectric crystal [2].

The conditions of the formation and propagation of bulk elastic waves in infinite plates have been considered in a large number of articles [3–13]. However, the focus was made on the study of the structure and dispersion of specific bulk waves for which the energy flow is parallel to the plate surface. The interest in this type of bulk phonons was determined, first and foremost, by the fact that the conditions of their existence are closely related to the conditions of formation of surface acoustic waves. Thus, the results obtained in [6–12] show that, in accordance with the possible existence of two types of accompanying surface oscillations

1063-7745/02/4701-0124$22.00 © 2002 MAIK "Nauka/Interperiodica"

in a finite piezoelectric plate whose surface is free of mechanical stresses, the specific first- and second-type bulk *SH*-waves are formed. For the first-type normal acoustic oscillations, the field of elastic displacements is a one-component bulk wave (in this case, no formation of the regions with the negative curvature is possible on the wave-vector surface spectrum irrespectively of the values of the elasticity moduli that can satisfy the stability conditions for the given crystalline state). For the second type of specific bulk waves, the spatial structure of the field of elastic displacements is two-component, because, along with the bulk component, it also includes an additional partially inhomogeneous oscillation localized at the crystal surface.

The influence of the piezoelectric effect on the dispersion law of the mode of the spectrum of bulk elastic *SH*-waves whose energy flow is not parallel to the mechanically free surface of the piezoelectric plate was analyzed in [3–5]. The computations performed in these studies showed that the dispersion curves $\Omega(k)$ characterizing the spectrum of symmetric elastic SH-oscillations can be related to the forward waves irrespectively of the mode, ν, and the wave number, k ($\partial\Omega/\partial k > 0$). The corresponding dispersion curve $\Omega(k)$ for the antisymmetric modes of the spectrum of acoustic *SH*-waves in the piezoelectric plate at the given mode number ν has the minimum at $k = k_* \neq 0$. Thus, at $k < k_*$, the formation of the backward SH-wave becomes possible ($\partial\Omega/\partial k < 0$). At the same time, the results obtained in [3–5] indicate that the metallization of both surfaces of the piezoelectric plate results in the disappearance of the minimum on the dispersion curves $\Omega(k)$ which belong to the spectrum of the antisymmetric bulk acoustic SH-waves. In this case, the condition $\partial\Omega/\partial k > 0$ for the dispersion curves of the transverse elastic waves is fulfilled irrespectively of the values of the wave number, the mode number **n**, and the spatial structure of their elastic field. Indirectly, this is confirmed in [5], where it is shown that the factor responsible for the formation of the backward bulk wave in the piezoelectric plate is the energy flux related to the electric field in vacuum. The direction of this flux is opposite to the direction of the phase velocity of the elastic bulk *SH*-wave, whereas its absolute value exceeds that of the energy flux related to the acoustic oscillations. At the same time, the analysis in [3–5] was performed for a piezoelectric crystal of the class C_{6v}, which means that all the specific characteristics of the spectrum of transverse bulk *SH*-waves were induced by the presence of the first-type accompanying surface oscillation. The effects of the second-type accompanying surface oscillations on the spectrum of the bulk elastic oscillations of the *SH*-type propagating along the piezoelectric plate have not been analyzed as yet.

In this connection, we had the aim to determine the condition whose fulfillment in the presence of the second-type accompanying surface oscillations (the existence of the regions with the negative Gaussian curvature on the refraction surface) would result in the formation of such anomalies in the spectrum of bulk phonons, which cannot exist either in the model of an infinite crystal or in a piezoelectric plate with two metallized surfaces in which the propagation of an elastic *SH*-wave is accompanied by the first-type oscillations (the Gaussian curvature of the corresponding surface of the backward phase velocities is positive at all the values of elastic moduli corresponding to the stability condition for the given elastic state). The study was performed on a cubic piezoelectric plate.

The article consists of several sections dedicated to the basic relationships and formulation of the boundary problem for a cubic piezoelectric plate with two metallized surfaces; the analysis of the characteristics of the spectrum of bulk *SH*-type phonons induced by the presence of a second-type accompanying surface oscillation propagating along the metallized piezoelectric plate with mechanically free surfaces; the correspondence between the configuration of the surface of the wave vectors of shear elastic oscillations of a cubic piezoelectric plate and the structure of the spectrum of bulk *SH*-phonons in the cubic piezoelectric plate; the main effects caused by the influence of the electrodynamical boundary conditions on the structure of the spectrum of the transverse bulk elastic *SH*-waves considered in previous sections; and, finally, some conclusions that can be drawn from the results obtained.

BASIC RELATIONSHIPS

As an example of a piezoelectric crystal in which the formation of a second-type accompanying surface oscillation (i.e. the formation on the surface of backward phase velocities in the regions with the negative local curvature) is possible, consider here a cubic piezoelectric crystal with the density of the thermodynamic potential in the form [1]

$$F = F_e + F_{pe} \tag{1}$$

$$\begin{aligned} F_{pe} &= -2e_{14}(E_y u_{zx} + E_x u_{zy} + E_z u_{xy}), \\ F_e &= 0.5c_{11}(u_{xx}^2 + u_{yy}^2 + u_{zz}^2) + c_{12}(u_{xx}u_{yy} \\ &+ u_{xx}u_{zz} + u_{yy}u_{zz}) + 2c_{44}(u_{zx}^2 + u_{zy}^2 + u_{xy}^2). \end{aligned} \tag{2}$$

where $\hat{e}$ and $\hat{c}$ are the piezoelectric-constant and elastic-modulus tensors, respectively.

If the plane of the elastic-oscillations propagation coincides with the (010) plane, the solutions of the equation of piezoacoustics show that the spectrum of the normal phonon oscillations can be factorized and, depending on the relative orientation of the lattice-displacement vector **u** and the normal to the plane of the wave propagation coinciding with the [010] direction, the corresponding expressions can be represented in the form $s_0^2 \equiv c_{44}/\rho$ and $\kappa_2^2 \equiv 4\pi e_{14}/(\epsilon c_{44})$, where ρ is the

crystal density, ϵ is the dielectric constant of the crystal, and $k_x^2/\mathbf{k}^2 \equiv \sin^2\theta$; $\mathbf{k}$ is the wave vector [1]:

$$\omega^2 = s_0^2(\mathbf{k}^2 + \kappa_2^2\sin^2 2\theta), \quad \mathbf{k}^2 \equiv k_x^2 + k_z^2, \quad \mathbf{u} \parallel [010], \tag{3}$$

$$k_\pm^2 = (A \pm (A^2 - aB)^{1/2})(2B)^{-1}, \quad \mathbf{u} \perp [010],$$

$$A \equiv \rho\omega^2(c_{44} + c_{11})/(c_{11}c_{44}),$$

$$B \equiv 1 + (1-\eta)(\eta - \xi)\eta^{-2}\sin^2 2\theta, \tag{4}$$

$$a \equiv 4\rho^2\omega^4/(c_{11}c_{44}), \quad \eta \equiv 2c_{44}/(c_{11} - c_{12}),$$

$$\xi \equiv c_{44}/c_{11}.$$

To analyze the spectrum of elastic oscillations of a piezoelectric plate of the thickness $2d$ with the surface normal $\mathbf{n}$ ($\mathbf{n}$, $\mathbf{k} \perp [010]$), the corresponding boundary conditions should be fulfilled. Depending on the choice of $\mathbf{n}$ and the orientation of the lattice-displacement vector u with respect to the sagittal plane (010), two physically different types of elastic boundary conditions are possible. We assume that at $\mathbf{u} \parallel [010]$ and $\mathbf{n} \parallel [101]$, both surfaces of the piezoelectric plate satisfy the conditions of rigid fixation (ξ is the coordinate along the surface normal of the film)

$$u_i = 0, \quad \xi = \pm d. \tag{5}$$

At $\mathbf{n} \parallel [100]$, the boundary conditions to be fulfilled at both surfaces of the piezoelectric plate correspond to the boundary with the tangential sliding [14] (where σ_{ik} is the elastic-stress tensor):

$$(\mathbf{un}) = 0, \quad [\mathbf{ns}] = 0, \quad s_i \equiv \sigma_{ik}n_k, \quad \xi = \pm d. \tag{6}$$

In terms of physics, this corresponds to the fulfillment of the conditions for completely incoherent conjugation [15] at the interface of two media, one of which is absolutely rigid. We also assume that, irrespectively of the relative orientations of the $\mathbf{u}$ and $\mathbf{n}$ vectors, both plate surfaces are metallized (the electrodynamic boundary conditions):

$$\phi = 0; \quad \xi = \pm d. \tag{7}$$

Using Eqs. (3)–(7), one can analyze the spectrum of acoustic oscillations propagating along an infinite plate of a cubic piezoelectric at $\mathbf{n}, \mathbf{k}_\perp \perp [010]$ (where $\mathbf{k}_\perp$ is the wave vector along the propagation direction of an elastic wave, $\mathbf{k}_\perp \perp \mathbf{n}$).

BULK SH-WAVE

The calculation shows that, depending on the orientation of the surface normal $\mathbf{n}$ in the sagittal (010) plane, the spectrum of a bulk *SH*-wave can be represented in the following way ($m_\nu \equiv \pi\nu/2d$; $\nu = 1, 2\ldots$):

$$\Omega_\nu^2(k_\perp) = s_0^2\left(m_\nu^2 + k_\perp^2 + 4\kappa_2^2\frac{m_\nu^2 k_\perp^2}{m_\nu^2 + k_\perp^2}\right), \quad \mathbf{n} \parallel [001], \quad \mathbf{u} \parallel [010], \tag{8}$$

$$\Omega_\nu^2(k_\perp) = s_0^2\left(m_\nu^2 + k_\perp^2 + \kappa_2^2\frac{(m_\nu^2 - k_\perp^2)^2}{m_\nu^2 + k_\perp^2}\right), \quad \mathbf{n} \parallel [101], \quad \mathbf{u} \parallel [010]. \tag{9}$$

The joint analysis of Eqs. (3), (8), (9) and the piezoacoustics equations shows that, in both cases, a propagating transverse elastic wave is accompanied by second-type surface oscillations, whose manifestation in the spectrum of this elastic wave is essentially associated with the choice of the relative orientation of the vector $\mathbf{n}$ in the (010) plane. In the case of Eq. (8), $\mathbf{n} \parallel [001]$ and all the dispersion curves irrespectively of the number ν are the forward waves at any wave number $k_\perp$. Thus, being compared with the case of a piezoelectric crystal ($\kappa_2 \longrightarrow 0$), the existence of the accompanying surface oscillation in this geometry only slightly modifies the spectrum of a bulk SH-wave. The analysis of Eq. (9) for the spectrum of shear elastic oscillations at $\mathbf{n} \parallel [101]$ shows that if $\kappa_2^2 > 1/3$, the existence of the accompanying surface oscillation at

$$\kappa_{*\nu}^2 \equiv m_\nu^2(2\kappa_2(1 + \kappa_2^2)^{-1/2} - 1) \tag{10}$$

provides the formation of a minimum on the dispersion curve of the mode ν which belongs to the spectrum of transverse acoustic oscillations described by Eq. (9). At $k_\perp < k_{*\nu}$, the corresponding dispersion curves $\Omega_\nu(k_\perp)$ are the backward waves ($\partial\Omega_\nu/\partial k_\perp < 0$). An additional characteristic of the spectrum (9) induced by the existence of the accompanying surface oscillation is the possible formation of the point of intersection ($k_{\nu\rho}$) of the dispersion curve of modes ν and ρ at $\kappa_2^2 > 1/3$, i.e., $\Omega_\nu(k_{\nu\rho}) = \Omega_\rho(k_{\nu\rho})$. In this case, $k_{\nu\rho}$ is the positive root of the equation

$$(k_{\nu\rho}^2 + m_\nu^2)(k_{\nu\rho}^2 + m_\rho^2) = 4\kappa_2^2 k_{\nu\rho}^2/(1 + \kappa_2^2). \tag{11}$$

As has already been indicated in the Introduction, the existence of the first- or second-type accompanying surface oscillation in the piezoelectric crystal is essentially dependent on the configuration of the refraction surface of the correspondent normal elastic wave in an infinite crystal. Now, consider the configuration of the refraction surface of the normal shear oscillations in an infinite cubic piezoelectric crystal with the anomalies in the spectrum of bulk *SH*-phonons in the piezoelectric plate established above.

EFFECT OF THE REFRACTIVE-SURFACE SHAPE

Since the wave vector of the wave in Eqs. (8) and (9) lies in the (010) plane, the solution of the formulated problem requires the use of Eq. (3) to study the shape of the section of the surface of backward phase velocities of the shear (**u** ∥ [010]) elastic wave (ω = const) by the (010) plane in the **k** space. The corresponding expression is represented in the following form ($k_x^2/\mathbf{k}^2 \equiv \sin^2\theta$; $\mathbf{k}^2 \equiv k_x^2 + k_z^2$):

$$\mathbf{k}^2 = \frac{\omega^2}{s_0^2(1 + \kappa_2^2\sin^2 2\theta)}. \quad (12)$$

The analysis of the extrema of the curve described by Eq. (12) [1] and their comparison with the anomalies in the shape of dispersion curves given by Eqs. (8) and (9) shows that the existence of the local minimum on the dispersion curve of the waveguide phonon Eqs. (8) and (9) is explained by the fact that the corresponding section of the refraction surface of an infinite crystal by the normal shear wave with the same polarization (12) provides the formation of the regions with the maximum negative curvature (at $\kappa_2^2 > 1/3$), whose position on the curve given by Eq. (12) in the **k** space is determined by the conditions $\partial k/\partial\theta = 0$ and is uniquely related to the frequency ω, the model number ν, the film thickness 2*d*, and the wave number $k_\perp$ of the waveguide phonon under consideration, which is described by Eqs. (8) and (9).

The analysis of the points common to curve (12) [1] and their comparison with the straight lines determined by the condition k_x = const or k_z = const, which intersect the refraction surface (12), yields the information on the spectrum structure of the corresponding waveguide phonon at the given wave number $k_\perp$, frequency ω, and the mode number ν [in this case, curves (8) and (9)]. If the direction of the surface normal **n** of the film in the k_x, k_z plane coincides with the ordinate axis (**n** ∥ [100]), the number of common points of the straight line $k_z = k_\perp$, and curve (12) determines the mode numbers ν of the spectrum of the *SH*-type bulk phonons which can propagate along the 0*Z* axis of the piezoelectric film of the thickness 2*d* with the same wave number $k_\perp$ and the frequency ω (crossover points). In the same geometry, the existence of common points of curve (12) and the straight line $k_x = m_\nu$ provides the determination of the wave numbers $k_\perp$ with which the given-type SH-phonon with the fixed mode number ν and frequency ω can propagate along the plate of thickness 2*d*. Since the outer normal to the refraction surface coincides with the direction of the group velocity of the wave [1], the joint analysis of Eqs. (8), (9), and (12) and the study of the local geometry of the section of isofrequency surface (12) allows one to determine the type of wave (forward or backward) propagating in the corresponding region of the dispersion curve of the waveguide phonon with the given ω, m_ν, and $k_\perp$ determined from Eqs. (8) and (9). In the case under consideration **k** ⊥ [010] (**n** ∥ [100]), the bulk elastic shear wave (9) propagating along the film is of the backward type if the projection of the outer normal to this surface onto the 0*Z* direction at the point of the intersection of the refraction surface and the straight line $k_x = m_\nu$ has the negative sign. If the projection is a positive forward wave, the corresponding wave at the given $k_\perp$, ω and m_ν is also a forward wave. If this projection onto the 0*Z* axis equals zero, the dispersion curve of the mode ν belonging to the spectrum of bulk oscillations propagating along the surface of the plate of the thickness 2*d* (**n** ∥ [100]) has an extremum at the frequency ω and $k_\perp \neq 0$, but whether or not this extremum is a maximum or a minimum is determined by the sign of the local Gaussian curvature of curve (12) at this point.

EFFECTS ASSOCIATED WITH THE CHANGE OF ELECTRODYNAMIC BOUNDARY CONDITIONS

Up to now, we assumed that the electrostatic potential ϕ at both surfaces of the piezoelectric film at $\xi = \pm d$ obeys the condition ϕ = 0. This allowed us to represent this potential in the explicit form. The corresponding dispersion equation for propagating bulk *SH*-phonons for certain orientation of **n** in the (010) plane and boundary conditions (5) and (6) can be represented in an explicit form. If these electrodynamic conditions for the given film geometry (the relative orientations of the vectors **n**, $\mathbf{k}_\perp$, and the crystallographic axes **n**, $\mathbf{k}_\perp \perp$ [010]) are not satisfied, e.g., for

$$\phi + \alpha_*\partial\phi/\partial\xi = 0; \quad \xi = \pm d, \quad (13)$$

but, as earlier, boundary conditions (5) and (6) are fulfilled at $\xi = \pm d$, then the spectrum of bulk phonons can be calculated using the approach developed earlier in [16, 17] for the analysis of the influence of the magnetic dipole interaction on the spectrum of the exchange bulk magnons in a thin ferromagnetic film.[1] With this aim, using Green's function at $\mathbf{k}_\perp \perp$ [010] (**n** ∥ [100]) [010] ($\Delta \equiv k_\perp \sinh(2k_\perp d)$)

$$G(\xi, t) = \begin{cases} \sinh(k_\perp(t-d))\sinh(k_\perp(\xi+d))/\Delta, & -d \le \xi \le t \\ \sinh(k_\perp(t+d))\sinh(k_\perp(\xi-d))/\Delta, & t \le \xi \le d \end{cases}. \quad (14)$$

and the electrostatic equations under the boundary condition (13), we can determine the relation between the amplitude of the electrostatic potential ϕ and the amplitude of oscillation of the *y*th component of the displacement vector **u** of the lattice under the assumption that

[1] This type of boundary conditions takes place, in particular, for an SH-wave traveling along a mechanically free piezoelectric plate with ideal metal screens located at a distance *t* on both its surfaces (ϕ = 0; $\xi = \pm(d + t)$), and $\alpha_* \longrightarrow 0$ at $t \longrightarrow 0$.

the spatial distribution of the latter vector along the surface normal of the film is a given function. This allows the elimination of the variable related to the electrostatic potential from the equations of piezoacoustics. Thus, in this case, the corresponding boundary problem is solved only under the elastic boundary conditions set by Eqs. (5) and (6). Using the method suggested in [16, 17], the solution of this boundary problem can be sought as an expansion of eigenfunctions of the elastic boundary problem. In particular, for Eq. (6), we have

$$u_y(\mathbf{r}, t) = \sum_{\nu=1} A_\nu \sin(m_\nu \xi)\exp(i\omega t - ik_\perp \tau), \quad \tau \parallel [101], \tag{15}$$

where τ is the current coordinate for the wave propagating along [101].

As a result, the dispersion equation which describes the spectrum of SH-type bulk phonons of the film (a cubic piezoelectric crystal) at $\mathbf{k} \in XZ$, $\mathbf{n} \parallel [101]$, and the boundary conditions (6) and (13) in the electrostatic approximation can be represented as an infinite system of algebraic linear equations with respect to the unknown amplitudes A_ν, namely,

$$\begin{gathered}(W_{\nu\nu}(k_\perp) - \omega^2)A_\nu + W_{\nu\rho}(k_\perp)A_\rho = 0,\\ \nu \neq \rho, \quad \nu, \rho = 1, 2\ldots;\\ W_{\nu\nu}(k_\perp) = s_0^2(m_\nu^2 + k_\perp^2 + P_{\nu\nu}), \quad W_{\nu\rho}(k_\perp) = s_0^2 P_{\nu\rho},\\ P_{\nu\nu} = (k_\perp^2 - m_\nu^2)\int_{-d}^{d}\sin(m_\nu\xi)\\ \times \hat{L}\left(\int_{-d}^{d} G(\xi, t)\sin(m_\nu t)dt\right)d\xi,\\ \hat{L} \equiv k_\perp^2 + \partial^2/\partial\xi^2,\\ P_{\nu\rho} = (k_\perp^2 - m_\nu^2)\int_{-d}^{d}\sin(m_\rho\xi)\hat{L}\\ \times\left(\int_{-d}^{d} G(\xi, t)\sin(m_\nu t)dt\right)d\xi.\end{gathered} \tag{16}$$

Assuming that $\alpha_* = 0$ in (13), we obtain $W_{\nu\rho}(k_\perp) = 0$ and $W_{\nu\nu}(k_\perp) = \Omega_\nu(k_\perp)$, where $\Omega_\nu(k_\perp)$ is set by Eq. (8). Thus, the nondiagonal elements of the infinite matrix $W_{\nu\rho}(k_\perp)$ can be considered as a perturbation with respect to the zeroth approximation determined by the diagonal elements of the infinite matrix $W_{\nu\nu}(k_\perp)$. Thus, it can be concluded that the structure of the spectrum of bulk phonon *SH*-oscillations in the zeroth approximation is qualitatively equal to one determined earlier from Eq. (9) for which, along with the boundary conditions (6), the condition of two-sided metallization of the film (7) was fulfilled. Now, for modes with the number ν and ρ ($\nu \neq \rho$), no crossover points of the spectrum $\Omega_\nu(k_\perp) = \Omega_\rho(k_\perp)$ can exist, because $W_{\nu\rho}(k_\perp) \neq 0$ at $\alpha_* \ll 1$. According to the second order of the perturbation theory for degenerate levels, the structure of the SH-phonon spectrum in the vicinity of a concrete intersection point can be represented as

$$(W_{\nu\nu}(k_\perp) - \omega^2)(W_{\rho\rho}(k_\perp) - \omega^2) - W_{\nu\rho}^2(k_\perp) \approx 0, \quad (\nu \neq \rho). \tag{17}$$

CONCLUSION

Thus, the results obtained above allow us to state the following.

Depending on the symmetry of a finite piezoelectric crystal, a backward elastic wave can be formed as well as the minimum on the dispersion curve of the mode of the spectrum of the bulk *SH*-oscillations, and the intersection points of the dispersion curves of the modes of bulk elastic oscillations with the same polarization but with different numbers.

Contrary to the results obtained in [3–5], the mechanism of formation of a backward shear elastic wave also takes place if there is no electrostatic-energy flux associated with the wave outside the film. This is explained by the fact that the type of surface oscillation accompanying the bulk *SH*-wave in the plate cut out from a cubic piezoelectric crystal is qualitatively different from the type of the accompanying surface oscillations formed during the propagation of the bulk elastic *SH*-wave in a plate cut out from a piezoelectric crystal described by the class C_{6v} [3–5].

The mechanism of the formation of the above characteristics in the spectrum of a propagating elastic wave is not necessarily associated with the effect of an electrostatic or a magnetic field. It is shown that the anomalies similar to those formed in the case of a piezoelectrically active *SH*-wave can also be formed if the elastic waves propagate along the plate are not piezoelectrically active, but the vector of elastic displacements of the lattice, **u**, lies in the sagittal plane. In the latter case, the appearance of these anomalies in the spectrum of a quasitransverse wave is explained by the formation of an accompanying surface oscillation at the expense of the long-range electrostatic field of quasilongitudinal elastic deformations.

There exists the one-to-one correspondence between the characteristics of the spectrum of normal elastic oscillations of a finite crystal and the local geometry of the slowness surface of acoustic oscillations of this type in an infinite crystal.

It should be emphasized that the formation of a region with negative local curvature on the surface of backward phase velocities of elastic waves can occur only if rather rigid conditions imposed onto the elastic

moduli of the crystal are fulfilled [19–21]. In particular, in a cubic piezoelectric crystal, the formation of a region with the negative curvature at **u** || [010] on the section of the surface of the wave vectors by the (010) plane requires the fulfillment of the condition $\kappa_2^2 > 1/3$, whereas in the case **u** ⊥ [010], the condition $\eta > 1$ should be satisfied. It is expected that these conditions would be satisfied, e.g., in the vicinity of the structural phase transitions. Thus, in a cubic crystal, the c_{44} modulus is "softened" in the vicinity of the Curie point in the ferroelastic phase transitions for KDP-type or Seignette-salt crystals, whereas a considerable reduction of the value of $(c_{11} - c_{12})$ is observed in the vicinity of the structural phase transition for Nb_3Sn, V_2Si, and some other crystals [13].

In this article, we only studied the case where the concavity of the surface of the backward phase velocities "embraces" only one of the symmetry axes (the so-called axial concavity). If the corresponding region with negative Gaussian curvature does not embrace the symmetry axis (the so-called intermediate concavity [20, 21]), all the anomalies of the spectrum of the corresponding type of bulk elastic oscillations still can be formed. In order to make the dispersion curve of a traveling bulk elastic wave of the given polarization to be correspondent to the backward (forward)-type wave, it is necessary that the surface normal of the plate, **n**, correspond to the direction along which the negative (positive) Gaussian curvature is formed on the corresponding section of the wave vector surface. The necessary condition for the formation of the intersection points of the dispersion curves of the modes belonging to the spectrum of normal bulk oscillations is the condition of collinearity of the propagation direction of the elastic wave under study and the direction along which the corresponding refraction surface has the maximum negative Gaussian curvature.

Up to now, we have considered only the piezoelectric mode of the spectrum of phonon oscillations in the cubic piezoelectric plate with **u** || [010]. Naturally, all the conclusions drawn above could also be extended to the case of transverse elastic oscillations in piezomagnetic crystals, because the basic relationships for a finite piezoelectric medium can also be applied, within the accuracy of notation, to a finite piezomagnetic crystal of the respective symmetry [2, 18]. It should also be indicated that the mechanism of formation of the above characteristics in the spectrum of a propagating bulk elastic wave is not necessarily related to the electrostatic or magnetostatic fields. In particular, it follows from Eqs. (4)–(6) that the anomalies similar to those observed for a piezoelectrically active SH-wave can also be observed in the case where the elastic waves propagating along the plate of an anisotropic crystal are piezoelectrically inactive, if the vector of the elastic displacements of the lattice **u** is located in the sagittal plane. In this case, the above anomalies in the spectrum of a quasitransverse wave is explained by the formation of an accompanying surface oscillation due to a far-range electrostatic field or quasilongitudinal elastic deformations.

ACKNOWLEDGMENTS

The author is grateful to E.P. Stefanovskiĭ, I.E. Dragunov, and T.N. Tarasenko for the approval of the concept used in this study and fruitful discussions.

REFERENCES

1. M. P. Balakirev and I. A. Gilinskiĭ, *Waves in Piezoelectric Crystals* (Nauka, Novosibirsk, 1982).
2. Yu. A. Kosevich and E. S. Syrkin, Fiz. Tverd. Tela (Leningrad) **28**, 248 (1986) [Sov. Phys. Solid State **28**, 134 (1986)].
3. P. V. Burliĭ, P. P. Il'in, and I. Ya. Kucherov, Pis'ma Zh. Tekh. Fiz. **8**, 568 (1982) [Sov. Tech. Phys. Lett. **8**, 247 (1982)].
4. V. N. Nechiporenko and Yu. G. Rapoport, Akust. Zh. **31**, 365 (1985) [Sov. Phys. Acoust. **31**, 215 (1985)].
5. I. Ya. Kucherov and E. V. Malyarenko, Akust. Zh. **44**, 492 (1998) [Acoust. Phys. **44**, 420 (1998)].
6. V. I. Alshits and V. N. Lyubimov, Kristallografiya **33**, 279 (1988) [Sov. Phys. Crystallogr. **33**, 163 (1988)].
7. V. I. Alshits and V. N. Lyubimov, Kristallografiya **33**, 286 (1988) [Sov. Phys. Crystallogr. **33**, 166 (1988)].
8. V. I. Alshits and V. N. Lyubimov, Kristallografiya **30**, 437 (1985) [Sov. Phys. Crystallogr. **30**, 252 (1985)].
9. V. I. Alshits, V. N. Lyubimov, and N. F. Naumenko, Kristallografiya **30**, 213 (1985) [Sov. Phys. Crystallogr. **30**, 123 (1985)].
10. G. G. Kessenikh and L. A. Shuvalov, Kristallografiya **23**, 1134 (1978) [Sov. Phys. Crystallogr. **23**, 641 (1978)].
11. V. I. Alshits, J. Lothe, and V. N. Lyubimov, Kristallografiya **28**, 635 (1983) [Sov. Phys. Crystallogr. **28**, 374 (1983)].
12. V. I. Alshits and V. N. Lyubimov, Kristallografiya **36**, 828 (1991) [Sov. Phys. Crystallogr. **36**, 463 (1991)].
13. Yu. A. Kosevich and E. S. Syrkin, Akust. Zh. **33**, 949 (1987) [Sov. Phys. Acoust. **33**, 552 (1987)].
14. V. A. Krasil'nikov and V. V. Krylov, *Introduction to Physical Acoustics* (Nauka, Moscow, 1984).
15. A. G. Khachaturyan, *The Theory of Phase Transformations and the Structure of Solids Solutions* (Nauka, Moscow, 1974).
16. B. A. Kalinikos, Izv. Vyssh. Uchebn. Zaved., Fiz. **24**, 42 (1981).
17. B. A. Kalinikos and A. N. Slavin, J. Phys. C **19**, 7013 (1986).
18. V. I. Alshits, A. N. Darinskii, and J. Lothe, Wave Motion **16**, 265 (1992).
19. C. G. Winternheimer and A. K. McCurdy, Phys. Rev. B **18**, 6576 (1978).
20. A. L. Shuvalov and A. G. Every, Phys. Rev. B **53**, 14906 (1996).
21. A. L. Shuvalov, Kristallografiya **42**, 210 (1997) [Crystallogr. Rep. **42**, 173 (1997)].

Translated by L. Man

Crystallography Reports, Vol. 47, No. 1, 2002, pp. 130–134. Translated from Kristallografiya, Vol. 47, No. 1, 2002, pp. 140–144.

CRYSTAL GROWTH

Growth of $K(D_xH_{1-x})_2PO_4$ Single Crystals from Solutions in the K_2O–P_2O_5–$(D,H)_2O$ System

L. V. Soboleva, A. E. Voloshin, V. A. Kirikov, and M. V. Biglova

Shubnikov Institute of Crystallography, Russian Academy of Sciences, Leninskiĭ pr. 59, Moscow, 117333 Russia

e-mail: voloshin@ns.crys.ras.ru

Received December 27, 2000; in final form, April 25, 2001

Abstract—Based on the analysis of the K_2O–P_2O_5–D_2O solubility phase diagram, the optimum conditions of KD_2PO_4 crystallization—the compositions of mother solutions and the temperature range of crystallization—in the KH_2PO_4–D_2O system have been determined. The technique of $K(D_xH_{1-x})_2PO_4$ growth is developed. The DKDP single crystals with deuterium concentration up to 88 wt % are grown on DKDP seeds from KH_2PO_4 solutions in D_2O by the method of temperature decrease. © *2002 MAIK "Nauka/Interperiodica".*

INTRODUCTION

Crystals of the KH_2PO_4 (KDP) family, in particular KDP and $K(D_xH_{1-x})_2PO_4$ (DKDP), are widely used in various electrooptical and nonlinear laser devices. The DKDP crystals may exist in two polymorphous modifications—the tetragonal modification (the symmetry class $\overline{4}2m$) isomorphous to KDP and the monoclinic one (the symmetry class 2). It is known that the electrooptical properties of tetragonal DKDP crystals are much better than those of KDP [1].

A partial replacement of hydrogen in KH_2PO_4 by deuterium leads to the formation of mixed $K(D_xH_{1-x})_2PO_4$ crystals with physical properties dependent on the deuterium concentration possessing ferroelectric phase transitions [1].

This study is aimed at (1) the determination of the optimum growth conditions (the optimum composition of the mother solutions, the temperature range of crystallization) from the analysis of the known physical and chemical data of the solubility phase diagrams K_2O–P_2O_5–H_2O, K_2O–P_2O_5–D_2O, and KH_2PO_4–D_2O (25–50°C); (2) the development of the method of growth of $K(D_xH_{1-x})PO_4$ crystals in dynamic mode; and (3) growth of DKDP crystals from solutions in the KH_2PO_4–D_2O system.

CHOICE OF THE SOLUTION COMPOSITIONS AND GROWTH OF $K(D_xH_{1-x})_2PO_4$ SINGLE CRYSTALS

Development of the method of $K(D_xH_{1-x})_2PO_4$ growth from the solutions of the K_2O–P_2O_5–$(D_xH_{1-x})_2O$ system is based on the analysis of the physical and chemical characteristics of the solubility phase diagram of the ternary K_2O–P_2O_5–H_2O [2, 3] and K_2O–P_2O_5–D_2O systems [4]. As is shown in [5], the phase diagrams of the ternary systems can be used to determine the optimum growth conditions for large stoichiometric solid single crystals of optical quality in the dynamic mode. The solubility phase diagram of the ternary K_2O–P_2O_5–H_2O system [2, 3] has nine branches of solubility curves corresponding to different compositions of solid phases (Fig. 1). The KH_2PO_4 solid phase is dissolved congruently and is stable in the temperature range from 0 to 50°C. Its solubility curve has a singular point *A* corresponding to the molar ratio K_2O : P_2O_5 = 1 : 1. The solution composition corresponding to the *A* point on the solubility curve remains unchanged with the variation of equilibrium conditions,

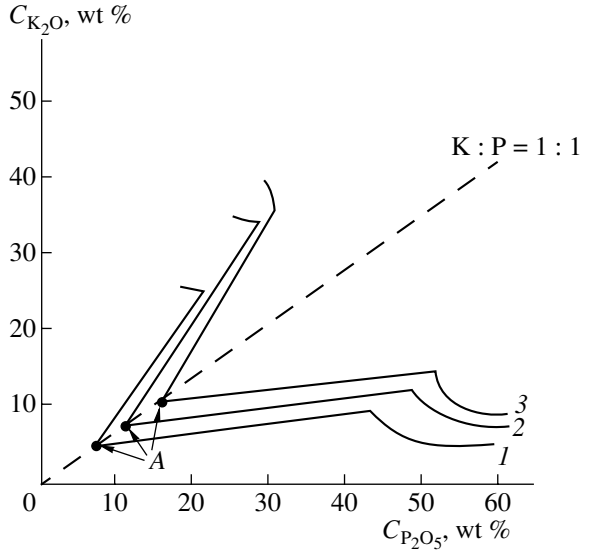

Fig. 1. Isotherms of KH_2PO_4 solubility in the ternary K_2O–P_2O_5–H_2) system [1, 2] at 0 (curve *1*), 25 (curve *2*), and 50°C (curve *3*); *A* is a singular point.

1063-7745/02/4701-0130$22.00 © 2002 MAIK "Nauka/Interperiodica"

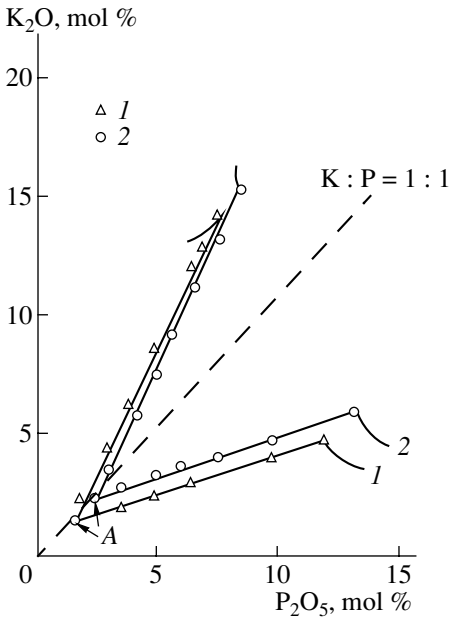

Fig. 2. Solubility isotherms in the ternary (*1*) K_2O–P_2O_5–H_2O, (*2*) K_2O–P_2O_5–D_2O systems at 25°C; *A* is a singular point.

which provides the crystallization of KH_2PO_4 from the KH_2PO_4–H_2O solutions in the temperature range from 0 to 50°C [6].

In the K_2O–P_2O_5–D_2O system, which is studied at 25°C [4] (Fig. 2), eight different solid phases are formed, and the phase diagram shows a complete analogy with the branches of the solubility curves of solid phases in the K_2O–P_2O_5–H_2O system [2] with the KD_2PO_4 phase being congruently soluble.

It is found that the KD_2PO_4 phase dissolves in heavy water better than the KH_2PO_4 phase in H_2O, which can be explained by the formation of the stronger deuterium bonds (more stable with respect to hydrogen ones) between the PO_4^{3-} ions and the D_2O molecules [4].

The determination of the optimum growth conditions for DKDP crystals is based on the closeness of the physical and the chemical characteristics of the solubility isotherms of KH_2PO_4 and KD_2PO_4 crystals in the ternary K_2O–P_2O_5–H_2O and K_2O–P_2O_5–D_2O systems at 25°C [2, 4] (Fig. 2). Thus, it is possible to construct the solubility branch for KD_2PO_4 at 50°C, with due regard for the fact that the KH_2PO_4 solubility at 50°C is about 5% higher than at 25°C (Fig. 1).

The solubility isotherms of the K_2O–P_2O_5–H_2O system at 50°C and the K_2O–P_2O_5–D_2O system at 25 and 50°C are shown on the triangular Gibbs diagram in Fig. 3 to facilitate the use of the concentration data of their components. On this diagram, point *1* corresponds to the saturation point of the KH_2PO_4 solution at 50°C (K_2O = 12.00, P_2O_5 = 15.00, and H_2O = 73.00 wt %);

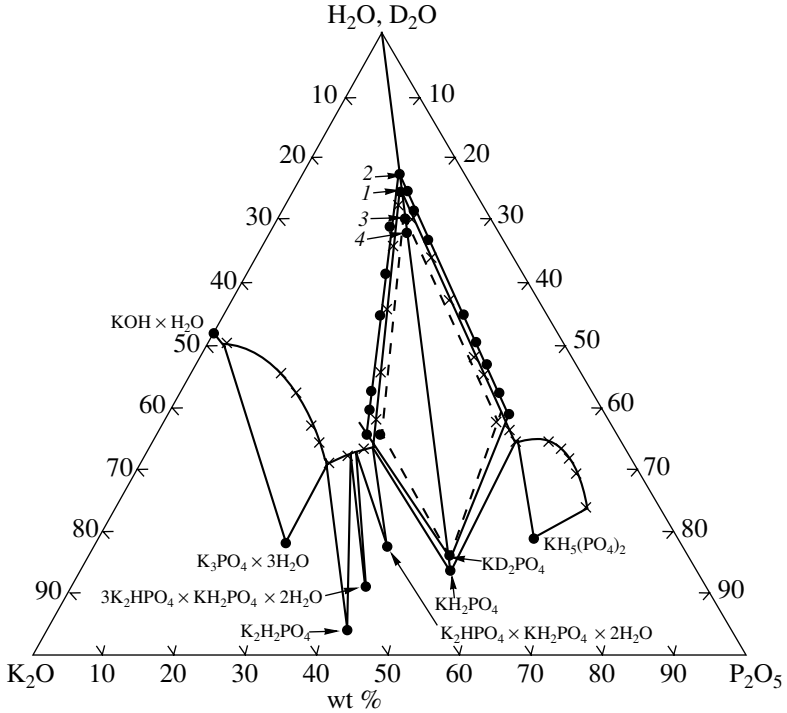

Fig. 3. Solubility isotherms of KH_2PO_4 in the K_2O–P_2O_5–H_2 system at 50°C (crosses); KD_2PO_4 in the K_2O–P_2O_5–D_2O system at 25°C (circles) and 50°C (dashed curve); (*1*) the composition of the saturated KH_2PO_4 solution at 50°C; (*2*) the composition of the saturated KD_2PO_4 solution at 25°C; (*3*) the probable saturation point in the KD_2PO_4 solution at 50°C; and (*4*) the point corresponding to the KH_2PO_4 supersaturation in the KH_2PO_4–D_2O system at 50°C.

Compositions of the solution corresponding to points *2*, *3*, and *4* in the K_2O–P_2O_5–D_2O and KH_2PO_4–D_2O systems

Component, wt %	Points		
	2	*3*	*4*
K_2O–P_2O_5–D_2O			
P_2O_5	13.77	18.80	19.00
K_2O	9.37	12.00	13.00
D_2O	76.86	69.20	68.00
KH_2PO_4–D_2O			
KH_2PO_4	26.50	34.48	36.65
D_2O	73.50	65.52	63.35

point *2* is the saturation point of the KD_2PO_4 solution at 50°C; and *4* is the point corresponding to a certain supersaturation of the KH_2PO_4 solution in the KH_2PO_4–D_2O system at 50°C.

The solubility of KD_2PO_4 in D_2O at 50°C calculated from the known data [1, 7] is equal to 35.54 wt % of KDP and 64.46 wt % of D_2O, which is close to the composition of point *4*. The ternary K_2O–P_2O_5–D_2O system used for growth of $K(D_xH_{1-x})_2PO_4$ crystals with different deuterium concentration allows one to use K_2O, P_2O_5, and D_2O components (in the form of KOH, H_3PO_4, and D_2O solutions) in certain weight ratios to prepare necessary mother solutions. The binary KH_2PO_4–D_2O system in the ternary K_2O–P_2O_5–D_2O system allows one to use KH_2PO_4 and D_2O as the initial components for preparing mother solutions. Using this approach, airtight setup, and a number of necessary kinetic parameters, we managed to grow $K(D_xH_{1-x})_2PO_4$ crystals with the maximum possible deuterium concentration.

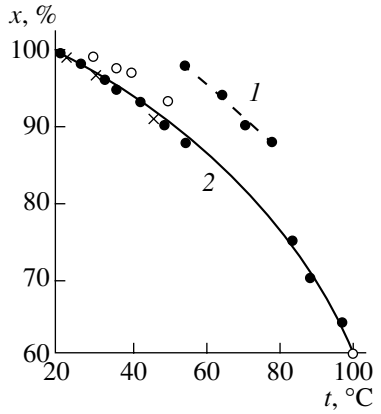

Fig. 4. Regions of existence of (*1*) the monoclinic and (*2*) the tetragonal phases in the $K(H,D)_2PO_4$ solutions; data [15] are shown by open circles; data [10], by filled circles; data [11] by crosses; and *x* is the degree of solution deuteration.

The solution compositions at points *2*, *3*, and *4* are listed in the table and show close values of KH_2PO_4 and KD_2PO_4 solubility in D_2O. The compositions of the components in the KH_2PO_4–D_2O system are determined by the lever rule [8] and are also listed in the table.

The data obtained lead to the conclusion that the compositions of mother solutions used for growing $K(D_xH_{1-x})_2PO_4$ crystals with the maximum deuterium concentration from the solutions in the KH_2PO_4–D_2O system correspond to the compositions of the saturated solutions at point *3* and certain supersaturation at point *4* on the K_2O–P_2O^{5-}–$(H,D)_2O$ solubility phase diagram at 50°C (see table).

Polymorphism of DKDP crystals hinders the choice of growth conditions for the tetragonal DKDP crystals, since the existence of the tetragonal or the monoclinic phase in the mother solution depends on the temperature and the deuterium concentration in this solution.

We analyzed the data [9–17] on the dependence of crystallization of the tetragonal and the monoclinic phases of KD_2PO_4 crystals and their mixture (mainly, under the conditions of spontaneous crystallization) on the degree of deuteration (60–100%), pH-value (1.6–4.2) and the temperature (5–100°C) of the $K(H,D)_2PO_4$ solutions in $(H,D)_2O$.

It is shown that under the above conditions, there are three crystallization regions—those of the tetragonal and the monoclinic $K(H,D)_2PO_4$ phases and the mixture of these two phases (Figs. 4, 5). The tetragonal phase is stable below the solubility curve of $K(H,D)_2PO_4$ in the temperature range from 20 to 100°C, pH 4, and the deuteration degree from 60 to 100% (Fig. 4). Similar features are also seen in Fig. 5; in this case, the decrease in from 4.2 to 1.8 results in the decrease of the existence region of the tetragonal phase in terms of temperature (17–50°C) and deuterium concentration (85–100%).

Based on the analysis of the known data and preliminary experiments on DKDP crystallization in the dynamic mode, we used the mother solutions with the following characteristics: the temperature ranging within 40–60°C, pH, ranging within 5–3, and the deuteration degree, about 98%.

The $K(D_xH_{1-x})_2PO_4$ single crystals were grown from solutions on seeds by the temperature decrease method. To prepare the mother solution for growing DKDP single crystals, we used a high-purity grade KH_2PO_4 and D_2O with the deuterium concentration of about 98%. The initial composition of the mother solution corresponded to the composition of point *4*: KDP concentration 36.65 wt % and D_2O concentration 63.35 wt %.

The DKDP single crystals were grown from solutions containing 167 g KDP in 300 ml D_2O (i.e., the composition corresponding to point *4*) with the decrease of the temperature from 50 to 45°C at the rate

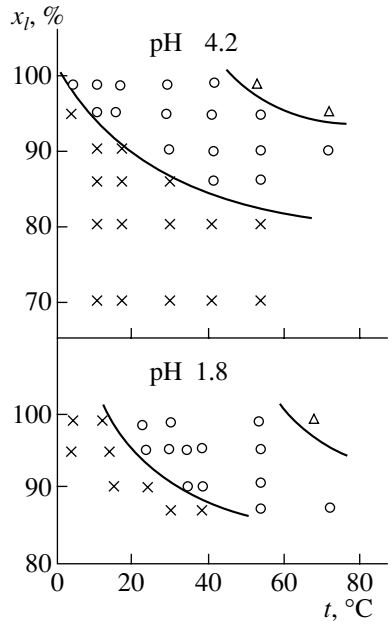

Fig. 5. Regions of spontaneous crystallization of solid phases in the $K(H,D)_2PO_4$ solutions; the tetragonal phase is shown by crosses; the monoclinic phase, by triangles; and the mixture of two phases, by open circles; x is the degree of solution deuteration.

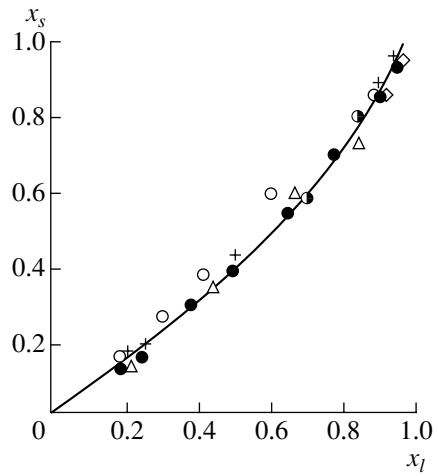

Fig. 6. Distribution of deuterium between the $K(H,D)_2PO_4$ crystals and the saturated solution. Curves are plotted by the data reported by different authors in accordance with the equation given in [7]. Open circles indicate data [14] at 30°C; triangles, data at 45°C; half-filled circles, data at 60°C; rhombuses indicate data [15]; crosses, data [16]; filled circles, data [17]; and x_s is the degree of crystal deuteration, and x_l is the degree of solution deuteration.

of temperature decrease equal to 0.11–0.16°C per day (24 h), and pH ranging within 3–5 (the variation in pH was attained by addition of $(D,H)_3PO_4$).

The reaction in the solution (50°C) proceeded by the scheme

$$KH_2PO_4 + D_2O \xrightarrow[H_2O]{D_2O} K(D_xH_{1-x})_2PO_4 + H_2O. \quad (1)$$

In comparison with the stoichiometric concentration of the components in the reaction (1), we had to use an amount of D_2O about 10 times higher in the mother solutions.

The deuterium concentration in the crystals grown was determined from the temperature of the tetragonal–orthorhombic phase transition and was equal to 87–88.6 wt %.

Proceeding from the exchange reaction [13],

$$H_2O + D_2O \rightleftharpoons 2HDO \quad (2)$$

and the deuterium concentration in crystals grown, we can rewrite reaction (1) in the schematic form as

$$KH_2PO_4 + D_2O \xrightarrow[H_2O]{D_2O} K(D_{0.87}H_{0.13})_2PO_4 + (H_{1.72}D_{0.28})_2O + D_2O. \quad (3)$$

It is known that the deuteration degree in $K(D_xH_{1-x})_2PO_4$ crystals is lower than in mother solutions. This leads to the assumption [19] that the change in deuterium concentration occurs during crystal growth.

Proceeding from data [7] (Fig. 6) and the maximum deuterium concentration (~88 wt %) in the crystals grown, we established that in the growth process the concentration of deuterium in the mother solution was about 92 wt %.

CONCLUSIONS

The analysis of the physical and chemical characteristics of the formation of the KD_2PO_4 solid phase in the K_2O–P_2O_5–D_2O and KH_2PO_4–D_2O systems in the temperature range 25–50°C has been performed.

The method for growing $K(D_xH_{1-x})_2PO_4$ crystals in dynamic mode has been developed.

The optimum conditions for growing DKDP crystals have been determined.

The $K(D_xH_{1-x})_2PO_4$ single crystals with the maximum deuterium concentration up to 88 wt % have been grown from the KH_2PO_4 solutions in $(D,H)_2O$ on a DKDP seed by the temperature decrease method.

REFERENCES

1. L. N. Rashkovich, *KDP-Family Single Crystals* (Adam Hilger, Bristol, 1991).
2. L. G. Berg, Izv. Akad. Nauk SSSR, Ser. Khim., No. 1, 147 (1938).
3. L. G. Berg, Izv. Akad. Nauk SSSR, Ser. Khim., No. 1, 160 (1938).
4. L. V. Barkova and I. N. Lepeshkov, Zh. Neorg. Khim. **13** (5), 1432 (1968).
5. L. V. Soboleva, Neorg. Mater. **31** (5), 614 (1995).
6. L. V. Soboleva, Neorg. Mater. **32** (8), 1007 (1996).
7. L. V. Barkova and I. N. Lepeshkov, Zh. Neorg. Khim. **11** (6), 1470 (1966).

8. V. Ya. Anosov and S. A. Pogodin, in *Basic Principles of the Physicochemical Analysis* (Akad. Nauk SSSR, Moscow, 1947), p. 83.
9. C. Belouet, M. Monnier, and R. Crouzier, J. Cryst. Growth **30** (2), 151 (1975).
10. M. Jiang, C. Fang, X. Yu, *et al.*, J. Cryst. Growth **53** (2), 283 (1981).
11. I. A. Batyreva, V. I. Bespalov, V. I. Bredihin, *et al.*, J. Cryst. Growth **53** (4), 832 (1981).
12. R. V. Strel'nikova and L. N. Rashkovich, Kristallografiya **22**, 844 (1977) [Sov. Phys. Crystallogr. **22**, 483 (1977)].
13. Ya. M. Varshavskiĭ and S. E. Vaĭsberg, Usp. Khim. **27**, 1434 (1957).
14. H. Havrankova and B. Brezina, Krist. Tech. **9** (1), 87 (1974).
15. C. Belouet, Prog. Cryst. Growth Charact. **3**, 181 (1980).
16. G. M. Loiacono, I. F. Balascio, and W. N. Osborn, Appl. Phys. Lett. **24**, 455 (1974).
17. V. I. Bespalov, I. A. Batireva, L. A. Dmitrenko, *et al.*, Sov. J. Quantum Electron. **7**, 885 (1977).
18. M. E. Lines and A. M. Glass, *Principles and Applications of Ferroelectrics and Related Materials* (Oxford Univ. Press, Oxford, 1977; Mir, Moscow, 1981).
19. Yu. M. Baĭkov, Zh. Fiz. Khim. **60** (3), 758 (1986).

Translated by T. Dmitrieva

Crystallography Reports, Vol. 47, No. 1, 2002, pp. 135–144. Translated from Kristallografiya, Vol. 47, No. 1, 2002, pp. 145–155.

CRYSTAL GROWTH

Bicrystallography of Nonisovalent Heterostructures with Different Crystal Lattices of the Components and Nonsingular Interfaces: GaN on $LiGaO_2$

A. N. Efimov and A. O. Lebedev

Ioffe Physicotechnical Institute,
Politekhnicheskaya ul. 26, St. Petersburg, 194021 Russia
e-mail: AndrewEfimov@usa.net

Received April 29, 1999; in final form, November 23, 2000

Abstract—The methodological aspects of the X-ray diffraction diagnostics of thin single-crystal layers on nonisomorphous substrates have been considered for low-symmetric crystals and nonsingular interfaces. The methods of their analysis suggested in the article allowed the determination of the stress and strain tensors in the layer and the precision description of the orientational relationships. The study of the model GaN/$LiGaO_2$ heterostructure with insignificant lattice mismatch showed that the latter is equivalent to the assumption on the pseudomorphic nature of epitaxial growth at its initial stage. However, the final state of the heterostructure corresponds to the deep elastic-energy relaxation. The misfit-dislocation density in the system indicates that the lattice mismatch is not the factor determining the epitaxial-layer perfection. © *2002 MAIK "Nauka/Interperiodica".*

1. INTRODUCTION

In recent years, we have seen evidence an ever growing practical interest in the creation of perfect heterostructures with the layer and substrate materials having not only considerably different lattice parameters but also different symmetries of the crystal lattices and the types of chemical bonding (including valences). They are also mutually insoluble which cannot be dissolved in one another. This interest is dictated, first and foremost, by the necessity of creating epitaxial layers of high-temperature superconductors and A^3B^5 nitrides [1–3], the materials that cannot be grown in the form of single crystals of required quality and dimensions because of a number of physicochemical factors.

The main laws of the defect formation in epitaxial heterostructures in *isovalent epitaxy* are well known [4]. At the same time, the experimental verification of the metric matching along the interface is far from being trivial even for cubic crystals. The situation becomes even more complicated if the heterostructure components are low symmetric or the interface orientation differs from the orientation described by small indices [5–7].

The above indicated features result in the fact that the hypothesis of the correlation between the metric match of the lattices and their crystalline perfection in epitaxial growth in the case of essentially different lattices of the components has not been verified.

Today, new single crystals of exotic compounds with the lattice parameters close to those of the layer are grown; the layers deposited onto these substrates provide the measurement of the broadening of X-ray diffraction lines. As a rule, such broadening is less than in the layer formation on the traditional substrates (implicitly, it was assumed that the mismatch in the lattice parameters is responsible for the degree of layer perfection).

It should be indicated that the study of growth of nitrides on various sapphire and aluminum–magnesium spinel cuts did not revealed any obvious correlation between the lattice mismatch and the structure perfection [6–8]. The same conclusion has also been drawn in the study of epitaxial gallium nitride films on various substrates [9].

Thus, we arrive at the necessity to develop the methods for exhaustive description of the geometric relationships (mutual location) of the heterostructure components with considerably different crystal lattices and study possible relation between the lattice mismatch and the physical characteristics of the layer (the degree of crystal perfection, strains, stresses, etc.).

2. METHODOLOGICAL ASPECTS OF THE DETERMINATION OF THE CRYSTAL GEOMETRY OF HETEROSTRUCTURES WITH PRONOUNCEDLY DIFFERENT CRYSTAL LATTICES OF THE COMPONENTS AND NONSINGULAR INTERFACES

2.1. Description of the Orientational Relationship in an Epitaxial System

An epitaxial orientational relationship determines the mutual spatial arrangement of the substrate and

layer lattices and is usually written in the form

$$(H_1H_2H_3) \parallel (h_1h_2h_3),$$
$$[K^1K^2K^3] \parallel [k^1k^2k^3], \quad (1)$$

where $(H_1H_2H_3)$ and $(h_1h_2h_3)$ are the Miller indices of the parallel planes of the layer and the substrate, respectively, and $[K^1K^2K^3]$ and $[k^1k^2k^3]$ are the Miller indices of parallel directions. As a rule, the indices $(h_1h_2h_3)$ in Eq. (1) are the indices of the substrate cut, whereas the direction usually lies in the cut plane, i.e., $h_ik^i = 0$ and, thus,

$$H_iK^i = 0. \quad (2)$$

Hereafter, the super- and subscripts belong to counter- and covariant tensor components, respectively, whereas the summation is performed over the repeating indices at various levels.

Such a description of the orientational relationship uniquely determines the mutual arrangement of the lattices if both metric tensors of the conjugating crystals are known. In practice, one often encounters the case where the metric parameters of, at least, one of the crystals are unknown (e.g., if the layer is elastically strained). Moreover, the orientational relationship in the form of Eq. (1) is somewhat ambiguous and does not allow one to identify the spatially equivalent relationships because

(1) the azimuth $[k^1k^2k^3]$ is arbitrary, even with due regard for Eq. (2);

(2) there is a large number of symmetrically equivalent but formally different variants of Eq. (1); and

(3) in practice, similar to the close-packed directions in the layer and the substrate, the singular planes are only approximately (with a deviation of several angular degrees) parallel to one another.

It was suggested [6] to describe the orientational relationship with the aid of the linear operator **M** such that

$$h_iM^i_j = H_j. \quad (3)$$

Similar relationships establish the relation between the indices of directions

$$M^i_jK^j = k^i \quad (4)$$

and the metric tensors of crystals

$$L_{ij} = M^k_iM^l_jS_{kl}, \quad (5)$$

where S and L are the metric tensors of the substrate and the layer, respectively. This form of the orientational relationship allows one to avoid the nonuniqueness of the relationship and considerably simplifies the problem of the search for the equivalent orientational relationship [6].

When considering the assumptions about the coherence degree of the heteroepitaxial boundary, it is convenient to write the orientational relationship as the constraints imposed onto the matrix of the operator **M**,

$$k^i = M^i_jK^j, \quad r^i = M^i_jR^j, \quad (6)$$

where k, K and r, R are the indices of two directions at the interface in the coordinate systems of the substrate and the layer, respectively, and M is an unknown "orientational-relationship matrix."

In what follows, we consider the case where the shape and the dimensions of the unit cells of the substrate and the layer only slightly differ from one another. As a rule, this condition is invalid for epitaxial growth with considerably different crystal lattices of the matrix and the layer. Therefore, as the first step, one has to invoke the coincidence-site lattice (CSL) concept [6, 10]. The use of the CSL concept is equivalent to the redetermination of the sets on the basis of vectors of the conjugated crystals, which, in turn, changes the matrix M.

Whereas the selection rules for the unit parallelepipeds for each crystal are strongly defined [11], the orientational-relationship matrix M can be chosen arbitrarily. We indicate here only the following property of the matrix M:

$$det(M) = V_{(L)}/V_{(S)}, \quad (7)$$

where $V_{(L)}$ and $V_{(S)}$ are the unit cell volumes of the layer and the substrate, respectively. Thus, it is necessary to redefine one (or both) unit cells which are compared in order to make the orientational-relationship matrix as close as possible to the unit matrix. With this aim, one has either to choose the unit cell with different dimensions or shape in the layer (substrate) lattice or to redefine the basic vectors in the given unit parallelepiped. The problem of the search for two- and three-dimensional superlattices (sublattices) was considered in a large number of works (see, e.g., [12–14]). We should like to emphasize here only the following features:

(1) The rules of the transition to a new coordinate system (the calculation of the metric-tensor values, the indices of the planes, and directions in the transformed unit cell) are similar to those indicated in (3)–(5);

(2) the determinant of the transformation matrix T of the unit cell equals the natural number for a superlattice (the so-called superlattice order) and the rational fraction for the sublattice;

(3) two compared transformed unit cells of the substrate and the layer should be of approximately equal volumes, i.e.,

$$det(M) \approx 1. \quad (8)$$

Obviously, the triad of the basis vectors (i.e., three noncoplanar vectors constructed on the unit-cell edges and having the common origin) can be set by several ways. The problem of the search for all the nonequivalent ways of the setting of the basis vectors in the unit cells of various symmetries was considered elsewhere [3]. It should be indicated that solving the problem associated with the reduction of the unit cells of the

conjugated crystals to the comparable forms, one has to consider all possible transformations of the basis vector including those which do not change the metric tensor of the crystal. For the right-hand triad of the vectors, the number of such transformation equals 24, whereas the permutation group of the basis vectors is isomorphic to the enantiomorphic hemihedral group of the cubic system.

It is logical to consider the following condition as a criterion of closeness of the resulting matrix M to the unit matrix I:

$$Sp(M) \sim 3, \tag{9}$$

where Sp is the matrix spur.

2.2. Method of Determining the Crystallogeometric Parameters of an Epitaxial System

Processing the experimental data and performing the calculations within the anisotropic linear theory of elasticity, we used the following assumptions: the heterostructure bending can be neglected (which is always true for sufficiently thin layers); the elastic properties and the equilibrium lattice parameters are uniform within the epitaxial layer; and the interface is planar.

The problem was considered in the following sequence. Using the experimental X-ray diffraction data, we determined the crystallogeometric characteristics of the epitaxial system. Then, we calculated the experimental values of the quantities characterizing the strained state of the epitaxial layer and the characteristics of the layer under a certain assumption on the coherence degree of the layer–substrate interface and, then, compared the data thus obtained with the experimental ones.

As a result of the X-ray diffraction experiment, one has to determine the quantities characterizing the mutual spatial orientation of the atomic planes in the layer and the substrate. Obviously, these quantities are φ and ψ (the polar angles of the normal to the corresponding reflecting planes in a certain common coordinate system) and the Bragg angles θ for the reflections from the layer and the substrate.

If a growing epitaxial layer is parallel to the substrate, the metric mismatch between the substrate and the layer unit cells is very small (characteristic of isostructural epitaxy), and the problem is solved with the invocation of the differential scheme of the rocking curves [15, 16]. This method requires the record of two X-ray diffraction maxima from the epitaxial layer–substrate system, which correspond to lattice parameters of the layer and the substrate. The angular distance between these maxima depends on the difference in the Bragg angles $\Delta\theta$ and the difference in the tilt angles $\Delta\varphi$ of the reflecting planes, whose contributions can be separated by recording the rocking curves in different geometries [15]. If the metric tensor of an unstrained crystal (substrate) is known reliably, one can determine the metric tensor of the strained crystal (layer).

At the same time, this method is inapplicable to a nonisotructural epitaxial pair, since the unit cells of the layer and the substrate are usually incommensurate and the orientational relationship is nontrivial. In this case, the quantities θ, φ, and ψ should be determined separately for each of the reflecting planes of the layer and the substrate.

The geometrical scheme of the experiment is shown in Fig. 1. We used a standard goniometric attachment. The vector **n** lies in the plane of the drawing corresponding to the equatorial plane of the diffractometer. The crystallographic plane is brought to the reflecting position by rotating the specimen by an angle ψ around its normal **n** and then by rotating it by an angle ω around the normal to the equatorial plane of the diffractometer.

For each layer and substrate plane, we measured the angles ω of the reflecting position of the plane (on the specimen scale) for four different positions of the specimen with respect to the X-ray beam (Fig. 1b). The polar angles φ and ψ and the Bragg angle θ were determined by averaging the data of four independent measurements. Thus, in accordance with Fig. 1, one can write the following equations for the measured $\omega_{(1)}$, $\omega_{(2)}$, $\omega_{(3)}$, and $\omega_{(4)}$ angles:

$$\begin{aligned}
\omega_{(1)} &= \theta - \varphi + \omega_{(0)},\\
\omega_{(2)} &= \theta + \varphi + \omega_{(0)},\\
\omega_{(3)} &= 180^\circ - \theta + \varphi + \omega_{(0)},\\
\omega_{(4)} &= 180^\circ - \theta - \varphi + \omega_{(0)},
\end{aligned} \tag{10}$$

where θ is the Bragg angle, φ is the angle of deviation of the plane normal from the specimen-surface normal (the first polar angle of the plane normal) and $\omega_{(0)}$ is the systematic error of the specimen scale. Obviously, it follows from Eqs. (10) that

$$\begin{aligned}
\theta &= (\omega_{(1)} + \omega_{(2)} - \omega_{(3)} - \omega_{(4)} + 360^\circ)/4,\\
\varphi &= (\omega_{(2)} - \omega_{(1)} + \omega_{(3)} - \omega_{(4)})/4.
\end{aligned} \tag{11}$$

At the same time, we also measured the angles $\psi_{(1)}$, $\psi_{(2)}$, $\psi_{(3)}$, and $\psi_{(4)}$ of the specimen rotation around its normal, which corresponded to bringing the given plane to the reflecting position. Then, using these angles, we determined the second polar angle ψ between the normal and the plane,

$$\psi = (\psi_{(1)} + \psi_{(2)} + \psi_{(3)} + \psi_{(4)} - 360^\circ)/4, \tag{12}$$

where the angle ψ was measured from a certain reference azimuth **r** (Fig. 1a) corresponding to the zero value of the scale.

The crystallogeometric characteristics of the epitaxial system include the metric tensors of the conjugated crystals, the orientational-relationship matrix, and the indices of the layer–substrate interface. For the unambiguous determination of the crystal geometry of the

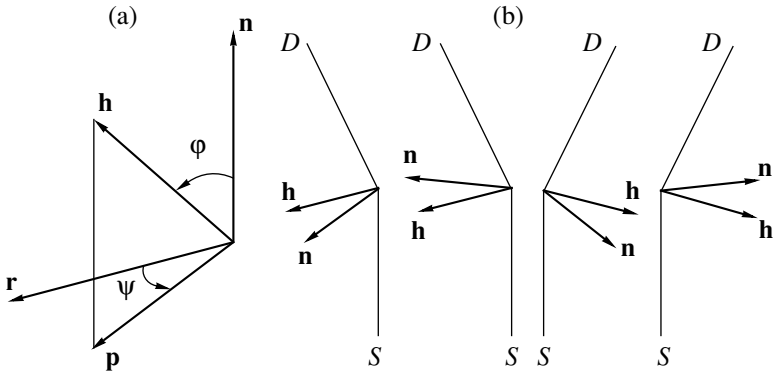

Fig. 1. Geometric scheme of the diffraction experiment. (a) Notation used for the vectors and the polar angles in the spherical coordinate system; (b) a plane in the reflecting positions: *S* is the X-ray source, *D* is the detector, **h** is the vector normal to the diffraction plane, and **n** is the vector normal to the specimen surface.

system, one has to determine, in accordance with Eqs. (3)–(5), the metric tensor of one of the crystals, the interface indices in the coordinate system of one of the crystals, and the components of the orientational-relationship matrix *M*. In reality, the X-ray diffraction data considered above dictate somewhat different sequence of the calculations. First, one has to calculate the metric tensors of both crystals from the experimental data on the angles θ, φ, and ψ, the indices of the interface and the directions in the interface in the corresponding coordinate systems, and, finally, the matrix *M*.

The components of the metric tensor *S* of the substrate are related by the following equations (the computations for the layer are similar):

$$1/d^2 = h_i S^{ij} h_j, \tag{13}$$

where *d* is the interplanar spacing for the $(h_1h_2h_3)$ plane of the substrate characterized by the experimental value of the angle θ. In the general case of a triclinic unit cell, one has to calculate six independent components S^{ij} from the system of equations of type (13), which requires the knowledge of six experimental values of interplanar spacings in the substrate lattice. In the case of the linear dependence of the equations, the number of the experimental points should correspondingly be increased. As a rule, the metric tensors are calculated by the least squares method with the number of equations exceeding the number of the components to be determined by a factor of two to three.

The indices n^i of the interface in the corresponding coordinate system can readily be determined by minimizing the following expression:

$$\Sigma(\cos\varphi - n^i h_i/|h|)^2, \tag{14}$$

where φ is the experimentally determined polar angle h_i of the plane, and the summation is performed over all the experimentally observed reflections. For definiteness, we assume that $|n| = 1$.

To determine the indices of a certain direction in the interface, one has to determine the indices of the projections of the vectors *h* of the normal onto the interface plane *n* from the following conditions:

$$\begin{aligned} h_i p^i &= |h|\cos(90^\circ - \varphi), \\ n_i p^i &= 0, \quad |p| = 1, \end{aligned} \tag{15}$$

where *p* are the indices of the vector projection *h* onto the plane *n*. Finally, the Miller indices of the sought direction *r* with the known polar angles φ and ψ are determined from the condition:

$$\Sigma(p_i r^i - \cos\psi)^2 \longrightarrow \min, \quad n_i r^i = 0, \quad |r| = 1, \tag{16}$$

where summation is performed over all the experimental reflections.

In some cases, one has also to know the indices of the direction *k* lying in the interface normally to *r*. We have for k^i

$$n_i k^i = 0, \quad r_j k^j = 0, \quad |k| = 1, \quad \mathbf{k}[\mathbf{n}\times\mathbf{r}] > 0, \tag{17}$$

i.e., $n_i r_j \delta^{ijm} k_m > 0$.

The above calculations are equivalent in the coordinate systems of both layer and substrate.

If the interface indices $(h_1h_2h_3)$ and $(H_1H_2H_3)$ and the indices of two directions $(r_1r_2r_3)$, $(R_1R_2R_3)$ and $(k_1k_2k_3)$, $(K_1K_2K_3)$ are known in the coordinate systems of both substrate and layer, then nine independent components of the matrix *M* of the orientational relationship can be determined from the system of nine inhomogeneous linear equations (3) and (4).

The characteristics of the elastically strained state are usually defined by the elastic-strain and the stress tensors and the scalar elastic-energy density. The calculations are performed in the following sequence:

First, the components of the elastic-strain tensor are determined as

$$\varepsilon_{ij} = (L_{ij} - L_{ij(0)})/2, \tag{18}$$

where $L_{ij(0)}$ are the components of the metric tensor of unstrained crystal of the layer material.

The stress-tensor components are determined as

$$\sigma^{pq} = C^{pqij}\varepsilon_{ij}, \quad (19)$$

where C is the tensor of elastic moduli of the layer material.

The elastic-energy density is determined as

$$E = \sigma^{pq}\varepsilon_{pq}/2. \quad (20)$$

In order to calculate the above quantities, one has to know the value of the metric tensor of unstrained crystal of the layer, i.e., the metric tensor characterizing the bulk single crystal or a rather thick and completely relaxed epitaxial layer of the given material. In some cases, this tensor can be determined directly from the experimental data.

The condition of the mechanical equilibrium of a strained solid at the free surface of a layer can be written as

$$\sigma^{p} = \sigma^{pq}H_q, \quad (21)$$

where H are the crystallographic indices of the layer surface (i.e., the indices of the layer–substrate interface in the coordinate system of the layer).

Substituting Eq. (18) into Eq. (19) and then Eq. (19) into Eq. (21), we arrive at the system of three inhomogeneous linear equations with respect to $L_{ij(0)}$

$$C^{pqij}H_q(L_{ij} - L_{ij(0)}) = 0. \quad (22)$$

The components of the metric tensor of an unstrained layer can be determined from system of equations (22) under the following conditions: (i) the number of independent components $L_{ij(0)}$ does not exceed three, i.e., the crystal has either high or moderate (but not low) symmetry; (ii) none of Eqs. (22) is degenerate, which usually takes place if the substrate plane deviates from the singular face; and (iii) the elastic moduli of the layer material are determined reliably.

If conditions (i) and (ii) are not met, the components of the metric tensor of an unstrained crystal cannot be determined unambiguously. However, even in this case, linear relationships between $L_{ij(0}$ determined by Eqs. (22) can exist.

2.3. Calculation of the Epitaxial-Structure Parameters for Various Mechanisms of Deformation

Under the assumption of a certain acting mechanism, the data obtained by the methods described above allow one to calculate the strained state of the layer corresponding to this mechanism and compare the experimental value of the strain tensor with the calculated one.

We assume that at the epitaxial temperature, the layer is elastically strained, whereas the plastic deformation is absent. When cooling the heterostructure to room temperature, we recorded no relaxation either. This phenomenon is usually observed if the unit-cell parameters of the layer and the substrate are close, i.e., if the orientational-relationship matrix can be represented, without loss of the generality, in the form

$$M^i_j = \delta^i_j + \Delta^i_j, \quad (23)$$

where δ^i_j is the Kronecker delta-function. Thus, we arrive at the following constraint:

$$|\Delta^i_j| \ll 1. \quad (24)$$

For a coherent layer at

$$R^iH_i = 0,$$

condition (6) is transformed to the form

$$R^i = M^i_jR^j, \quad (25)$$

i.e., the crystallographic indices of any vector lying in the interface plane form the orientational-relationship matrix M with the eigenvalue $\lambda = 1$.

In terms of the *O*-lattice concept [10], condition (25) signifies that the lattices of the layer and the substrate form the *O*-lattice degenerate in the *O*-plane with the interface orientation coinciding with this *O*-plane.

Condition (25) imposes certain constraints on the number of independent components of the matrix M, namely,

$$\Delta^i_j = a^iH_j, \quad (26)$$

where a is a certain vector parameter and H are the interface indices. Substituting Eq. (26) into Eq. (23) and then Eqs. (23), (18), (19), and (5) into (21) and taking into account Eq. (24), we obtain

$$\sigma^{p} = C^{pqij}H_q(S_{ij} - L_{ij(0)} + 2S_{ik}a^kH_j)/2 = 0, \quad (27)$$

where $p = 1\ldots3$ and $L_{ij(0)}$ is the metric tensor of an unstrained crystal layer.

Using system of Eqs. (27), one can readily determine the vector parameter a and then, using Eqs. (23) and (26), also the matrix M. Then, using Eq. (5), one can also determine the metric tensor of the coherent layer, and using Eqs. (18)–(20), the characteristics of the elastically strained layer.

At the epitaxial temperature, the layer is completely relaxed, and elastic stresses can arise only during the heterostructure cooling down to room temperature because of the different values of the linear expansion coefficients of the layer and the substrate. Thus, at the growth temperature, the conjugated crystals are characterized by equilibrium metric tensors (at the given temperature). If the linear expansion coefficients at the given temperature are known for both materials, with the substrate orientation being also known, it is possible to obtain (from the experimental data or symmetric considerations) the indices of a definite direction in the interface simultaneously in the coordinate systems of

both layer and substrate. Then conditions (6) are transformed to

$$k^i_{(0,T)} = M^i_{j(T)}K^j_{(0,T)}, \quad r^i_{(0,T)} = M^i_{j(T)}R^j_{(0,T)}, \qquad (28)$$

where the symbols (*O*, *T*) indicate that these equations are valid for the materials of the substrate and the layer characterized by the equilibrium metric tensors at the growth temperature *T*.

Cooling the specimen from the epitaxial temperature, we observed no plastic deformation and, therefore, despite the temperature dependence on the metric tensors and the components M^i_j, condition (28) remains valid at any temperature, i.e.,

$$k^i = M^i_j K^j, \quad r^i = M^i_j R^j, \qquad (29)$$

It should be emphasized that Eqs. (29) include the vectors of the layer whose lengths are determined not by the equilibrium but by the real metric tensor of the layer existing at the given temperature. Rewriting (29) with due regard for Eq. (23), we have

$$r^i = R^i + \Delta^i_j R^j, \quad k^i = K^i + \Delta^i_j K^j. \qquad (30)$$

Moreover, Equation (21) with due regard for Eqs. (26), (23), (19), and (18) yields

$$\sigma^p = C^{pqij} \times H_q(S_{ij} - L_{ij(0)} + 2S_{ik}\Delta^k_j + \Delta^m_i\Delta^l_j S_{ml})/2 = 0. \qquad (31)$$

If the unit-cell parameters of the layer and the substrate are close, the term of the second-order with respect to Δ can be omitted. Thus, we can determine nine independent components Δ^m_i from nine equations (30) and (31). Then, using Eqs. (18)–(20) with due regard for Eqs. (23) and (5), we calculate the characteristics of the elastically strained state of the layer.

Let the stresses existing in the epitaxial layer be of the "temperature nature." Then, with due regard for Eqs. (28), one can write the following equations at the epitaxial-growth temperature *T*

$$\begin{aligned} k^i S_{ij(0,T)}k^j &= K^i L_{ij(0,T)}K^j, \\ r^i S_{ij(0,T)}r^j &= R^i L_{ij(0,T)}R^j, \\ r^i S_{ij(0,T)}k^j &= R^i L_{ij(0,T)}K^j \end{aligned} \qquad (32)$$

with the symbol 0, *T* having the meaning of "equilibrium at the given temperature."

If one knows the linear expansion coefficients at a given temperature, the metric tensors in Eq. (32) can be written in the numerical form. If the vector components in Eqs. (29) or (30) are determined experimentally in the numerical form, then the verification of the hypothesis of the temperature origin of stresses reduces to checking the validity of Eqs. (32).

It can happen that the *TKl* data for one of the crystals are unknown. Then, there are grounds to believe that the temperature approximation is valid and, then, conditions (29) and (32) can be used to evaluate the unknown metric tensor at the growth temperature. It should be indicated that in this case the unique solution of the system is obtained if the number of independent components of the metric tensor does not exceed three.

3. "GALLIUM NITRIDE (GAN) ON LITHIUM GALLATE ($LIGAO_2$)" HETEROSTRUCTURE

3.1. Determination of the Crystallogeometric Characteristics of the Heterostructure from the Experimental Data

We studied the epitaxial GaN layer grown by the method of organometallic synthesis on a lithium gallate substrate β-$LiGaO_2$ under reduced pressure. The growth temperature was ~800°C, the substrate thickness was ~500 μm, the layer thickness was 0.77 μm, and the ratio of the layer thickness to the thickness of the substrate was 0.0015. The estimation of the heterostructure curvature at the given thickness ratio determined by the method suggested in [4] shows that the variation in the lattice parameters of the substrate and the layer caused by possible heterostructure curvature are negligibly small.

Gallium nitride is hexagonal, sp. gr. $P6_3mc$. The reliable equilibrium lattice parameters of GaN at room temperature measured on both bulk gallium nitride and thick (hundreds of micrometers) relaxed epitaxial GaN layers grown by the method of organometallic synthesis are $a = 3.1880$ and $c = 5.1851$ Å [17]. The elastic moduli of GaN used in the further calculations were

$$C_{11} = 377, \quad C_{12} = 160, \quad C_{13} = 114,$$
$$C_{33} = 209, \quad C_{44} = 81.4 \text{ GPa [18]}.$$

Lithium gallate β-$LiGaO_2$ is orthorhombic (sp. gr. $Pna2_1$), its lattice parameters are characterized by pronounced scatter: $a = 5.402$, $b = 6.372$, and $c = 5.007$ Å [19] and $a = 5.4063$, $b = 6.3786$, and $c = 5.0129$ Å [20].

The measurements were performed on a standard DRON-2M diffractrometer with a GUR-8 goniometer, a Ge(111) monochromator, and the CoK_α-radiation. To increase the accuracy, we also used the CuK_α-radiation. We determined the Bragg angles of reflections and the polar coordinates of the following planes: for the $LiGaO_2$-substrate, {205}, {324}, {244}, {002}, {004}, and {006} and for the GaN layer, {10.3}, {10.4}, {10.5}, {00.2}, {00.4}, and {00.6}. The unit-cell parameters calculated by the least squares method for standard setting are: for the $LiGaO_2$ substrate, $a = 5.4090 \pm 0.0007$, $b = 6.3801 \pm 0.0010$, $c = 5.0112 \pm 0.0008$, $\alpha = 90.001 \pm 0.001$, $\beta = 89.999 \pm 0.002$, and $\gamma = 90.000 \pm 0.003$; for the GaN layer, $a = 3.180 \pm 0.002$, $b = 3.191 \pm 0.002$, $c = 5.187 \pm 0.003$, $\alpha = 89.95 \pm 0.01$, $\beta = 90.02 \pm 0.01$, $\gamma = 119.81 \pm 0.05$. The substrate lattice is orthogonal, which confirms once again the correctness of the initial assumptions on negligibly small

elastic strains in the substrate. It is also essential that the layer unit cell considerably differs from the equilibrium hexagonal unit cell, which indicates the strong layer–substrate interaction. For comparison, we also give here our data on the lattice parameters of the layer and the substrate obtained for the heterostructure "GaN layer grown on the sapphire substrate misoriented from the (0001) plane".

For the α-Al_2O_3 substrate, $a = 4.7583 \pm 0.0004$, $b = 4.7581 \pm 0.0004$, and $c = 12.991 \pm 0.002$, $\alpha = 89.998 \pm 0.004$, $\beta = 90.001 \pm 0.004$, and $\gamma = 119.995 \pm 0.007$. For the GaN layer, $a = 3.1870 \pm 0.0005$, $b = 3.1870 \pm 0.005$, $c = 5.1885 \pm 0.0010$, $\alpha = 90.003 \pm 0.006$, $\beta = 89.990 \pm 0.006$, and $\gamma = 120.010 \pm 0.009$.

Obviously, because of considerable lattice mismatch in this system, the layer–substrate interaction is weakened, and the layer "makes no attempts" to match the substrate.

The interface indices in the coordinate systems of the layer and the substrate were determined by the least squares method with the use of the experimentally determined polar angles φ and ψ (see Fig. 1). The interface (covariant) indices for the $LiGaO_2$ substrate are n = (0.2147, –0.1975, and 5.0049); for the GaN layer, the interface covariant indices are n = (–0.1024, 0.1701, and 5.1795).

To determine the azimuthal rotation of the layer with respect to the substrate, one has to know the coordinates of any vector lying in the interface plane in the crystallographic coordinate systems of both layer and substrate. It is convenient to use the vector corresponding to the zero azimuthal coordinate of the goniometric head. The coordinates of this vector were also determined by the least squares method using the experimental ψ values.

The countervariant indices for the $LiGaO_2$ substrate are: r = [0.0615, –0.1478, –0.0032].

The countervariant indices for the GaN layer (in three-index notation) are: r = [–0.3570, –0.1232, –0.0030].

For the further interpretation of lattice conjugation, one has to reduce the unit cells of the layer and the substrate to a form providing their comparison. This is done with the aid of the linear operators of transition to new coordinate systems (Fig. 2).

The transition to the substrate sublattice. The matrix of transition to a new setting is

$$T = \begin{pmatrix} 1/2 & 0 & 0 \\ -1/4 & 1/2 & 0 \\ 0 & 0 & 1 \end{pmatrix}.$$

The values of the crystallogeometrical parameters for the new substrate setting are $a = 3.1398$, $b = 3.1900$, $c = 5.0112$; $\alpha = 90.00$, $\beta = 90.00$, $\beta = 120.53$; n = (–0.0580, –0.0987, 5.0049); r = [0.1229, –0.2341, –0.0032].

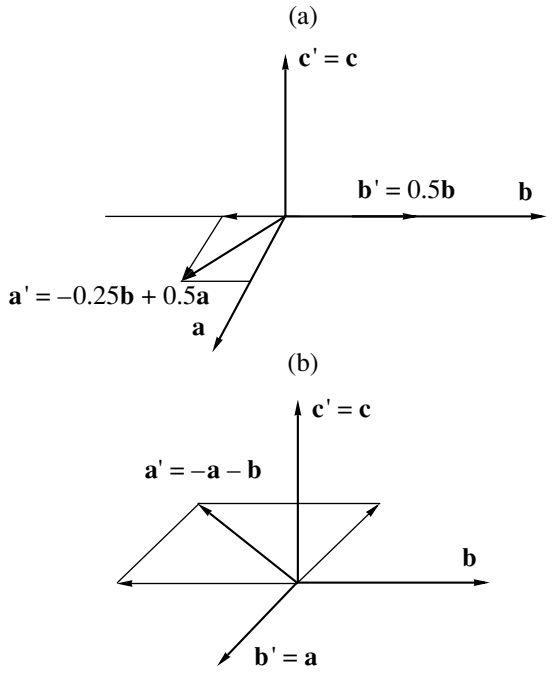

Fig. 2. Illustrating the transition to a new coordinate system: **a**, **b**, and **c** are the vectors of the "old" unit cell, **a**', **b**', and **c**' are the vectors of the transformed unit cell; (a) the transition to the substrate sublattice, (b) the new notation of the unit-cell of the layer.

New notation of the layer unit cell. The matrix of the transition to a new setting is

$$T = \begin{pmatrix} -1 & 1 & 0 \\ -1 & 0 & 0 \\ 0 & 0 & 1 \end{pmatrix}.$$

The values of the crystallogeometric parameters for the new layer setting are: $a = 3.195$, $b = 3.180$, $c = 5.187$; $\alpha = 90.02$, $\beta = 90.03$, $\gamma = 119.93$; n = (–0.0677, –0.1024, 5.1794); r = [0.1232, –0.2338, –0.0030].

Such a choice of the new settings is based on the closeness of the crystallogeometric parameters of the layer and the substrate in these settings, the small dimensions of the transformed unit cells, and on the fact that, as will be shown below, the interface is only slightly incoherent.

Thus, the experimental values of the components of the orientational-relationship matrix for the transformed unit cells are

$$M_j^i = \begin{pmatrix} 1.0184 & 0.0108 & 0.0052 \\ 0.00163 & 1.0023 & 0.00347 \\ -0.00169 & -0.00056 & 1.035 \end{pmatrix}.$$

It should be indicated that the above matrix is close to the unit matrix.

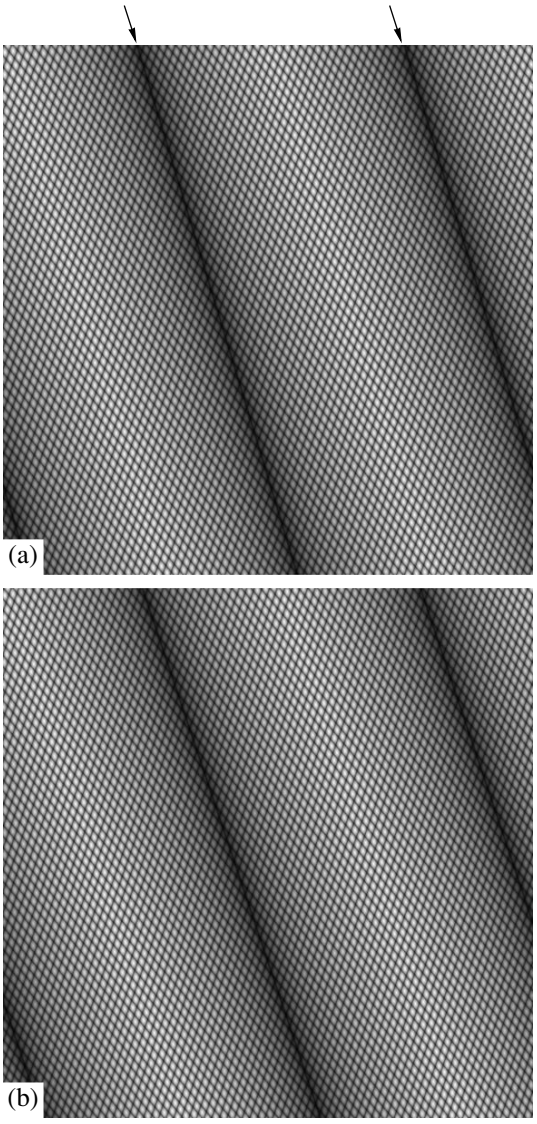

Fig. 3. Illustrating the reconstruction of the translation symmetry of the interface plane: (a) gallium nitride layer; the 200×200 Å area. The drawing plane in Figs. 3 and 4 coincides with the interface plane; the horizontal side of the square is parallel to the reference vector. Dark lines indicated by the arrows correspond to the surface steps formed due to the deviation of the interface from the plane with the rational indices; (b) the same for the substrate.

Now, determine the characteristics of the elastically strained state of the layer. Using the most reliable unit-cell parameters of the unstressed layer, $a = 3.1880$, $b = 3.1880$, $c = 5.1851$, $\alpha = 90.00$, $\beta = 90.00$, and $\gamma = 120.00$ [17], we arrive at the components of the metric tensor of unstrained layer of the crystal

$$L_{(0)} = \begin{pmatrix} 10.1722 & -5.0861 & 0.0 \\ -5.0861 & 10.1722 & 0.0 \\ 0.0 & 0.0 & 26.8898 \end{pmatrix}.$$

Now, using the metric tensor of the strained layer obtained from the experimental lattice parameters,

$$L = \begin{pmatrix} 10.2081 & -5.0693 & -0.0092 \\ -5.0693 & 10.1146 & -0.0057 \\ -0.0092 & -0.0057 & 26.9014 \end{pmatrix},$$

we obtain, in accordance with Eq. (18), the experimental values of the components of the elastic-strain tensor

$$\varepsilon = \begin{pmatrix} 0.0179 & 0.0084 & -0.0046 \\ 0.0084 & -0.0288 & -0.0029 \\ -0.0046 & -0.0029 & 0.0058 \end{pmatrix}.$$

Using Eq. (19) and the known elastic moduli, we can calculate the stress-tensor components

$$\sigma = \begin{pmatrix} 0.0679 & 0.0172 & -0.0048 \\ 0.0172 & -0.0628 & -0.0041 \\ -0.0048 & -0.0041 & 0.0003 \end{pmatrix}$$

and using Eq. (20), also the elastic-energy density, $E = 0.0017$ GJ/m^3.

3.2. Calculation of Crystallogeometric Characteristics in the Approximation of Coherent Interface

To estimate the closeness of the heterostructure state to coherent, one has to calculate the crystallogeometry of the layer under the assumption of the interface coherency with due regard for the experimentally determined substrate orientation. Using Eqs. (27), (23), and (26), we determine the components of the matrix of the orientational relationship in the form

$$M_j^i = \begin{pmatrix} 1.00003 & 0.00006 & -0.00282 \\ 0.0 & 1.00001 & -0.00032 \\ -0.00055 & -0.00093 & 1.0472 \end{pmatrix},$$

whence, with due regard for Eq. (5), we obtain the lattice parameters of the strained layer, $a = 3.1399$, $b = 3.1900$, $c = 5.2479$, $\alpha = 90.05$, $\beta = 90.14$, and $\gamma = 120.53$.

Then, we can also obtain the elastic strain tensor

$$\varepsilon = \begin{pmatrix} -0.1565 & -0.0008 & -0.0200 \\ -0.0008 & 0.0018 & -0.0069 \\ -0.0200 & -0.0069 & 0.3255 \end{pmatrix};$$

the stress tensor

$$\sigma = \begin{pmatrix} -0.8317 & -0.4156 & -0.0186 \\ -0.4156 & -0.3889 & -0.0135 \\ -0.0186 & -0.135 & 0.0077 \end{pmatrix};$$

and the elastic-energy density $E = 0.0668$ GJ/m^3.

4. DISCUSSION OF RESULTS

First of all, we should like to emphasize that the data on the mutual lattice orientation of the layer and the substrate are consistent with the assumption of interface coherence. The necessary (but not sufficient) condition of the coherency is the coincidence of the crystallographic indices of the interface plane and the reference direction lying in this plane in the comparable layer and substrate bases.

We have the following experimental data. In the crystallographic coordinate system: the interface indices are (–0.0677, –0.1024, 5.1794), the reference direction indices are [0.1232, –0.2338, –0.0030]; in the coordinate system of the substrate, (–0.0580, –0.0987, 5.0049) and [0.1229, –0.2341, –0.0032].

This almost exact (within the measurement error) coincidence of the indices cannot be accidental.

On the other hand, the elastic-energy density calculated under the assumption of the system coherence for the observed interface orientation is $E_{coh} = 0.0668$ GJ/m^3, whereas its real value, $E_{coh} = 0.0017$ GJ/m^3, indicates deep stress relaxation. This obvious contradiction can be explained by the fact that, at the initial stages, the layer growth was coherent, but with an increase of the layer thickness, the relaxation process occurred.

The further consideration of the interface structure requires a more detailed analysis of the heterostructure geometry. To visualize the interface, we cut the crystal by an arbitrary plane parallel to the interface and color the plane obtained in such a way that the point is the brighter, the closer it is to the unit-cell center and the point is the darker, the closer it is to the interface. Obviously, the pattern thus obtained is strictly periodic for rational interfaces with the translation symmetry corresponding to the translation symmetry of the given plane. The pattern for the irrational planes is quasisymmetric. Figures 3a and 3b show the thus reconstructed contacting surfaces of the layer and substrate. Because the geometry of the heterostructure is close to the coherent state, one cannot distinguish the boundary between the drawings with a naked eye.

To visualize the dislocation structure, we invoked the Bollmann *O*-lattice concept [10]. The network of misfit dislocations at the interface is identified with the section of the *O*-cells by the interface plane (the moire pattern). Similar to Figs. 3a and 3b showing the sections of the unit cells of the layer and substrate, Figures 4a–4c show the sections of the *O*-lattice formed by the interference of the layer and the substrate lattices. It is seen that to compensate the lattice mismatch, one has to introduce into consideration three systems of misfit dislocations with the average interdislocation distance along the *a*–*a* direction being 108; along the *b*–*b* direction, 780; and along the *c*–*c* direction, 2400 Å. Identifying the minimum distance with the dimensions of the coherent-scattering region, we obtain that the broadening of the 002 GaN reflection (the ω scan, CoK_α radia-

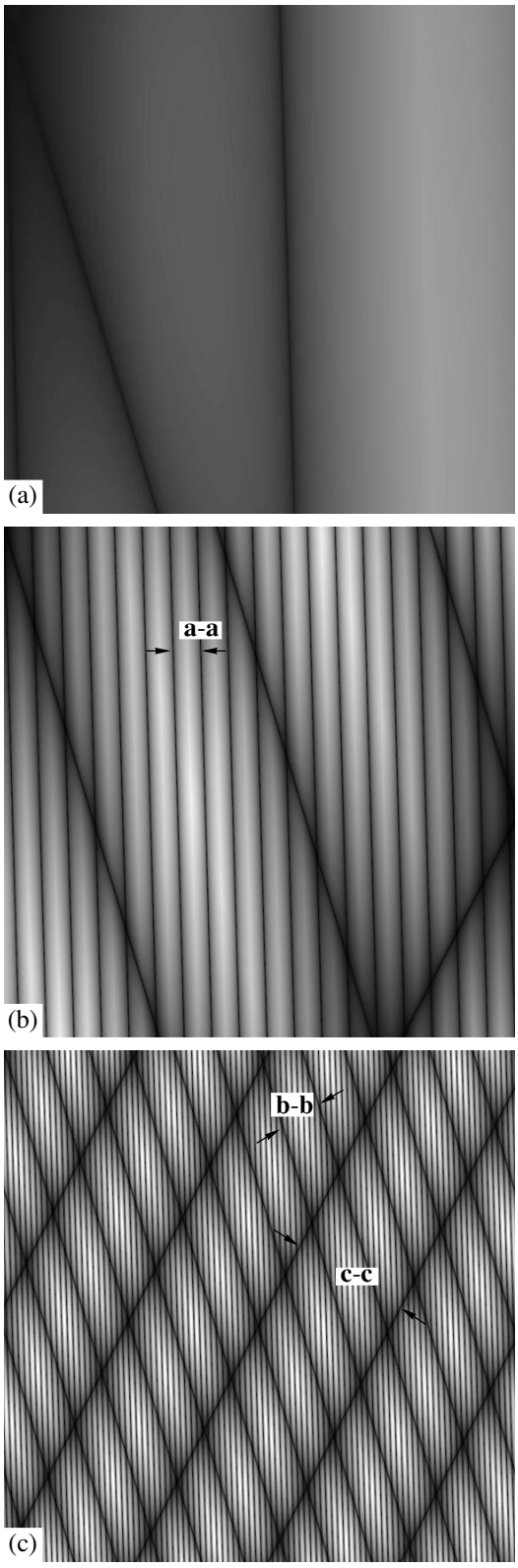

Fig. 4. Illustrating the reconstruction of the dislocation structure of the specimen. The orientation is the same as in Fig. 3. The dark lines indicated by arrows correspond to three systems of misfit dislocations: (a) the 200 × 200, (b) the 2000 × 2000, (c) the 10000 × 10000 Å area.

tion) would have exceeded the value of several degrees [21], whereas the data obtained in our and other measurements do not exceed a value of several angular minutes. Thus, the geometric lattice mismatch cannot be regarded as the main factor affecting the structural perfection of GaN layers, and the problem of growing high-quality heterostructures cannot be reduced (at least at the present level of the technology) only to the search for an ideal geometrically matching substrates. This conclusion is also confirmed by the absence of the explicit relationships between the degree of the geometric matching and the structural perfection in epitaxial growth on various substrates [6, 8, 9].

ACKNOWLEDGMENTS

This study was supported by the Russian Foundation for Basic Research, project no. 97-02-18017. The authors are grateful to Prof. M. Razeghi from Northwestern University, Illinois, USA who kindly supplied us with the specimens.

The package of programs used in our study can be obtained from the authors.

REFERENCES

1. A. N. Efimov and A. O. Lebedev, J. Supercond. **6** (5), 317 (1993).
2. A. N. Efimov and A. O. Lebedev, Fiz. Tverd. Tela (St. Petersburg) **36** (3), 595 (1994) [Phys. Solid State **36**, 328 (1994)].
3. A. N. Efimov and A. O. Lebedev, Surf. Sci. **344**, 276 (1995).
4. Yu. A. Tkhorik and L. S. Khazan, *Plastic Deformation and Misfit Dislocations in Epitaxial Structures* (Naukova Dumka, Kiev, 1983).
5. A. N. Efimov, Kristallografiya **42** (3), 509 (1997) [Crystallogr. Rep. **42**, 462 (1997)].
6. A. N. Efimov, A. O. Lebedev, and A. M. Tsaregorodtsev, J. Appl. Crystallogr. **31**, 461 (1998).
7. A. N. Efimov and A. O. Lebedev, Thin Solid Films **260**, 111 (1995).
8. A. N. Efimov, A. O. Lebedev, V. V. Lundin, and A. S. Usikov, Kristallografiya **45** (2), 345 (1999) [Crystallogr. Rep. **45**, 312 (2000)].
9. R. N. Kyutt, V. V. Ratnikov, G. N. Mosina, and M. P. Shcheglov, Fiz. Tverd. Tela (St. Petersburg) **41** (1), 30 (1999) [Phys. Solid State **41**, 25 (1999)].
10. W. Bollmann, *Crystal Defects and Crystalline Interfaces* (Springer-Verlag, New York, 1970).
11. N. M. F. Henry and K. Lonsdale, in *International Tables for X-ray Crystallography* (The Kynoch Press, Birmingham, 1952), Vol. 1, p. 6.
12. A. Santoro, A. D. Mighell, and J. R. Rodgers, Acta Crystallogr., Sect. A: Cryst. Phys., Diffr., Theor. Gen. Crystallogr. **36**, 796 (1980).
13. R. Bucksch, J. Appl. Crystallogr. **5**, 96 (1972).
14. A. Zur and T. C. McGill, J. Appl. Phys. **55**, 378 (1984).
15. Yu. P. Khapachev and F. N. Chukhovskiĭ, Kristallografiya **34** (3), 788 (1989) [Sov. Phys. Crystallogr. **34**, 465 (1989)].
16. V. A. Gan'shin, Yu. N. Korkishko, and V. A. Fedorov, Kristallografiya **40** (2), 342 (1995) [Crystallogr. Rep. **40**, 308 (1995)].
17. M. Leszczynski, T. Teisseyre, T. Suski, *et al.*, Appl. Phys. Lett. **69** (1), 73 (1996).
18. R. B. Schwarz, K. Khachaturyan, and E. R. Weber, Appl. Phys. Lett. **70** (9), 1122 (1997).
19. P. Kung, A. Saxler, and X. Zhang, Appl. Phys. Lett. **69** (14), 2116 (1996).
20. Powder Diffraction File (Joint Committee on Powder Diffraction Standards. International Centre for Diffraction Data, Swarthmore, 1989).
21. L. S. Palatnik, M. Ya. Fuks, O. G. Alaverdova, and L. P. Shpakovskaya, Kristallografiya **22** (3), 608 (1977) [Sov. Phys. Crystallogr. **22**, 346 (1977)].
22. Yu. I. Sirotin and M. P. Shaskolskaya, *Fundamentals of Crystal Physics* (Nauka, Moscow, 1975; Mir, Moscow, 1982).

Translated by L. Man

Crystallography Reports, Vol. 47, No. 1, 2002, pp. 145–151. Translated from Kristallografiya, Vol. 47, No. 1, 2002, pp. 156–162.

CRYSTALLOGRAPHIC SOFTWARE

Structure Analysis by Reduced Data. III. Method of Interexperimental Minimization

A. P. Dudka

Shubnikov Institute of Crystallography, Russian Academy of Sciences, Leninskiĭ pr. 59, Moscow, 117333 Russia

e-mail: dudka@crys.ras.ru

Received October 19, 2000; in final form, December 27, 2001

Abstract—Being logically justified, a new algorithm of the interexperimental minimization (IEM) has been formally described. The IEM method is the generalization of the optimization method to the case of several independent measurements and is characterized by the following basic features: (1) the structural model refined is divided into the basic model and the model–perturbation; (2) the goal function of the method has four terms, of which the first two correspond to independent measurements, the third one, to averaged measurements, and the fourth one, to the normalized interexperimental difference; (3) in the IEM refinement, the weighting scheme adequately reflecting the accuracy of the experimental data is automatically formed; (4) the interexperimental minimization method includes the algorithm for reducing interparametric correlations; (5) the basic criterion of the IEM method is the statistical test of reproducibility of the results; (6) the IEM method uses the quantum–mechanical and molecular-dynamics calculations to normalize the experimental data; and (7) the physical reliability of the results obtained upon the refinement by the IEM method also depends on the coupling relations imposed onto the structural and functional parameters. © *2002 MAIK "Nauka/Interperiodica".*

INTRODUCTION

In the first two parts of this article [1–5] dedicated to a new direction in diffraction studies, which we call the synthesis–analysis, we reviewed the published data which indicate the necessity of the appropriate changes in the methodology of the precision structure studies. In short, these reasons can be reduced to the following. First, the level of the relative accuracy of the results already achieved in the experimental studies of highly symmetric crystals has not been improved from the beginning of the 1980s, which is explained by the unchanged experimental conditions and the theoretical models. Second, certain progress in an increase of the level of the result reproducibility is not absolute because of some objective reasons. Third, the correlation errors in the parameters can make the physical properties of crystals calculated from the values of the structural parameters somewhat erroneous (the physical reliability of the structural results and the "structure–property" problem).

It was shown [2, 4] that the use of the new algorithm of the structural synthesis–analysis can considerably (by 30–60%) increase the relative accuracy of the results. The progress is achieved using the conventional experimental setup only because of an increasing number of measurements—it is necessary to make the second independent experiment [1]. It was also shown [5] that the minimization of interexperimental differences increases the level of the result reproducibility.

There are two aspects in the problem of correlation between the refined parameters.

If the model does not take into account some features of the scattering process, the errors of the first order of smallness can arise because of incomplete correspondence of the calculated and the measured structure factors. Such systematic errors can be caused, e.g., by the neglect of the effect of thermal diffuse scattering (TDS) reducing the atomic-displacement parameters, with the correlation coefficients being close to 100%. Most often, this effect cannot be taken into account because of the absence of information on the elastic constants of a crystal. To solve the problem, we used the concepts [6–8] of the profile analysis of reflections to introduce the empirical correction for thermal diffuse scattering. The corresponding program for the integrated-profile analysis had became a prototype of the joint program for primary processing of diffraction data (i.e., the program reducing the measurements to the form corresponding to the expression for the structure factor to be calculated). The first version of this program allowed us to calculate the value of the averaged weighted sound velocity in a crystal from the conventional diffraction data [3].

To reduce the effect of correlations, which are of the mathematical and computational nature (the second order of smallness), we used the refinement of the correlating parameters by different measured data sets and the weighting scheme adequately reflecting the accu-

1063-7745/02/4701-0145$22.00

racy of the experimental data (the interexperimental minimization (IEM) method [2]).

The application of new algorithms has shown their high efficiency. Accumulated experience allows us one to state that the IEM algorithm is quite efficient in the search for the structural solution based on real experimental data. However, the scheme of a new algorithm is rather cumbersome and is of a semiempirical nature, which makes its "reproduction" rather difficult. Below, we consider the formal description of the IEM algorithm based on the least squares (LS) method and show its advantages and the possibility of its comparatively simple implementation.

SUBSTANTIATION OF THE IEM ALGORITHM

First of all, it should be emphasized that the LS and the IEM methods are aimed at different goals. The LS method is aimed at the minimization of the "model–experiment" difference and attainment of the maximum possible relative accuracy (the minimization of the reliability factor). In the simplest case, the goal function in the LS method has the form

$$\Phi = \sum_{i=1}^{n_1} w_i (Y_{i\,\mathrm{obs}} - Y_{i\,\mathrm{calc}})^2 \longrightarrow \min, \qquad (1)$$

where $Y_{i\mathrm{obs}}$ is the ith measurement of the data set with the weight w_i, $i = 1 \ldots n_1$, and $Y_{i\mathrm{calc}}$ is the corresponding calculated quantity obtained with the use of the refined parameters.

However, the criterion of the relative accuracy is only one of the possible minimization criteria. It should be recognized that from the natural standpoint, the criterion of the attainment of the reproducibility and physical reliability of the structural results is more justified. The actual criterion is not the coincidence of the theory and a single experiment, but the coincidence of the theory and a series of independent experiments.

The insensitivity of the LS method to systematic errors in the experimental data is explained mainly by the form of the goal function. In general, the following theorem is valid: the solution of the LS problem for nonlinear functions is not unique [9]. The practical experience also shows that sometimes such a solution can have no physical sense at all.

Since the solution is not unique with respect to the initial data in our possession, we have to search for it with respect to all the possible sets of experimental data. Then, it is possible to state that the general part of the problem solution,

$$\Phi = \lim_{N\to\infty} \frac{1}{N} \sum_{k=1}^{N} \sum_{i=1}^{n_k} w_i^{(k)} (Y_{i\,\mathrm{obs}}^{(k)} - Y_{i\,\mathrm{calc}}^{(k)})^2 \longrightarrow \min \qquad (2)$$

will be unique by construction. For understandable reasons, this problem cannot be solved. Nevertheless, it seems possible to prove the theorem that reads that for any $\varepsilon > 0$, there exists such a value of N that the problem solution differ from solution (2) by less than ε. It seems that the solution can be obtained with sufficient accuracy if the number of the experimental data sets is equal to the number of the parameters to be refined. Moreover, the method can be used euristically because our assumptions are practically justified by the induction method with the consistent use of some additional experimental data sets [4, 5].

Now, let us change the summation order in (2) and rewrite it in a somewhat different form (for a restricted number of experiments)

$$\Phi = \sum_{i=1}^{n \le n_k} w_i \left(\frac{1}{N} \sum_{k=1}^{N} Y_{i\,\mathrm{obs}}^{(k)} - Y_{i\,\mathrm{calc}} \right)^2 \longrightarrow \min. \qquad (3)$$

In expression (3), we made the change $Y_{i\mathrm{calc}} = \frac{1}{N}\sum_{k=1}^{N} Y_{i\,\mathrm{calc}}^{(k)}$, which is valid only if the models corresponding to all the experimental data sets are adequate. However, it is not the case in many practical applications and the summation $Y_{i\,\mathrm{cross}} = \frac{1}{N}\sum_{k=1}^{N} Y_{i\,\mathrm{obs}}^{(k)}$ is incorrect. Hereafter, the subscript *cross* indicates the averaged quantities; the specially obtained average data set with the special weighting scheme $w_{i\,\mathrm{cross}}$ of the dimension $n_{\mathrm{cross}} = n_{j1} \cap n_{j2}$ is called the *cross set*. In particular, different data sets in the structure analysis have *a priori* different energy scales and can also have different values of the effects associated with the real structure of specimens. Thus, it is appropriate to single out from the model the part common for all the experiments and to write (3) in the form

$$\Phi = \sum_{i=1}^{n_{\mathrm{cross}}} w_{i\,\mathrm{cross}} \left(\frac{1}{N} \sum_{k=1}^{N} Y_{i\,\mathrm{obs}}^{(k)\,\mathrm{norma}} - Y_{i\,\mathrm{calc}}^{\mathrm{base}} \right)^2$$

$$= \sum_{i=1}^{n_{\mathrm{cross}}} w_{i\,\mathrm{cross}} (Y_{i\,\mathrm{cross}}^{\mathrm{norma}} - Y_{i\,\mathrm{calc}}^{\mathrm{base}})^2 \longrightarrow \min,$$

where the cross set is defined as

$$Y_{i\,\mathrm{cross}}^{\mathrm{norma}} = \frac{1}{N} \sum_{k=1}^{N} K_w^{(k)} Y_{i\,\mathrm{obs}}^{(k)\,\mathrm{norma}},$$

$$w_{i\,\mathrm{cross}} = f(w_i^{(k)}, Y_{i\,\mathrm{obs}}^{(k)\,\mathrm{norma}}),$$

whereas the values of *interfactors* K_w ($K_w^{(1)} \equiv 1$) play the role of the criteria of the accuracy of the experimental data reduction to the common scale.

SEPARATION OF THE MODEL INTO THE BASIC MODEL AND THE MODEL–PERTURBATION

Thus, there are physical reasons for separating the structural model into the basic model (common for all the data) and the additional model–perturbation. Then, $Y_{i\,\mathrm{calc}}^{\mathrm{base}}$ has the same meaning as $Y_{i\,\mathrm{calc}}^{(k)}$ but depends on the smaller number of parameters. On the contrary, now, $Y_{i\,\mathrm{obs}}^{(k)\,\mathrm{norma}}$ is not the initial measured quantity but the function of the parameters of the model–perturbation.

It is expedient to construct the basic model (considered in the structure analysis) using the parameters of the kinematical model of scattering from an ideal defect-free crystal (the atomic coordinates and the displacement parameters of the atoms, the coefficients of multipole expansion). In this case, the parameters of the model–perturbation are the scale factor, the extinction parameters, the dimensions and the composition of the crystal necessary for the precision allowance for absorption, the efficiency of the monochromator for allowance for the radiation polarization, the ratio of the microtwinning partners, the parameters of thermal diffuse scattering (the sound velocity or the elastic constants), the characteristics of the superstructure, the occupancies of the positions for impurity atoms, any other defects inherent in the crystal structure or composition, etc. In fact, the separation of the groups of parameters can also be made based on any other characteristic. For example, in such a way that highly correlating parameters would belong to different groups. Or else, in such a way that one group would include the parameters which are the coefficients of a higher-order expansion (isotropic–anharmonic displacements, core–multipole coefficients, etc.).

Under certain conditions, the separation of parameters can be rather formal.

Then it is necessary to verify experimentally the assumption that the attainment of a given degree of solution reproducibility can be attained with the use of only two independent data sets and to perform several runs over the number of possible variants of the model separation. In this case, it is necessary to minimize not only the difference between the average measurements from the basic model, but also the differences between the average measurement and each normalized measurement, namely, the function

$$\Phi_{\delta_1} = \sum_{k=1}^{N}\left(\sum_{i=1}^{n_{\mathrm{cross}}} w_{i\,\mathrm{cross}}\left(Y_{i\,\mathrm{cross}}^{\mathrm{norma}} - Y_{i\,\mathrm{obs}}^{(k)\,\mathrm{norma}}\right)^2\right) \longrightarrow \min.$$

GOAL FUNCTION IN THE INTEREXPERIMENTAL MINIMIZATION METHOD

Thus, for the case of two independent experimental data sets of the dimensions n_1 and n_2, the goal function in the IEM method is written as a sum of four terms

$$\begin{aligned}\Phi &= \Phi_\alpha + \Phi_\beta + \Phi_{\mathrm{cross}} + \Phi_\delta \\ &= \alpha\sum_{i=1}^{n_1} w_i^{(1)}\left(Y_{i\,\mathrm{obs}}^{(1)\,\mathrm{norma}} - Y_{i\,\mathrm{calc}}^{(1)\,\mathrm{base}}\right)^2 \\ &+ \beta\sum_{i=1}^{n_2} w_i^{(2)}\left(Y_{i\,\mathrm{obs}}^{(2)\,\mathrm{norma}} - Y_{i\,\mathrm{calc}}^{(2)\,\mathrm{base}}\right)^2 \\ &+ \gamma\sum_{i=1}^{n_{\mathrm{cross}}} w_{i\,\mathrm{cross}}\left(Y_{i\,\mathrm{cross}}^{\mathrm{norma}} - Y_{i\,\mathrm{calc}}^{\mathrm{base}}\right)^2 \\ &+ \delta\sum_{i=1}^{n_{\mathrm{cross}}} w_{i\,\mathrm{cross}}\left(Y_{i\,\mathrm{obs}}^{(1)\,\mathrm{norma}} - K_w Y_{i\,\mathrm{obs}}^{(2)\,\mathrm{norma}}\right)^2.\end{aligned} \tag{4}$$

The extension to the case of an arbitrary number of experiments meets no difficulties. Traditionally, the diffraction data have some "gaps," but, of course, it is possible to collect the experimental data in such a way that all the measurements of one data set would have the correspondent measurements in another experimental data set. Hereafter, we assume that this condition is met, so that $n_1 = n_2 = n_{\mathrm{cross}} = n$.

The first two terms of the above function are the traditional LS-functionals written in the explicit form indicating that it is just the measured and not the calculated structure factors that are modified by the scale factor and the extinction effect. Thus, already at the initial stage of the study even in the case of the insufficiently good initial approximation, the IEM algorithm coincides with the LS one ($\gamma = \delta = 0$).

The third term or the cross functional is responsible for the calculation of the basic parameters from the cross set data; in other words, the basic model should satisfy the whole set of the experimental data.

The forth term or the δfunctional "directs" the search for the global minimum in a way to achieve the minimization of the interexperimental difference. Moreover, the δ-functional can also be written in the alternative form when the difference of the individual data sets and their averaged values are minimized

$$\Phi_{\delta_2} = \delta\frac{1}{N}\sum_{k=1}^{N}\sum_{i=1}^{n} w_{i\ \mathrm{cross}}\left(Y_{i\ \mathrm{cross}}^{\mathrm{norma}} - Y_{i\ \mathrm{obs}}^{(k)\,\mathrm{norma}}\right)^2,\quad N = 2.$$

At the last stages, only two last terms "work" ($\alpha = \beta = 0$), because they include the measurements reduced to the absolute scale, the adequate weighting scheme, and the cross set possessing the highest accuracy not

attainable by any other experimental or computational methods. The latter statement should be understood in the sense that the application of the IEM algorithm to the already collected data can do nothing but improve the final results.

The parameters of the basic model are varied in the cross functional, whereas the parameters of the model–perturbation, in the δ-functional. At the first stages, all the parameters in the α and β-functionals are varied, whereas, at the later stages, only the parameters of the model–perturbation are varied. In the general case, the coefficients α, β, γ, and δ can also be refined as parameters.

MODIFICATION OF THE WEIGHTING SCHEME

The necessity of refining the weighing scheme in the measurements is determined by the choice of the goal function. Indeed, the minimization of the cross functional requires the calculation of the weights of the cross set proceeding from the standard parameter uncertainties for individual reflections. The additional possibility for the creation of the weighting scheme adequately reflecting the accuracy of the experimental data is the minimization of the δ-functional. For measurements containing only random errors, the set of the normalized experimental errors (the terms under the sum sign in Φ_δ) should have the standardized normal distribution (which follows from the central limit theorem [10]). The fulfillment of this requirement results in the random character of the error distribution in the cross set and provides the refinement with $\chi^2 \approx 1.0$ for the qualitatively adequate structure models [1]. In this process, no preliminary information on the model is used.

REDUCTION OF THE EFFECT OF INTERPARAMETRIC CORRELATIONS

The efficiency of the above algorithm has been analyzed theoretically [2] and then verified practically [2, 4]. In essence, the method reduces to the refinement of the correlating parameters of different experimental data sets. For example, the extinction parameters are calculated by minimizing the interexperimental differences (the δ-functional), whereas the atomic displacement parameters, by minimizing the cross functional.

This approach not only provides a solution for certain shortcomings inherent in the LS method, but also allows one to include into the refinement process a group of additional parameters whose joint refinement was not possible earlier because of their mutual correlations.

Thus, using the δ-functional, one can refine the following: (a) the dimensions of the crystalline specimens used for the calculation of absorption and extinction; (b) the value of the efficiency coefficient of a diffractometer monochromator (the quantity used to take into account this effect is usually known only approximately); (c) the value of the averaged weighted sound velocity, which later would allow the refinement of the characteristics of isotropic thermal diffuse scattering together with the atomic displacement parameters; and (d) the unit-cell parameters of the crystal within the errors of their determination from the diffractometric data. Moreover, we also hope that it would be possible to determine the anisotropy of polarization effects [11] from conventional diffractometric data. The use of reflections obtained in symmetrically independent regions of the reciprocal space as individual experimental data sets can also be promising for studying anisotropy in the properties of crystalline specimens.

REPRODUCIBILITY OF RESULTS AND OTHER MINIMIZATION CRITERIA

The IEM algorithm is aimed at improving the reproducibility of the results obtained. It minimizes the interexperimental differences. The criteria of the quantity reproducibility are given by the mathematical statistics. We suggest the use of the universal and obvious test based on the Abrahams–Keve normal probability plots [12]. The accuracy of the correspondence to the scale of the basic model can be estimated from the deviation of the *interfactor* (K_w) from unity. The degree of the interexperimental agreement can be estimated from the corresponding reliability factors [1, 2]. Some other possible criteria were considered in [5].

NORMALIZATION OF EXPERIMENTAL DATA

The experimental data can be normalized by at least five different methods. In the general case, the determination of the normalizing factor can require the solution of a rather complicated problem.

1. The simplest and most accurate method is the *analytical* one. The data can be normalized if a nonlinear multiparametric function (structure factor dependent on *p* parameters) is represented as a product of single-parametric functions of the type

$$Y_{\text{calc}}(x_1 \ldots x_p) = \prod_{j=1}^{p} y_j(x_j).$$

The factorization of the initial function depends on the real needs associated with singling out the contribution from the model parameters under consideration. Normalization to the number of most critical parameters for a stable refinement is performed by the analytical method. Normalization to the scale factor and the extinction effect is performed in the conventional way.

In the general case, it is useful to obtain the expansion in orthogonal functions,

$$Y_{\text{calc}}(x_1 \ldots x_p) = \prod_{j=1}^{p} y_j(x_j, \theta_{jk}),$$

where θ_{jk} are certain fitting parameters. For normalization, it is sufficient to make a fitting expansion, e.g., into Chebyshev polynomials. However, it is desirable to select the function type in such a way that the number of the additional parameters would be minimal and the results of the expansion would have clear physical interpretation.

2. The *computational method* can yield only approximated values of the normalizing factor, but the method is simple and universal. The normalized structure factor is obtained as the ratio of the calculated structure factor with due regard for the perturbation, to the factor $Y'_{i\,\text{calc}}$ without the allowance for this perturbation, $Y_{i\,\text{calc}}$, as

$$Y_{i\,\text{obs}}^{\text{norma}} = \frac{\sum_i Y'_{i\,\text{calc}}}{\sum_i Y_{i\,\text{calc}}} Y_{i\,\text{obs}} = k_{\text{norma}} Y_{i\,\text{obs}}.$$

The above ratio is valid to the extent to which one can ignore the correlations between the parameters.

3. *Mathematical method* is also universal, but can be used only for small perturbations of the model, e.g., in localization of impurities or defects. The structure factor is expanded into series in the parameter x analyzed at the point corresponding to the basic model,

$$Y'_{\text{calc}} = Y_{\text{calc}}|_{\text{base}} + \partial Y_{\text{calc}}/\partial x_j|_{\text{base}} \Delta x_j + \ldots,$$

and then k_{norma} values are calculated.

When using experimental data in the normalization, we expect that the invocation of the data calculated by the molecular dynamics and quantum mechanical methods would also be very useful. On the other hand, since the cross sets consist of highly accurate data, they, in turn, can be used for the verification of the data calculated by these methods as well.

4. *Molecular dynamics* (MD) method of numerical experiments with moving molecules has been developed quite well, including its application to crystals [13]. Thus, in principle, the problem of comparative calculations for structures of ideal defect-free crystals and crystals with defects is solvable. At present, the accuracy of the MD computations is determined mainly by the accuracy of the description of atomic interactions.

5. *Quantum-mechanical* (QM) method can be used, first, for calculating potentials of atomic interactions [14] (for the MD method); second, for the *ab initio* calculations of the crystal structures (the theory of the density potential [15, 16]); and, third, for detalization of the scattering process and modification of the formula of the structure factor.

The high efficiency of the analytical normalization method is uniquely indicated by the considerable reduction of the interexperimental reliability factors [2, 4]. One cannot state *a priori* which of the possible normalization methods would provide the best interexperimental agreement. The preliminary data indicate that computational normalization reduces the interexperimental reliability factors if the model–perturbation has from three to eight additional electrons (in comparison with the basic model) per one thousand electrons.

PHYSICAL RELIABILITY OF RESULTS

The physical reliability of the results can readily be verified if some structural parameters or their functions can be obtained by the independent nondiffraction physical methods. Unfortunately, this is possible only for some crystals.

To satisfy the criterion of the physical reliability is more difficult than the reproducibility criterion because the problem is complex and its solution requires the fulfillment of at least three conditions. First, some physical characteristics of the crystal analytically related to the structural parameters should be measured. Second, the scattering process should be described fully and adequately. Obviously, the results are statistically valid only if the parameters only slightly influencing the value of the structure factor are determined with a high accuracy. And, third, the parameters should not be distorted by mutual correlations. Although the development of the theory of radiation scattering is beyond structural synthesis–analysis, the practical application of various multiparametric models in combination with this method would yield the best results, because, as has already been indicated, the IEM algorithm considerably reduces the effect of mutual parameter correlations refined by different data sets with the weighting scheme adequately reflecting the accuracy of the experimental data; in other words, because the third condition is fulfilled to a large degree.

If the first two conditions (having no direct relation to the structural synthesis–analysis) are also met, one can make another step in modifying the IEM algorithm in order to ensure the automatic fulfillment of the criterion of the physical reliability of the atomic-model parameters.

Let a value characterizing a certain physical property, *1*, and the analytical expression relating it to the atomic structural parameters be known. Then, according to the "structure–property" method, the refined results are considered to be reliable if it is possible to attain a sufficiently good coincidence between the calculated and measured properties *1*. In fact, we use here not an algorithm providing a good result, but the trial and error method.

Within the IEM approach, this leads to a rather promising method "property *1*—structure—property *2*." The above analytical expression is used directly for the model refinement as a coupling equation for the atomic-structure parameters. Attributing a number of parameters to the reference point, we also change the values of the remaining parameters related to the first ones by mutual correlations; moreover, these values are consistent with physical property *1*. Thus, most of the structural parameters become physically reliable and can now be used for calculating physical property *2* (in particular, to verify the efficiency of the above algorithm or calculate the crystal characteristics that cannot be measured directly).

The existence and the form of the analytical coupling equations are dependent on each concrete crystal. As an example, consider the relation between the atomic displacement parameters and some thermodynamic characteristics of sphalerite-type crystals.

Using the experimental dependence of specific heat on temperature, one can calculate the Debye temperature. The equation relating the atomic displacement parameters and the Debye temperature for such crystals can be found in [17]. On the other hand, knowing the values of the root-mean square deviation of atoms, one can calculate a number of thermodynamic characteristics, e.g., the activation energy of vacancy formation [18, 19] or the normal elasticity modulus [20].

CONCLUSION

The test of the IEM algorithm on crystal structures of two types with the use of eight experimental data sets proved its high efficiency [1, 2, 4, 5]. Suffice it to say that the refinement of the structure model of a low-symmetric alexandrite crystal yielded an extraordinarily high relative accuracy $R/R_w \sim 0.55/0.45\%$ over 750–900 reflections, whereas the traditional LS procedures yielded only $R/R_w \sim 1.0$–1.5% over 1000–1500 reflections [4].

If the solution of the optimization problem exists, it is logical to expect that, under certain initial conditions, various methods (the LS, least moduli [9], material point [21] simplex [22], Monte-Carlo [23] methods, etc.) would give a certain approximation to this solution (with a certain error). At the same time, in principle, minimization of expression (4) can yield a solution (and not only with respect to the error) different from such an approximate solution. Therefore, one can state that, in terms of computational mathematics, the IEM method provides the creation of a new class of minimization algorithms, which not only compare the experimentally measured and theoretically calculated values, but also the values of different measured data sets. Thus, the method described in this article should be called the interexperimental minimization by the least square method (IEM-LSM). Using the analogy, it is also possible to use the terms EM-LM, MM-simplex, etc. methods.

The successful use of the IEM algorithm requires the normalization of the experimental data and the analysis of the interexperimental and the intermodel differences, which can be either larger or smaller than the model–experiment difference. Thus, in terms of physics, the IEM is a new method for constructing models of various physical phenomena. The normalization of experimental data is, in fact, an instrument for the *quantitative* verification of new theories of radiation scattering and the methods of theoretical calculation of crystal structures. Singling out the contribution of the concrete detail of the scattering process from the total structure factor, one can determine whether this detail is described appropriately or not prior to the creation of the exact general theory of scattering.

It should be emphasized that the separation of the model to be refined into the basic model and the model–perturbation, normalization of the experimental data, and the necessity of using cross sets are the results of the attempt to obtain the unique solution of the minimization problem, i.e., of the attempt to obtain reproducible results by using different experimental setups. The further formalization of the normalization procedure should increase the field of the IEM application—it would be possible to consider minimization over groups of measurements. The criterion for creating such groups (normalization) should preferably be selected based on physical reasons, but the analytical, computational, and mathematical methods of normalization are also sufficiently abstract.

In application to structure analysis, the last statement can be illustrated by the following reasoning. What is the difference between the integrated intensities of the same reflection from two different data sets? The answer is their scale factors, the fraction of various effects, e.g., extinction, and the influence of impurities and defects. All these characteristics can be refined upon normalization of the experimental data in the course of minimization of the interexperimental difference. What is the difference between the intensities of two equivalent reflections in one data set? Their energy scale is the same and, on the whole, the "levels" of the extinction effects are also equal. Thus, the differences between their intensities can be caused only by some anisotropic effects. In other words, there is the possibility of determining the differences in extinction, absorption, etc. along different crystallographic directions, whereas the accuracy of the averaged parameters remains the same as in the traditional refinement. What is the difference between the intensities of a reflection measured using different radiations at different temperatures and different external factors? The kinematical expression for the structure factor does not allow the analytical normalization to these effects. However, the solution can be found by the use of the corresponding expansion in orthogonal functions. And, finally, what is

the difference between the intensities of two arbitrarily chosen reflections of one data set? This question cannot be answered, but it is clear that the formulas for the structure factor in this case should be drastically changed.

The implementation of the algorithm differs from expression (4) in that no full-matrix refinement is needed. In the δ-functional, only the *interfactor* is varied. Obviously, these features reduce the efficiency of the respective computations. We hope to overcome the above shortcomings in the third version of the program.

ACKNOWLEDGMENTS

The author is grateful to M.Kh. Rabadanov, A.K. Ivanov–Shitz, and V.E. Dmitrienko for useful consultations without which this study would not be complete and expresses the hope for further cooperation. The author is especially grateful to B.M. Shchedrin, whose severe but benevolent criticism helped him to correct some mistakes and provided more exact formulation of some terms.

REFERENCES

1. A. P. Dudka, A. A. Loshmanov, and B. P. Sobolev, Kristallografiya **43**, 605 (1998) [Crystallogr. Rep. **43**, 557 (1998)].
2. A. P. Dudka, A. A. Loshmanov, and B. A. Maksimov, Kristallografiya **43**, 613 (1998) [Crystallogr. Rep. **43**, 565 (1998)].
3. A. P. Dudka, A. A. Loshmanov, and B. A. Maksimov, Poverkhnost, No. 2, 28 (2001).
4. A. P. Dudka and A. A. Loshmanov, Kristallografiya **46** (3), 565 (2001) [Crystallogr. Rep. **46**, 511 (2001)].
5. A. P. Dudka and A. A. Loshmanov, Kristallografiya **46** (6), 1135 (2001) [Crystallogr. Rep. **46**, 1049 (2001)].
6. V. A. Strel'tsov and V. E. Zavodnik, Kristallografiya **34**, 1369 (1989) [Sov. Phys. Crystallogr. **34**, 824 (1989)].
7. A. P. Dudka and V. A. Strel'tsov, Kristallografiya **37**, 517 (1992) [Sov. Phys. Crystallogr. **37**, 269 (1992)].
8. A. I. Stash and V. E. Zavodnik, Kristallografiya **41**, 428 (1996) [Crystallogr. Rep. **41**, 404 (1996)].
9. B. M. Shchedrin, I. N. Bezrukova, and E. M. Burova, in *Program Library for Studying Structure and Composition of Materials by Diffraction Methods* (Mosk. Gos. Univ., Moscow, 1987).
10. G. A. Korn and T. M. Korn, *Mathematical Handbook for Scientists and Engineers* (McGraw-Hill, New York, 1968; Nauka, Moscow, 1984).
11. E. V. Dmitrienko, in *Structure Analysis of Crystals* (Nauka, Moscow, 1996).
12. S. C. Abrahams and E. T. Keve, Acta Crystallogr., Sect. A: Cryst. Phys., Diffr., Theor. Gen. Crystallogr. **27**, 157 (1971).
13. W. G. Hoover, *Molecular Dynamics* (Springer-Verlag, Berlin, 1986), Lect. Notes Phys. **258** (1986).
14. H. Balamane, T. Halicioglu, and W. A. Tiller, Phys. Rev. B **46**, 2250 (1992).
15. P. Hohenberg and W. Kohn, Phys. Rev. **136** (3B), 864 (1964).
16. W. Kohn and L. J. Sham, Phys. Rev. **140** (A4), 1133 (1965).
17. M. G. Shumskiĭ, V. G. Bublik, S. S. Gorelik, *et al.*, Kristallografiya **16**, 779 (1971) [Sov. Phys. Crystallogr. **16**, 674 (1971)].
18. R. H. Glyde, J. Phys. Chem. Solids **28**, 2061 (1967).
19. V. G. Bublik, S. S. Gorelik, and M. D. Kapustina, Izv. Vyssh. Uchebn. Zaved., Radioelektron. **11**, 142 (1968).
20. I. N. Frantsevich, in *Problems of Powder Metallurgy and Materials Strength* (Akad. Nauk USSR, Kiev, 1956), Vol. 3.
21. B. M. Shchedrin, N. V. Belov, and N. P. Zhidkov, Dokl. Akad. Nauk SSSR **170** (5), 1070 (1966) [Sov. Phys. Dokl. **11**, 833 (1967)].
22. G. B. Dantzig, *Linear Programming and Extensions* (Princeton Univ. Press, Princeton, 1963; Progress, Moscow, 1966).
23. N. Metropolis, A. W. Rosenbluth, M. N. Rosenbluth, *et al.*, J. Chem. Phys. **21**, 1087 (1953).

Translated by L. Man

Crystallography Reports, Vol. 47, No. 1, 2002, pp. 152–159. Translated from Kristallografiya, Vol. 47, No. 1, 2002, pp. 163–171.

CRYSTALLOGRAPHIC SOFTWARE

Structure Analysis by Reduced Data. IV. IEM—a New Program for Refinement of Structure Models of Crystals

A. P. Dudka

Shubnikov Institute of Crystallography, Russian Academy of Sciences, Leninskiĭ pr. 59, Moscow, 117333 Russia

e-mail: dudka@crys.ras.ru

Received January 23, 2001

Abstract—A new program for the refinement of models of atomic structures by the X-ray, neutron, and electron diffraction data has been described. The program is based on a special form of the goal function including the term responsible for minimizing the difference between the normalized measurements [the interexperimental minimization (IEM) method] and the adaptive nonlinear algorithm of minimization based on the Lavrent'ev–Levenberg–Marquardt regularization. As a result, it became possible to determine a new solution to the problem different from that obtained by the classical least squares method. To a large extent, the program allows one to overcome the effect of parameter correlations on the procedure of refinement and the results obtained. The test of the program on 17 experimental data sets showed the fast and stable convergence in all the cases. Under the identical initial conditions, the new program provided lower reliability factors for most of the crystals studied. *© 2002 MAIK "Nauka/Interperiodica".*

INTRODUCTION

Earlier [1–4], we suggested refining crystal structure by the new method of interexperimental minimization (IEM). Every user encountered the situation in which the same functional minimum in the least square procedure could correspond to a large number of different sets of parameters to be refined.

The theoretical consideration of the problem [1, 4] showed that a sufficient accuracy of the solution can be attained by changing the form of the goal function used by introducing a term corresponding to the interexperimental difference into it. The initial variants of the corresponding program [1, 2] yielded the results which confirmed the efficiency of the new algorithm. However, the practical implementation of the method turned out to be rather cumbersome because the minimization of different terms of the new functional was performed by various sequentially named programs.

The need for a new program arose in the development and the practical use of the program for extended profile analysis (EPA) [5, 6] in which the initial experimental data (reflection profiles) are divided into the components corresponding to various aspects of radiation scattering. The first-type profiles corresponding to Bragg scattering are recalculated into the integrated intensities and are used for conventional refinement of the structure model, whereas the second-type profiles or the *phenomenon profiles* are used for calculating, e.g., elastic constants of the crystal, and, potentially, can also be used for calculating parameters of real structures (structures with defects) of crystals.

The first computations yielded a considerably reduced value of the average weighted sound velocity in an alexandrite crystal, which then was used to introduce the empirical correction for thermal diffuse scattering (TDS) in the isotropic approximation. This signifies that the "phenomenon profiles" include, in addition to the TDS profile, some other components. It was reasonable to assume that all the significant phenomena and, first of all, the phenomena of the row "TDS—radiation absorption—extinction—crystal defects" should be considered not as individual but as mutually related ones. In the conventional LS procedure, the simultaneous refinement of the TDS and the atomic-displacement parameters is very difficult. The IEM algorithm allows a new approach to the solution of these problems. Thus, it became necessary to design a program for refining the parameters of the above-listed phenomena simultaneously with the structural parameters using the diffraction-reflection profiles. We should like to emphasize an important characteristic feature of this new approach which distinguishes it from other approaches, e.g., from the one described in [7]. The measurements used in such a program are not only the counts of quanta composing the profile, but also the shape of the reflection line (in the extended profile analysis, the TDS parameters are determined only from the regular changes in the shape of the reflection line).

Above, we mentioned only the reasons and possible ways of modifying the methods that can be used in the structure analysis by reduced data. The importance and the significance of the problems formulated above are

1063-7745/02/4701-0152$22.00

obvious as well as its time- and labor-consuming character. Below, we describe the possibilities provided by the third version of the IEM program based on the measurements of integrated intensities.

GOAL FUNCTION AND OTHER FEATURES OF THE ALGORITHM

The IEM method is based on the theorem according to which the solution to the LS problem (for nonlinear functions) is not unique [8], which is confirmed by the experience of the numerous repeated structural studies which show that no results are quite reproducible in the statistical sense.

The attempts of finding the general solution using several different sets of measurements result in the change of the form of the goal function and the inclusion into it of the norm of the interexperimental difference [4]. The extension of the result to an arbitrary number of repeated measurements allows the modification of the goal function to the form

$$\Phi = \Phi_\alpha + \Phi_{cross} + \Phi_\delta$$

$$= \frac{1}{2N}\left\{\alpha\sum_{k=1}^{N}\sum_{i=1}^{n_{cross}} w_i^{(k)}\left(Y_{i\,obs}^{(k)\,norm} - Y_{i\,calc}^{(k)\,base}\right)^2\right.$$

$$+\gamma\sum_{i=1}^{n_{cross}} w_{i\,cross}\left(Y_{i\,cross}^{norm} - Y_{i\,calc}^{base}\right)^2$$

$$\left.+\delta\sum_{j<k}^{N}\sum_{i=1}^{n_{cross}} w_{i\,cross}\left(Y_{i\,obs}^{(j)\,norm} - K_w Y_{i\,obs}^{(k)\,norm}\right)^2\right\},$$

where $Y_{i\,obs}$ is the ith measurement with the weight w_i and $Y_{i\,calc}$ is the corresponding value calculated with the use of the parameters to be refined. Then, either $N = 2, 3, 4, \ldots$ is the number of the independent data sets and n_{cross} is the number of reflections in the region of the intersection or $N = 2, 4, \ldots 48$ is the number of the crystallographically equivalent reflections of only one data set and then n_{cross} is the number of independent reflections. To be able to average these data, one has, first, to reduce them to one scale (i.e., to normalize the superscript *norm* in the above formula). Thus, the whole structure model is divided into two parts—the basis model and the model-perturbation. Then the *cross*-set is defined as

$$Y_{i\,cross}^{norm} = \frac{1}{N}\sum_{k=1}^{N} K_w^{(k)} Y_{i\,obs}^{(k)\,norm},$$

$$w_{i\,cross} = f\left(w_i^{(k)}, Y_{i\,obs}^{(k)\,norm}\right),$$

whereas the values of the *interfactors* K_w ($K_w^{(1)} \equiv 1$) play the role of an accuracy criterion in the reduction of the experimental data to one scale. The equivalent reflections (for only one data set) are normalized to anisotropic effects so that we always have ($K_w^{(k)} \equiv 1$).

The physical sense of individual "links" of the functional was considered in [4], where some other features of the IEM algorithm were also discussed including the automatic formation of the adequate weighting scheme, the algorithm for minimizing the interparametric correlations, the use of the quantum-mechanical and molecular-dynamics computations, the reduction of the structural parameters to the physical scale, etc.

It should be emphasized once again that the introduction of a new goal function is the consequence of the attempt to obtain the unique solution of the minimization problem. In turn, the form of the goal function allows one to obtain the solution that differs from that obtained in the classical LS procedure. This can be seen from experiments (6–9) on alexandrite crystals (see below), in which the scale factors differ by 2% from the initial scale factors with the corresponding changes in the other parameters.

SOLUTION STABILITY

A "stable working" program provides the full-matrix refinement and reduces to a minimum labor-consuming manual operations. The result of the refinement depends, first of all, on how successfully the algorithm "overcomes" the difficulties associated with the correlations between the parameters. The IEM method uses two mutually complementing algorithms to minimize the effect of correlations.

In its essence, the IEM method reduces to the refinement of the correlating parameters by different sets of experimental data. Thus, the extinction parameters are calculated by minimizing the interexperimental differences (the δ-functional Φ_δ), whereas the atomic-displacement parameters, by minimizing the *cross*-functional Φ_{cross}. The efficiency of this algorithm was analyzed theoretically [1] and verified in practice [1, 2].

Another method of diminishing the effect of correlations is implemented in the adaptive nonlinear minimization algorithm with the use of the Lavrent'ev–Levenberg–Marquardt regularization [9, 10]. Hereafter, for the sake of brevity, this algorithm is referred to as the nonlinear LS (N-LS) method.

As is well known, the least square method is one of the methods of local minimization and is rather efficient in the refinement in the vicinity of a local (or global) minimum [11]. If the procedure is started at an arbitrary point and if the correlations between the parameters are rather strong, then the model parameters are characterized by too pronounced displacements along "wrong" directions and, therefore, the refinement process can stop prior to the attainment of the global minimum or can even be interrupted.

In this sense, the most stable LS algorithms are those written in the 1970s–1980s in which the displace-

Illustration of possibilities provided by the IEM program

No.	General data				L-LS	N-LS	New possibilities provided by the IEM method (part 3)		
	crystal	radiation	reference	N_{refl}/N_{par}	R/R_w, %	R/R_w, %	refinement	N_{refl}/N_{par}	R/R_w, %
1	CdTe, 22 C	*X*	[24]	209/9	0.915/0.964	0.891/0.957	N-LS	209/19	0.747/0.874
2	CdTe, 218 C	*X*	[24]	184/9	1.380/1.192	1.290/1.014	N-LS	184/19	1.021/0.840
3	CdTe, 300 C	*X*	[24]	151/9	1.486/1.203	1.426/1.122	N-LS	151/19	1.200/1.018
4	$LiNbO_3$, I	*X*	[25]	635/25	1.590/1.590	1.475/1.543	N-LS	635/29	1.141/1.194
5	$LiNbO_3$, II	*X*	[25]	695/25	1.390/1.510	1.296/1.515	N-LS	695/29	1.067/1.285
6	Al_2BeO_4 : Cr, I	*X*	[2, 3]	1303/41	1.157/1.257	1.153/1.257	IEM (+9)	1270/41	0.729/0.715
7	Al_2BeO_4 : Cr, II	*X*	[2, 3]	1137/41	1.521/1.552	1.516/1.552	IEM (+8)	789/41	0.807/0.688
8	Al_2BeO_4 : Cr, III	*X*	[2, 3]	972/41	1.040/1.003	1.036/1.002	IEM (+6)	931/41	0.739/0.567
9	Al_2BeO_4 : Cr, IV	*X*	[2, 3]	1596/41	0.990/1.122	0.990/1.122	IEM (+8)	931/41	0.639/0.553
10	$La_{0.96}Ba_{0.04}F_{2.96}$, I	*N*	[26]	406/52	2.342/3.018	2.374/3.028	IEM (+11)	363/52	1.462/1.468
11	$La_{0.96}Ba_{0.04}F_{2.96}$, II	*N*	[26]	443/52	2.974/4.282	2.993/4.263	IEM (+10)	363/52	1.462/1.468
12	$Nd_{0.95}Ca_{0.05}F_{2.95}$, I	*N*	[26]	374/52	2.810/3.422	2.905/3.460	IEM (+13)	329/52	1.432/1.610
13	$Nd_{0.95}Ca_{0.05}F_{2.95}$, II	*N*	[26]	412/52	2.695/3.148	2.727/3.113	IEM (+12)	329/52	1.432/1.610
14	MgO, I	*X*	[27]	52/2	1.45/2.44	1.442/1.700	N-LS	52/8	0.986/1.048
15	MgO, II	*E*	[28]	30/5	1.40/1.66	1.201/1.387	N-LS	30/7	1.201/1.387
16	LiF	*E*	[28]	30/4	0.99/1.36	0.907/0.742	N-LS	30/8	0.907/0.742
17	NaF	*E*	[28]	30/5	1.65/2.92	0.766/0.720	N-LS	30/5	0.766/0.720

ments in the parameters are calculated with the aid of the inverted matrix of normal equations. At pronounced correlations, the matrix of normal equations is ill-posed (up to the appearance of zeroth diagonal elements), which excludes the matrix inversion and can result in an abend.

As is well known, modern programs envisage no matrix inversion and the parameter displacements are calculated upon the reduction of the matrix of normal equations to the triangular form (the QR factorization). Such an algorithm is more stable to the effect of correlations between the parameters than the previously used one, but both algorithms are, in fact, the linear least-squares (L-LS) methods.

In linear LS (L-LS) methods, the matrix of derivatives (the Jacobian) is obtained by expanding the nonlinear function (where the calculated structure factor are independent of the model parameters) into a Taylor series in the vicinity of the initial point so that the terms higher than those of the first order are rejected. Therefore, the displacements are determined with considerable errors and the trajectory of the motion toward the minimum is far from being optimal.

In the nonlinearly regularized LS procedure (used in the IEM method), both the above problems—the selection of the direction of the search and the negative effect of the correlations on the degree of matrix conditioning—are solved to a large extent. First, the expansion of the nonlinear function to be minimized takes into account the second derivatives. Second, the Hessian is calculated by the modified Davidon–Fletcher–Powell iteration method not requiring matrix inversion. Third, to avoid unpleasant consequences of possible Hessian singularity, the method uses the additional Lavrent'ev–Levenberg–Marquardt regularization. The test of the algorithm showed its high efficiency.

BRIEF DESCRIPTION OF EXPERIMENTS

The test of the IEM method on 17 experimental data sets (hereafter the experiment numbers are indicated in parentheses) are listed in the table. The first part of table shows the initial results obtained by the L-LS procedure using the following complexes of programs:

1. PROMETHEUS (1–14) [12];

2. DSD (JANA) (10–13) [13] which yields the results coinciding with the results (10–13) obtained by [12];

3. κ-minimization (for electron diffraction data) (15–17) [14].

The second part of table yields the results obtained by the N-LS procedure for the experimental data sets identical to those used for the first part of table and the same sets of the parameters to be refined. For experiments (15–17), no comparison was made because, by different reasons, it was impossible to provide identical conditions for the refinement of the initial and the IEM computations. The models for taking into account

extinction in microtwin components in experiments (10–13) were not quite identical either.

The third part of table demonstrates, first, the possibilities of the program in the refinement of different structure models (of different complexities), which is seen from a larger number of model parameters in the corresponding column (1–5, 14–17); second, the results of the application of the IEM algorithm providing the simultaneous use of two experimental data sets with the additional experiment number being indicated in parentheses (6–13). The number of the parameters to be refined was the same as in the initial computations indicated in the first part of table, but the number of measurements can be reduced (because not all the reflections have the corresponding pair reflection in other data set and because the inconsistent measurements are rejected).

All the structural models except for two were automatically refined within one cycle consisting of four to twelve full-matrix iterations without any analysis of interparametric correlations. Let us define the change in the relative precision of the results as $\delta r = 2(r - r_0)/(r + r_0)$, where $r = R$ or $r = R_w$. At the fixed set of measurements and the fixed set of parameters to be refined, the use of the N-LS procedure alone increases the relative precision by 5 and 4% for R and R_w, respectively (1–5, part 1).

STRUCTURE MODEL IN THE IEM PROGRAM

The IEM program was tested on the following structure models.

1. *Goal function*: refinement by $|F|$ values (1–5, 14); refinement by $|F|^2$ values (6–13, 15–17), and the IEM refinement (6–13). In the refinement by *2*, the *R* factors were recalculated to the form corresponding to $|F|$.

2. *Radiation type*: X-rays (*X*) (1–9, 14), neutrons (*N*) (10–13), and electrons (*E*) (15–17).

3. *Allowance for the additional symmetry*: twinning by (pseudo)merohedral law (10–13).

4. *Effects not taken into account by the kinematical model of diffraction*: extinction correction by Zachariasen (4–9) [15] and Becker–Coppens (1–3, 10–13) [16].

5. *Model of atomic displacements*: isotropic (14–17) and anisotropic (6–9) thermal vibrations, Fourier-transform of the Gram–Charlier expansion of the probability density function up to the fourth (4, 5) and the sixth (1–3, 10–13) orders.

6. *Model of charge-density distribution*: Coppens κ-model (14–17) (9 is not shown) [17].

7. *Elemental composition*: (4–13).

The considerable part of the program deals with the refinement of the position occupancies (4–13). It is well known that these parameters strongly correlate with the displacement parameters of the same atoms, which hinders the refinement. The reduction of the effect of such correlations allowed the refinement of the position occupancies in the following mode: it was possible to impose arbitrary constraints on these parameters, including, nonlinear ones; it was possible to refine both the total and partial occupancies of the positions simultaneously (4, 5); the κ-model provided the description of each impurity atom by its own set of electron shells; and the atoms of the same kind occupying different positions could have either the same or different sets of electron shells (6–9). The IEM algorithm envisaged that the position occupancies could be refined by independent experimental data ($\Phi_{\alpha,\delta}$) at the fixed values of the atomic displacements, whereas the displacement parameters were refined by the cross-set at the fixed position occupancies, which considerable reduced the corresponding correlations.

NONLINEAR LS AND IEM METHODS

Consider the results of experiments (1–5) (computation by the L-LS and N-LS methods) with those of experiments (6–13) refined by the L-LS, the N-LL, and the IEM methods with the use of *linear* LS procedure from [12].

The application of N-LS method to (1–5) allows the considerable approach to the functional minimum. The situation for sets (6–9) is quite different: either there is no improvement at all or the improvement attained is insufficient. The point is that the starting model in all the refinements (for identical crystal) for (6–9) was the same—the model obtained in the best IEM refinement could correspond to the global minimum. Thus, for crystals (6–9), the refinement was started for the model corresponding to E and R_w equal to 0.639 and 0.553%, respectively (the model obtained upon simultaneous averaging (8) and (9)). Therefore, it is not surprising that the minimum decrease in the reliability factors is observed for (6–8), whereas for (9), there is no difference between the data obtained by the linear and nonlinear least-squares procedures. In other words, examples obtained for (6–9) lead to the conclusion that, within a sufficiently close vicinity of the global minimum, the use of the LS or the N-LS algorithm in the further computations yields the same result.

However, the analysis of (10–13) shows that this conclusion should be somewhat modified. First of all, the schemes of the allowance for extinction in the microtwin components in the IEM and in the method suggested in [12] slightly differ (the models are not fully identical). The L-LS refinement for crystals (10–13) is unstable—the correlations attain a value of up to 98%, no full-matrix refinement is possible, and the refinement procedure consists of 52 cycles. The full-matrix N-LS refinement yields somewhat worse results than sorting of all the groups of parameters in the L-LS method, although the refinement process converges quite satisfactorily, especially, for set (13). Thus, under

the above conditions, the N-LS method does not completely overcome the negative effect of interparametric correlations. Using the terminology of the material-point method [18], one can state that, in this case, the "correlation force" turned out to be strong enough to overcome the effect of the "force of gravity" in the refinement and to "lift" the material point from the region of the minimum. The consistent application of the L-LS method reduces the correlations between the parameters to admissible limits and also decreases the "deviation" of the material point from the vicinity of the minimum.

Even more pronounced correlations between the scale factor, the parameters of isotropic thermal displacements, and the occupancies of the valence shells of the atoms were observed in the refinement by (15–17). The full-matrix refinement by the N-LS method yields physically senseless results, but satisfactorily terminates the program at the maximum correlation coefficient 100.00% [(17), occupancies of the shells of a fluorine atom]. Upon the division of all the parameters into two to three groups, we arrived at the physically admissible values of the parameters with the *R*-factors being close to the minimum ones obtained in the full-matrix approximation.

ALLOWANCE FOR ADDITIONAL CHARACTERISTICS OF THE STRUCTURE MODEL

It was shown above that the extremely high values of correlations between the parameters do not affect the refinement procedure by the IEM program. The worst result of such a refinement is the attribution of physically absurd values to parameters. Our experience in the refinement of structure models by various programs led us to the conclusion that in such situations, another equally deep minimum corresponding to physically correct values of the parameters should exist. However, the search for this minimum is somewhat hindered because of the data correlations and errors. In particular, studying data (15), we obtained the initial minimum at the negative parameters of the isotropic atomic displacements, whereas a more thoroughly planned refinement provided the correct solution at equally low *R* factors.

Thus, it is possible to organize the search for additional parameters of structure models. Below, we indicate the additional parameters whose variations can minimize the functional.

1. For crystals (1), the minimum *R* factors are obtained by the refinement of the unit-cell parameter.

2. In the refinement of the structure model by data (1) (a CdTe crystal at 22°C), we obtained the pronounced functional minimum upon the refinement of the correction for anomalous scattering (or, rather, the product of the corrections). The tabulated value of this parameter is 2.0141. The refined value with the allowance for the third-order anharmonicity is equal to –1.0661, with the reduction of the reliability factors *R* and R_w from 1.054 and 1.089% to 0.945 and 0.997, respectively (using 209 reflections). This parameter enters the acentric part of the structure factor and, therefore, the existence of the corresponding minimum of the functional can be explained either by the ignorance of anomalous scattering of a certain impurity atom, the nonspherical nature of the charge density, or else by the improperly detailed anharmonicity of atomic displacements. No matter what causes the additional minimum, it is clear that we obtain a simple and fast method for detecting impurities, nonsphericity or anharmonism without their direct refinement, which would require preparation of much more complicated computations. The introduction into the model of the anharmonism of atomic displacements up to the fourth order (four additional parameters) reduced the reliability factors *R* and R_w to 0.891 and 0.957%, respectively, but the new refinement of the anomalous-scattering coefficient (one parameter) showed that this effect has not completely been taken into account, because the reliability factors *R* and R_w reduced again to the values 0.843 and 0.917%, respectively. The anharmonic model taking into account the values up to the sixth order of magnitude did not result in the complete allowance for this effect either. The study of this effect will be continued within the framework of the model of a nonspherical atom.

3. As was indicated earlier, the IEM method allows the simultaneous refinement of the total and partial occupancies of the positions of impurity atoms. This was confirmed in the refinement by data sets (4,5) and (6–9). In alexandrite crystals (6–9), the introduction of four additional parameters almost did not change the reliability factors, whereas the reduction of the total occupancies by 4–5% was compensated by an increase of the fraction of more strongly scattering Cr atoms, in other words, the total scattering power did not change.

4. Somewhat different situation was observed in Zn-doped $LiNbO_4$ crystals (4, 5). The refinement with the use of four additional parameters reduced the reliability factors *R* and R_w from 1.475 and 1.543% to 1.141 and 1.194% by data (4) and from 1.296 and 1.515% to 1.067 and 1.285% by data (5). The refinement of the fractional occupancies by L-LS method was completed at the *R* and R_w level of 1.163 and 1.219% by data (4) and 1.236 and 1.442% by data (5), but the total occupancy could be determined only by the trial-and-error method.

5. For (9), we determined the functional minimum from the value of the average weighted sound velocity, so that we hope to be able to determine the characteristics of isotropic TDS in the course of the structure-model refinement at unknown values of elastic constants of crystals.

The reduced effect of interparametric correlations allows the introduction into the refinement of some

other parameters which, traditionally, were considered to be crystal or diffractometer constants such as the monochromator efficiency, the radius of a spherical specimen, the characteristics of the primary beam, etc.

The use of experimental data for reflections recorded in the symmetrically nonequivalent regions of the reciprocal space as the individual experimental data sets is also a promising method for studying the anisotropy in the properties of crystalline specimens.

For problems where the possibilities of the N-LS method in the reduction of the parameter correlations on the final results are only limited, the IEM algorithm provides the universal scheme for a solution. According to this scheme, each new parameter is refined by individual (independent) data sets, whereas the parameters correlating with this parameter, by the cross-set [1, 2].

MODIFICATION OF STRUCTURE MODEL

We knew *a priori* that the structure model initially used in the program would be constantly modified because of the use of new parameters to be refined. This fact was taken into account in the following way.

The program consists of two interacting parts—an interface and a minimizing program. The universal program interface, UPI, written in Delphi generates automatically a system of menus for the input of the initial data into the minimizing program [19]. To facilitate the compatibility with numerous libraries of programs for scientific and technological computations, the second part of the mimimizing program is written in FORTRAN-90.

The main algorithm [9, 10] almost does not limit the initiative of the user both in increasing the speed of computations and in modifying the model. To modify the structure model, one needs only to code the algebraic expression of the structure factor, because there is no need to calculate the derivatives in the explicit form, because they are calculated from the finite differences during the program execution. To increase the computations speed, it is sufficient to introduce a "branch" for analytical calculation of the Jacobian.

In this context, it is very important to impose the appropriate constrains onto the parameters. In doing so, the most general method of solving the minimizing problem is the Lagrange principle of lifting these constraints [20, p. 253]. However, the practical application of this principle in the structure analysis is limited by an increasing number of variables. Therefore, it is more convenient to use the constraints in the explicit form, which reduces the problem dimension. The solution of the problems for linear constraints is considered in [21, p. 609]. In the IEM method, the constraints are treated even easier: if the constraints are nonlinear, then, similar to the case of the structure factors, one has to set the analytical expression for the constraints in a special subprogram (the linear constraints are taken into account by the universal method). The program also envisages the constraints imposed in the form of inequalities.

The above characteristics of the program structure allowed fast coding of a rather detailed structure model.

SERVICE AND OTHER POSSIBILITIES OF IEM PROGRAM

The service possibilities of the program are understood as the methods of setting the input information, representation of the final results, and convenient use of the program. In this sense, the UPI flexibility is the most important characteristic. For the user, the IEM program is represented in the standard of the operational system MS Windows with the system of menus and hot keys. The only difference is that the UPI menus are dynamical, their configurations are self-adapting to the structure model used and other software. The minimizing is performed by one of the interface-controlled programs. Thus, the software consists of a number of computational and service programs. The fact that the UPI is written in Delphi provides its easy integration into the system of the Active X and the COM elements (and, first of all, the graphical and service ones) and, on the other hand, the use of FORTRAN-90 as the basic language in programming numerical computations allows the adaptation of the software developed by other programmers.

The computations within the program are performed with double accuracy, all the information is stored in the random-access memory, and the dimension of the problem is limited only by the computer configuration.

The IEM method uses a number of nontraditional criteria of refinement of which the main one is the *interfactor* value [1, 4]. The evaluation of the effect of individual measurements on the final results is made by the method of regression analysis.

EFFICIENCY OF THE IEM PROGRAM

Today, the N-LS [9, 10] seems to be the most efficient algorithm for local minimization over the real experimental data (the sum of residues is rather large [21, p. 600]). The comparison of parts 1 and 2 of the table shows that the relative accuracy of the results calculated by this algorithm increases by approximately 5%. However, the comparison of parts 2 and 3 of the table shows that the IEM algorithm for the same models and the same initial approximations yields the results with a considerably higher (by 30 to 60%) relative accuracy.

This can be explained by the influence of the measurement errors on the final results. Both linear and nonlinear least squares methods are sensitive to the errors in the experimental data. The refinement yields the more correct results and uses the more adequate weighting scheme, which reflects the errors in the ini-

tial data, with the other conditions being the same. In short, the *equally accurate measurements should give equal contributions into the goal function*. If both strong and weak reflections measured with the same accuracy are to affect equally the minimization, their weights should be inversely proportional to the integrated intensity. If the intensities of these reflections are distorted (e.g., by extinction), the ratio of their weights should be modified. This example alone helps one to understand that the use of the adequate weighting scheme in the traditional refinement depends on scientist's intuition, because it is impossible to take into account all the possible sources of errors.

The methods for estimating the standard uncertainties of reflections are considered in a large number of publications. The new nomenclature of statistical descriptors introduced by the International Union of Crystallography [22] only slightly facilitated the practical work. Our studies show that no universal solution of this problem has yet been found. The IEM algorithm provides a solution based on the methods of mathematical statistics, which allow more appropriate interpretation of the experimental data.

Insufficient attention given to the problem of correct evaluation of measurement errors (it is commonly believed that it is more important to obtain the exact data, improve the statistics of calculating quanta, etc.) results in a paradoxical situation. Let us assume that the experiment quality is inversely proportional to the *R*-factor of the refinement. Then, the analysis of data (6–13) leads to two following conclusions: (a) the IEM algorithm always provides the improvement of the results obtained by the LS method and (b) the addition of the data of a low-quality experiment to the data of a high-quality one reduces the reliability factors, which is most clearly seen for data (9) supplied with data (7) indicated in the table as (9) + (7) and the corresponding reliability factors $R/R_w = 0.872/0.810$. These conclusions would be paradoxical if we combined only the measurements, but the IEM method also uses the standard uncertainties of these measurements. The accuracy of the data cannot be increased by any subsequent mathematical treatment, but the correct treatment, especially for an increased volume of the initial information, allows one to extract those results from the initial data which better correspond to the physical reality. Often, it is more important to estimate adequately the accuracy of the experimental data (which is provided by the additional use of low-quality experiments) than to increase the relative accuracy of the data by increasing the time of the measurements.

IEM AS AN OPTIMIZATION METHOD

The information on the crystal structure is contained in each individual reflection. However, it is impossible to extract the structure model based on only one measurement. One can state that there exists only two methods based on different algorithms for constructing the structure model from the experimental data.

Consider either the linear or the nonlinear problem in the close vicinity of the minimum upon its linearization in this vicinity. As is well known, in this case, the calculation of the *p*-parameters of the model requires *p* measurements and the unique solution of the system of *p* equations with *p* unknowns (for simplicity, the case of inconsistent measurements is not considered). It is clear that the problem is not always solvable and that, in the general case, other *p* measurements would yield other solutions. Here, for the first time, we encounter the nonunique solution, which depends on the choice of the data used for its determination (the errors in the initial data).

If the solution depends on the measurement errors, it should be averaged *over all* possible errors. The corresponding definition of the notion of a solution was suggested by Gauss in 1794. This resulted in the creation of the least squares method providing the determination of a new type of solution in cases where the number of measurements, *n*, exceeds the number of unknowns, *p*, and the sum of the residues differs from zero. Geometrically, the LS method can be interpreted as the minimization of a certain quantity (norm) upon the projection of a multidimensional vector of the data onto the space of solutions of a lower dimension [23]. Two hundred years of the use of the LS method proved its high efficiency. The main difficulty in its application is associated with the fact that not all the possible errors are averaged. The difficulty lies not only in the nonunique solution obtained by the LS method with respect to *possible* systematic errors in the experimental data. The solution is also nonunique with respect to the whole set of the destabilizing factors in the row "errors in the data—errors in the estimate of these data–correlation between the parameters," i.e., it is practically always nonunique.

The IEM method is the generalization of the LS (or another minimization method) in which the solutions are averaged over a large number of the error sources. In this case, the dimension of the vector of measurements does not increase, instead a new subspace of the vectors of interexperimental differences is introduced, and the minimization of the norm of the interexperimental vector is also performed along with minimization of other factors. In terms of geometry, the IEM method uses the solution-vector decomposition in the basis of measurements. It is clear that if the experimental data sets are independent and the basis is orthogonal, the effect of the systematic errors on the solution presents no problem any more. The reduction of the effect of other unfavorable factors is not so obvious, but our studies confirm this conclusion both theoretically [1, 4] and experimentally [2, 3]. A practically interesting case is presented by partly independent data. In this instance, the study is performed using only one set of the experimental data, and the role of individual mea-

surements is played by the sets of symmetrically independent reflections. In this case, the possibilities of the IEM method are rather limited and determined by the angle formed by the measurement vectors and the difference in the projections of the phenomenon under study (i.e., of some parameters of the model) on to these vectors. Under favorable conditions, this method provides a more accurate determination of anisotropy of some phenomena accompanying Bragg scattering.

Thus, we have shown the high efficiency of the IEM program. Of course, the program requires further verification and its test on various experimental data. We plan the further improvement and modernization of the program and call for cooperation with all those who are interested in the problem considered above. The program can be obtained from the author free of charge.

ACKNOWLEDGMENTS

The concept of the structure analysis by reduced data, on the whole, and the method of interexperimental minimization, in particular, were formulated by the author following discussions with his colleagues A.A. Loshmanov, V.N. Molchanov, M. Kh. Rabadanov, N.B. Bolotina, B.A. Maksimov, and V.L. Nosik. The third version of the IEM program would not have been possible without the fruitful consultations and help of V.V. Volkov. The consultation on the problems of electron diffraction and distribution of the charge density was given by G.G. Lepeshov and A.S. Avilov. The author is grateful to them all and hopes for their further cooperation. The author is also grateful to L.I. Man for her careful reading of the manuscript, valuable remarks on terminology and notation, their consistency throughout the article, and translation of all the articles into English. Special thanks go to B.M. Shchedrin, whose consultations provided more rigorous formulations of the basic notions of the IEM method and the establishment of its place among other minimizing methods.

REFERENCES

1. A. P. Dudka, A. A. Loshmanov, and B. A. Maksimov, Kristallografiya **43**, 613 (1998) [Crystallogr. Rep. **43**, 565 (1998)].
2. A. P. Dudka and A. A. Loshmanov, Kristallografiya **46**, 565 (2001) [Crystallogr. Rep. **46**, 511 (2001)].
3. A. P. Dudka and A. A. Loshmanov, Kristallografiya **46**, 1135 (2001) [Crystallogr. Rep. **46** (6), 1049 (2001)].
4. A. P. Dudka, Kristallografiya **47** (1), 156 (2002) [Crystallogr. Rep. **46** (1), 145 (2002)].
5. A. P. Dudka, A. A. Loshmanov, and B. A. Maksimov, in *Proceedings of the 2nd National Conference on Application of X-rays, Synchroton Radiation, Neutrons and Electrons for Study of Materials (RSNE), Moscow, 1999*, p. 33.
6. A. P. Dudka, A. A. Loshmanov, and B. A. Maksimov, Poverkhnost, No. 2, 2833 (2001).
7. D. Schwarzenbach and H. D. Flack, Acta Crystallogr., Sect. A: Found. Crystallogr. **47**, 134 (1991).
8. A. N. Tikhonov and V. Ya. Arsenin, *Solutions of Ill-Posed Problems* (Nauka, Moscow, 1979, 2nd ed.; Halsted Press, New York, 1977).
9. J. E. Dennis, D. M. Gay, and R. E. Welsch, ACM Trans. Math. Softw. **7** (3), 348 (1981).
10. J. E. Dennis, D. M. Gay, and R. E. Welsch, ACM Trans. Math. Softw. **7** (3), 369 (1981).
11. B. M. Shchedrin, I. N. Bezrukova, and E. M. Burova, in *Library of Programs for Study of Structure and Properties of Materials by Diffraction Methods* (Mosk. Gos. Univ., Moscow, 1987).
12. U. Zucker, E. Perenthaler, W. F. Kuhs, *et al.*, J. Appl. Crystallogr. **16**, 398 (1983).
13. V. Petříček, *SDS94* (Institute of Physics, Prague, 1994).
14. A. K. Kulygin, G. G. Lepeshov, and A. S. Avilov, in *Proceedings of the Russian Conference on Electron Microscopy, Chernogolovka, 1998*, p. 105.
15. W. H. Zachariasen, Acta Crystallogr. **23**, 558 (1967).
16. P. J. Becker and P. Coppens, Acta Crystallogr., Sect. A: Cryst. Phys., Diffr., Theor. Gen. Crystallogr. **30**, 129 (1974).
17. P. Coppens, T. N. Guru Row, P. Leung, *et al.*, Acta Crystallogr., Sect. A: Cryst. Phys., Diffr., Theor. Gen. Crystallogr. **35**, 63 (1979).
18. B. M. Shchedrin, N. V. Belov, and N. P. Zhidkov, Dokl. Akad. Nauk SSSR **170** (5), 1070 (1966) [Sov. Phys. Dokl. **11**, 833 (1967)].
19. A. P. Dudka and V. A. Strel'tsov, Kristallografiya **37**, 517 (1992) [Sov. Phys. Crystallogr. **37**, 269 (1992)].
20. É. M. Galeev and V. M. Tikhomirov, *Optimization: Theory, Examples, Problems* (Éditorial URSS, Moscow, 2000).
21. *International Tables of Crystallography* (Kluwer, Dordrecht, 1992), Vol. C, p. 609.
22. D. Schwarzenbach, S. C. Abrahams, H. D. Flack, *et al.*, Acta Crystallogr., Sect. A: Found. Crystallogr. **51**, 565 (1995).
23. B. M. Shchedrin, *Lectures for Students of Faculty of Physics of Moscow State University: Mathematical Aspects of Processing of the Data of Physical Experiments* (Mosk. Gos. Univ., Moscow, 1996).
24. M. Kh. Rabadanov, I. A. Verin, Yu. M. Ivanov, *et al.*, Kristallografiya **46** (4), 703 (2001).
25. T. S. Chernaya, B. A. Maksimov, and A. V. Arekcheeva, in *Proceedings of the 2nd National Conference on Application of X-rays, Synchroton Radiation, Neutrons and Electrons for Study of Materials (RSNE), Moscow, 1999*, p. 126.
26. A. P. Dudka, A. A. Loshmanov, and B. P. Sobolev, Kristallografiya **43**, 605 (1998) [Crystallogr. Rep. **43**, 557 (1998)].
27. P. L. Sanger, Acta Crystallogr., Sect. A: Cryst. Phys., Diffr., Theor. Gen. Crystallogr. **25**, 694 (1969).
28. V. G. Tsirelson, A. S. Avilov, G. G. Lepeshov, *et al.*, submitted to J. Phys. Chem.

Translated by L. Man

Semiconductors, Vol. 36, No. 2, 2002, pp. 153–156. Translated from Fizika i Tekhnika Poluprovodnikov, Vol. 36, No. 2, 2002, pp. 160–163.

ELECTRONIC AND OPTICAL PROPERTIES OF SEMICONDUCTORS

Influence of Laser Pump Density on the Characteristic Time Constant and the Intermediate-Field Electromodulation E_0 Component of the Photoreflectance Signal

R. V. Kuz'menko*, A. V. Ganzha*, É. P. Domashevskaya*, S. Hildenbrandt, and J. Schreiber****

** Voronezh State University, Universitetskaya pl. 1, Voronezh, 394893 Russia*
e-mail: roman@ftt.vsu.ru
*** Fachbereich Physik der Martin-Luther Universität Halle-Wittenberg, 06108 Halle/Saale, Germany*
Received March 12, 2001; accepted for publication May 25, 2001

Abstract—The influence of the laser pump density L on the intensity and the characteristic time constant of the intermediate-field electromodulation E_0 component of photoreflectance spectra in a direct-gap semiconductor was studied. The experiments were carried out using GaAs samples with carrier concentration $n \approx 10^{16}$ cm^{-3} and laser pump densities in the range $L = 100$ μW/cm^2 – 1 W/cm^2. For all of the samples under study, the logarithmic dependence of the intensity of the electromodulation signal on the laser radiation density was ascertained. No effect of the attendant variations of the characteristic time constant on the measured signal was observed. © *2002 MAIK "Nauka/Interperiodica".*

INTRODUCTION

Photoreflectance (PR) spectroscopy is widely used for studying electronic, optical, and structural properties of semiconductors because of the comparatively simple experimental implementation of the method combined with the great variety of data contained in the spectra. The main body of information can be extracted by intermediate- or low-field measurements of the electromodulation component arising in the region of a direct-gap (valence band)–(conduction band) transition [1]. This component stems from the periodic modulation of the surface electric field under laser irradiation with a photon energy greater than the semiconductor band gap. According to [2–4], the main parameter that defines the spectral line shape and the intensity of the electromodulation signal is the modulation depth of the surface electric field. Thus, laser pump density (LPD) turns out to be one of the most important parameters that affects measurements of the spectra. However, only the low-field components have been considered in the studies on LPD influence reported so far [5–7]. There is little or no information available about the LPD effect on the characteristic time constant of the τ component, which is a first approximation of the delay time between the modulated reflectance signal and the pump [8, 9].

The aim of this study was to gain insight into the LPD influence on the intensity and characteristic time constant of the intermediate-field electromodulation E_0 component. The measurements were conducted at room temperature with the use of the setup described in [10]. Phase analysis (PA) of spectra [9] from GaAs samples ($E_0 = 1.424$ eV [4]) with the carrier concentration $n \approx 10^{16}$ cm^{-3} was carried out with an SR850 two-channel phase-sensitive amplifier (PSA). LPD values (a red He–Ne laser) ranged from 100 μW/cm^2 to 1 W/cm^2. Lower LPD resulted in such a weak signal that it could not be measured without switching the PSA amplification range. In contrast, for LPD exceeding 10 W/cm^2, saturation of the PR signal intensity and phase angle was observed for some of the samples. The modulation frequency was in the range $f = 50 – 500$ Hz, which excluded its influence on the modulation signal being measured.

The line shape of the PR intermediate-field E_0 spectra obtained in experiments agrees qualitatively with that recently published [4]. The one-component character of the spectra was proved by simulations in terms of a generalized multilayer model [4], as well as by plotting the phase diagrams [9].

CHARACTERISTIC TIME CONSTANT

The PR signal measured with a two-channel PSA can be represented as the square root of the sum of the squared components, one of which is in phase with the reference signal and the other is shifted with respect to the reference signal by 90° [9]. However, the intensity of the PR signal may differ from the true value $\Delta R/R(E)$ defined by the parameters of modulation. As was shown in [10], a complex PR signal depends on the cyclic fre-

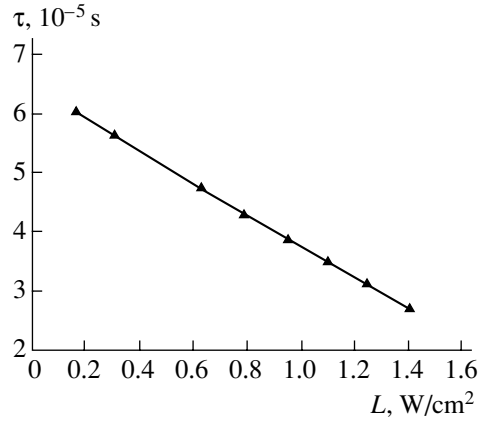

Fig. 1. Characteristic time constant of the electromodulation E_0 component τ vs. laser pump density L. The linear dependence is observed down to $L \lesssim 100$ μW/cm^2 (not shown).

quency $\omega = 2\pi f$, where f is the frequency of modulation, and on the characteristic time constant τ of the component:

$$\frac{\overline{\Delta \mathbf{R}}}{\mathbf{R}}(E, \omega, \tau) = \frac{\Delta R}{R}(E)\frac{1 + e^{-i\pi/\omega\tau}}{1 + \omega^2\tau^2}(1 + i\omega\tau). \quad (1)$$

Thus, a necessary condition for the intensity of the modulation signal obtained in experiment to coincide with its true value is $\omega\tau \ll 1$.

In the context of PA, estimating τ from the phase of delay φ implies a strictly specified time shape of the signal $\Delta R(t)$ during the laser irradiation and after the pump is turned off. One of the most frequently cited models for $\Delta R(t)$ was proposed by Seebauer [8]. According to this model, an increase in the electric field strength under the laser irradiation is due to the drift and recombination of the minority carriers with the majority carriers captured by the surface states of the traps. Since both the recombination and drift of the minority carriers occur within a nanosecond time scale, they cannot ensure a noticeable delay when the density of nonequilibrium carriers is sufficiently high. In contrast, the restoration of the surface charge after the laser pump is turned off implies the capture of the majority carriers and, thus, is characterized by the time constants from the μs–ms interval [11, 12]. Hence, it follows that the time constant of the PR signal after switching the pump off is independent of LPD. According to the model, for $1/\omega\tau \longrightarrow \infty$, we should expect $\varphi \longrightarrow 0$; in the other limiting case of $1/\omega\tau \longrightarrow 0$, $\varphi \longrightarrow 32.48°$ is expected.

Shen *et al.* [13] attribute modulation of the electric field to the interaction of the surface states with the charge carriers of both signs. Recombination with the photogenerated minority carriers reduces the amount of charge at the surface states; concurrently with this, capture of the majority carriers (the so called "restoration" current) occurs. The time required for these two processes to come to equilibrium is the same one that defines τ. This time is governed by the capacitance-related effects in the space charge region (SCR), and for low and intermediate depths of modulation it is expressed as

$$\tau = RC = \frac{dJ_{res}}{dV_s}C = \frac{\varepsilon\varepsilon_0}{d}\frac{kT}{q}\frac{1}{AT^2}\exp\left(\frac{qV_s}{kT}\right). \quad (2)$$

Here, C and R are the capacitance and resistance of the surface–SCR system, respectively; J_{res} is the density of the restoration current; ε is the permittivity; q is the elementary charge; d is the thickness of the space charge layer; k is the Boltzmann constant; T is the temperature; A is the Richardson constant; $V_s = V_{s,0} - V_p$, with $V_{s,0}$ being the surface potential in the absence of irradiation; and V_p is the photovoltage. Since V_s depends on LPD (in terms of V_p), Eq. (2) predicts a decrease in τ with LPD. On the assumption that the time constants for the growth and decay are identical, we derived τ in the following form (see [9, 10]):

$$\tan\varphi = \omega\tau. \quad (3)$$

For the spectra being studied, a decrease in LPD resulted in a reduction in the signal intensity and clockwise rotation of the phase diagram. Rotation of the phase line indicates that the phase angle increases. Since the measurements were carried out without a preset of the PSA phase, the phase angle φ might be determined as the angle between the phase line and the X axis [9]. A certain spread in the phase angle was observed, but it was no greater than a few percent. Although the values of φ obtained in the experiment were within those predicted by the Seebauer model ($\varphi = 5°$–$10°$), the variations observed are sufficient to indicate the failure of this model in the case under study.

In order to check the above-mentioned assumption of equality between the growth and the decay time constants, the dependence $\Delta R(t)$ at a fixed photon energy was read from an oscilloscope for one of the samples. Although the signal shape was only slightly different from a rectangular one, the growth and decay regions displayed a noticeable delay with respect to the pump signal. Visually, the growth and decay of $\Delta R(t)$ were judged to be exponential with approximately equal time constants. This fact allows us to calculate τ from (3). Figure 1 shows the $\tau(L)$ function recalculated for a typical dependence $\varphi(L)$. As is evident from Fig. 1, the thus obtained $\tau(L)$ can be closely approximated by a straight line. In view of the logarithmic dependence of photovoltage on LPD [5, 6], a linear $\tau(L)$ dependence is predicted by (2). This result presents another argument in favor of the Shen model.

The τ values obtained are within the range of $(3–6) \times 10^{-5}$ s. According to formula (1), this means that, for the considered LPD values, the nonzero characteristic time constant does not noticeably affect the measured signal. Therefore, the electromodulation signal intensity obtained in the experiment may be interpreted as a true

value, which is conditioned only by the parameters of the modulation process.

In order to exclude the influence of the laser wavelength, we performed a series of experiments with a blue He–Cd laser (λ = 441.6 nm). No qualitative disagreement with previously obtained results was observed. With the blue-light irradiation, however, the values of τ were smaller, which can easily be explained by shifting the region of nonequilibrium-carrier generation towards the sample surface.

THE $A(L)$ DEPENDENCE

The concept of an amplitude factor A has, thus far, only been introduced for a low-field case, when the spectral line shape depends neither on the electric field strength nor on its modulation depth. As has been shown previously [5–7], this case corresponds to a linear dependence of the electromodulation signal on photovoltage or on a variation in the surface potential ΔV_s. From the logarithmic dependence of ΔV_s on both the current of the photoinduced minority carriers towards the surface J_{pc} and the "restoration" current J_{res}, and from the linear dependence of J_{pc} on L, the logarithmic character of $A(L)$ immediately follows.

For an intermediate-field component, the concept of amplitude factor may be introduced analytically only under the conditions of (i) uniformity of the electric field over the region of PR generation and (ii) complete suppression of this field by the irradiation [14, 15]. In this case, the amplitude factor might be defined as a coefficient of proportionality between the broadened electrooptical G function [15] and the spectral line under investigation. As was previously demonstrated [3, 4], these conditions are actually not satisfiable and the spectral component shape cannot be described by a single analytical expression. Nevertheless, the calculations performed within the generalized multilayer model [4] suggest that, within the interval of the electric field modulation depth $\xi > 0.05$, the line shape, period, and energy position of Franz–Keldysh oscillations remain nearly constant and are defined merely by the electric field in the absence of irradiation and the energy of the electron–optical transition. In contrast, within the interval specified above, the signal intensity only depends on the depth of modulation of the surface electric field. The above considerations justify using the magnitude of Franz–Keldysh oscillations as an amplitude factor for an intermediate-field electromodulation signal.

The dependences $A(L)$ thus determined for several samples are plotted in Fig. 2. As an amplitude factor, the magnitude of the second positive Franz–Keldysh oscillation was used. For a fixed LPD, a considerable sample-to-sample spread of the amplitude factor was observed. Because of this, the results were normalized before being compared. Quantitative analysis indicates that all of the dependences $A(L)$ found in experiments

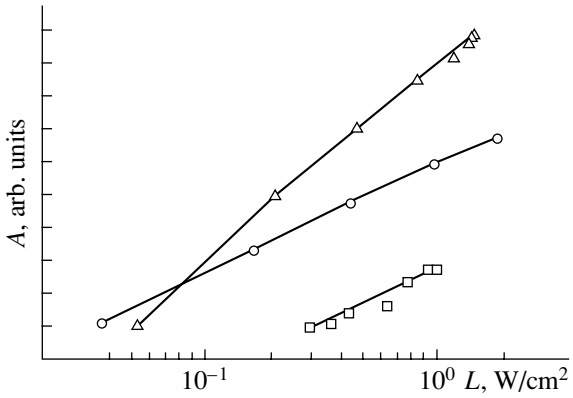

Fig. 2. Typical dependences of the photoreflectance signal on laser pump density $A(L)$ for the three samples studied.

can be well approximated by a logarithmic function. This circumstance led us to the conclusion about a linear relationship between the amplitude factor of the intermediate-field electromodulation signal and the photovoltage or variation in the surface potential ΔV_s within the LPD range considered.

CONCLUSION

To summarize, we would like to remind the reader that this study was aimed at gaining insight into the LPD influence on the characteristic time constant τ and the intensity of the intermediate-field electromodulation component. Varying LPD within the range L = 100 μW/cm^2 – 1 W/cm^2 results in a change in τ. This change, however, has practically no effect on the measured signal. Using experimental data and the results of calculations based on the generalized multilayer model, we introduced a concept of the amplitude factor for the intermediate-field component and proposed a method for determining it. For the samples under investigation, the logarithmic dependence $A(L)$ was established. By comparing the results obtained with those published elsewhere, the amplitude factor of the intermediate-field electromodulation signal was found to be a linear function of photovoltage. We may conclude that the typical response of the intermediate-field component to a change in LPD over a wide range of L values was obtained.

REFERENCES

1. D. E. Aspnes, Surf. Sci. **37**, 418 (1973).
2. H. Shen and M. Dutta, J. Appl. Phys. **78**, 2151 (1995).
3. J. P. Estrera, W. M. Duncan, and R. Glosser, Phys. Rev. B **49**, 7281 (1994).
4. R. Kuz'menko, A. Ganzha, É. P. Domashevskaya, *et al.*, Fiz. Tekh. Poluprovodn. (St. Petersburg) **34**, 1086 (2000) [Semiconductors **34**, 1045 (2000)].
5. R. Ditchfield, D. Llera-Rodríguez, and E. G. Seebauer, Phys. Rev. B **61**, 13710 (2000).

6. E. R. Wagner and A. Manselis, Phys. Rev. B **50**, 14228 (1994).
7. H. Shen, S. H. Pan, Z. Hang, *et al.*, Appl. Phys. Lett. **53**, 1080 (1988).
8. E. G. Seebauer, J. Appl. Phys. **66**, 4963 (1989).
9. A. V. Ganzha, W. Kircher, R. V. Kuz'menko, *et al.*, Fiz. Tekh. Poluprovodn. (St. Petersburg) **32**, 272 (1998) [Semiconductors **32**, 245 (1998)].
10. S. Hildebrandt, M. Murtagh, R. Kusmenko, *et al.*, Phys. Status Solidi A **152**, 147 (1995).
11. P. M. Pires, P. L. Souza, and J. P. von der Weid, Appl. Phys. Lett. **65**, 88 (1994).
12. T. Kanata, M. Matsugana, T. Takakura, and Y. Hamakawa, J. Appl. Phys. **69**, 3691 (1991).
13. H. Shen, M. Dutta, R. Lux, *et al.*, Appl. Phys. Lett. **59**, 321 (1991).
14. D. E. Aspnes, Phys. Rev. **147**, 554 (1966).
15. D. E. Aspnes, Phys. Rev. **153**, 972 (1967).

Translated by A. Sidorova-Biryukova

Crystallography Reports, Vol. 47, No. 1, 2002, pp. 160–161. Translated from Kristallografiya, Vol. 47, No. 1, 2002, pp. 172–173.

OBITUARY

Georgiĭ Borisovich Bokij (October 9, 1909–September 4, 2001)

On September 4, 2001, Georgiĭ Borisovich Bokij (Bokii), a well-known crystallographer, Professor, Corresponding Member of the Russian Academy of Sciences, one of the creators and organizers of Russian crystal chemistry, passed away.

G.B. Bokij was born on October 9, 1909 in St. Petersburg into the family of an outstanding mining engineer Professor of the Mining Institute Boris Ivanovich Bokij and studied at the Mining Institute, where his teachers were A.K. Boldyrev and N.S. Kurnakov. Upon successful graduation from the institute in 1930, Bokij started studying the optical properties of crystals by the Fedorov method under the supervision of A.V. Shubnikov at the Lomonosov Institute. In 1931, he also began growing crystals–ferroelectrics at the Physicotechnical Institute.

Bokij continued improving his crystallographic knowledge by self-education. Every morning, three young future celebrities—Bokij, Shubnikov, and M.P. Shaskol'skaya—delivered in turn lectures on various aspects of crystallography to one another.

In 1934, the Lomonosov Institute moved to Moscow, where Bokij started working under the guidance of N.S. Kurnakov. In 1935, he organized the Laboratory of Crystallography (later, the Laboratory of Crystal Chemistry) at the Institute of General and Inorganic Chemistry of the USSR Academy of Sciences and started studying coordination compounds of the metals of the platinum group. In 1939, Bokij began studying crystal structures by the X-ray diffraction method and, in 1940, solved the NH_4IrCl_6 structure. In the same year, he published the book *Fundamentals of Crystallography* written in coauthorship with Shubnikov and E.E. Flint. Bokij together with G.G. Lemmlein investigated the rounded diamond crystals. At the same time, he also determined theoretically the number of physically different simple crystal forms.

During the Great Patriotic War of 1941–1945, Bokij was evacuated to Kazan, where, on the initiative of

1063-7745/02/4701-0160$22.00 © 2002 MAIK "Nauka/Interperiodica"

A.N. Nesmeyanov, he delivered his first course on crystal chemistry to his collegues. In 1942, Bokij defended his Doctoral Dissertation and, in 1943, became a Professor.

Upon his return from Kazan to Moscow, Bokij started teaching crystallography at the Moscow State University (1945) and organized there the Chair of Crystallography and Crystal Chemistry at the Faculties of Geology and Chemistry. In 1951, Bokij together with M.A. Porai–Koshits published the first volume of the handbook entitled *Practical Course of X-ray Structure Analysis*, which was used by several generations of Soviet crystallographers engaged in structure analysis. In 1954, he completed the study of the quantitative characteristics of trans-influence in the compounds of tetravalent platinum. The fundamental theoretical study entitled *To the Theory of Daltonides and Berthollides* was published in Russian in 1956 and in the English translation in 1958. In 1954, his famous handbook—*Crystal Chemistry*—was published, which run three editions and is still recognized to be the best Russian book on crystal chemistry. In 1958, Bokij was elected Corresponding Member of the USSR Academy of Sciences. In the period 1958–1962, Bokij lived and worked in Siberia, where he became one of the founders of the Institute of Inorganic Chemistry and organized the Laboratory of X-ray Diffraction Analysis. In this period, Bokij also organized the *Zhournal Strukturnoĭ Khimii* (Journal of Structural Chemistry) and became its Editor-in-Chief.

In 1963, Bokij returned to Moscow and started working at the Institute of Radio Engineering and Electronics and later also at the All-Union Institute of Scientific Information (VINITI). Since 1972 and till the very last days of his life, Bokij worked at the Institute of Geology of Ore Deposits, Petrography, Mineralogy and Geochemistry (IGEM) of the USSR (later Russian) Academy of Sciences. The most remarkable event of that period was his participation in the study of regular changes of the structures in the isomorphous series of $A^{III}B^{V}$ semiconductors, which was recorded as a discovery in 1978.

Since 1955 and till the end of his life, Bokij had made considerable efforts in studying the problems of informatics and systematics of crystal structures, and, in particular, systematics of minerals. He developed new principles of mineral classification based on the Mendeleev Periodic Law—the so-called natural classification.

In 1976–1981, four volumes of the *Mineralogical Thesaurus* were published. In 1979, Bokij became the Chairman of the Commission on Classification of the Council of Scientific and Engineering Societies.

In 1993, he headed the work on the publication of multivolume handbook *Minerals*, a fundamental work which contains exhaustive information (including the structural data) on all the known varieties of minerals. As a result, no. 3 of Volume IV was published and no. 1 of volume V was prepared for publication. Bokij also started preparing for publication no. 2 of Volume V. In 1997, VINITI published Bokij's book *Systematics of Natural Silicates* which was followed by the 1998 English edition. In 2000, *Systematics of Natural Oxides* was published, and Bokij proceeded to the classification of natural borates.

Bokij was the last member of the pleiad of outstanding crystallographers—founders of Russian crystal chemistry and the related disciplines—N.V. Belov, A.V. Shubnikov, V.I. Iveronova, G.S. Zhdanov, A.I. Kitaigorodsky, M.A. Porai-Koshits, Z.G. Pinsker, and B.K. Vainshtein. All of them were not only brilliant scientists, but also outstanding and erudite personalities.

Bokij never refused anybody who needed his consultation and helped everyone who addressed him. If something was necessary for science, he could address "higher spheres" as was the case with the discovery mentioned above—first, it found no support and only Bokijs intervention helped to register it as a discovery.

Bokij was a genuine St. Petersburg intellectual with a deep self-respect and a fine sense of humor and was always benevolent to all people.

All those who were fortunate to work and communicate with Professor Bokij will always miss and remember him.

Translated by L. Man

Crystallography Reports, Vol. 47, No. 1, 2002, pp. 162–163. Translated from Kristallografiya, Vol. 47, No. 1, 2002, pp. 174–175.

REVIEW

Review of the Handbook *X-ray Diffraction of Minerals* by D. Yu. Pushcharovsky,

Moscow: Geoinformmark, 2000 (289 pp.)

X-ray, neutron, and electron diffraction analyses as methods of studying ideal atomic and real (with due regard for defects) atomic structures of solids have been developed in depth in structural crystallography. In turn, crystallography, upon the formulation of its subject, has separated from mineralogy and become an independent science. The structural studies are based on the X-ray, neutron, and electron diffraction methods, which proved to be a powerful and universal instrument for the analysis of matter and are now widely used in structural chemistry, solid state physics, molecular biology, and, of course, as earlier, in mineralogy. These methods are successfully applied to various minerals, metals, and alloys, inorganic and organic compounds, proteins, nucleic acids, and even viruses. Such a large variety of objects also inevitably leads to specialization of the structural methods themselves. Obviously, the lectures on the methods of structural studies of crystals for mineralogists, chemists, physicists, and biologists should be somewhat different. This need is met by a new handbook entitled *X-ray Diffraction Analysis of Minerals* written by the Corresponding Member of the Russian Academy of Sciences Professor D.Yu. Pushcharovsky published in 2000. Obviously, the handbook is addressed to students and, I should like to add, also to all those beginning structural research of the geological profile. One more confirmation of the necessity in highly specialized courses is also the handbook *Crystallography* with the focus on the structural methods written by E.V. Chuprunov, A.F. Khokhlov, and M.A. Faddeev from Nizhniĭ Novgorod University obviously addressed mainly to students-physicists and also published in 2000.

An attractive feature of the handbook written by Pushcharovsky is a short excursus into the history of some fundamental discoveries underlying the science of crystal structure. For the first time, one can see the facsimiles of the title pages of the Roentgen manuscript on the discovery of the new type of radiation and the published article to the effect. One reads with keen interest the description of the first experiments on X-ray diffraction from a single crystal performed by Laue and his colleagues and the first structural determination of Bragg-father and Bragg-son. The author of the handbook have spent more than a few hours at the University libraries of different countries to find the original documents on these and many other pioneering studies of the founders of crystallography.

The structure of the handbook noticeably differs from the traditional handbooks written in the second half of the past 20th century. The first Part of the handbook is dedicated to the nature and the properties of X-rays, whereas the principles of their interaction with matter are considered only in the third Part. The second Part is dedicated to the X-ray diffraction analysis of polycrystal materials. Eighty pages are given to the methods of obtaining powder diffraction patterns in the Debye–Scherrer and Guinier cameras and in diffractometers for polycrystal specimens, indexing of powder X-ray diffraction patterns, and the examples of their use for solving typical problems of mineralogy. The author considers the phase analysis of mixtures, diagnostics of feldspars and layer silicates, and the diffraction studies of pyrite, arsenopyrite, pyrrhotite, and other rock-forming minerals. This Part is concluded by the analysis of microstresses and the determination of the dimensions of crystallites from X-ray powder diffraction patterns. The focus on the studies of polycrystal materials and, first of all, mineral identification, is quite justified for mineralogists. It is this diffraction method that can also be used under field conditions and aboard research vessels. In the third Part of the handbook, the author considers the scattering of X-rays by an electron, atoms, and crystals. Then, he analyzes the factors that influence diffraction-reflection intensities. A separate Section is devoted to the formation of line intensities on powder diffraction patterns with due regard for the regular absences of reflections depending on the character of unit-cell centering and the presence in crystals of symmetry elements (screw symmetry axes, symmetry planes with the glide components). On an example of fluorite, the author compares the experimental and the theoretically calculated (according to the structure model) diffraction patterns.

The fourth Part of the handbook is dedicated to the structure determinations based on the X-ray diffraction data. The material in this Part is stated in the chronological sequence of the development of various methods of structure analysis—from the trial-and-error method to the methods of extraction of structural information from the Patterson function of interatomic vectors. Naturally, first, the localization of a heavy atom is considered, then the Harker sections are analyzed, and, finally,

1063-7745/02/4701-0162$22.00 © 2002 MAIK “Nauka/Interperiodica”

the superposition methods of singling out the structure from the function of interatomic vectors are stated. The author begins the consideration of the direct methods of determining structure-factor phases from the Harker–Kasper inequalities, which today are of interest only in the historical aspect. In fact, I have not encountered any structural study by this method already for several decades. Today, the phases of structure factors are usually determined by the direct statistical methods used in numerous complexes of computer programs. I believe that this Part of the handbook should be complemented with a short description of some of the most popular computer programs widely used in the whole world.

The fifth Part of the handbook stands somewhat separate. The author considers some recent results obtained by X-ray diffraction methods in various fields of the science. It seems that it would be more expedient to devote this Part completely to the X-ray diffraction analysis under extreme pressure and temperature conditions on specimens. It would have been better if the author would have concluded this Part with the data on the composition of the mantle and the phase transformations occurring in it and would have transferred the data on synchrotron-radiation sources, area-sensitive detectors, modulated structure, methods of structure refinement by the data of the Rietveld full-profile analysis, and deformational electron-density maps into the corresponding Sections of the first four Parts of the handbook.

One thing is certain—Russian readers have received an excellent modern clearly written specialized handbook on the X-ray diffraction analysis of minerals. Each Part of the handbook is ended with well thought-out problems based on the material considered in the preceding Part, whose solution should help the reader to master the material and its active use. I should like to congratulate both the author and his future readers on the appearance of a new excellent handbook.

Professor V.I. Simonov

Translated by L. Man

Crystallography Reports, Vol. 47, No. 1, 2002, pp. 17–23. Translated from Kristallografiya, Vol. 47, No. 1, 2002, pp. 24–29.

STRUCTURE OF INORGANIC COMPOUNDS

New Oxygen- and Lead-Deficient Lead Borate $Pb^{(I)}_{0.9}Pb^{(II)}_{0.6}[BO_{2.25}]_2 = 2Pb_{0.75}[BO_{2.25}]$ and Its Relation to Aragonite and Calcite Structures

E. L. Belokoneva, Yu. K. Kabalov, A. G. Al-Ama, O. V. Dimitrova, V. S. Kurazhkovskaya, and S. Yu. Stefanovich

Faculty of Geology, Moscow State University, Vorob'evy gory, Moscow, 119899 Russia

e-mail: elbel@geol.msu.ru

Received March 6, 2001

Abstract—Anhydrous oxygen- and lead-deficient lead borate of the composition $Pb^{(I)}_{0.9}Pb^{(II)}_{0.6}[BO_{2.25}]_2 = 2Pb_{0.75}BO_{2.25}$ (sp. gr. *P*312) has been obtained by the hydrothermal synthesis. New acentric borate possesses optical nonlinearity comparable with the optical nonlinearity of α-quartz. The crystal structure of new borate is determined and refined by two X-ray diffraction methods—the single crystal diffractometry and the full-profile analysis. All the positions in the structure, except for those of the boron atom in the triangular coordination, are occupied only partly; one of the two lead positions is split. It is established that new borate is closely related to calcium carbonates—aragonite, calcite, and paralstonite. With an increase of the temperature, new borate undergoes the reversible phase transition into the centrosymmetric, most probably, aragonite-like phase.

INTRODUCTION

Despite the fact that it has already been shown that some lead-containing borates are promising materials for nonlinear optics, the conditions of their synthesis and their structures and properties have been studied insufficiently. At present, this group includes only eight representatives—PbB_4O_7 [1], $Pb_6B_{10}O_{21}$ [2]. $Pb_3B_{10}O_{18} \cdot 2H_2O$ [3], $Pb_5B_3O_8(OH)_3H_2O$ [4], $Pb_6B_{12}O_{24} \cdot H_2O$ [5], centrosymmetric hilgardite $Pb_2[B_5O_9](OH) \cdot H_2O$ [6] and its polar variety $Na_{0.5}Pb_2[B_5O_9]Cl(OH)_{0.5}$ [7], $Pb[B_6O_{10}(OH) \cdot B_2O(OH)_3]$ [8], and $Pb_3(OH)[B_9O_{16}] \cdot [B(OH)_3]$ [9], of which four [1, 4, 7, and 9] possess considerable optical nonlinearity. This study continues our investigation of crystal chemistry of lead borates and the attempts to establish relationships between their structures and properties.

EXPERIMENTAL

Synthesis of Single Crystals and Primary Diagnostics

Single crystals of new lead borate were synthesized under the hydrothermal conditions in standard 5–6 cm^3-large Teflon-futerated autoclaves. The hydrothermal synthesis was performed under the pressure $P \approx 70$ atm in the temperature range $T = 270$–280°C. The lower temperature limit was set by the kinetics of hydrothermal reactions, whereas the upper one, by the possibilities provided by the apparatus. The experiment duration (18–20 days) provided complete proceeding of the reaction. The coefficient of the autoclave filling was chosen in such a way that the pressure would remain constant. The crystals were formed at the molar ratio $PbO : B_2O_3 = 1 : 3$. The use of the HCOOH (1*M*) mineralizer allowed the formation of colorless turbid (in some occasions transparent) single crystals in the shape of hexagonal plates about 1.25 mm in diameter and up to 0.3–0.4-mm in thickness. The crystals showed the characteristic perfect cleavage along the (001) plane. The optical microscopy study of the crystals showed that the uniaxial (i.e., possessing the moderate symmetry) crystals were far from being perfect.

The powder diffraction patterns obtained on a DRON-UM1 diffractometer (Co-radiation, 40 kV, 25 mA) had no analogues in the PDF data base, which indicated that the crystals synthesized could be identified as a new compound. The crystal composition was determined by qualitative X-ray spectral analysis (Chair of Petrography, Faculty of Geology, Moscow State University) on a CAMSCAN 4DV scanning electron microscope with the LINK attachment for the energy-dispersive analysis. This analysis confirmed the presence of lead in the crystals. The test for second-harmonic generation performed in the reflection mode with the aid of a pulsed YAG : Nd laser [10] proved the absence of the center of inversion in new lead borate.

1063-7745/02/4701-0017$22.00 © 2002 MAIK "Nauka/Interperiodica"

IR Spectroscopy

We selected a small number of the best crystals (with the minimum quantities of defects and inclusions) to prepare the specimen as a finely dispersed film on the KBr substrate. The IR spectrum was recorded on a Specord-75 IR spectrophotometer in the frequency ranges 1800–400 cm^{-1} and 3800–3000 cm^{-1}. The absence of the characteristic absorption bands of BO_4-tetrahedra, the B–O–B bonds, and the OH-groups and H_2O in the spectra allowed us to conclude that the compound synthesized is anhydrous borate containing isolated BO_3 groups. The most intense absorption band at 1190 cm^{-1} was attributed to the asymmetric stretching vibrations ν_3 of the B–O bonds in BO_3 triangles; the bands at 735 and 715 cm^{-1} were attributed to nonplanar bending vibrations ν_4 of this triangle. Only one band was observed for each of the vibration regions ν_3 and ν_4, which indicated the degeneration of the stretching and bending vibrations and the position symmetry of the BO_3 triangle (not lower than C_3). If the triangular ion had no threefold axis (e.g., in aragonite, the group C_3 and aragonite-like borates), the degeneration of the ν_3 and ν_4 vibrations is lifted, and two bands for each of these vibrations appear in the spectrum. The spectrum had no band of the symmetric valence vibration ν_1, which indicated the presence of the center of inversion or a horizontal twofold axes in the space group of the crystal. Thus, the IR spectroscopy data indicate the following possible space groups—D_3, D_{3d}, or D_{3h}. In comparison with the spectra of other orthoborates [11], all the bands of the spectrum of new lead borate are shifted toward low frequencies. Thus, the band due to ν_3 vibrations is shifted by 50 cm^{-1} and even more, the bands due to the ν_2 and ν_4 vibrations, by 30 cm^{-1} and even more. Such pronounced shifts of the absorption bands can be associated with the incorporation of Pb^{+2} ions into the structure and weaker boron–oxygen bonds.

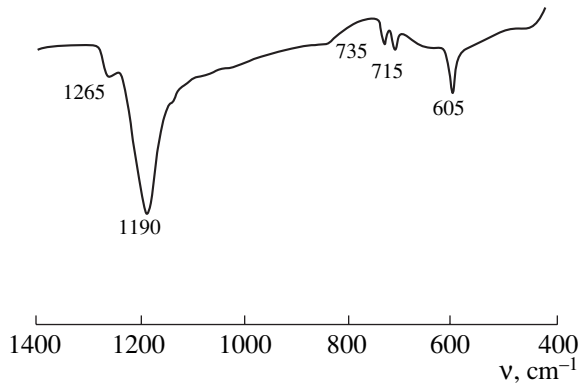

Fig. 1. Infrared spectrum of $Pb^{(I)}_{0.9}Pb^{(II)}_{0.6}(BO_{2.25})_2$.

Single-Crystal X-ray Diffraction Analysis

The low quality of the crystals and considerable absorption of the Mo-radiation hindered the determination of symmetry from the Laue diffraction patterns. The orientation of the platelet-like specimens normally to the primary beam and the use of the oscillation diffraction patterns showed that the most probable diffraction classes are $\bar{3}$ and $\bar{3}m1$. We also observed the pseudohexagonal symmetry. The diffraction experiment was first made on the most transparent isometric blocks cleaved from the crystals. However, the diffraction reflections were considerably blurred because of the crystal deformation and perfect cleavage, which hindered the proper centering of the reflections on a Syntex $P\bar{1}$ diffractometer and did not allow the determination of the lattice parameters and the orientation matrix necessary for the data set. Thus, we selected a rather transparent almost isometric $0.022 \times 0.022 \times 0.01$ mm-large platelet. The trigonal unit-cell parameters were determined and refined on the same diffractometer. The three-dimensional set of I_{hkl} (about 1260 reflections) for the structure determination was collected within a quarter of the reciprocal space. The processing of intensities and their recalculation into F^2_{hkl} were made by the PROFIT program [12], with all the other computations being performed by the CSD complex.

The correction for pronounced absorption was introduced for a crystal faceted with two simple forms—a hexagonal prism and a pinacoid. No regular absences of reflections were revealed. According to the earlier data, the most probable space groups were $P3$ and $P312$ and we used these groups for the analysis of the equivalent reflections. The intensities of these reflections indicated the presence of a threefold axis, however, in the sp. gr. D_{3d}, the satisfactory convergence was observed even without averaging the Friedel pairs of reflections, which could be explained by anomalously high scattering of the molybdenum radiation by lead atoms.

The vector $u = 2/3$ $v = 1/3$ $w = 0.445$ on the P_{uvw} synthesis with the coordinate w different from the fixed value of 1/2 indicated a possible variant of location of two Pb atoms in special positions xxx on threefold axes: the Pb(1) atom in the position (000) with the symmetry 3 or 312 and the Pb(2) atom in the position on another threefold axis in the position (2/3, 1/3, z) but with the statistical occupancy not exceeding 1/2 of the occupancy of the position in a more symmetric group. The refinement of these two Pb atoms provided the satisfactory reliability factor in both space groups. The consideration of a number of difference electron-density syntheses in the sp. gr. $P3$ provided the localization of B atoms on the threefold axis 1/3. 2/3 at the heights ≈1/4 and ≈3/4. Two independent O atoms were localized in the general positions provided the triangular coordination of B atoms at almost the same heights. The structure model thus obtained corresponded to the symmetry

*P*312, and therefore this space group was selected as the final one. Locating the Pb(1) atom in the position 1(*a*), the Pb(2) atom in the position 2(*i*) ($z = 0.55$), the B atom in the position 2(*h*) ($z = 0.263$), and the O atom in the position 6(*l*) ($x = 0.0475$, $y = 0.667$, $z = 0.264$), we obtained two excessive negative charges in the formula under the condition of 50% occupancy of the Pb(2) position and 100% occupancy of all the other positions. The refinement yielded the overestimated thermal corrections for Pb(2) and O atoms. Thus, we concluded that these positions are occupied statistically with the occupancies 0.25 for Pb(2) and 0.75 for O, which provided the electrically neutral structural formula $Pb^{(I)}_{1.0}Pb^{(II)}_{0.5}[BO_{2.25}]_2$. Considerable absorption and its pronounced anisotropy required the introduction of the correction for these factors for a crystal of an arbitrary shape by the DIFABS program [13] at the final stage of the study. The overestimated reliability factor $R \approx 0.10$ caused by insufficiently high quality of the single crystal and too high absorption, which was difficult to take into account, and also a considerable deficit of some atoms in the structure with respect to oxygen gave rise to some doubts in the results of the structure determination. Therefore we also used the Rietveld method.

Study of the Structure by the Rietveld Method

The X-ray diffraction spectrum from the powder sample was recorded on an automated ADP-2 diffractometer (λCo-K_α radiation, Fe filter) by 2θ scanning the crystal with a step of 0.02° at the exposure of 15 s. The main characteristics of the experiment and the structure refinement are listed in Table 1. The spectrum obtained showed anomalous broadening of peaks and the absence of any splitting of the Co-$K_{\alpha1,\,\alpha2}$ lines (high-order reflections). These facts confirmed the presence of defects in the structure, which could be associated with the presence of defects and structure disorder established earlier by single crystal data. All the computations were performed by the WYRIET program, version 3.3 [14] within the sp. gr. *P*312. The model considered above was used as the initial one. The peak shape was described with the aid of the Pearson function at 10FWHM, where FWHM is the average peak width at the half height. We used the ionic scattering curves. The refinement was performed by gradual inclusion into the refinement of new parameters at the constant graphical modeling of the background. The refinement of the parameter r^b of the texture along the [001] direction with the use of the March–Dollase function was necessary because of the perfect cleavage of the crystals. This resulted in a considerable reduction of R_{wp} (~5%) and a better convergence of the profile, especially for the basal (002)-type reflections.

At the concluding stage of the refinement, we constructed electron-density syntheses, which revealed all the peaks corresponding to the atoms of the structure model with the corresponding heights. The syntheses showed an additional maximum with a height close to that of the O peak with the coordinates (0, 0, ~0.2), which corresponded to the position inside the Pb(1) octahedron close to its triangular base. Taking into account that the structure is oxygen- and lead-deficient, this additional maximum can be explained either by the incorporation of organic radicals into the structure (from the organic mineralizer in the solution) or with the distortion of the hexagonal close packing of oxygen layers.

Thus, the single-crystal diffractometric data provided the establishment of the major features of the structure model, however, the pronounced absorption and the low quality of the crystal did not allow us to solve the structure completely. The use of the Rietveld method was very successful and showed the existence of the pronounced texture in the specimen ($r^b = 0.519$)

Table 1. Crystallographic data and characteristics of the experiment and the refinement of the $Pb^{(I)}_{0.9}Pb^{(II)}_{0.6}(BO_{2.25})_2$ structure by the Rietveld method

Characteristic	
Unit-cell parameters	
a, Å	4.9253(2)
c, Å	6.3884(2)
V_o, Å^3	134.210(8)
Number of formula units, *Z*	1
Sp. gr.	*P*312
2θ-interval, deg	14–135
Asymmetry, 2θ, deg	80
Number of Bragg reflections	170
Number of points measured	6050
Number of parameters refined	25
R_p, %	2.14
R_{wp}, %	2.93
R_{exp}, %	2.20
R_B, %	1.56
R_F, %	1.09
S	1.33
*DWD**	1.12
σ_x^{**}	2.065
Texture parameter r^b along [001]	0.519

* Durbin–Watson statistics.
** Factor for calculating standard deviations.

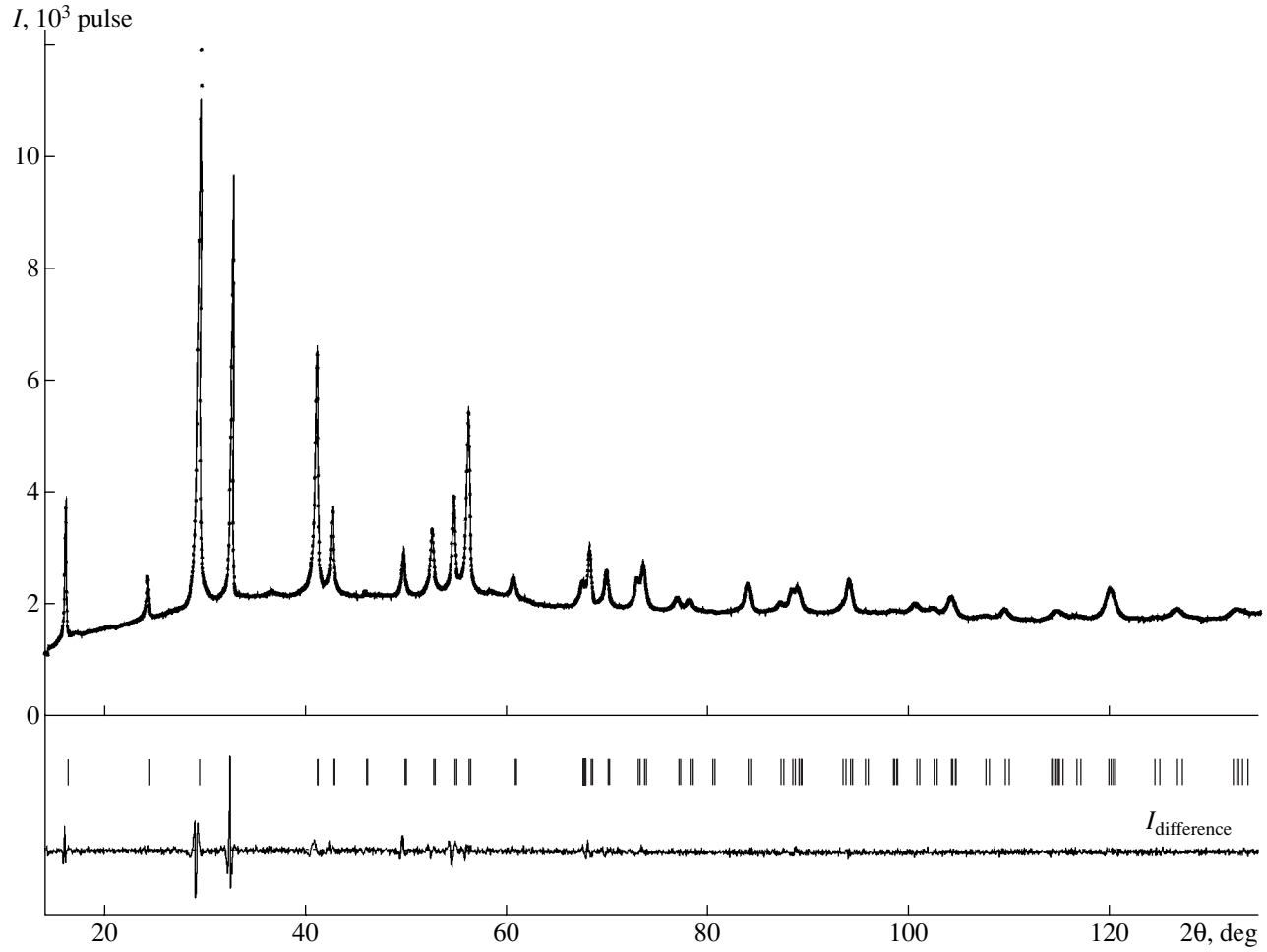

Fig. 2. Experimental (solid line) and theoretical (asterisks) X-ray diffraction spectra of $Pb^{(I)}_{0.9}Pb^{(II)}_{0.6}(BO_{2.25})_2$.

associated with the crystal cleavage and allowed us to take these factors into account. The diffraction data for high-order reflections provided the refinement of the occupancies of the Pb(1) and Pb(2) positions and the correction of the structural formula, $Pb^{(I)}_{0.9}Pb^{(II)}_{0.6}[BO_{2.25}]_2$, and improvement of the spectrum convergence (Fig. 2). This study confirmed the oxygen- and lead-deficient structure model. The concluding atomic coordinates and the corresponding interatomic distances are listed in Table 2.

Description of the $Pb^{(I)}_{0.9}Pb^{(II)}_{0.6}[BO_{2.25}]_2 = 2Pb_{0.75}[BO_{2.25}]$ *Structure and Its Comparison with Aragonite, Calcite, and Paralstonite Structures*

According to the X-ray diffraction analysis performed, the crystals of new borate are characterized by the triangular coordination of boron atoms (Figs. 3a and 3b) with the interatomic B–O distances characteristic of the B-triangles (Table 3). The formation of regular triangles (symmetry 3) is also confirmed by the

Table 2. Atomic coordinates and thermal factors B_j(Å^2), refined multiplicities of the positions q, and their occupancies p in the $Pb^{(I)}_{0.9}Pb^{(II)}_{0.6}(BO_{2.25})_2$ structure

Atom	Position	*x*/*a*	*y*/*b*	*z*/*c*	B_j	*q*	*p*
Pb(1)	1*a*	0	0	0	0.80(5)	0.1491(2)	0.8922
Pb(2)	2*i*	2/3	1/3	0.472(1)	1.7(2)	0.0993(4)	0.1981
B	2*h*	1/3	2/3	0.265(4)	2.2(5)	0.333	1.
O	6*l*	0.07(2)	0.68(3)	0.264(1)	3.2(5)	0.750	0.750

major lines of the IR spectrum. At the same time, the hexagonal close packing of oxygen atoms has vacancies because the O positions are occupied for 3/4. Under the assumption of the statistical disorder, a small number of boron–oxygen triangles are oxygen-deficient, which is confirmed by the shift of the bands in the IR spectrum and the appearance of a weak additional band at 1265 cm^{-1} interpreted as the band corresponding to the local B–O stretching vibrations in oxygen-deficient triangles. The anion-deficient structure is also characteristic of the γ-Bi_2O_3 = $2BiO_{1.5}$ phase with the fluorite structure [15].

The coordination polyhedra of Pb atoms are octahedra formed by statistically distributed O atoms. The Pb(1) octahedra are described by the point group 312 and are slightly elongated in the direction of the *z*-axis (O–O" = 3.61 Å and O'–O" = 4.07 Å) (Table 3) and are partly occupied by Pb atoms located in their centers (Table 2). In the Pb(2)-octahedron possessing the same symmetry and occupied even to a lesser degree than the Pb(1) octahedron, the central position is split with the Pb(2)–Pb(2)' distance being 0.364 Å, which results in the scatter of the Pb(2)–O distances (Table 3).

In terms of the close packing of O atoms, only the octahedral voids in the structure are filled. In the layer, these voids are filled according to the anticorundum (carbonate) motif [16] characteristic of calcite and aragonite. The alternation of the filled and empty voids along the *z*-axis corresponds to the aragonite motif: in two columns (0, 0, *z* and 2/3, 1/3, *z*), two occupied octahedra are followed by an empty one, whereas the third column of octahedra (1/3, 2/3, *z*) is formed only by empty octahedra. In the shared horizontal faces of each pair of empty octahedra, the BO_3 triangles are located. Ignoring the deficiency in the anionic packing, the occupancy of the octahedral positions, and also the split central position of the Pb atom of the second octahedron, we can state that new lead borate $Pb_{1.5}[BO_{2.25}]_2$ has a higher symmetry than aragonite $Ca_2[CO_3]_2$—trigonal instead of orthorhombic. Contrary to aragonite, paralstonite $BaCa(CO_3)_2$ from the aragonite group is characterized by the trigonal symmetry, sp. gr. *P*321 [17], with its unit cell being slightly smaller than that of Pb-borate with the parameters c = 6.148 Å and the parameters $a = b$ = 8.692 Å being slightly larger than the corresponding diagonal in borate. The identification

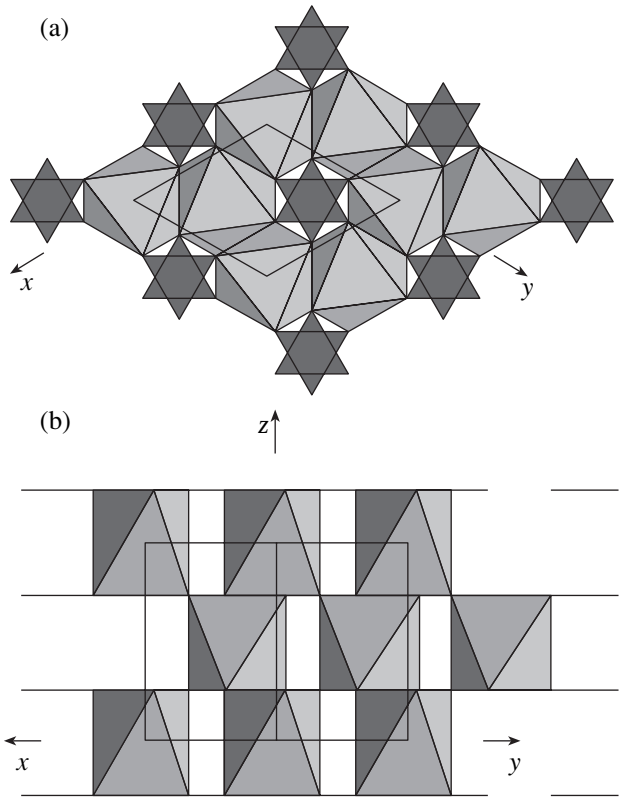

Fig. 3. Crystal structure of $Pb^{(I)}_{0.9}Pb^{(II)}_{0.6}(BO_{2.25})_2$ in polyhedra: projections of the structure onto the (a) (001) and (b) (110) planes. One can see (a) Pb-octahedra and B-triangles, (b) the B-triangles projected onto the (110) plane are depicted by horizontal solid lines.

of the Ca and Ba positions leads to the selection of a smaller unit cell practically coinciding with the unit cell of lead borate and with the space group being transformed into sp. gr. *P*312. Similar to the MBO_3 borates (where M^{3+} = In, Lu, Sc), rare earth borates $LnBO_3$ [18] [19] have the structure types of aragonite, calcite, and vaterite, which is explained by the simple scheme of heterovalent isomorphism $Ca^{2+} + C^{4+} = Ln^{3+} + B^{3+}$, whereas in lead borate, the valence balance is attained only at partly occupied anionic positions. The search in the JCPDF data base indicated that the compound studied is $RbGeIO_6$ possessing the same space group and

Table 3. Interatomic distances (Å) in the $Pb^{(I)}_{0.9}Pb^{(II)}_{0.6}(BO_{2.25})_2$ structure

Pb(1)-octahedron	Pb(2)-octahedron	B-triangle
Pb(1)–O × 6 – 2.47(3)	Pb(2)–O × 3 – 2.26(2)	B–O × 3 – 1.32(1)
	O' × 3 – 2.49(2)	O–O' – 2.29(2)
O–O' × 6 – 3.13(4)	O–O' × 6 – 3.18(3)	
O–O" × 3 – 3.61(5)	O–O" × 3 – 3.77(5)	
O'–O" × 3 – 4.07(5)	O'–O" × 3 – 3.30(5)	

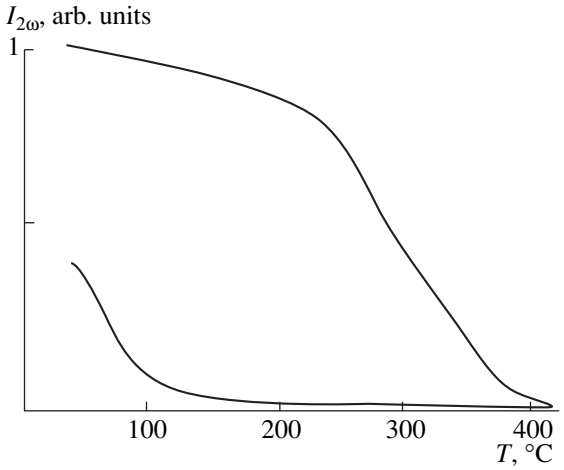

Fig. 4. Temperature dependence of the second harmonic for the $Pb^{(I)}_{0.9}Pb^{(II)}_{0.6}(BO_{2.25})_2$ powder during heating (the upper curve) and cooling (the lower line).

the same unit-cell parameters as new lead borate with octahedral Pb(1) and Pb(2) positions occupied by Rb and I atoms, respectively, whereas an empty octahedron with the faces formed by BO_3-triangles being filled with Ge atoms lying at the same height along the *z*-axis as the I atom. Because of the considerable difference in the ionic radii of Ge^{4+} and I^{7+}, on the one hand, and a much larger size of the Rb^{+1} ion, on the other hand, the Rb octahedron is considerably elongated in the direction of the *z*-axis.

The Study of $Pb_{0.75}BO_{2.25}$ *by the Method of Second-Harmonic Generation*

In full accordance with the nonsymmetric structure, new lead borate possesses quadratic optical nonlinearity, which manifests itself in the second-harmonic generation (SHG). The quantitative determination of optical nonlinearity was made by comparing the intensity $I_{2\omega}$ of the second-harmonic signal from the powder specimens of different dispersion with the analogous specimens cut out from the α-crystal having the same point group 32 as lead borate under study. The existence of the only nonzero nonlinearity coefficient, d_{11}, for both substances allows the direct determination of nonlinearity from the simple relationship $d_{11} = d_{11}(q)[I_{2\omega}/I_{2\omega}(q)]^{1/2}$, where $d_{11}(q) = 0.364$ pm/V is the nonlinear susceptibility of α-quartz and $I_{2\omega}(q)$ is the corresponding second-harmonic intensity. The above relationship is fulfilled most accurately at the minimum light absorption by the substance, which can be attained by the use of finely dispersed (3–5 μm) powder specimens. Taking that the SHG value of the quartz powder of such dispersion is unity and determining the value $I_{2\omega} = 0.4$ for the analogous powder of $Pb_{0.75}BO_{2.25}$ experimentally, we obtain that $d_{11} = 0.23$ pm/V, i.e., the nonlinearity value is close to that of quartz.

With an increase of the temperature above 240°C, the SHG signal of the $Pb_{0.75}BO_{2.25}$ powder rapidly decreases and practically disappears at 400°C. With a decrease of the temperature below 100°C, the SHG signal shows the tendency to restoration (Fig. 4), however, no complete restoration of the signal is observed because the rate of the process is too low. Thus, the transition into the centrosymmetric phase is accompanied by considerable changes in the structure and pronounced ion diffusion at a rate lower than the diffusion rate during the formation of the nonsentrosymmetric phase $Pb_{0.75}BO_{2.25}$ at the temperature lower than that of the fast process occurring with an increase in the temperature.

CONCLUSIONS

The crystallochemical analysis allows one to assume the existence of the structure of the high-temperature centrosymmetric modification of lead borate (the paraelectric phase). The addition of the center of inversion to the structure does not change the unit cell and the crystal system but leads to the space groups with $\bar{3}$ axes or to the groups with the vertical symmetry planes, which, in turn, requires the filling with Pb atoms of empty octahedra alternating with the filled ones along the *z*-axis or filling of empty octahedra, whose upper and lower faces are formed by boron triangles. Similar structural transformations are rather complicated and can destroy the structure. A more probable structure transformation would occur with lowering of the symmetry to orthorhombic and the transformation of the structure into the lead- and oxygen-deficient aragonite structure. The newly appeared center of inversion provides the equivalence of the Pb(1) and Pb(2) positions, i.e., reduces splitting of the Pb(2) position to the value described by the overestimated thermal vibrations analogous to those observed for the Pb(1) position. The geometric characteristics of these two Pb-octahedra should also become symmetrically equivalent ($\bar{1}$).

ACKNOWLEDGMENTS

The authors are grateful to V.I. Fel'dman and O.V. Parfenova for optical measurements of the crystals and to E.A. Guseva for the X-ray spectral analysis of these crystals.

REFERENCES

1. D. L. Corker and A. M. Glazer, Acta Crystallogr., Sect. B: Struct. Sci. **52**, 260 (1996).
2. J. Krogh-Moe and P. S. Wold-Hansen, Acta Crystallogr., Sect. B: Struct. Crystallogr. Cryst. Chem. **29**, 2242 (1973).
3. H. H. Grube, Fortschr. Mineral., Beih. **59**, 58 (1981).

4. R. K. Rastsvetaeva, A. V. Arakcheeva, D. Yu. Pushcharovsky, *et al.*, Z. Kristallogr. **213**, 1 (1998).
5. E. L. Belokoneva, O. V. Dimitrova, and T. A. Korchemkina, Zh. Neorg. Khim. **44** (2), 187 (1999).
6. E. L. Belokoneva, O. V. Dimitrova, T. A. Korchemkina, and S. Yu. Stefanovich, Kristallografiya **43**, 864 (1998) [Crystallogr. Rep. **43**, 810 (1998)].
7. E. L. Belokoneva, O. V. Dimitrova, T. A. Korchemkina, and S. Yu. Stefanovich, Kristallografiya **45**, 814 (2000) [Crystallogr. Rep. **45**, 744 (2000)].
8. E. L. Belokoneva, T. A. Korchemkina, and O. V. Dimitrova, Zh. Neorg. Khim. **44** (6), 889 (1999).
9. E. L. Belokoneva, S. Yu. Stefanovich, T. A. Borisova, and O. V. Dimitrova, Zh. Neorg. Khim. **46** (11), 1788 (2001).
10. S. Yu. Stefanovich, in *Abstracts of the European Conference on Lasers and Electro-Optics (CLEO-Europe'94), Amsterdam, 1994*, p. 249.
11. V. C. Farmer, *Infrared Spectra of Minerals* (Adlard and Son Ltd., London, 1974).
12. V. A. Strel'tsov and V. E. Zavodnik, Kristallografiya **34** (6), 1369 (1989) [Sov. Phys. Crystallogr. **34**, 824 (1989)].
13. N. Walker and D. Stuart, Acta Crystallogr., Sect. A: Found. Crystallogr. **39** (1), 158 (1983).
14. J. Schneider, in *Profile Refinement on IBM-PC's: Proceedings of the IUCr. International Workshop on the Rietveld Method, Petten, 1989*, p. 71.
15. S. Boyapati, E. D. Wachsman, and N. Jiang, Solid State Ionics **140**, 149 (2001).
16. N. V. Belov, *Structure of Ionic Crystals and Metal Phases* (Akad. Nauk SSSR, Moscow, 1947).
17. H. Effenberger, Neues Jahrb. Mineral., Monatsh., 353 (1980).
18. N. I. Leonyuk and L. I. Leonyuk, *Crystal Chemistry of Anhydrous Borates* (Mosk. Gos. Univ., Moscow, 1983).
19. V. V. Rudenko, Neorg. Mater. **34** (12), 1483 (1998).

Translated by L. Man

Crystallography Reports, Vol. 47, No. 1, 2002, pp. 24–28. Translated from Kristallografiya, Vol. 47, No. 1, 2002, pp. 30–34.

STRUCTURE OF INORGANIC COMPOUNDS

Crystal Structure of New Decaborate $Na_2Ba_2[B_{10}O_{17}(OH)_2]$

S. A. Vinogradova*, D. Yu. Pushcharovsky*, A. V. Arakcheeva, and O. V. Dimitrova***

** Faculty of Geology, Moscow State University, Vorob'evy gory, Moscow, 119899 Russia*

*** Baikov Institute of Metallurgy, Russian Academy of Sciences, Leninskiĭ pr. 49, Moscow, 117334 Russia*

Received January 30, 2001

Abstract—The crystal structure of a newly synthesized compound $Na_2Ba_2[B_{10}O_{17}(OH)_2]$ has been determined (Syntex $P\bar{1}$ diffractometer, MoK_α radiation, 1784 crystallographically nonequivalent reflections, anisotropic approximation, R = 1.7%). The parameters of the monoclinic unit cell are a = 11.455(7), b = 6.675(4), c = 9.360(7) Å, β = 93.68(5)°, Z = 2, sp. gr. $C2$. The structure consists of double pseudohexagonal layers built by BO_4-tetrahedra and BO_3-triangles forming three-membered rings of two mutually orthogonal orientations. The neighboring layers along the [001] direction are bound by Na-polyhedra and hydrogen bonds with participation of OH groups. The interlayer tunnels along the [100] direction are filled with columns of Ba-polyhedra. The crystallochemical characteristics of a number of synthetic Ba-borates (to which the structure of new decaborate is related) are considered in terms of borate building blocks singled out in the structure. © *2002 MAIK "Nauka/Interperiodica".*

INTRODUCTION

Growth of borate single crystals and their study, and especially of alkali-earth borates, are associated with the search for new materials possessing nonlinear optical properties first observed in β-$Ba_3[B_3O_6]_2$ and LiB_3O_5 crystals [1]. These experiments are a part of the program on the study of crystal chemistry of heavy-element borates obtained by hydrothermal synthesis. One of the first Ba-borate crystals were $Ba[B(OH)_4]_2 \cdot H_2O$ [2] and $Ba[B(OH)_4]_2$ [3] containing isolated $B(OH)_4$-tetrahedra. The subsequent refinement of their structures provided the localization of protons [4, 5]. It was shown that the structures of anhydrous Ba-borates $Ba[B_4O_7]$ [6] and $Ba[B_8O_{13}]$ [7] are based on highly condensed borate frameworks. Recently, a number of new compounds of this class have been synthesized—$Ba_5[B_{20}O_{33}(OH)_4] \cdot H_2O$ [8], $Ba[B_5O_8(OH)] \cdot H_2O$ and $LiBa_2[B_{10}O_{16}(OH)_3]$ [9], and $Ba_2[B_5O_9]Cl \cdot 0.5H_2O$ and $Ba_2[B_5O_8(OH)_2](OH)$ [10]. Despite their similar compositions, the structural characteristics of these compounds are different—they have various configurations of anion complexes, different dimensions of cationic polyhedra, and are characterized by different coordination numbers of Ba-atoms and differently distorted B-tetrahedra and B-triangles. In this connection, the study of a new representative of the family of Ba-borates would be of a considerable interest and would provide better understanding of the correlations between the composition and the structure of these chemically close compounds and would also give new information on phase formation in the A_2O–BaO(PbO)–B_2O_3–H_2O systems (A = Na, K, Rb, and Cs).

EXPERIMENTAL

Crystals of new decaborate $Na_2Ba_2[B_{10}O_{17}(OH)_2]$ were synthesized as a part of the investigation of the phase formation in the Na_2O–BaO–B_2O_3–H_2O system by the hydrothermal method in standard Teflon-futerated autoclaves under a pressure of 100 atm and a temperature of 280°C. The experiment continued for 20 days. The charge was a mixture of Na_2O, BaO, and B_2O_3 oxides in the proportion 1 : 1 : 2 with CO_3^{2-} ions as mineralizers. The $Na_2Ba_2[B_{10}O_{17}(OH)_2]$ crystals grew in a weakly acid medium. The X-ray diffraction study (DRON-UM1 diffractometer, λCuK_α radiation) showed that the compound obtained cannot be identified with any of the known alkali and alkali earth borates.

The presence of Ba and Na ions in the new borate structure was confirmed by the electron-probe analysis (Cameka SX 50 microprobe, 15 kV accelerating voltage, 20 mA current).

The IR spectra obtained on a SHIMADZU IR-435 spectrometer confirmed the presence of a borate complex consisting of boron-tetrahedra (the absorption bands in the range 1100–900 cm^{-1}) and boron-triangles (absorption bands in the range 1450–1300 cm^{-1}) (Fig. 1). The absorption bands in the range of 1170 and 790 cm^{-1} are explained by deformation vibrations of hydroxyl groups $(OH)^-$.

We synthesized 0.3-mm-long colorless transparent crystals with a pseudo-orthorhombic isometric habit. The structural study was performed on a 0.18 × 0.1 × 0.1-mm-large single crystal. The diffraction data were

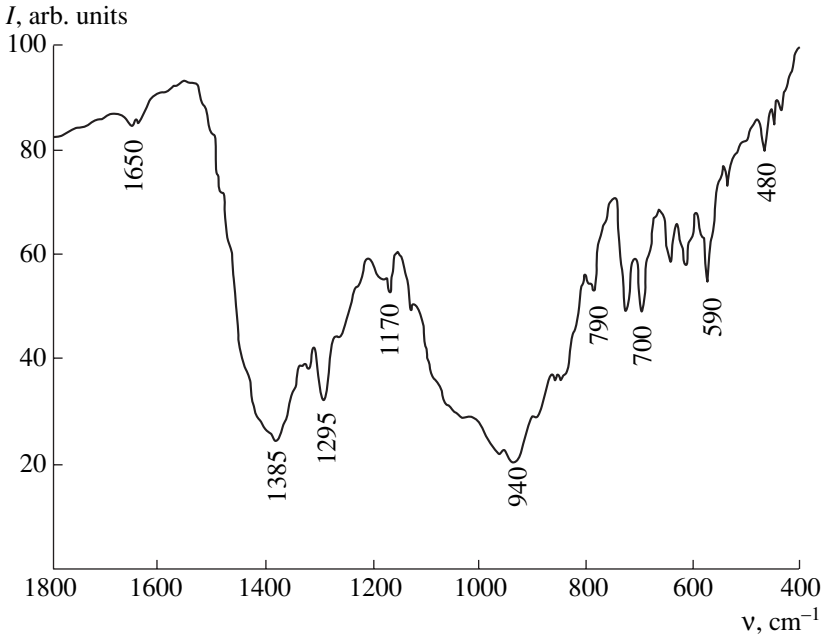

Fig. 1. IR spectrum of $Na_2Ba_2[B_{10}O_{17}(OH)_2]$.

collected on an automated Syntex $P\bar{1}$ diffractometer. The crystallographic characteristics and the main parameters of the experiment and refinement are listed in Table 1.

All the computations, including the correction for anomalous scattering, were performed by the AREN program [11]. The structure was solved by the direct method. The *e*-synthesis with the minimum *R* factor (sp. gr. *C*2) provided the localization of one Ba and two Na atoms. The B and O atoms were localized from the difference electron-density syntheses in several stages. The structure determined was refined in the anisotropic full-matrix approximation. The calculation of the valence balance (Table 2) [12] allowed the localization of the O atoms of the hydroxyl groups OH. One of the residual maxima on the zeroth electron density synthesis was attributed to the H atom of a hydroxyl group (the position O(6) was attributed to OH). The structure

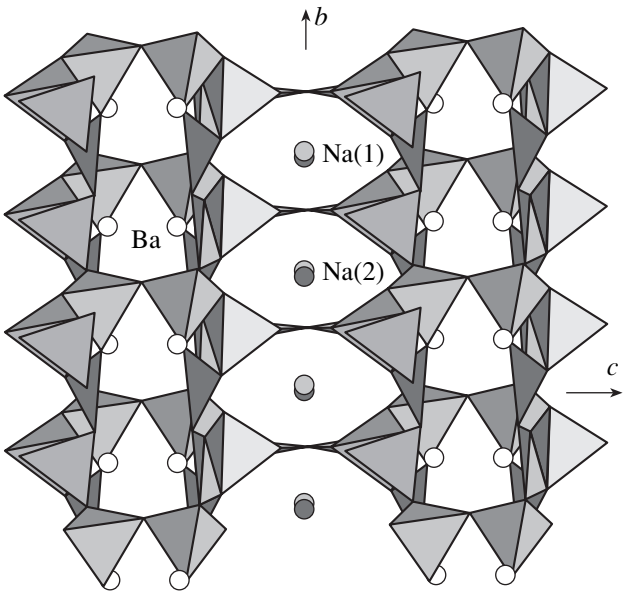

Fig. 2. The structure of $Na_2Ba_2[B_{10}O_{17}(OH)_2]$ projected along the [100] direction.

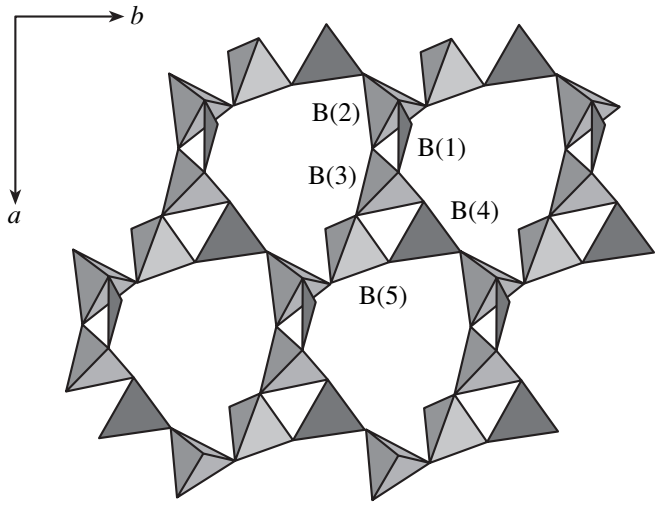

Fig. 3. Boron–oxygen layer in the $Na_2Ba_2[B_{10}O_{17}(OH)_2]$ structure with the shaded B-triangles.

Table 1. Crystallographic and experimental data

Formula	$Na_2Ba_2[B_{10}O_{17}(OH)_2]$
Unit-cell parameters, Å	a = 11.455(7)
	b = 6.675(4)
	c = 9.360(7)
	β = 93.68(5)°
Sp. gr.	$C2$
Unit-cell volume V, Å^3	714.2(1)
Number of formula units, Z	2
Calculated density ρ, g/cm^3	3.415
Absorption coefficient μ, mm^{-1}	5.827
Molecular weight	1469.48
F_{000}	676.0
Diffractometer	Sintex $P\bar{1}$
Wavelength, Å	0.71069
Total number of reflections	2982
Number of independent reflections with $\|F\| > 4\sigma(F)$	1784
R_{av}, %	3.00
R_F in the isotropic approximation, %	3.10
R_F in the anisotropic approximation, %	2.71
Extinction parameter E	0.000021(3)
$\Delta\rho_{max}$, e/Å^3	2.09
$\Delta\rho_{min}$, e/Å^3	–1.39

model was tested by the MYSSYM program [13]; no pseudosymmetry elements was revealed. The final coordinates of the basic atoms, the atomic thermal parameters, and the main interatomic distances are listed in Tables 3 and 4. The final R-factor upon the refinement of the positional and isotropic thermal parameters of hydrogen atom corresponds to the formula $Na_2Ba_2[B_{10}O_{17}(OH)_2]$ (Z = 2, ρ_{calc} = 3.415 g/cm). Two projections of the structure calculated by the subprogram ATOMS [14] are shown in Figs. 2 and 3.

DESCRIPTION OF THE STRUCTURE AND DISCUSSION

The crystal structure $Na_2Ba_2[B_{10}O_{17}(OH)_2]$ consists of two pseudohexagonal boron–oxygen layers $[B_{10}O_{17}(OH)_2]$ normal to the [001] direction. The fundamental building block is a pentaborate group formed by three crystallographically nonequivalent B-tetrahedra and two B-triangles. Similar building blocks were also found in the structures of ulexite $NaCa[B_5O_6(OH)_6] \cdot 5H_2O$ [15], probertite $NaCa[B_5O_7(OH)_4] \cdot 3H_2O$ [16, 17], $KMg_2H[B_7O_8(OH)_5]_2 \cdot 4H_2O$[1] [17], and tuzlaite $NaCa_2[B_5O_8)OH)_2] \cdot 3H_2O$ [18] and also in the structures of synthetic Ba-borates $Ba[B_5O_8(OH)_2] \cdot H_2O$, $LiBa_2[B_{10}O_{16}(OH)_3]$ [9], $Ba_5[B_{20}O_{33}(OH)_4] \cdot H_2O$ [8], and $Ba_2[B_5O_9]Cl \cdot 0.5H_2O$ [10] (the hilgardite structure type kaliborite KMg).

A decrease in the number of hydroxyl groups in the composition of pentaborate complexes is accompanied by a gradual change of their configuration in the transition from isolated (B,O)-complexes in ulexite to the

[1] In kaliborite, the chains of pentaborate complexes are bound by an additional B-triangle via the vertex of one of the tetrahedra.

Table 2. Calculation of the valence balance

	O(1)	O(2)	O(3)	O(4)	O(5)	O(6)*	O(7)	O(8)	O(9)	O(10)	Σ
Ba	0.177	0.204		0.186 0.159		0.186	0.189	0.169 0.164	0.184 0.174	0.201 × 2	1.993
Na(1)			0.178 × 2		0.148 × 2		0.172 × 2				0.996
Na(2)	0.169 × 2		0.183 × 2		0.147 × 2						0.998
B(1)			1.075		1.014	0.909					2.998
B(2)				0.843	0.632			0.812	0.710		2.997
B(3)	0.692		0.622	0.818			0.866				2.998
B(4)	0.954	1.054							0.990		2.998
B(5)		0.673					0.719	0.803		0.803 × 2	2.998
Σ	1.992	1.931	2.058	2.006	1.941	1.095	1.946	1.948	2.058	2.008	

* The O(6) position corresponds to OH.

(B,O)-chains in probertite and kaliborite, then to the layers in tuzlaite and synthetic $Ba[B_5O_8(OH)_2] \cdot H_2O$, and, finally, to the framework in the structures–analogues of hilgardite. The network configuration in the compound studied in our work is very close to the boron–oxygen layers in tuzlaite with the only difference—unlike tuzlaite, the neighboring networks in new decaborate [related by a twofold axis along the [100] direction passing through the O(10) vertex of the B(5)-tetrahedron] form characteristic double layers (Fig. 2).

A similar formation of double boron–oxygen networks related by twofold rotation axes was also observed in gowerite [19] and synthetic Ba-hydroborate $Ba_5[B_{20}O_{33}(OH)_4] \cdot H_2O$ [8].

The distances in BO_4-tetrahedra and BO_3-triangles are close to their statistically averaged values, 1.476 and 1.370 Å, respectively [20]. The interatomic distances in BO_4-tetrahedra show that the fraction of *s*-orbitals in sp^3-hybridized bonds is about 24% [20].

The columns of eleven-vertex Ba-polyhedra (with the Ba–O distances 2.718–2.999 Å) are located in the intralayer tunnels parallel to the [100] direction, whereas the Na-octahedra fill the interlayer space and connect double boron–oxygen layers. These interlayer contacts are "reinforced" by hydrogen O(6)–H···O(8) bonds with participation of the protons from OH-groups located at the end vertices of the triangles: $B(1)O_2(OH)$: O···O 2.767(3), O–H 0.88(1), H···O 1.99(1) Å, O–H···O 145.4(1)°.

Boron is an element seldom found in the earth's crust, but the processes occurring in the crust provide its incorporation into numerous minerals with diverse structures. A new approach to the structural systematics of borates based on the separation of the fundamental building blocks (FBB) whose combination leads to the formation of the most stable structural fragments was suggested in [20–22]. These fragments are built by the following building blocks (the number of minerals in which these blocks are encountered is indicated in parentheses): isolated tetrahedra (31), isolated complexes (27), chains (10), layers (15), and frameworks (15). This approach can also be used to consider the main crystallochemical characteristics of a series of synthetic Ba-borates and establish their possible similarity to many minerals of this class (Table 5).

Analyzing the data in Table 5, we see that, similar to natural borates [20], synthetic Ba-borates form characteristic three-membered rings consisting either of two tetrahedra and one triangle or of two triangles and one tetrahedron. In Table 5, these rings are indicated by the pointed brackets. It is these groups sharing a tetrahedron in the structures of Ba-borates that create pentaborate clusters consisting either of three tetrahedra and two triangles or of three triangles and two tetrahedra.[2] According to [21], the formation of three-membered borate rings ⟨⟩ is very advantageous energetically, which is explained by the attainment of the local balance of valence strengths and the flexibility of these rings, which provides their contacts with polyhedra of

[2] This type of combination of three-membered rings in a fundamental building block is shown by horizontal etching in Table 6.

Table 3. Coordinates and thermal parameters of basic atoms

Atom	*x*/*a*	*y*/*b*	*z*/*c*	B_{eq}, Å^2
Ba	0.6689(0)	0	0.8932(0)	0.61(4)
Na(1)	0	0.3084(6)	0.5	1.22(4)
Na(2)	0.5	0.2877(8)	0.5	1.90(6)
B(1)	0.7489(4)	0.0553(9)	0.4695(5)	0.67(6)
B(2)	0.6645(3)	0.017(1)	0.2221(4)	0.61(6)
B(3)	0.8824(4)	0.0602(9)	0.2677(5)	0.58(5)
B(4)	0.5328(4)	0.3272(7)	0.1722(5)	0.46(5)
B(5)	0.0531(4)	0.1943(8)	0.1359(5)	0.64(5)
O(1)	0.4299(3)	0.3559(6)	0.2379(4)	0.79(4)
O(2)	0.9047(3)	–0.016(1)	0.8766(3)	0.77(4)
O(3)	0.8591(3)	0.0575(6)	0.4260(4)	0.78(4)
O(4)	0.7739(3)	0.1069(6)	0.1850(3)	0.63(3)
O(5)	0.6504(3)	0.0318(5)	0.3821(3)	0.77(4)
O(6)*	0.2707(4)	0.0823(8)	0.3876(5)	1.46(6)
O(7)	0.9707(3)	0.2115(5)	0.2503(3)	0.60(4)
O(8)	0.1589(3)	0.3105(5)	0.1732(3)	0.66(4)
O(9)	0.5653(2)	0.1317(5)	0.1508(3)	0.63(4)
O(10)	0	0.2650(8)	0	0.67(6)
H	0.211(6)	0.146(4)	0.343(6)	2.16(2)**

* OH.
** B_{iso}.

Table 4. Interatomic distances

Bond type	c.n.	Interatomic distances, Å	
		range of variation	average
Ba–O	11	2.718(3)–2.999(3)	2.847
Na(1)–O	6	2.396(5)–2.579(4)	2.467
Na(2)–O	6	2.487(6)–2.710(4)	2.589
B(1)–O	3	1.349(6)–1.385(7)	1.364
B(2)–O	4	1.450(6)–1.516(5)	1.478
B(3)–O	4	1.446(6)–1.521(6)	1.480
B(4)–O	3	1.360(6)–1.376(6)	1.370
B(5)–O	4	1.451(5)–1.495(6)	1.471

Table 5. Fundamental building blocks in the structures of Ba-borates

Borate complex*	Formula of mineral	Method of connection of fundamental building blocks	Type of boron–oxygen complex
3△2□	$Ba[B_5O_8(OH)]H_2O$**	⟨△2□⟩–⟨2△□⟩	Layers
5△5□	$LiBa_2[B_{10}O_{16}(OH)_3]$	⟨△2□⟩–⟨△2□⟩ ⟨△2□⟩–⟨2△□⟩	Layers
5△5□	$Ba_5[B_{20}O_{33}(OH)_4] \cdot H_2O$	⟨△2□⟩–⟨△2□⟩ ⟨△2□⟩–⟨2△□⟩	Double layers
2△3□	$B_2[B_5O_8(OH)_2](OH)$, $NaCa[B_5O_8(OH)_2] \cdot 3H_2O$ tuzlaite	⟨△2□⟩–⟨△2□⟩	Layers
2△3□	$Na_2Ba_2[B_{10}O_{17}(OH)_2]$	⟨△2□⟩–⟨△2□⟩	Double layers
2△3□	$Ba_2[B_5O_8]Cl \cdot 0.5H_2O$***	⟨△2□⟩–⟨△2□⟩	Framework

* △ and □ denote a triangle and a tetrahedron, respectively.
** Biringuccite structure type.
*** Hilgardite structure type.

different dimensions. Moreover, the widespread occurrence of these rings in the structures of a large group of borates seems to be associated with their presence in the mineral-forming medium and, thus, also with their presence in a growing crystal.

Obviously, all the above stated opens new vistas for studying crystallochemical aspects of crystal genesis of Ba-borates, many of which are promising materials for various practical applications.

ACKNOWLEDGMENTS

This study was supported by the Russian Foundation for Basic Research, projects nos. 00-05-65399 and 00-15-96633, and the Program *Russian Universities*. The authors are grateful to N.V. Zubkova for the discussion of the structure model and V.S. Kurazhkovskaya for obtaining the IR spectra of new decaborate

REFERENCES

1. C. Chen, Y. Wu, and R. Li, J. Cryst. Growth **99**, 790 (1990).
2. L. Kustchabsky, Acta Crystallogr., Sect. B: Struct. Crystallogr. Cryst. Chem. **25**, 1811 (1969).
3. V. Kravchenko, J. Struct. Chem. **6**, 724 (1965).
4. M. A. Simonov, O. G. Karpov, Ya. Ya. Shvirkst, and G. K. Gode, Kristallografiya **34** (5), 1292 (1989) [Sov. Phys. Crystallogr. **34**, 778 (1989)].
5. K. Watanabe and Sh. Sato, Bull. Chem. Soc. Jpn. **67**, 379 (1994).
6. A. Block and A. Perloff, Acta Crystallogr. **19**, 297 (1965).
7. J. Krogh-Moe and M. Ihara, Acta Crystallogr. **25**, 2153 (1969).
8. A. V. Arakcheeva, S. A. Vinogradova, D. Yu. Pushcharovsky, *et al.*, Kristallografiya **45** (3), 448 (2000) [Crystallogr. Rep. **45**, 405 (2000)].
9. D. Yu. Pushcharovsky, S. Merlino, O. Ferro, *et al.*, J. Alloys Compd. **306**, 163 (2000).
10. O. Ferro, S. Merlino, S. A. Vinogradova, *et al.*, J. Alloys Compd. **305**, 63 (2000).
11. V. I. Andrianov, Kristallografiya **32** (1), 228 (1987) [Sov. Phys. Crystallogr. **32**, 130 (1987)].
12. I. D. Brow and R. D. Shanon, Acta Crystallogr., Sect. A: Cryst. Phys., Diffr., Theor. Gen. Crystallogr. **29**, 226 (1973).
13. Y. Le Page, J. Appl. Crystallogr. **21**, 983 (1988).
14. E. Dowty, *Atoms 3.2: A Computer Program for Displaying Atomic Structures*, TN 37663 (Kingsport, 1995).
15. S. Ghose, Ch. Wan, and J. R. Clark, Am. Mineral. **63**, 160 (1978).
16. S. Menchetti, C. Sabelli, and R. Trosti-Ferroni, Acta Crystallogr., Sect. B: Struct. Crystallogr. Cryst. Chem. **38**, 3072 (1982).
17. P. C. Burns and F. C. Hawthorne, Can. Mineral. **32**, 885 (1994).
18. V. Bermanec, T. Armbruster, D. Tibljas, *et al.*, Am. Mineral. **79**, 562 (1994).
19. J. A. Konnert, J. R. Clark, and C. L. Christ, Am. Mineral. **57**, 381 (1972).
20. F. C. Hawthorne, P. C. Burns, and J. D. Grice, Rev. Mineral. **33**, 41 (1996).
21. P. C. Burns, J. D. Grice, and F. C. Hawthorne, Can. Mineral. **33**, 1131 (1995).
22. J. D. Grice, P. C. Burns, and F. C. Hawthorne, Can. Mineral. **37**, 731 (1999).

Translated by L. Man

Crystallography Reports, Vol. 47, No. 1, 2002, pp. 29–32. Translated from Kristallografiya, Vol. 47, No. 1, 2002, pp. 35–39.

STRUCTURE OF INORGANIC COMPOUNDS

Neutron Diffraction Study of Sodium Hydrogen Selenate $Na_3H_5(SeO_4)_4$. Comparison with the X-ray Diffraction Data

S. I. Troyanov*, M. A. Zakharov*, M. Reehuis, and E. Kemnitz*****

** Faculty of Chemistry, Moscow State University, Vorob'evy gory, Moscow, 119899 Russia*

*** Hahn–Meitner Institut, Berlin, Germany*

**** Institut für Chemie, Humboldt Universität, Brook-Taylor str. 2, Berlin, 12489 Germany*

e-mail: karpova@inorg.chem.msu.ru

Received February 5, 2001

Abstract—The neutron diffraction study of $Na_3H_5(SeO_4)_4$ single crystals at 298 and 85 K has confirmed the positions of nonhydrogen atoms obtained in the X-ray diffraction study. Contrary to the X-ray diffraction data, the neutron diffraction data indicate that all the three independent protons are ordered and participate in two asymmetric and one symmetric hydrogen bonds, with the O··O distances being 2.68, 2.61, and 2.48 Å. The system of hydrogen bonds is built by complicated chains. © *2002 MAIK "Nauka/Interperiodica".*

Crystal structures of alkali metal hydrogen sulfates and selenates have been studied in sufficient detail only for their potassium, rubidium, and cesium derivatives. The intense study of these compounds was undertaken in connection with the discovery of phase transitions in Rb and Cs salts accompanied by the appearance of ferroelectric properties or high protonic conductivity. The structures of the compounds formed by light alkali metals (lithium and sodium) have been established only recently because of the considerable experimental difficulties of their synthesis such as high viscosity of the solutions used, high concentration of selenic acid, and high hygroscopicity of the compounds synthesized. The structures of anhydrous lithium hydrogen sulfates ($LiHSO_4$ [1], $Li_2(HSO_4)_2(H_2SO_4)$ [2], $Li(HSO_4)(H_2SO_4)_3$ [3] and sodium hydrogen sulfates ($NaHSO_4$ [3], $Na_2(HSO_4)_2(H_2SO_4)$ [4], and $Na(HSO_4)(H_2SO_4)_2$ [4]) are studied in more detail than those of hydrogen selenates. The crystal structures of hydrogen selenates have been determined only for three anhydrous compounds ($LiHSeO_4$ [5], $NaHSeO_4$ [6], and $Na_3H_5(SeO_4)_4$ [6]) and one hydrate ($Na_5H_3(SeO_4)_4 \cdot 2H_2O$ [7]). While hydrogen sulfates and selenates of heavier alkali metals are usually isotypic, lithium and sodium hydrogen selenates are crystallized in the structure types different from those of hydrogen sulfates. Also, the stoichiometry of $Na_3H_5(SeO_4)_4$ "superacid" selenate is unique among the sodium and other alkali metal superacid sulfates.

In addition to technical difficulties encountered in the synthesis and the study of lithium and sodium hydrogen selenates, the determination of their structures by X-ray diffraction methods also encounters considerable difficulties. This is explained by anomalous scattering of MoK_α radiation by selenium atoms. Therefore, it is very difficult to determine the positions of hydrogen atoms in selenates quite reliably, which, in turn, hinders the analysis of fine characteristics of the system of hydrogen bonds in these crystals.

At the same time, the positions of hydrogen atoms in the selenates of the composition MHSeO$_4$ (M = Li, Na) are determined quite reliably, which cannot be made for $Na_3H_5(SeO_4)_4$ in which, according to the X-ray diffraction data [6], one of the three independent hydrogen atoms is disordered over two positions. Therefore, we undertook the neutron diffraction study of single crystals of this compound with the aim to refine the positions of hydrogen atoms and establish the specific features of the system of hydrogen bonds in $Na_3H_5(SeO_4)_4$. The results of this study are presented below and compared with the corresponding X-ray diffraction data.

EXPERIMENTAL

Long (4–5 mm) $Na_3H_5(SeO_4)_4$ crystals were obtained upon slow (for two months) removal of water from the solution prepared by dissolving sodium carbonate in the concentrated (seven-times excess in comparison with the stoichiometric ratio [6]) selenic acid. The $5.0 \times 4.0 \times 2.5$ mm-large crystal in the shape of an oblique-angled parallelipiled was selected for the further study. This crystal was fixed with the aid of epoxy resin in a thin-walled glass capillary tube in a glove box and then was sealed.

1063-7745/02/4701-0029$22.00 © 2002 MAIK "Nauka/Interperiodica"

Table 1. Crystallographic characteristics, experimental conditions, and details of the refinement of the $Na_3H_5(SeO_4)_4$ structure at 293 and 85 K

Temperature, K	293(2)	85(2)
System	Triclinic	
Sp. gr.	$P\bar{1}$	
a, Å	5.857(1)	5.795(2)
b, Å	7.254(1)	7.229(2)
c, Å	8.943(2)	8.855(3)
α, deg	104.83(2)	104.68(2)
β, deg	91.69(2)	91.65(2)
γ, deg	105.41(2)	105.62(1)
V, Å^3	352.15(11)	343.7(2)
Z	1	1
ρ_{calc}, g/cm^3	4.102	4.203
Total number of reflections	2390	2313
Number of independent reflections	2333	2039
Number of reflections with $I > 2\sigma(I)$	1883	1622
Number of reflection/parameters used in the LS refinement	2008/131	1656/131
R_1/wR_2	0.0395/0.0979	0.0613/0.1296

Table 2. Interatomic distances (Å) in the $Na_3H_5(SeO_4)_4$ structure according to the X-ray and neutron diffraction data

Distance	X-ray diffraction analysis	Neutron diffraction	Neutron diffraction
	293 K	293 K	85 K
Se(1)–O(1)	1.620(4)	1.619(1)	1.631(3)
Se(1)–O(2)	1.611(3)	1.609(1)	1.607(2)
Se(1)–O(3)	1.626(3)	1.621(1)	1.619(3)
Se(1)–O(4)	1.708(4)	1.707(1)	1.703(2)
Se(2)–O(5)	1.607(4)	1.603(1)	1.606(3)
Se(2)–O(6)	1.609(4)	1.609(1)	1.610(2)
Se(2)–O(7)	1.659(4)	1.659(1)	1.655(3)
Se(2)–O(8)	1.692(4)	1.689(1)	1.688(2)
Na(1)–O(1)	2.391(4)	2.396(2)	2.375(4)
Na(1)–O(2)	2.380(4)	2.382(2)	2.364(4)
Na(1)–O(2')	2.384(4)	2.380(2)	2.353(4)
Na(1)–O(5)	2.366(4)	2.373(2)	2.345(4)
Na(1)–O(5')	2.450(4)	2.451(2)	2.418(4)
Na(1)–O(6)	2.438(4)	2.440(2)	2.412(4)
Na(2)–O(3)	2.346(4)	2.354(1)	2.329(2)
Na(2)–O(6)	2.390(4)	2.388(1)	2.370(2)
Na(2)–O(7)	2.497(4)	2.503(1)	2.467(2)

The neutron diffraction experiment was made on a four-circle E5 diffractometer on a BER II (BENSC, Berlin) reactor. The beam monochromatization to λ = 0.889 Å was attained by reflection from the (220) plane of a copper single crystal. The data were collected with the use of an area position-sensitive (90×90 mm^2) ^{3}He-detector at room temperature (2390 reflections), at 85 K (2313 reflections), and 11 K (968 reflections). The intensity measurements at low temperature were hindered by random overlap of measured reflections with the reflections from the aluminum container. Therefore, these reflections were not used in the profile analysis. At room temperature, the structure was refined with the use of the unit-cell parameters obtained earlier by the X-ray diffraction method [6]; in the refinement at 85 K, the unit cell parameters were determined using 200 centered reflections. The measurements at 11 K have not been completed, therefore, no exact calculations at this temperature were possible. The coherent neutron-scattering amplitudes were taken from [8]. The initial coordinates of nonhydrogen atoms were taken from [6]. All the three independent protons were localized by strong negative peaks on the Fourier syntheses. The refinement of the structure model by the SHELXL-93 program [9] was performed in the anisotropic approximation for all the atoms. The crystallographic data and the details of the structure refinement are indicated in Table 1. The atomic coordinates and the anisotropic displacement parameters for the structures at room temperature and 85 K are deposited in the Inorganic Crystal Structure Database (FIZ, Kalsruhe, Germany) under the registration numbers CSD 411719 and 411720.

RESULTS AND DISCUSSION

The neutron diffraction study of $Na_3H_5(SeO_4)_4$ single crystals at room temperature showed that the structural parameters of all the atoms, including hydrogen ones, are obtained with a rather high accuracy (Table 2). Despite the fact that the reliability factor R_1 in the X-ray diffraction study [6] is lower (0.032), the positions of oxygen atoms are determined with a slightly lower accuracy, whereas hydrogen atoms are localized with a rather low accuracy. This had to be expected because of pronounced anomalous scattering of MoK_α radiation by selenium atoms and the difficulties associated with the allowance for absorption in the crystal. Nevertheless, the interatomic distances for nonhydrogen atoms obtained by both methods are almost the same. Both sodium atoms are characterized by somewhat distorted octahedral environment—six oxygen atoms at the 2.35–2.50 Å distances. The Se–O distances are essentially dependent on the additional functions performed by the corresponding oxygen atoms. The longest distances are characteristic of Se–OH bonds with the O(4) and O(8) oxygen atoms playing the role of proton donors in hydrogen bonds (Table 3). The

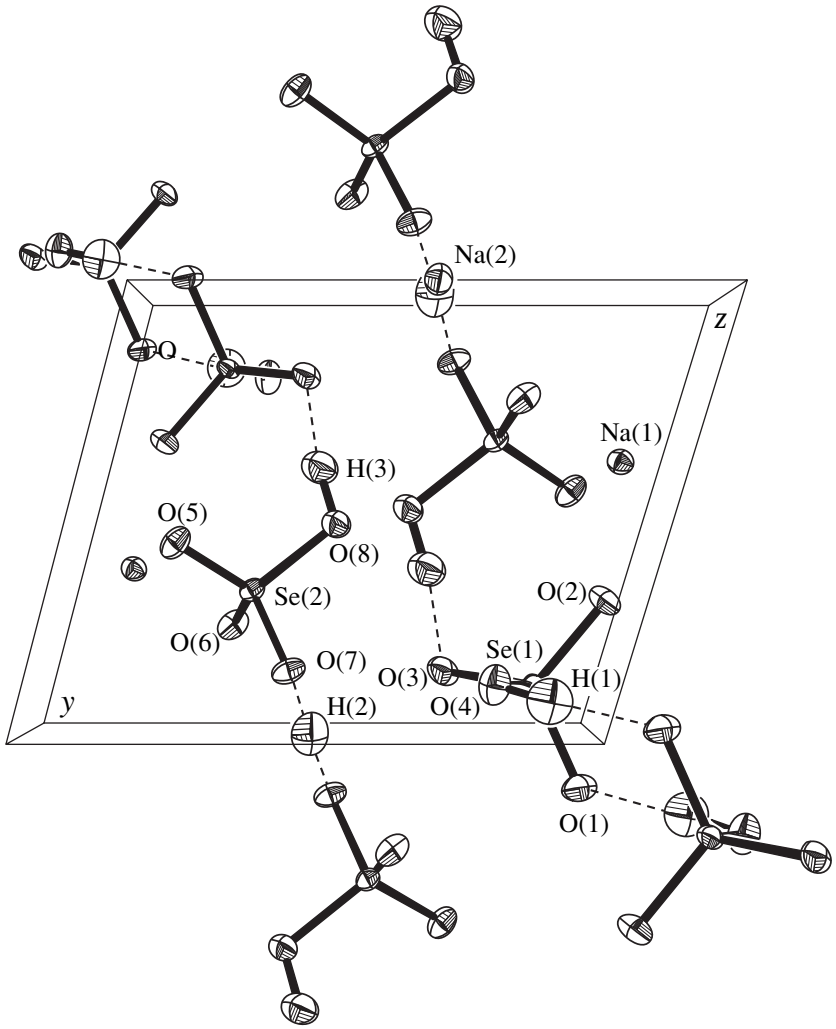

System of hydrogen bonds in the $Na_3H_5(SeO_4)_4$ structure represented as chains of SeO_4-tetrahedra connected by hydrogen bonds.

Se–O(7) distance is somewhat shorter because the O(7) atom is a half-donor and a half-acceptor in the O(7)··H(2)··O(7') hydrogen bond with H(2) atom located at the center of inversion. The shortest bonds are the Se–O bonds with the O(1) and O(3) atoms playing the role of acceptors in hydrogen bonds and also with O(2), O(5), and O(6) atoms participating only in weak ionic interactions with sodium atoms.

According to the X-ray diffraction data [6], the H(1) and H(3) atoms participate in asymmetric hydrogen bonds, whereas the H(2) atom is disordered over two positions around the center of inversion. On the contrary, the neutron diffraction study showed that all the protons are ordered, with the H(2) atom being in the center of inversion and, thus, participating in the symmetric linear O(7)··H(2)··O(7') hydrogen bond. In accordance with the well-known correlations [10], this hydrogen bond is the shortest, 2.484(2) Å. Two remaining hydrogen bonds are much longer with their lengths, 2.679(2) and 2.610(2) Å, correlating with the angle at the corresponding hydrogen atoms H(1) (166.9(2) Å) and H(3) (172.5(2) Å). Because of the high accuracy of localization of hydrogen atoms, it is possible to reveal a slight reduction in the Se–OH bond lengths with an increase of the O–H distances, although the difference in the oxygen distances to the H(1) and H(3) is only 0.01 Å. The difference in the position of the H(2) atom determined from the neutron and X-ray diffraction studies demonstrate the specific features of both methods reflecting the distribution of the nuclear and electron density in a crystal, respectively. This is the so-called Kroon–Kanters–McAdam (KKM) effect often observed for strong (shorter than 2.5 Å) hydrogen bonds. Different values of the electron and nuclear density of H (D) atoms were revealed on an example of acid salts of hydrogen tartrates and succinates [11, 12] and later also in the structures of acid salts of other organic acids [13, 14]. Recently, a similar effect was also established by comparing the neutron and X-ray diffraction data for potassium hydrogen selenate–phosphate $K_4(HSeO_4)_3(H_2PO_4)$ [15].

Table 3. Hydrogen bonds in $Na_3H_5(SeO_4)_4$ crystals according to the neutron and X-ray diffraction (italic) data

D–H···*A*	*D*–H, Å	H···*A*, Å	*D*···*A*, Å	∠*D*–H···*A*, deg	*T*, K
O(4)–H(1)···O(1)*	0.997(2)	1.698(3)	2.679(2)	166.9(2)	293
	0.992(5)	1.675(5)	2.648(3)	166.1(4)	85
	0.68(7)	*2.03(7)*	*2.679(5)*	*160(9)*	*293*
O(7)···H(2)···O(7)**	1.242(1)	1.242(1)	2.484(2)	180	293
	1.229(2)	1.229(2)	2.458(4)	180	85
	0.6(1)	*2.0(1)*	*2.505(9)*	*170(17)*	*293*
O(8)–H(3)···O(3)***	1.006(2)	1.609(2)	2.610(2)	172.5(2)	293
	1.024(5)	1.578(5)	2.598(3)	173.0(4)	85
	0.8(1)	*1.8(1)*	*2.611(5)*	*175(10)*	*293*

Note: Symmetry transformations: * $1-x, 2-y, 2-z$, ** $1-x, 2-y, 1-z$, and *** $-x, 1-y, 1-z$.

The comparison of the neutron diffraction data at 293 and 85 K showed that cooling affects the coordination of selenium atoms only slightly. However, it results in a considerable (by 0.02–0,03 Å) decrease in the Na–O distances. All three hydrogen bonds become slightly shorter, but no considerable differences in the character of proton distribution is observed. It should be emphasized that the amplitudes of thermal vibrations of all the atoms are reduced by almost a factor of two, with the maximum reduction being observed for the H(2) atom. At room temperature, the ellipsoid of thermal vibrations of this atoms has the maximum elongation along one of the axes (figure). At 85 K, the maximum "contraction" of the ellipsoid is also observed along this axis, so that all the three protons are characterized by approximately equal axial ratios (about 2 : 1). The structure refinement performed by the incomplete experimental data at 11 K indicates the absence of any phase transitions and considerable changes in the $Na_3H_5(SeO_4)_4$ structure during crystal cooling to this temperature.

The system of hydrogen bonds is formed by infinite chains of SeO_4-tetrahedra connected by hydrogen bonds (figure). When describing the chain structure, one has to distinguish between two types of dimers formed by SeO_4-tetrahedra. The cyclic centrosymmetric $[HSe(1)O_4]_2$ dimers are formed by the pairs of O(4)–H(1)··O(1) hydrogen bonds, whereas the second-type centrosymmetric $[H(HSe(2)O_4)_2]$ dimers consist of two tetrahedral $(HSeO_4)^-$ anions bound by the symmetric O(7)··H(2)··O(7') hydrogen bond. The dimers of both types are connected by hydrogen bonds O(8)–H(3)··O(3) and form infinite chains along the [221] direction. With due regard for the above features of the crystal structure, the formula of sodium hydrogen selenate studied above can be written as $Na_3[H(HSeO_4)_2](HSeO_4)_2$. The singly charged anions $[H(HSeO_4)_2]^-$ were revealed only in this structure, whereas an analogous sulfate anion is observed in the structure of lithium "superacid" sulfate $Li[H(HSO_4)_2](H_2SO_4)$ [3].

REFERENCES

1. E. Kemnitz, C. Werner, H. Worzala, *et al.*, Z. Anorg. Allg. Chem. **621**, 675 (1995).
2. C. Werner, E. Kemnitz, H. Worzala, *et al.*, Z. Anorg. Allg. Chem. **621**, 1266 (1995).
3. C. Werner, S. Troyanov, E. Kemnitz, and H. Worzala, Z. Anorg. Allg. Chem. **622**, 337 (1996).
4. S. Troyanov, C. Werner, E. Kemnitz, and H. Worzala, Z. Anorg. Allg. Chem. **621**, 1617 (1995).
5. M. A. Zakharov, S. I. Troyanov, and E. Kemnitz, Zh. Neorg. Khim. **44** (8), 1242 (1999).
6. M. A. Zakharov, S. I. Troyanov, V. B. Rybakov, *et al.*, Zh. Neorg. Khim. **44** (3), 448 (1999).
7. N. P. Kozlova, L. D. Iskhakova, V. V. Marugin, *et al.*, Zh. Neorg. Khim. **35** (6), 1363 (1990).
8. *International Tables of Crystallography*, Ed. by A. J. C. Wilson (Kluwer, Dordrecht, 1992), Vol. C, p. 383.
9. G. M. Sheldrick, *SHELXL93: Program for Crystal Structure Refinement* (University of Göttingen, Göttingen, 1993).
10. I. Olovsson and P.-G. Jönsson, *The Hydrogen Bond—Recent Development in Theory and Experiments*, Ed. by P. Schuster *et al.* (North-Holland, Amsterdam, 1976), Vol. II, Chap. 8, p. 393.
11. J. Kroon, J. A. Kanters, and A. F. Peerdeman, Nature (London), Phys. Sci. **229**, 120 (1971).
12. A. McAdam, M. Currie, and J. C. Speakman, J. Chem. Soc., 1994 (1971).
13. A. L. MacDonald, J. C. Speakman, and D. Hadži, J. Chem. Soc. Perkin Trans. **2**, 825 (1972).
14. M. Currie, J. C. Speakman, J. A. Kanters, and J. Kroon, J. Chem. Soc. Perkin Trans. **2**, 1549 (1975).
15. S. I. Troyanov, I. V. Morozov, M. Reehuis, and E. Kemnitz, Z. Kristallogr. **215**, 377 (2000).

Translated by L. Man

Crystallography Reports, Vol. 47, No. 1, 2002, pp. 33–38. Translated from Kristallografiya, Vol. 47, No. 1, 2002, pp. 40–45.

STRUCTURE OF INORGANIC COMPOUNDS

Atomic Structure and Enormous Anisotropy of Thermal Expansion in NiSi Single Crystals. I. Refinement of Structure Models

M. Kh. Rabadanov* and M. B. Ataev**

** Shubnikov Institute of Crystallography, Russian Academy of Sciences, Leninskiĭ pr. 59, Moscow, 117333 Russia*

*** Dagestan State University, Makhachkala, Dagestan, Russia*

e-mail: rab_mur@ns.crys.ras.ru

Received February 26, 2001; in final form, April 13, 2001

Abstract—The atomic structure of NiSi single crystals has been studied by the methods of X-ray diffraction analysis at 295 and 418 K. The refinement of the structure models with due regard for anharmonicity of atomic vibrations revealed the pronounced anisotropy of thermal vibrations and the considerable contribution of the fourth-order anharmonicity. The maps of the probability density function of atomic displacements and single-particle potentials of both atoms were constructed. *© 2002 MAIK "Nauka/Interperiodica".*

INTRODUCTION

It has been established that nickel monosilicide crystals possess giant anisotropy of thermal expansion and that with an increase of the temperature, the crystals are "compressed" along one of the crystallographic axes [1]. At the same time, the information about the crystallochemical characteristics of these single crystals is rather scarce [2–4]. Therefore it was of considerable interest to make precision structural studies of the crystals at different temperatures, analyze the relationship between the structural characteristics and the enormous anisotropy of their thermal expansion, and establish the physical sense of the thermal parameters (including the anharmonic ones) obtained in the LS refinement of the structure model. The first part of our article presents the results of the X-ray diffraction studies of orthorhombic NiSi single crystals at the temperatures of 295 and 418 K. We consider the relationships between the thermal parameters obtained and the thermal expansion. We also plan the further analysis of the relation between the structural characteristics of the crystals and enormous anisotropy of thermal expansion observed.

EXPERIMENTAL

We studied a NiSi specimen (0.298(9) mm in diameter) chosen from NiSi single crystals rolled to the spherical shape, which gave the best diffraction pattern. The experimental sets of diffraction reflections were obtained on a CAD-4F Enraf Nonius diffractometer (MoK_α radiation, $\theta/2\theta$ scan) at 295 and 418 K. A special high temperature attachment used in experiments was described elsewhere [5]. The stability of the diffractometer and the functioning of the high-temperature attachment was checked each 60 minutes by measuring the intensities of two reference reflections. At 418 K, the specimen orientation was checked and refined upon measurement of each 200 reflections. The experimental conditions during the refinement of the unit-cell parameters are indicated in Table 1. It was established that the *b*-parameter considerably decreased, whereas the *a*- and *c*-parameters noticeably increased with an increase of the temperature from 295 to 418 K accompanied by an increase of the unit-cell volume. The intensities of the recorded reflections were corrected for the Lorentz factor, polarization, and

Table 1. Experimental conditions and refined unit-cell parameters for NiSi single crystals

T, K	295	418
a, Å	5.1752(7)	5.194(1)
b, Å	3.3321(5)	3.3232(8)
c, Å	5.6094(9)	5.629(1)
V, Å^3	96.73(1)	97.15(1)
μr	3.002	2.989
Scanning range	$1.2 + 0.35\tan\theta$	$1.2 + 0.35\tan\theta$
Detector window, mm	3×1	3×1
$\sin\theta/\lambda$, Å^{-1}	0.13–1.10	0.13–1.10
Number of measured reflections	2986	3085
Number of independent reflections	435	432
R_{av}	1.61	1.92

Table 2. Results of the refinement of three structure models of a NiSi single crystal (b_{ij}, Å^2; c_{ijk}, Å^3; d_{ijkl}, Å^4)

T, K		295			418		
		Model 1	Model 2	Model 3	Model 1	Model 2	Model 3
	K	8.735	8.741	8.754(10)	8.576	8.556	8.573(10)
Ni:	x/a	.00779	.00792	.00785(2)	.00757	.00757	.00757(2)
	y/b	.25	.25	.25	.25	.25	.25
	z/c	.18752	.18757	.18731(2)	.18772	.18773	.18772(2)
	b_{11}	.00249	0.00249	.00237(4)	.00528	0.00524	.00507(4)
	b_{22}	.00631	0.00635	.00667(4)	.00989	0.00985	.01026(4)
	b_{33}	.00425	0.00426	.00436(4)	.00682	0.00679	.00661(4)
	b_{13}	–.00003	–0.00003	–.00002(1)	–.00003	–0.00002	–.00001(1)
	c_{111}		0.00095	.00030(22)		–0.00019	–.00027(22)
	c_{333}		–0.00018	–.00195(21)		0.00016	–.00025(24)
	c_{122}		0.00009	.00008(15)		–0.00039	–.00015(22)
	c_{113}		0.00034	–.00018(16)		0.00010	.00013(17)
	c_{133}		0.00035	.00026(16)		0.00037	.00044(18)
	c_{223}		0.00048	–.00011(16)		–0.00014	–.00012(20)
	d_{1111}			–.00050(76)			–.0034(6)
	d_{2222}			.0061(8)			.0070(9)
	d_{3333}			.0017(7)			–.0035(7)
	d_{1113}			.00009(38)			.00062(48)
	d_{1122}			–.00097(44)			–.00016(44)
	d_{1133}			–.00059(46)			.00004(45)
	d_{1223}			.00092(25)			.00068(38)
	d_{1333}			–.00066(41)			–.00060(52)
	d_{2233}			–.0000(5)			–.00047(52)
Si:	x/a	.32128	.32148	.32152(6)	.32099	.32093	.32090(6)
	y/b	.75	.75	.75	.75	.75	.75
	z/c	.08250	.08230	.08166(6)	.08163	.08166	.08168(6)
	b_{11}	.00335	0.00335	.00304(8)	.00621	0.00619	.00599(8)
	b_{22}	.00557	0.00560	.00583(7)	.00846	0.00849	.00878(8)
	b_{33}	.00569	0.00572	.00585(8)	.00882	0.00871	.00892(8)
	b_{13}	–.00024	–0.00021	–.00022(3)	–.00036	–0.00036	–.00029(3)
	c_{111}		0.00138	.0016(6)		–0.00026	–.00109(61)
	c_{333}		–0.00088	–.0048(6)		0.00134	.00179(71)
	c_{122}		0.00049	.0008(4)		0.00017	.00042(51)
	c_{113}		–0.00021	–.0017(4)		–0.00016	–.00022(43)
	c_{133}		–0.00018	.0003(4)		–0.00033	–.00032(50)
	c_{223}		–0.00090	–.0024(4)		–0.00112	–.00063(51)
	d_{1111}			–.0043(15)			–.0012(18)
	d_{2222}			.0019(15)			.0062(18)
	d_{3333}			.0011(15)			.0047(17)
	d_{1113}			.0006(11)			–.0007(12)
	d_{1122}			.0004(9)			.0003(11)
	d_{1133}			–.0012(9)			–.0015(10)
	d_{1223}			–.0007(7)			.0001(10)
	d_{1333}			.0009(11)			.0031(13)
	d_{2233}			.0015(9)			–.0005(10)
	R_w	.0124	.0119	.0104	.0115	.0111	.0103
	R	.0104	.0101	.0088	.0113	.0110	.0104
	S	1.42	1.41	1.27	1.32	1.31	1.25

absorption. The lack of the necessary information did not allow the introduction of the correction for thermal diffuse scattering (TDS).

REFINEMENT OF THE MODELS OF THE ATOMIC STRUCTURE AND DISCUSSION OF RESULTS

The structure models were refined by the PROMETHEUS package of programs [6, 7]. The orthorhombic MnP (or FeP) structure type characteristic of the NiSi structure is pseudohexagonal and can be described as a distorted NiAs structure type. The space group is *Pnma* with four formula units in the unit cell, $Z = 4$. Both crystallographically independent atoms occupy special 4*c* positions with the symmetry *m* and the coordinates Ni (x, 0.25, z) and Si (x, 0.75, z)

The refinement was started with the harmonic model and isotropic atomic thermal vibrations. The parameters to be refined were the scale factor K, the extinction parameter, two positional parameters and one isotropic thermal parameter for each atom (altogether eight parameters). At both temperatures, this model was refined only to $R = 5\%$. The allowance for the anisotropy of thermal vibrations (hereafter referred to as model 1) reduced the reliability factors to ~2%, which showed that the atomic thermal displacements in the single crystals studied are essentially anisotropic. In this model, we considered four thermal parameters, b_{11}, b_{22}, b_{33}, and b_{12}, for each atom. The extinction parameter for all the models was introduced in the Becker–Coppens formalism (isotropic type 1, Lorentzian distribution of the blocks of mosaics), because all the other methods of allowance for extinction yielded higher values of reliability factors.

It was of considerable interest to analyze the results of the refinement of the anharmonic models and establish the relationship between the anharmonic parameters and the specific characteristics of thermal expansion. The models with due regard for only the third-order anharmonicity (model 2) and the third- and fourth-order anharmonicity (model 3) were refined using the complete set of the structure factors and only the sets of high-order reflections. For a more reliable analysis, the refinement was performed by three sets of high-order reflections with $(\sin\theta/\lambda)_{\min} \geq 0.7$, 0.8, and 0.9 Å^{-1}. The comparative analysis of the results obtained showed that the model parameters were almost independent of $(\sin\theta/\lambda)_{\min}$. In the further analysis, we used the results obtained in the refinement by the sets of high-order reflections with $(\sin\theta/\lambda) \geq 0.8$ Å^{-1} (Table 2).

In Table 2, the standard deviations of the refined parameters are listed only for model 3, because the values of the parameters common to all the models were almost the same. For a more convenient analysis, we retained all the anharmonic parameters admitted by the symmetry of the atomic positions despite the fact that some of these parameters were determined with considerable errors. Table 2 also lists the R/R_w and S factors for each model.

The scale factor and the extinction parameter were refined over the complete set of reflections, whereas the tensors of the thermal parameters were refined only by the sets of high-order reflections. In the refinement of model 3, considerable correlations were established only between the scale factor, harmonic thermal and anharmonic fourth-order thermal parameters. In this case, an increase of the scale factor resulted in the displacement of the fourth-order anharmonic parameters toward negative values. It should also be indicated that the refinement of models 1 and 2 showed no considerable correlations, and the scale factors for these models were almost the same in all the refinement procedures. However, the refinement of model 3 with different K different values (e.g., overestimated by 5–6σ) often resulted in essentially different values, which were more pronounced at $T = 295$ K, probably, because of insignificant anharmonicity. The refinement of the model parameters at the fixed overestimated K ($K = 8.85$, whereas the initial value was $K = 8.74(2)$) at the temperature $T = 295$ K resulted in such an increase of the negative contributions of the fourth-order anharmonicity parameters to the probability density function (PDF) of the displacements of Ni atoms from their equilibrium positions that the values in the PDF center were negative. In this case, the R_w/R factors increased only slightly (by 0.02–0.03). This example shows the necessity of a careful interpretation of the anharmonic parameters obtained and the analysis of the refined anharmonic models.

The analysis of the harmonic thermal parameters obtained shows that, first, only the diagonal parameters b_{11}, b_{22}, and b_{33} are significant and, second, the diagonal parameter b_{22} has the maximum value for both atoms (for Ni atoms, it exceeds the b_{33} value by a factor of 1.5). However, with an increase in the temperature, the b_{11}-value increased by a factor of about 2.5, the b_{33} value, by factor of about 2, whereas b_{22}, only by a factor of about 1.5.

The ellipsoids of atomic thermal vibrations of Ni atoms in model 1 are smaller and are rotated about the crystallographic axes by smaller angles than the ellipsoids of Si atoms. The thermal vibrations of Ni atoms are characterized by a more pronounced anisotropy than those of Si atoms. The ellipsoids of thermal vibrations of Si atoms are close to biaxial. For Ni atoms, the root-mean square deviation along the crystallographic direction are maximal along the *y*-axis and the ellipsoid is elongated in the direction of this axis, whereas for Si atoms, the considerable root-mean square deviations were observed along both *y*- and *z*-axes.

Table 2 shows that the third-order anharmonicity of thermal vibrations is insignificant, whereas some fourth-order parameters have considerable values. In this case, the parameters d_{2222} for both atoms at both

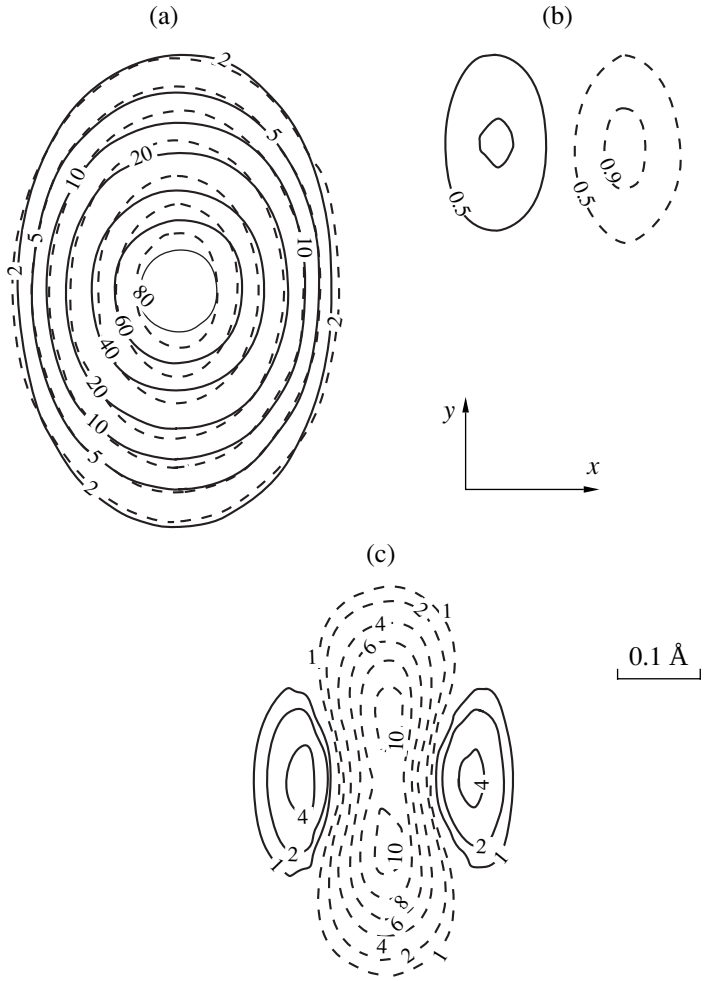

Fig. 1. (a) Probability density function (PDF) of displacements of atoms from their equilibrium positions in the harmonic (dashed line) and anharmonic (solid line) approximations and the contribution of the (b) third- and (c) fourth-order anharmonicity to the PDF (dashed line corresponds to the negative values) for a Ni atom in the *xy* plane in NiSi crystals at 418 K ($z/c = 0.188$).

temperatures are positive, whereas d_{1111} and d_{3333} have either low values or are negative. This result was obtained in the refinement with the use of both sets of high-order reflections and the complete set of reflections.

The results obtained were interpreted physically by constructing the probability density functions (PDFs) and calculating the contributions of anharmonicity to these functions for both atoms in the *xy, yz,* and *xz* planes at both temperatures. As an example, Figures 1 and 2 show the PDFs for Ni and Si atoms in the harmonic and anharmonic approximations (Figs. 1a, 2a) and the contribution of the third- (Figs. 1b, 2b) and fourth-order (Figs. 1c, 2c) anharmonicity in the *xy* plane at $T = 418$ K. The PDF values and the contribution of anharmonicity are indicated in percent with respect to the PDF value in the center of equilibrium. In all the cases, we observed deviations from the harmonic approximation which correlated with the specific features of the atomic environment. The contributions of the fourth-order anharmonicity prevail over those of the third-order anharmonicity. The analysis of the PDF maps obtained shows that the allowance for the anharmonicity of atomic displacements reduces the PDF values for both atoms along the direction of the negative expansion (*b*-axis) and increase them along two other axes. If the values of the anharmonicity parameters are overestimated (which can be caused by correlations, see above), these effects become even more pronounced.

The knowledge of the PDFs of atomic displacements from their equilibrium positions allows the calculation of single-particle potentials of atoms. Figure 3 shows the single-particle potentials of Ni and Si atoms along the crystallographic *x*-, *y*-, and *z*-axes at $T = 418$ K. It is seen that the single-particle potentials of both atoms with allowance for anharmonicity along the *y*-axis are more steep than those calculated in the harmonic approximation, whereas along the *x*- and *z*-axes, the potentials in the anharmonic approximation are smoother. Thus, the anharmonicity contributions to the

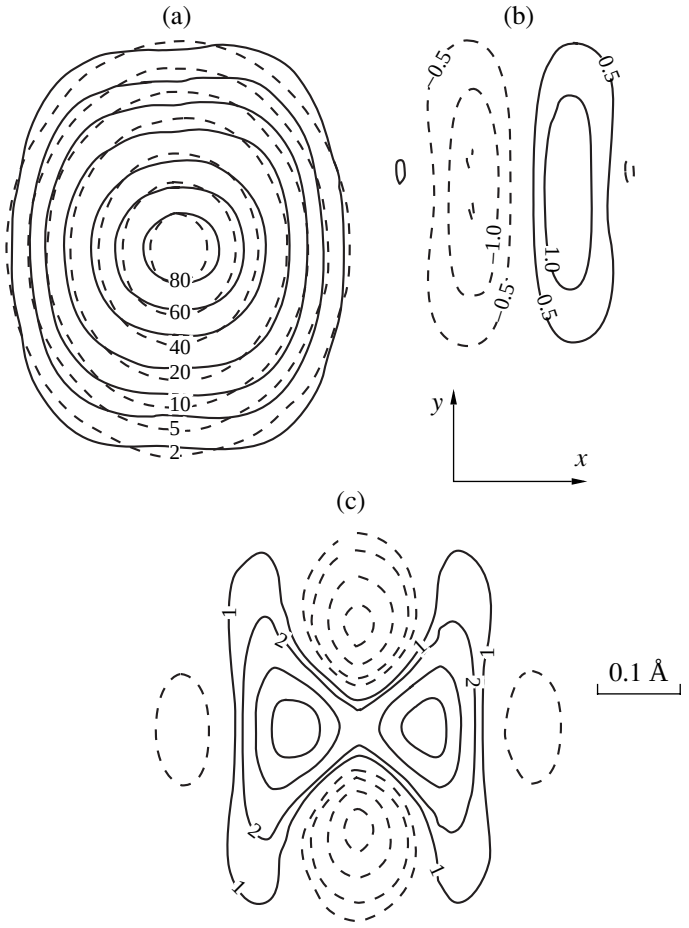

Fig. 2. (a) Probability density function of the displacement of Si atoms in the *xy* plane in NiSi at 418 K ($z/c = 0.082$) in the harmonic (dashed line) and anharmonic (solid line) approximations and the contributions of the (b) third- and (c) fourth-order anharmonicity to the PDF (dashed line corresponds to negative values).

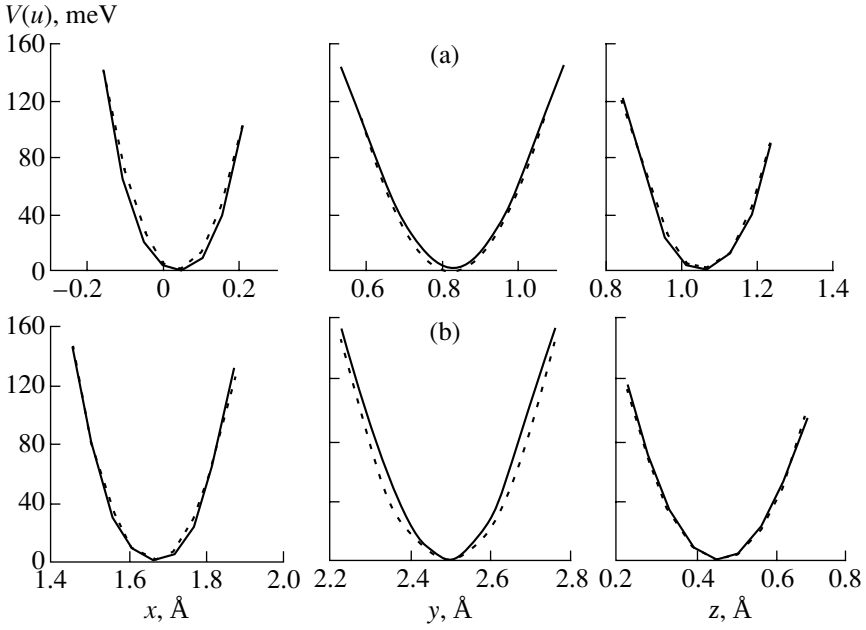

Fig. 3. Single-particle potential of (a) Ni and (b) Si atoms along the crystallographic *x*-, *y*-, and *z*-axes at $T = 418$ K ($kT = 36$ MeV). The dashed line corresponds to the harmonic approximation.

single-particle potentials for both atoms along the *y*-axis and the *x*- and *z*-axes have opposite signs, which is consistent with the specific features of thermal expansion of the crystals studied.

Thus, the refinement of the models of the atomic structure provided the determination of relative coordinates and the parameters of thermal vibrations of atoms in NiSi crystals at 295 and 418 K. It is established that the thermal vibrations of the Ni and Si atoms are strongly anisotropic and that the ellipsoids of their thermal vibrations are elongated in the direction of the *y*-axis, whereas the linear expansion coefficient along the *y*-axis is negative. The results obtained in the refinement of the anharmonic models are consistent with the experimentally observed thermal expansion and allow its better understanding and interpretation.

ACKNOWLEDGMENTS

The authors are grateful to G.I. Guk for the specimens and I.A. Verin for his help in the performance of experiments.

REFERENCES

1. S. M. Barmin and A. A. Frolov, Fiz. Tverd. Tela (Leningrad) **32** (5), 1535 (1990) [Sov. Phys. Solid State **32**, 897 (1990)].
2. K. Toman, Acta Crystallogr. **4** (5), 462 (1951).
3. V. S. Neshpor, Kristallografiya **11** (3), 466 (1961) [Sov. Phys. Crystallogr. **6**, 370 (1961)].
4. E. I. Gladyshevskiĭ, *Crystal Chemistry of Silicides and Germanides* (Metallurgiya, Moscow, 1971).
5. F. Tuinstra and G. M. Fraase Storm, J. Appl. Crystallogr. **11**, 257 (1978).
6. U. Zucker, E. Perenthaler, W. F. Kuhs, *et al.*, J. Appl. Crystallogr. **16**, 398 (1983).
7. L. A. Muradyan, M. I. Sirota, I. P. Makarova, and V. I. Simonov, Kristallografiya **30** (2), 258 (1985) [Sov. Phys. Crystallogr. **30**, 148 (1985)].

Translated by L. Man

Crystallography Reports, Vol. 47, No. 1, 2002, pp. 39–42. Translated from Kristallografiya, Vol. 47, No. 1, 2002, pp. 46–49.

STRUCTURE OF INORGANIC COMPOUNDS

Determination of the Crystal Structure of Khanneshite by the Rietveld method

Yu. V. Belovitskaya*, I. V. Pekov*, E. R. Gobechiya*, Yu. K. Kabalov*, and J. Schneider**

** Department of Geology, Moscow State University, Vorob'evy gory, Moscow, 119899 Russia*

e-mail: mineral@geol.msu.ru

*** Institute for Crystallography and Applied Mineralogy, Ludwig Maximillian University, Theresienstrasse 41, D-80333 Munich, Germany*

Institut für Kristallographie und Angewandte Mineralogie, Universität München

Received October 4, 1999; in final form, February 22, 2001

Abstract—The crystal structure of khanneshite $(Na_{2.75}Ca_{0.23})_{2.98}(Ba_{1.08}Sr_{0.63}Ca_{0.46}Ce_{0.46}La_{0.18}Nd_{0.15}Pr_{0.04})_{3.00} \cdot (CO_3)_5$ found in carbonatites from the Khibiny massif (the Kola Peninsula) was solved by the Rietveld method. The X-ray diffraction data were collected on a focusing STOE-STADIP diffractometer equipped with a bent Ge(111) primary-beam monochromator ($\lambda MoK\alpha_1$ radiation, $2.00° < 2\theta < 54.98°$, 311 reflections). All the calculations were performed within the sp. gr. $P6_3mc$; $a = 10.5790(1)$ Å, $c = 6.5446(1)$ Å, $V = 634.31(1)$ Å^3, $R_P = 2.38$, $R_{wp} = 3.26$, $R_B = 1.42$, $R_F = 1.79$. The atoms of the cations were refined with anisotropic thermal parameters. © *2002 MAIK "Nauka/Interperiodica".*

INTRODUCTION

Khanneshite (Na, Ca)$_3$(Ba, Sr, *TR*, Ca)$_3$(CO$_3$)$_5$ belongs to the burbankite structural family including hexagonal and monoclinic pseudohexagonal carbonates of the general formula $A_{3-4}B_{2-3}(CO_3)_5$, where *A* = Na, Ca, or □ and *B* = Sr, Ba, *TR*, or Ca.

Khanneshite, the Ba-dominant member of the family, is the most rare of all the burbankite-like minerals. This mineral was discovered in the Khanneshin carbonatite complex (Afghanistan) in 1982. After the first publication, a number of questions remained open, because the original material analyzed by the wet method was substantially contaminated with other carbonates and barite. Based on the X-ray diffraction powder pattern, the authors discovered Khanneshite assumed that the new mineral is structurally similar to burbankite $(Na,Ca)_3(Sr,Ca,TR,Ba)_3(CO_3)_5$, determined its unit-cell parameters, and interpreted them within the hexagonal system ($a = 10.65$ Å, $c = 6.58$ Å) [1].

We revised the structure data based on the results of local X-ray spectral analysis of a holotypic specimen of khanneshite from Khanneshin. On the one hand, our investigation confirmed the existence of the Ba-dominant chemical analogue of burbankite and, on the other hand, demonstrated that the substance under study occurred as thin concretions of this phase with barium-rich burbankite, mckelveyite, and barite [2]. This material was unsuitable for precision X-ray diffraction study. Hence, the structure type of khanneshite remained unknown. We found this mineral also in carbonatites from the Khibiny alkaline massif (the Kola Peninsula). The latter specimens appeared to be homogeneous [2]. However, all the attempts to study several seemingly single-crystal (according to the optical characteristics) grains of khanneshite from the Khibiny massif by the Laue method have failed: the Laue patterns taken from these grains had no reflections at all. At the same time, the X-ray diffraction powder patterns of the mineral had high quality, and their reflections were adequately indexed within a hexagonal unit cell of the burbankite type. In this connection, we used the Rietveld method for determining the structure of this mineral.

EXPERIMENTAL

Khanneshite from the Khibiny massif was discovered in the only fragment of a core sample from a well on the shore of the Tul'ilukht gulf located in the east part of the massif [2]. The mineral was found in the

Table 1. Chemical composition (wt %) of khanneshite

Na_2O	11.86	Ce_2O_3	10.46
CaO	5.37	Pr_2O_3	1.01
SrO	9.04	Nd_2O_3	3.60
BaO	22.99	CO_2	(30.59)
La_2O_3	4.07	Total	98.99

Note: The CO_2 concentration was calculated from the stoichiometry.

Table 2. Unit-cell parameters and characteristics of the refinement of the khanneshite structure by the Rietveld method

a, Å	10.5790(1)	R_p	2.38
c, Å	6.5446(1)	R_{wp}	3.26
c/a	0.6186	R_{exp}	5.34
V, Å^3	634.31(1)	R_B	1.42
Sp. gr.	$P6_3mc$	R_F	1.79
2θ range, deg	2.00–54.98	s*	1.55
Number of reflections	311	DWD**	0.74
Number of parameters to be refined	54	σ_x***	1.814

* $s = R_{wp}/R_{exp}$, where R_{exp} is the expected R_{wp} value.
** DWD is the Durbin–Watson statistics [9].
*** The multiplier in the calculations of standard deviations [10].

form of irregularly shaped grains up to 2 mm in diameter and the bright carrot-red aggregates of such grains located in a zonal carbonate vein. Khanneshite occurs in association with magnetite, calcite, and dawsonite. The chemical composition of khanneshite (Table 1) was determined by X-ray spectral analysis (a Camebax microbeam instrument; analyst I.M. Kulikova, Institute of Mineralogy, Geochemistry, and Crystal Chemistry of Rare Elements).

X-ray diffraction study was performed with the use of homogeneous khanneshite grains. The X-ray spectrum of a powdered sample was measured on a focusing STOE-STADIP diffractometer equipped with a bent Ge(111) primary-beam monochromator (λMo$K\alpha_1$ radiation, $2.00° < 2\theta < 54.98°$, 311 reflections). All the calculations were performed with the use of the WYRIET program (version 3.3) [3] within the sp. gr. $P6_3mc$. The atomic coordinates reported in [4] were used as the starting model. The ionic scattering curves were used. The peak profiles were approximated by the Pearson-VII function with 6FWHM. The asymmetry was refined at $2\theta < 40°$. The refinement was made with the gradual addition of parameters to be refined with the continuous automatic modeling of the background until the attainment of stable R factors. The isotropic refinement converged to the R_{wp} factor of 3.40%.

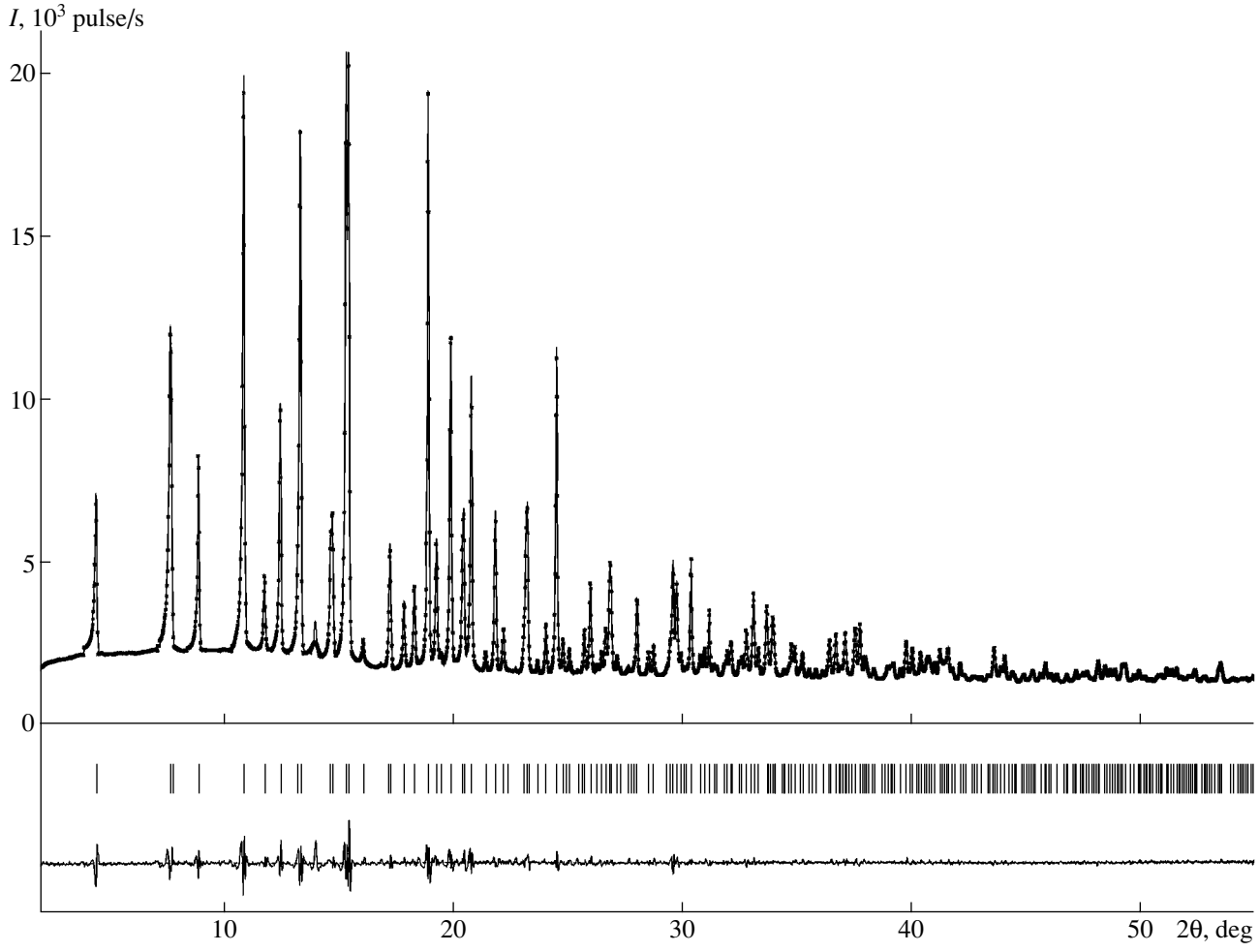

Fig. 1. Experimental (solid line) and calculated (dots) X-ray diffraction spectra of khanneshite.

Table 3. Coordinates, thermal parameters (Å^2), and position occupancies in the khanneshite structure

Atom	Characteristic	Value	Atom	Characteristic	Value
A	*x*	0.5246(5)	C(3)	*x*	1/3
	y	0.4754(5)		*y*	2/3
	z	0.308(2)		*z*	0.50(2)
	B_j	1.1(2)		B_j	3(1)
	q (Na)	2.57(4)	O(1)	*x*	0.379(1)
	q (Ca)	0.43(4)		*y*	0.085(1)
B	*x*	0.8403(2)		*z*	0.629(2)
	y	0.1597(2)		B_j	1.6(3)
	z	0	O(2)	*x*	0.928(1)
	B_j	0.85(3)		*y*	0.072(1)
	q (Sr)	0.63(1)		*z*	0.344(3)
	q (*TR* + Ba)	1.90(1)		B_j	3.7(6)
	q (Ca)	0.46(1)	O(3)	*x*	0.405(1)
C(1)	*x*	0.799(1)		*y*	0.595(1)
	y	0.201(1)		*z*	0.486(8)
	z	0.541(6)		B_j	1.9(4)
	B_j	1.4(8)	O(4)	*x*	0.774(1)
C(2)	*x*	0		*y*	0.226(1)
	y	0		*z*	0.359(3)
	z	0.838(9)		B_j	2.4(5)
	B_j	1(1)			

Note: The calculations for *TR* and Ba atoms were made with the use of the *f*-curve for Ba.

Some selected characteristics of X-ray data collection and the results of the refinement of the khanneshite structure with anisotropic (the *A* and *B* cations) and isotropic (the oxygen and carbon atoms) thermal parameters are given in Table 2. The experimental (solid line) and the calculated (dots) X-ray spectra of khanneshite are shown in Fig. 1. The unindexed reflection (2θ = 14.00°, *d* = 2.91 Å, *I* = 4 arb. units) apparently belongs to a mineral–impurity (probably, clinopyroxene). The atomic coordinates, the isotropic thermal parameters, and the occupancies of the positions in the khanneshite structure are listed in Table 3.

RESULTS AND DISCUSSION

Similar to the burbankite structure [5], the crystal structure of khanneshite contains two independent cationic positions corresponding to the eight-vertex *A*-polyhedron (Na and Ca) and the ten-vertex *B*-polyhedron (Ba, Sr, *TR*, and Ca), and three types of triangular carbonate groups (C(1), C(2), and C(3)) having different orientations (Fig. 2). The average distances in the polyhedra are as follows: *A*–O, 2.50 Å; *B*–O, 2.71 Å; C(1)–O, 1.27 Å; C(2)–O, 1.32 Å; and C(3)–O, 1.31 Å. The *A* and *B* positions are statistically occupied by the corresponding cations.

The unit-cell parameters of khanneshite are larger than those of burbankite (*a* = 10.48–10.53 Å, *c* = 6.48–6.53 Å [4, 5]) due to the incorporation of large barium cations. This also explains the fact that the average interatomic distance in the ten-vertex *B*-polyhedron in khanneshite (2.71 Å) is the largest one of all the analogous distances in the structures of other known representatives of the burbankite family: burbankite (2.68–2.70 Å) [4, 5, 6], calcioburbankite (2.67 Å) (our data), remondite-(Ce) (2.63 Å) [7], and petersenite-(Ce)

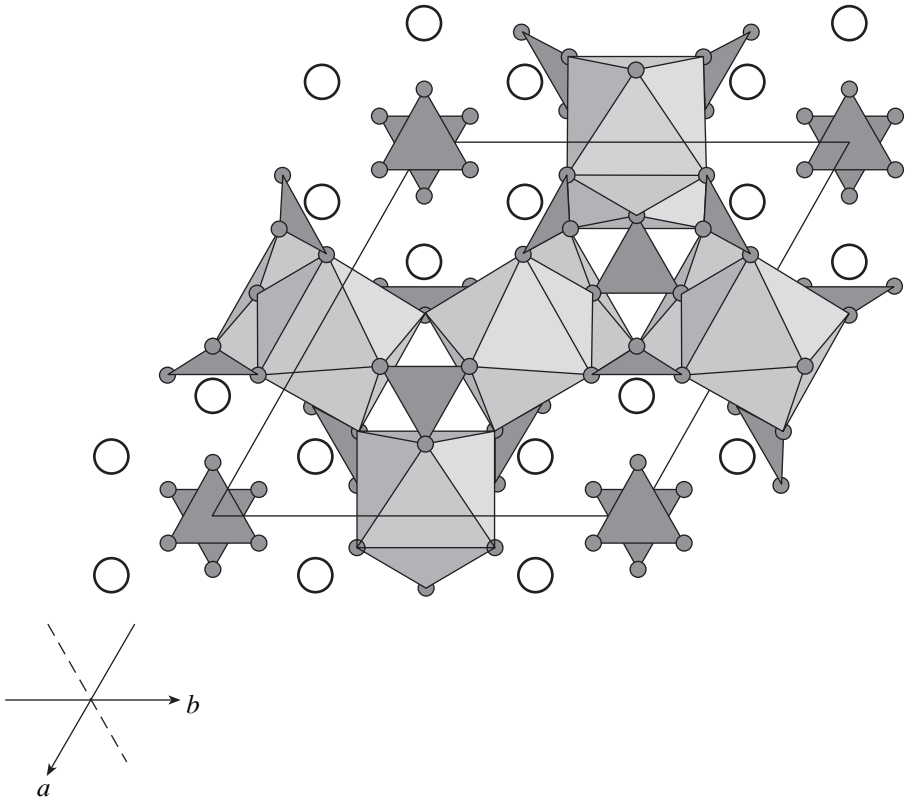

Fig. 2. The khanneshite structure projected onto the *ab* plane; the eight-vertex *A*-polyhedra are indicated by shaded circles, the centers of the ten-vertex *B*-polyhedra are indicated by empty circles, and the CO_3^{-2} triangular anions are indicated by solid circles.

(2.59 Å) [8]. In the transition from burbankite to khanneshite, the physical properties also change because of the replacement of Sr by the heavier Ba cation. The density and the refractive indices in this series increase regularly.

CONCLUSIONS

Khanneshite and burbankite form a continuous series of compositions [2]. Moreover, these two minerals are isostructural ($P6_3mc$). Thus, contrary to the replacement of Sr by *TR*, the incorporation into the structure of larger Ba ions instead of Sr does not change the structural type. Indeed, the burbankite-like mineral remondite $Na_3(TR, Sr, Ca, Na)_3(CO_3)_5$, having a similar structural motif, is characterized by the monoclinic symmetry ($P2_1$) [7]. However, on the whole, the burbankite structural type is unfavorable for barium-rich compositions. This is evidenced by the fact that khanneshite occurs very rarely in nature against the background of the rather often occurrence of burbankite forming commercially important deposits.

REFERENCES

1. G. K. Eremenko and V. A. Vel'ko, Zap. Vseross. Mineral. O–va. **111** (1), 321 (1982).
2. I. V. Pekov, N. V. Chukanov, and Yu. V. Belovitskaya, Zap. Vseross. Mineral. O–va. **127** (2), 92 (1998).
3. J. Schneider, in *Profile Refinement on IBM-PC's: IUCr International Workshop on the Rietveld Method, Petten, 1989*, p. 71.
4. H. Effenberger, F. Kluger, H. Paulus, and E. R. Wolfel, Neues Jahrb. Mineral., Monatsh. **4**, 161 (1985).
5. A. A. Voronkov and N. G. Shumyatskaya, Kristallografiya **13**, 246 (1968) [Sov. Phys. Crystallogr. **13**, 192 (1968)].
6. Yu. V. Belovitskaya, I. V. Pekov, and Yu. K. Kabalov, Kristallografiya **45**, 32 (2000) [Crystallogr. Rep. **45**, 26 (2000)].
7. P. D. Ginderow, Acta Crystallogr., Sect. C: Cryst. Struct. Commun. **45**, 185 (1989).
8. J. D. Grice, J. van Velthuizen, and R. A. Gault, Can. Mineral. **32**, 405 (1994).
9. R. Hill and H. Flack, J. Appl. Crystallogr. **20**, 356 (1987).
10. J.-F. Berar and P. Lelann, J. Appl. Crystallogr. **24**, 1 (1991).

Translated by T. Safonova

Crystallography Reports, Vol. 47, No. 1, 2002, pp. 43–46. Translated from Kristallografiya, Vol. 47, No. 1, 2002, pp. 50–53.

STRUCTURE OF INORGANIC COMPOUNDS

Crystal Structure of New Micalike Titanosilicate—Bussenite, $Na_2Ba_2Fe^{2+}[TiSi_2O_7][CO_3]O(OH)(H_2O)F$

H. Zhou*, R. K. Rastsvetaeva, A. P. Khomyakov***, Z. Ma****, and N. Shi******

** China University of Geosciences, Wuhan, 430074 China*

*** Shubnikov Institute of Crystallography, Russian Academy of Sciences, Leninskiĭ pr. 59, Moscow, 117333 Russia*

e-mail: rast@ns.crys.ras.ru

**** Institute of Mineralogy, Geochemistry, and Crystal Chemistry of Rare Elements, ul. Veresaeva 15, Moscow, 121357 Russia*

***** China University of Geosciences, Beijing, 100083 China*

Received April 16, 2001

Abstract—The crystal structure of mineral bussenite, $Na_2Ba_2Fe[TiSi_2O_7][CO_3]O(OH)(H_2O)F$, found in the Khibiny massif (the Kola Peninsula) has been determined. The parameters of the triclinic unit-cell are a = 5.399(3) Å, b = 7.016(9) Å, c = 16.254(14) Å, $\alpha = 102.44(8)°$, $\beta = 93.18(6)°$, $\gamma = 90.10(7)°$, sp. gr. $P\bar{1}$, R = 0.054 for 1418 reflections with $|F| > 2.5\sigma(F)$. The mineral studied belongs to the family of layered titanosilicates, in which, unlike the sulfate- and phosphate-containing representatives of this family, the interlayer spaces are filled with carbonate groups. © *2002 MAIK "Nauka/Interperiodica".*

A peculiar group of natural compounds crystallizing from derivates of nepheline–syenite magmas highly supersaturated with alkaline and volatile components includes hybrid minerals with the structures consisting of alternating blocks of essentially silicate and salt compositions [1, 2]. We studied the crystal structure of the new mineral, bussenite [2–4], the first carbonate-containing representative of this group.

Bussenite was discovered in a sodalite–natrolite–calcite veinlet from the Khibiny alkaline massif (the Kola Peninsula). The mineral occurs as curved yellowish-brown micalike platelets 2–5 cm in length and 0.5 mm in thickness. The mineral is characterized by perfect cleavage along the (001) plane and moderate cleavage along the (110) and (1–10) planes. Both visually and in a microscope, bussenite resembles high-barium lamprophyllite Na(Sr, Ba)(Ti, Fe)Ti$[Si_2O_7](O, OH)_2$ [5]. However, the new mineral differs from the latter by a number of characteristic features. In particular, the IR spectrum of the new mineral has absorption bands at 1410 and 1445 cm^{-1} attributed to vibrations of carbonate groups. The chemical composition of bussenite corresponds (the cation sum is 8; Z = 2) to the empirical formula $(Na_{1.94}K_{0.09})(Ba_{1.25}Sr_{0.44}Ca_{0.19})(Fe^{2+}_{0.63}Mn_{0.44}) \cdot (Ti_{0.97}Nb_{0.05}) \cdot Si_2O_{7.27}(CO_3)_{0.87}(OH)_{2.89}F_{0.98}$.

The investigation of the mineral structure was hindered by the absence of a single crystal suitable for X-ray diffraction analysis. Finally, the collaborative study undertaken by Russian and Chinese researchers was crowned with the first results of the structure investigation of bussenite reported earlier [3]. The X-ray diffraction study performed on an automated single-crystal AFC5R diffractometer demonstrated that the mineral possesses the triclinic structure, which was solved by the Patterson methods and refined within the acentric sp. gr. $P1$ to R = 0.070 by the SHELXL93 program package. Thus, the structural motif of the mineral and its general crystallochemical formula were established. However, the formula contradicted a number of essential details of the chemical analysis.

The subsequent refinement of the structure based on the construction of mixed scattering curves for some cationic positions was performed using the AREN program [6]. This allowed us to remove the above-mentioned inconsistencies and to obtain the adequate crys-

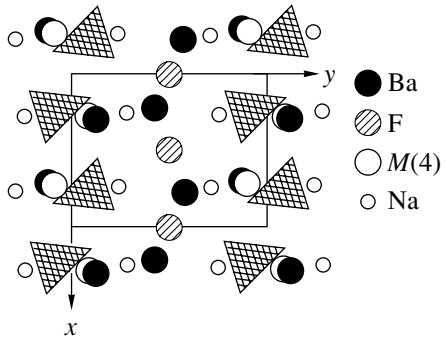

Fig. 1. A bussenite layer having the salt composition projected onto the (001) plane; CO_3 groups are shown by hatched triangles; large cations are indicated by circles.

Table 1. Structural data and details of X-ray diffraction study

Characteristic	Value
Unit-cell parameters, Å, deg	$a = 5.399(3)$, $b = 7.016(9)$, $c = 16.254(14)$, $\alpha = 102.44(8)$, $\beta = 93.18(6)$, $\gamma = 90.10(7)$
Unit-cell volume, Å^3	$V = 600.3$
Sp. gr.; Z	$P\bar{1}$; 1
Density ρ_{exp}, ρ_{cal}, g/cm^3	3.63(2), 3.65
Hardness	4
Radiation; λ, Å	MoK_α; 0.71073
Crystal dimensions, mm	$0.2 \times 0.15 \times 0.1$
Diffractometer	AFC5R
Scan mode	$\omega/2\theta$
$\sin\theta/\lambda$	0.807
Ranges of the indices of measured reflections	$-8 < h < 8$, $-11 < k < 10$, $0 < l < 25$
Total number of reflections	4487
Number of independent reflections	1418 $\lvert F\rvert > 2.5\sigma(F)$
R-factor upon anisotropic refinement	0.054
Program for absorption correction	AREN [6]

Table 2. Atomic coordinates, equivalent thermal parameters, multiplicities (Q), and occupancies of the positions (q)

Atom	x/a	y/b	z/c	B_{eq}, Å^2	Q	q
Si(1)	0.1911(7)	0.0583(5)	0.6684(2)	0.76(6)	2	1
Si(2)	0.8083(7)	0.3887(5)	0.3315(2)	0.81(6)	2	1
Ti	0.6951(4)	0.3449(3)	0.6897(1)	0.87(4)	2	1
M(1)	0.0073(5)	0.2513(4)	0.5030(1)	0.65(4)	2	1
M(2)	0.5	0	0.5	0.75(7)	1	1
M(3)	0.5	0.5	0.5	0.53(6)	1	1
M(4)	0.2789(7)	0.0938(6)	0.1870(2)	2.50(6)	2	0.53(2)
Ba(1)	0.2234(2)	0.4246(1)	0.8493(1)	1.80(3)	2	1
Ba(2)	0.2933(3)	0.1222(2)	0.2449(1)	1.56(4)	2	0.47(2)
Na(1)	0.733(4)	0.243(2)	0.9527(8)	3.1(3)	2	0.50(2)
Na(2)	0.251(3)	0.289(2)	0.0461(8)	2.4(2)	2	0.50(2)
C	0.758(6)	0.052(3)	0.106(1)	4.6(4)	2	1
F(1)	0.5	0.5	0	3.7(2)	1	1
F(2)	0	0.5	0	5.7(2)	1	1
O(1)	0.957(2)	0.165(1)	0.7119(6)	1.0(2)	2	1
O(2)	0.045(2)	0.451(2)	0.2870(6)	1.4(2)	2	1
O(3)	0.555(2)	0.450(2)	0.2863(6)	1.4(2)	2	1
O(4)	0.449(2)	0.162(2)	0.7134(6)	1.7(2)	2	1
O(5)	0.800(2)	0.150(2)	0.3044(8)	2.0(2)	2	1
O(6)	0.180(2)	0.032(2)	0.5690(6)	2.2(2)	2	1
O(7)	0.822(2)	0.460(2)	0.4302(6)	2.5(2)	2	1
O(8)	0.677(2)	0.292(2)	0.5809(6)	1.7(2)	2	1
O(9)	0.154(5)	0.097(3)	0.902(1)	9.6(2)	2	1
O(10)	0.889(4)	0.213(2)	0.106(1)	7.9(2)	2	1
O(11)	0.555(4)	0.138(3)	0.095(1)	9.4(2)	2	1
OH	0.338(2)	0.215(2)	0.4314(7)	1.8(2)	2	1
H_2O	0.719(2)	0.417(2)	0.8360(9)	2.7(2)	2	1

Table 3. Characteristics of the coordination polyhedra

Position	Composition, $Z = 1$	Coordination number	Distance *K*–*A*, Å	
			range	average
Si(1)	2Si	4	1.58–1.63	1.60
Si(2)	2Si	4	1.57–1.63	1.60
Ti	1.9Ti + 0.1Nb	6	1.72–2.31	1.98
M(1)	1.0Na + 0.55Mn + 0.45Fe	6	2.17–2.28	2.24
M(2)	0.5Fe + 0.4Na + 0.1Mn	6	2.09–2.35	2.22
M(3)	0.5Na + 0.4Fe + 0.1Mn	6	2.11–2.33	2.22
M(4)	0.64Sr + 0.42Ca	7	2.23–3.02	2.82
Ba(1)	1.6Ba + 0.4K	11	2.57–3.21	2.80
Ba(2)	0.94Ba	9	2.61–3.21	2.81
Na(1)	1.0Na	7	2.22–3.01	2.57
Na(2)	1.0Na	6	2.16–2.49	2.32
C	2C	3	1.13–1.33	1.22

tallochemical formula of bussenite ($Z = 1$): $\{Na_2(Ba_{2.54}Sr_{0.64}Ca_{0.42}K_{0.40})[CO_3]_2F_2\}\{Na_{1.90}Fe_{1.35}Mn_{0.75}) \cdot (OH)_2[(Ti_{1.9}Nb_{0.1})(Si_2O_7)_2]O_2 \cdot (H_2O)_2\}$. In this formula, the compositions of the salt and titanosilicate blocks are given in braces. The main characteristics of the crystal and the details of the X-ray diffraction study are listed in Table 1. The atomic coordinates corresponding to the final value $R = 0.054$ (the absorption was ignored) for the centrosymmetric structure are listed in Table 2. The main characteristics of polyhedra are presented in Table 3.

The refinement within the acentric space group resulted in the correlation between the thermal parameters of the atoms related by an inversion center and resulted in a slightly lower *R* factor and revealed no ordering in the sites characterized by mixed compositions.

As can be seen from Figs. 1, 2, and 3, large Ba cations occupy two positions. One of these positions, is also filled with K atoms. The distance between the Ba(2) position and the *M*(4) (Sr,Ca)-position is 0.917(4) Å. The Na atoms also occupy two positions with 50% occupancy. The possible distribution of the Mn atoms over three octahedral positions, *M*(1)–*M*(3), corresponds to the average cationic radii in these positions. The F^{1-} ions occupy the inversion centers in the interlayer space. The O, F, OH, and H_2O were distributed over fluorine and oxygen positions based on the calculated local balance of valence strengths at the anions. The water molecule participates in the distorted octahedral coordination of the Ti atom. The distance from the Ti atom to this water molecule equals 2.31 Å, whereas the distance of this Ti atom to the O atom at opposite vertex is shortened (1.72 Å). Such a distortion of the Ti-octahedron allows one to consider it as a pseudopentagonal pyramid and, thus, to relate this mineral to lamprophyllite [5] and monoclinic astrophyllite [7]. In the latter two minerals, Ti atoms have the coordination number five.

Bussenite belongs to the family of titanosilicate micas [8] or, according to the nomenclature proposed in [9], to heterophyllotitanosilicates. The structures of these minerals consist of triple layers responsible for the constant values of the *a*- and *b*-parameters of the

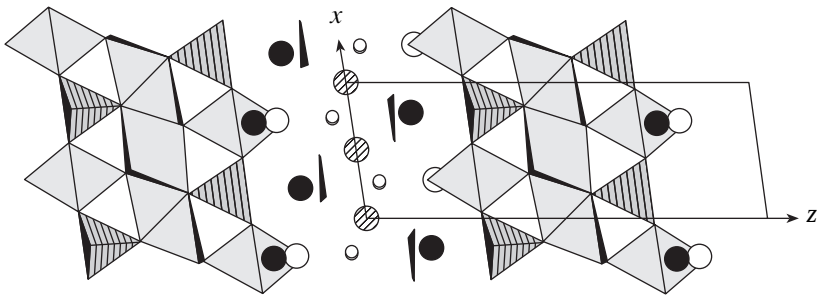

Fig. 2. Bussenite structure projected onto the (010) plane; Si_2O_7-diortho groups are hatched with solid lines; CO_3 groups are represented by black triangles; cations are indicated by circles (for description, see Fig. 1).

unit cell. The middle layer in the bussenite structure consists of the close-packed (Na,Fe,Mn)-octahedra; the side layers are composed by Ti-octahedra and $[Si_2O_7]$-diortho groups. The latter groups have the standard Si–O bond lengths, and the Si(1)–O(5)–Si(2) angle characterizing rotation of tetrahedra equals 149.3(8)°. The character of filling of the space between the triple layers, which determines the *c*-parameter of the unit cell, in the minerals of this group is essentially different. Comparing the formulas of bussenite and heterophyllotitanosilicates such as lomonosovite $\{2NaPO \cdot Na_2\}\{Na_2Ti_4Si_4O_{18}\}$ [10] and innelite $\{2BaSO_4(Ba, K)_2\}\{(Na, Ca)_3Ti_3Si_4O_{18}$ [11], we see that compositions of the interlayer considerably differ (the first fragment enclosed in braces). The $[CO_3]^{2-}$ group found in bussenite is the new specific component of this fragment.

ACKNOWLEDGMENTS

We are grateful to D.Yu. Pushcharovsky for helpful discussion of the results.

This study was supported by the National Science Foundation of China (NSFC; project no. 49872019) and by the Russian Foundation for Basic Research (project nos. 96-05-64381 and 99-05-65035).

REFERENCES

1. A. P. Khomyakov, Int. Geol. Rev. **29** (12), 1446 (1987).
2. A. P. Khomyakov, *Mineralogy of Hyperagpaitic Alkaline Rocks* (Nauka, Moscow, 1990; Clarendon, Oxford, 1995).
3. Huyun Zhou, PhD Thesis (Beijing, 1997).
4. A. P. Khomyakov, Yu. P. Men'shikov, G. N. Nechelyustov, and Huyun Zhou, Zap. Vseross. Mineral. O–va. **130** (3), 50 (2001).
5. R. K. Rastsvetaeva and M. D. Dorfman, Kristallografiya **40** (6), 1026 (1995) [Crystallogr. Rep. **40**, 951 (1995)].
6. V. I. Andrianov, Kristallografiya **32** (1), 228 (1987) [Sov. Phys. Crystallogr. **32**, 130 (1987)].
7. Nicheng Shi, Zhesheng Ma, Guowu Li, *et al.*, Acta Crystallogr., Sect. B: Struct. Sci. **54** (2), 109 (1998).
8. Yu. K. Egorov-Tismenko and E. V. Sokolova, in *Comparative Crystal Chemistry* (Mosk. Gos. Univ., Moscow, 1987), p. 96.
9. G. Ferraris, A. P. Khomyakov, E. Belluso, and S. V. Soboleva, in *Proceedings of the 30th International Geology Congress, 1996*, Vol. 16, p. 17.
10. R. K. Rastsvetaeva, V. I. Simonov, and N. V. Belov, Dokl. Akad. Nauk SSSR **197** (1), 81 (1971) [Sov. Phys. Dokl. **16**, 33 (1971)].
11. A. N. Chernov, V. V. Ilyukhin, B. A. Maksimov, and N. V. Belov, Kristallografiya **16** (1), 87 (1971) [Sov. Phys. Crystallogr. **16** (1), 87 (1971)].

Translated by T. Safonova

Crystallography Reports, Vol. 47, No. 1, 2002, pp. 47–50. Translated from Kristallografiya, Vol. 47, No. 1, 2002, pp. 54–57.

STRUCTURE OF INORGANIC COMPOUNDS

Crystal Structure of Aminoguanidinium Hexahydro-*closo*-Hexaborate Dihydrate, $(CN_4H_7)_2B_6H_6 \cdot 2H_2O$

I. N. Polyakova, V. N. Mustyatsa, and N. T. Kuznetsov

Kurnakov Institute of General and Inorganic Chemistry, Russian Academy of Sciences, Leninskiĭ pr. 31, Moscow, GSP-1, 119991 Russia

e-mail: sokol@igic.ras.ru

Received April 5, 2001

Abstract—The $(HAgu)_2B_6H_6 \cdot 2H_2O$ compound was synthesized and its crystal structure was determined [R = 0.0385 for 2018 reflections with $I > 2\sigma(I)$]. The structure consists of $HAgu^+$ cations, centrosymmetric $B_6H_6^{2-}$ anions, and water molecules. The anions have an almost regular octahedral structure. The bond lengths and angles lie within the following narrow ranges: B–B, 1.715–1.726(2) Å; B–H, 1.08–1.14(2) Å; B–B–B, 59.72°–60.29(9)° and 89.63°–90.20(11)°; and B–B–H, 133.2°–137.0(9)°. The $HAgu^+$ cations and water molecules are involved in the O–H···O, N–H···O, and N–N···N hydrogen bonds and participate in numerous (N, O)–H···H–B specific interactions with the $B_6H_6^{2-}$ anions, which results in splitting and high-frequency shift of the band of B–H stretching vibrations in the IR spectrum. © *2002 MAIK "Nauka/Interperiodica"*.

INTRODUCTION

In recent years, the salts of the *closo*-borate anions with organic cations attracted the attention of researchers due to the cation–anion interactions revealed in their crystals [1–4]. These interactions show themselves, in particular, in splitting and high-frequency shift of the band of the B–H stretching vibrations in the IR spectra. The salts of this type with the hexaborate anion $B_6H_6^{2-}$ have not been studied as yet because all the attempts to synthesize these salts usually resulted in the formation of stable compounds with $B_6H_7^-$ anions. It could be expected that, owing to the increased charge at the boron atoms, the $B_6H_6^{2-}$ anions provide more intense specific interactions than the salts with larger polyhedral anions.

We synthesized aminoguanidinium *closo*-hexaborate and grew single crystals of its dihydrate $(HAgu)_2B_6H_6 \cdot 2H_2O$ (**I**), where $HAgu^+ = (NH_2)_2CNHNH_2$. In this paper, the results of the X-ray diffraction study of compound **I** are reported.

EXPERIMENTAL

Compound **I** was obtained by the reaction between the stoichiometric amounts of $Na_2B_6H_6$ and $(HAgu)_2SO_4$ in an aqueous solution. The solution was concentrated on a sand bath and cooled to 0°. Two days later, colorless prismatic crystals precipitated. Being kept in air, the crystals became turbid.

Found, %: C, 9.20; H, 9.37; and N, 43.10.

Calculated for $(CN_4H_7)_2B_6H_6 \cdot 2H_2O$, %: C, 9.34; H, 9.41; and N, 43.58.

The IR absorption spectra were recorded on a Specord M80 spectrophotometer in the range 4000–400 cm^{-1}. The specimens were prepared as suspensions in petrolatum oil.

In the IR spectrum of **I**, the intense split band with the maxima at 2468 and 2444 cm^{-1} is observed in the range of ν(BH) stretching vibrations. This band is shifted by ~40 cm^{-1} to high frequencies with respect to similar bands in the spectra of the hexaborate salts of alkali metals [5] but located much lower than the ν(BH) band in the $B_6H_7^-$ anion (2535 cm^{-1} [6]). The bands of the ν(NH) stretching vibrations in **I** appear at 3424, 3312, and 3268 cm^{-1}, i.e., at frequencies slightly lower than those in the spectra of the salts of the $B_{10}H_{10}^{2-}$ and $B_{12}H_{12}^{2-}$ anions [7].

The crystals suitable for the X-ray experiment were obtained by recrystallization from an aqueous solution. The crystals are triclinic, a = 7.304(3) Å, b = 10.132(4) Å, c = 10.200(3) Å, α = 93.81(3)°, β = 95.85(3)°, γ = 105.12(3)°, V = 721.5(5) $Å^3$, d_{calc} = 1.184 g/cm^3; μ(Mo) = 0.083 mm^{-1}, sp. gr. $P\bar{1}$, and Z = 2.

Table 1. Atomic coordinates and parameters of thermal vibrations U_{eq} (for H atoms, U_{iso}) in structure **I**

Atom	*x*	*y*	*z*	U_{eq}/U_{iso}, Å
O(1*w*)	−0.0563(2)	0.2388(1)	0.0788(1)	0.0556(3)
O(2*w*)	0.3257(2)	0.3084(1)	0.6524(1)	0.0520(3)
N(1)	0.2613(2)	0.0697(1)	0.9068(1)	0.0459(3)
N(2)	0.3497(3)	0.1058(2)	1.1290(2)	0.0578(4)
N(3)	0.1814(2)	−0.1090(1)	1.0335(2)	0.0476(4)
N(4)	0.1527(2)	−0.0132(1)	0.7960(1)	0.0476(3)
N(5)	−0.0630(2)	0.5246(2)	0.7317(1)	0.0467(3)
N(6)	−0.1248(3)	0.7099(2)	0.6399(2)	0.0581(4)
N(7)	−0.2459(3)	0.4947(2)	0.5306(2)	0.0662(5)
N(8)	0.0256(2)	0.6101(2)	0.8467(1)	0.0480(3)
C(1)	0.2644(2)	0.0218(1)	1.0243(2)	0.0377(3)
C(2)	−0.1455(2)	0.5768(2)	0.6341(2)	0.0438(4)
B(1)	0.3405(2)	0.0169(2)	0.4840(2)	0.0390(4)
B(2)	0.5267(2)	0.0610(2)	0.6096(2)	0.0368(4)
B(3)	0.5643(2)	0.1081(2)	0.4537(2)	0.0397(4)
B(4)	−0.4922(2)	0.4501(2)	1.1052(2)	0.0381(4)
B(5)	−0.4252(2)	0.4170(2)	0.9517(2)	0.0364(4)
B(6)	−0.6571(2)	0.4209(2)	0.9664(2)	0.0363(4)
H(1)	0.199(2)	0.035(2)	0.472(2)	0.057(5)
H(2)	0.556(2)	0.116(2)	0.708(2)	0.049(4)
H(3)	0.616(2)	0.203(2)	0.409(2)	0.060(5)
H(4)	−0.482(2)	0.408(2)	1.206(2)	0.052(4)
H(5)	−0.360(2)	0.342(2)	0.909(1)	0.045(4)
H(6)	−0.798(2)	0.351(2)	0.940(1)	0.048(4)
H(1*a*)	0.304(3)	0.146(2)	0.907(2)	0.065(6)
H(2*a*)	0.366(3)	0.077(2)	1.204(2)	0.064(6)
H(2*b*)	0.401(3)	0.185(2)	1.120(2)	0.060(6)
H(3*a*)	0.132(2)	−0.157(2)	0.965(2)	0.045(5)
H(3*b*)	0.178(3)	−0.136(2)	1.106(2)	0.061(6)
H(4*a*)	0.224(3)	−0.017(2)	0.738(2)	0.074(6)
H(4*b*)	0.060(3)	0.025(2)	0.764(2)	0.089(7)
H(5*a*)	−0.082(3)	0.443(2)	0.728(2)	0.066(6)
H(6*a*)	−0.062(3)	0.758(2)	0.707(2)	0.065(6)
H(6*b*)	−0.179(3)	0.741(2)	0.582(2)	0.077(7)
H(7*a*)	−0.262(3)	0.410(2)	0.533(2)	0.074(7)
H(7*b*)	−0.297(4)	0.526(3)	0.456(3)	0.106(9)
H(8*a*)	−0.043(3)	0.591(2)	0.912(2)	0.079(7)
H(8*b*)	0.133(3)	0.594(2)	0.872(2)	0.080(7)
H(1*w*1)	0.047(4)	0.249(2)	0.678(2)	0.077(7)
H(2*w*1)	−0.136(3)	0.191(2)	0.643(2)	0.070(6)
H(1*w*2)	0.390(3)	0.355(2)	0.716(2)	0.083(7)
H(2*w*2)	0.379(3)	0.250(2)	0.639(2)	0.074(7)

The intensities of the reflections were measured on a CAD-4 automated diffractometer (λMoK_α, graphite monochromator, ω-scan mode, and $2° < \theta < 28°$) from two single crystals. The first crystal was coated with an epoxy resin film, which, nevertheless, did not prevent it from decomposition: within a day after the beginning of data collection, the intensities of the standard reflections decreased by 50%. The second crystal was protected more safely, and the intensities did not decrease. The processing of the first part of the experimental data included the correction for crystal decomposition.

The structure was solved by the direct method (SHELXS97 [8]). The positions of the H atoms were located from the difference Fourier synthesis. The structure was refined by the least-squares procedure (SHELXL97 [9]) in the aniso-isotropic approximation with due regard for secondary extinction [$c = 0.046(7)$]. The final estimates of the refinement are $R1 = 0.0385$ and $wR2 = 0.0992$ for 2018 reflections with $I > 2\sigma(I)$; $R1 = 0.0923$ and $wR2 = 0.1196$ for the complete set of 3442 reflections; and $S = 1.017$. The atomic coordinates are listed in Table 1.

RESULTS AND DISCUSSION

The crystals consist of aminoguanidinium cations, centrosymmetric $B_6H_6^{2-}$ anions, and water molecules. There are two independent structural units of each type in the unit cell. A fragment of the structure with atomic numbering is shown in the figure.

The C(1)N(1)N(2)N(3) and C(2)N(5)N(6)N(7) guanidinium fragments of the cations are planar (the mean atomic deviations from the planes are 0.001 and 0.002 Å, respectively). The N(4) and N(8) atoms of the amino substituents deviate from these planes by 0.157 and 0.148 Å.

The anions have an almost regular octahedral structure. The bond lengths and angles in the anions vary within the following narrow ranges: B–B, 1.715(2)–1.726(2) Å; B–H, 1.08(2)–1.14(2) Å; B–B–B, 59.72(9)°–60.29(9)° and 89.63(11)°–90.20(11)°; and B–B–H, 133.2(9)°–137.0(9)°. Hence, splitting of the band of the ν(BH) stretching vibrations and its shift to higher frequencies (see experimental) should be interpreted with the invocation of specific intermolecular interactions of the $B_6H_6^{2-}$ anions.

In [10], the intense color of the $(H\textit{Bipy})_2B_{10}H_{10}$ and $(H_2\textit{Bipy})B_{10}H_{10}$ compounds is attributed to the charge transfer from the anion to the cation through the (B)H··H(N) interaction. Later [11], it was found that the peak in the region of the short (B)H··H(N) contact [1.91(3) Å] in the map of the difference electron density of the $(H_2\textit{Bipy})B_{10}H_{10}$ crystal deviates from the H··H segment and appears between the B–B edge and the N atom. This allowed the authors to assume that the charge transfer from the $B_{10}H_{10}^{2-}$ anion to the $H_2\textit{Bipy}^{2+}$

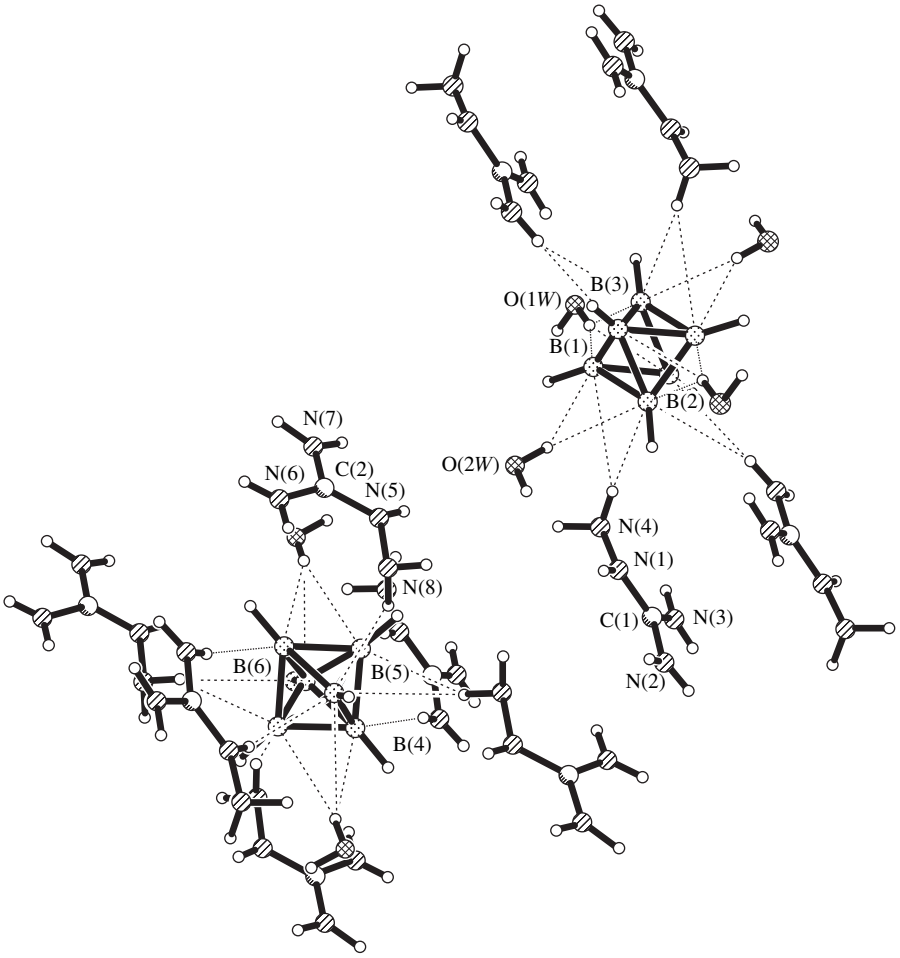

The environment of two independent $B_6H_6^{2-}$ octahedral anions in structure **I**. The dotted lines indicate the (O,N)–H··B specific interactions.

cation proceeds through the interaction between the B and N atoms, whereas the short H··H contact is a consequence of this interaction. We cannot rule out that the specific interactions, similar to the valence bonds in the hydroborate anions, are of the multicenter type.

In structure **I**, some of the H atoms of the H*Agu*$^+$ cations and water molecules form conventional O–H··O, N–H··O, and N–H··N hydrogen bonds. The characteristics of the hydrogen bonds are given in Table 2. The visual and geometric analysis indicates that, most likely, the remaining H atoms of the cations and water molecules [except H(4*b*)] are involved in specific interactions with the $B_6H_6^{2-}$ anions. Evidently, it is not accidental that the N–H bonds of the cations and the O–H bonds of water molecules are directed to the vertices, edges, or faces of the boron octahedra (figure). It is log-

Table 2. Characteristics of the hydrogen bonds in structure **I**

X–H···*Y*	Symmetry code for the *Y* atom	H···*Y*, Å	*X*···*Y*, Å	*X*–H···*Y*, deg
O(1*w*)–H(1*w*1)···O(2*w*)	*x*, *y*, *z*	2.02(3)	2.823(2)	164(2)
N(3)–H(3*a*)···N(8)	*x*, *y* – 1, *z*	2.47(2)	3.190(2)	147(2)
N(3)–H(3*a*)···N(4)	*x*, *y*, *z*	2.32(2)	2.677(2)	107(1)
N(3)–H(3*b*)···O(1*w*)	–*x*, –*y*, 2 – *z*	2.36(2)	3.130(2)	160(2)
N(5)–H(5*a*)···O(1*w*)	*x*, *y*, *z*	2.13(2)	2.904(2)	165(2)
N(6)–H(6*a*)···N(8)	*x*, *y*, *z*	2.30(2)	2.659(2)	107(2)
N(7)–H(7*b*)···O(2*w*)	–*x*, 1 – *y*, 1 – *z*	2.11(3)	2.947(2)	149(2)

Table 3. Characteristics of the *X*–H… H–B (*X* = O or N) interactions in structure **I**

X–H···H–B	Symmetry code for the B atom	H···H, Å	H···B, Å	*X*···B, Å	*X*–H···B, Å
O(1*w*)–H(2*w*1)···H(1)–B(1)	$-x, -y, 1-z$	2.41(3)	2.44(2)	3.252(2)	156(2)
O(1*w*)–H(2*w*1)···H(2)–B(2)	$x-1, y, z$	2.35(3)	2.45(2)	3.133(2)	136(2)
O(1*w*)–H(2*w*1)···H(3)–B(3)	$x-1, y, z$	2.87(3)	2.68(2)	3.516(2)	162(2)
O(2*w*)–H(1*w*2)···H(4)–B(4)	$-x, 1-y, 2-z$	2.39(3)	2.51(2)	3.258(2)	157(2)
O(2*w*)–H(1*w*2)···H(5)–B(5)	$1+x, y, z$	2.58(3)	2.59(2)	3.349(2)	159(2)
O(2*w*)–H(1*w*2)···H(6)–B(6)	$1+x, y, z$	2.78(3)	2.68(2)	3.307(2)	136(2)
O(2*w*)–H(2*w*2)···H(1)–B(1)	x, y, z	2.63(3)	2.69(2)	3.349(2)	141(2)
O(2*w*)–H(2*w*2)···H(2)–B(2)	x, y, z	2.21(3)	2.45(2)	3.246(2)	175(2)
N(1)–H(1*a*)···H(6)–B(6)	$1+x, y, z$	2.40(3)	2.74(2)	3.453(2)	157(2)
N(2)–H(2*a*)···H(2)–B(2)	$1-x, -y, 2-z$	2.38(3)	2.61(2)	3.418(2)	161(2)
N(2)–H(2*a*)···H(3)–B(3)	$x, y, 1+z$	2.65(3)	2.76(2)	3.512(2)	150(2)
N(2)–H(2*b*)···H(4)–B(4)	$1+x, y, z$	2.27(3)	2.61(2)	3.410(2)	169(2)
N(4)–H(4*a*)···H(2)–B(2)	x, y, z	2.50(3)	2.65(2)	3.438(2)	157(2)
N(4)–H(4*a*)···H(1)–B(1)	x, y, z	2.79(3)	2.82(2)	3.592(2)	154(2)
N(8)–H(8*a*)···H(6)–B(6)	$-1-x, 1-y, 2-z$	2.13(3)	2.60(2)	3.415(2)	154(2)
N(8)–H(8*b*)···H(5)–B(5)	$-x, 1-y, 2-z$	2.58(3)	2.68(2)	3.478(2)	155(2)
N(8)–H(8*b*)···H(6)–B(6)	$1+x, y, z$	2.76(3)	2.77(2)	3.548(2)	151(2)

ical to characterize the geometry of these interactions with the same parameters as the geometry of hydrogen bonds. The (*X*)H··B, *X*··B, and (*X*)H··H(B) contacts and the *X*–H··B angles, where *X* = N or O, are given in Table 3. It is well known that the energy of weak interactions varies only slightly with distance, and, thus, it is impossible to determine the limiting distance at which the secondary interaction disappears. In structure **I**, the (*X*)H··B, O··B, and N··B contacts range within 2.44–3.08(2), 3.133–3.516(2), and 3.410–3.818(2) Å, respectively. Table 3 includes the interactions, for which the *X*··B distance does not exceed 3.6 Å. Judging from the values of the contacts, no strengthening of the specific interatomic interactions in the salt of the $B_6H_6^{2-}$ anion in comparison with larger *closo*-borate anions is observed, which may be associated with a large number of interactions.

The total set of intermolecular interactions in the crystal interlinks the H*Agu*$^+$ cations, $B_6H_6^{2-}$ anions, and water molecules into a three-dimensional framework.

ACKNOWLEDGMENTS

This study was supported by the Russian Foundation for Basic Research, project nos. 99-03-32589 and 00-15-97394.0. We are also grateful to this Foundation for the payment of the licence for using the Cambridge Structural Database, project no. 99-07-90133.

REFERENCES

1. E. A. Malinina, L. V. Goeva, K. A. Solntsev, and N. T. Kuznetsov, Zh. Neorg. Khim. **36** (9), 2414 (1991).
2. E. A. Malinina, L. V. Goeva, K. A. Solntsev, and N. T. Kuznetsov, Koord. Khim. **18** (4), 378 (1992).
3. E. A. Malinina, L. V. Goeva, K. A. Solntsev, and N. T. Kuznetsov, Koord. Khim. **18** (4), 382 (1992).
4. S. B. Katser, E. A. Malinina, V. N. Mustyatsa, *et al.*, Koord. Khim. **18** (4), 387 (1992).
5. A. V. Agafonov, D. M. Vinitskiĭ, K. A. Solntsev, *et al.*, J. Neorg. Khim. **30** (2), 335 (1985).
6. D. M. Vinitskiĭ, K. A. Solntsev, N. T. Kuznetsov, and L. V. Goeva, J. Neorg. Khim. **31** (9), 2326 (1986).
7. E. A. Malinina, L. V. Goeva, V. N. Mustyatsa, and N. T. Kuznetsov, Koord. Khim. **27** (6), 403 (2001).
8. G. M. Sheldrick, *SHELXS97: Program for the Solution of Crystal Structures* (Univ. of Göttingen, Göttingen, 1997).
9. G. M. Sheldrick, *SHELXS97: Program for the Refinement of Crystal Structures* (Univ. of Göttingen, Göttingen, 1997).
10. D. J. Fuller, D. L. Kepert, B. W. Skelton, and A. H. White, Aust. J. Chem. **40** (12), 2097 (1987).
11. C. T. Chantler and E. N. Maslen, Acta Crystallogr., Sect. B: Struct. Sci. **45** (3), 290 (1989).

Translated by I. Polyakova

Crystallography Reports, Vol. 47, No. 1, 2002, pp. 51–54. Translated from Kristallografiya, Vol. 47, No. 1, 2002, pp. 58–61.

STRUCTURE OF COORDINATION COMPOUNDS

Structure of the $[Co(NioxH)_2(PPh_3)_2]F$ Complex

S. T. Malinovsky*, E. B. Coropcheanu*, V. E. Zavodnik, and O. A. Bologa***

** Institute of Chemistry, Academy of Sciences of Moldova, Academiei 3, Chisinau, 20-28 Moldova*

*** Karpov Research Institute of Physical Chemistry, State Scientific Center, ul. Vorontsovo pole 10, Moscow, 103064 Russia*

e-mail: stanis@mail.md

Received February 22, 2001

Abstract—Compound $[Co(NioxH)_2(PPh_3)_2]F$ is synthesized in the $CoF_2 \cdot 4H_2O$–$NioxH_2$–PPh_3 system (where *Nox*H is the 1,2-cyclohexanedione dioxime monoanion and P*Ph*$_3$ is triphenylphosphine), and its structure is determined by X-ray diffraction. It is shown that the cobalt atom has the octahedral environment. Two nioxime residues that are related by the center of symmetry lie in the equatorial plane and are linked by the O–H··O hydrogen bond. The 1,6-positions of the octahedron are occupied by the phosphorus atoms of the triphenylphosphine ligands. The formation of the crystal structure of this compound is discussed. © *2002 MAIK "Nauka/Interperiodica".*

INTRODUCTION

Compounds of the 3*d* elements with α-dioximes have attracted considerable interest due to the wide variety of stereochemical and electronic structures [1]. The knowledge of their features can be useful for revealing the generalities in the composition and structure of these compounds.

The coordination mode of dioximines in their metal complexes [2–6] is rather stable. The chelates have a stereotypic structure: two monodeprotonated dioximate ions lying in the same plane are linked through intramolecular hydrogen bonds. In this respect, the synthesis of compounds of this type with new ligands that have more flexible chemical structures is a topical problem.

1,2-Cyclohexanedione dioxime *Nox*H$_2$ is a reagent for cobalt determination. This compound readily dissolves in water and forms complexes with Co(III) ions [7].

With the purpose of revealing the specific features of the Co(III) coordination polyhedron and the crystal structure as a whole, we studied the structure of $[Co(NioxH)_2(PPh_3)_2]F$, which is the product of the reaction in the $CoF_2 \cdot 4H_2O$–$NioxH_2$–P*Ph*$_3$ system (where *Nox*H is the 1,2-cyclohexanedione dioxime monoanion and P*Ph*$_3$ is triphenylphosphine).

EXPERIMENTAL

Synthesis of $[Co(NioxH)_2(PPh_3)_2]F$. A solution of 1,2-cyclohexanedione dioxime (0.14 g, 0.001 mol) in methanol (20 ml) and a solution of triphenylphosphine (0.26 g, 0.001 mol) in methanol (30 ml) were added to a solution of $CoF_2 \cdot 4H_2O$ (0.09 g, 0.0005 mol) in methanol (20 ml). The resultant solution was heated in a water bath in a graphite crucible at 50°C for 5–6 min. Upon slow cooling, prismatic dark brown crystals precipitated from the dark brown solution. The yield was ~35%. The compound is soluble in alcohols and organic solvents but insoluble in water.

For $C_{48}H_{48}CoFN_4O_4P_2$, anal. calcd. (%): Co, 6.66; C, 65.17; H, 5.47; N, 6.33. Found (%): Co, 6.04; C, 64.83; H, 5.39; N, 6.21.

X-ray structure determination. A prismatic dark brown single crystal ($0.48 \times 0.14 \times 0.13$ mm in size) was chosen for the X-ray diffraction experiment. The crystal is monoclinic. The unit cell parameters are as follows: $a = 9.407(2)$ Å, $b = 15.699(3)$ Å, $c = 14.867(3)$ Å, $\beta = 102.43(3)°$, space group $P2_1/n$, and $Z = 2$ (for $C_{48}H_{48}CoFN_4O_4P_2$) at $\rho_{calcd} = 1.429$ g/cm^3.

The experimental data were collected on a CAD4 diffractometer (MoK_α radiation, graphite monochromator, θ–2θ scan mode). The structure was solved by the direct method with the SHELXS86 program package [8]. The Lorentz and polarization factors were included in the conversion of the intensities into the squares of the structure amplitudes. Absorption of X-rays by the crystal was ignored. A total of 960 unique reflections with $I \geq 2\sigma(I)$ were used for structure determination and refinement.

The refinement of the non-hydrogen atoms was performed in the full-matrix anisotropic approximation, and the hydrogen atoms were refined isotropically within the rigid-group model. The calculations were performed with the SHELXL93 program package [9].

Coordinates ($\times 10^4$) and isotropic thermal parameters ($Å^2 \times 10^3$) of non-hydrogen atoms

Atom	*x*	*y*	*z*	U_{eq}
Co	5000	5000	5000	26(1)
F(1')	–1615(17)	468(10)	3930(10)	120(4)
F(1)	285(6)	–302(3)	4533(4)	106(2)
P(1)	3934(1)	3998(1)	3846(1)	30(1)
O(1)	5167(2)	6142(1)	3543(1)	38(1)
O(2)	2577(2)	4722(1)	5851(1)	37(1)
N(1)	4393(2)	5890(1)	4148(1)	30(1)
N(2)	3163(2)	5198(1)	5259(1)	29(1)
C(1)	3172(3)	6256(2)	4197(2)	32(1)
C(2)	2448(3)	5854(2)	4859(2)	31(1)
C(3)	1053(3)	6175(2)	5036(2)	42(1)
C(4)	310(4)	6815(2)	4314(2)	56(1)
C(5)	1374(4)	7432(2)	4057(3)	58(1)
C(6)	2490(4)	6987(2)	3616(2)	44(1)
C(7)	2511(3)	4470(2)	2954(2)	34(1)
C(8)	2604(4)	4560(2)	2040(2)	47(1)
C(9)	1432(4)	4890(2)	1406(2)	64(1)
C(10)	174(4)	5126(2)	1667(3)	64(1)
C(11)	69(4)	5031(2)	2564(3)	56(1)
C(12)	1222(3)	4705(2)	3209(2)	44(1)
C(13)	3017(3)	3056(2)	4176(2)	34(1)
C(14)	3657(4)	2571(2)	4936(2)	45(1)
C(15)	3053(4)	1805(2)	5115(2)	53(1)
C(16)	1814(4)	1513(2)	4547(3)	60(1)
C(17)	1165(4)	1978(2)	3791(3)	66(1)
C(18)	1763(4)	2743(2)	3602(2)	49(1)
C(19)	5297(3)	3541(2)	3283(3)	54(1)
C(20)	5736(3)	2691(2)	3426(2)	41(1)
C(21)	6797(4)	2360(2)	3015(2)	50(1)
C(22)	7407(4)	2857(2)	2440(2)	51(1)
C(23)	6981(3)	3699(2)	2288(2)	47(1)
C(24)	5966(3)	4042(2)	2719(2)	37(1)

The final parameters of the refinement are as follows: *R*1 = 0.023, *wR*2 = 0.062, and *GOOF* = 1.008. The atomic coordinates and thermal parameters with e.s.d.'s are listed in the table.

RESULTS AND DISCUSSION

The IR spectra of the complex exhibit sets of vibrational frequencies that are characteristic of the Co(III) dioximines in the *trans* configuration. The ν_{ac}(PC) and ν_c(PC) frequencies (at ~570 and ~448 cm^{-1}, respectively) indicate that triphenylphosphine is coordinated in the complex [10].

The UV spectra contain two absorption bands. The band at 272 nm is attributed to the charge transfer from the cobalt atom to the chelate ring and corresponds to the Co(*Niox*H)$_2$ group. The band at 377 nm is associated with the triphenylphosphine molecules in the *trans* positions relative to each other in the complex.

The structural units of the crystal are the $[Co(NioxH)_2(PPh_3)_2]^+$ centrosymmetric cationic complex and the statistically disordered F^- ion. The structure of the cationic complex is shown in Fig. 1. The cobalt atom has the octahedral (4N2P) environment. Two nioxime residues are located in the equatorial plane and bound to the metal atom through four nitrogen atoms. The Co–N bond lengths are equal to 1.807(2) and 1.890(2) Å. The phosphorus atoms of the triphenylphosphine ligands occupy the 1,6-positions of the octahedron. The Co–P distance is 2.384(1) Å. In the centrosymmetric cationic complex, two nioxime residues are linked by the intramolecular O–H···O hydrogen bond, for which the O···O distance is equal to 2.555 Å, the O–H bond is 0.90 Å, and the angle at the hydrogen atom is 171.0°. The results obtained agree with those reported in the literature [6] and with the data of the spectral analysis.

The CoN(1)C(1)C(2)N(2) equatorial metallocycle and the C(7)C(8)C(9)C(10)C(11)C(12) phenyl ring of the triphenylphosphine ligand are arranged relative to each other in such a way that the dihedral angle between their planes is 34.6°. By analogy with [6], we assume that there occurs the intramolecular π–π interaction between these two moieties. The atomic deviations from the rms planes of the nioxime residues have the following values (Å): Co, 0.011; N(1), –0.025; C(1), 0.028; C(2), –0.014; O(1)*[1], 0.071; and O(2)*, –0.248 Å; and C(1), –0.022; C(2), –0.052; C(3), 0.092; C(4), –0.302; C(5), 0.342; and C(6), –0.102 Å. Therefore, the conformation of the cyclohexyl fragment in the nioxime residue can be considered a twist conformation. The dihedral angle between the above two planes is 6.3°.

The electronegative fluoride ion plays a significant role in the formation of the crystal structure (Fig. 2). This ion is disordered over two equiprobable positions, F(1) and F(1'). The F(1)···F(1') distance is 2.184 Å. Apparently, there exists an electrostatic interaction between the F(1) and C(16) atoms (the F(1)–C(16) dis-

[1] Hereafter, the atoms that are not included in the calculation of the plane are marked with an asterisk.

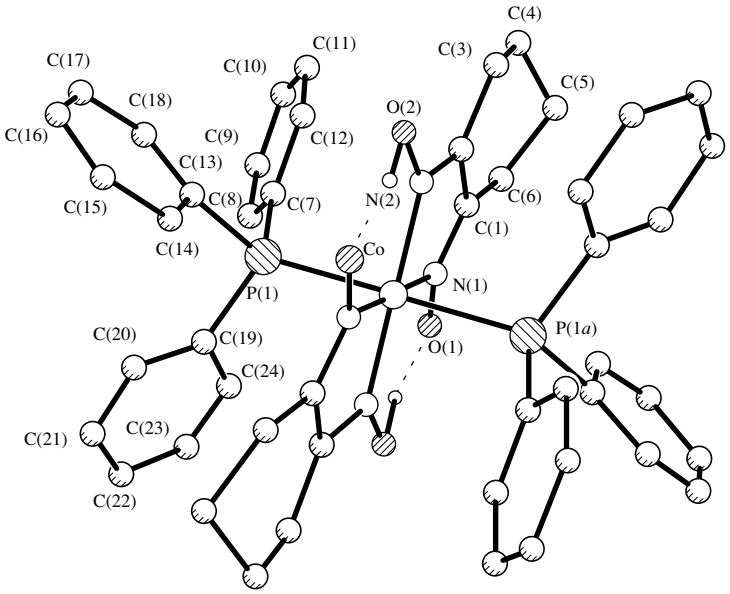

Fig. 1. Structure of the [Co(*Niox*H)$_2$(P*Ph*$_3$)$_2$]$^+$ centrosymmetric cation.

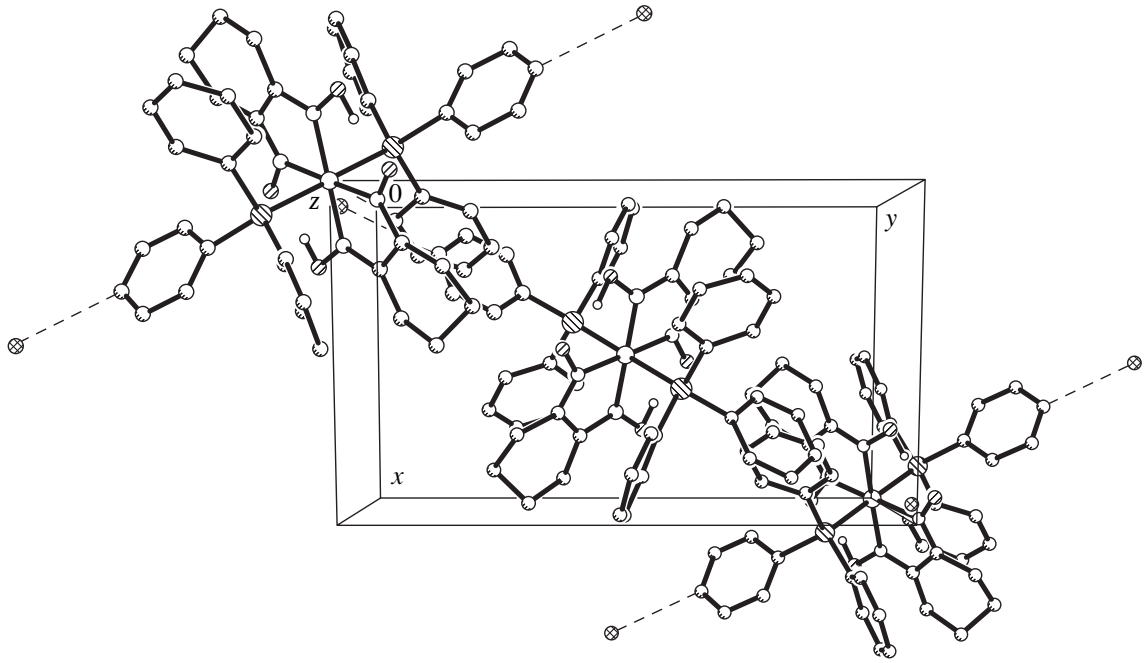

Fig. 2. A fragment of the crystal structure of [Co(*Niox*H)$_2$(P*Ph*$_3$)$_2$]F.

tance is 3.18 Å). The other intermolecular distances in the structure exceed the relevant sums of the van der Waals radii.

Thus, the replacement of the $[SiF_5]^-$ anion in the crystal studied earlier [11] by the fluoride ion leaves the configuration and the structure of the cationic complex unchanged but results in substantial changes in the crystal structure as a whole.

REFERENCES

1. M. M. Botoshanskiĭ, A. A. Dvorkin, and Yu. A. Simonov, in *Crystal Structures of Inorganic Compounds*, Ed. by T. I. Malinovsky (Shtiintsa, Kishinev, 1974), p. 26.
2. Yu. A. Simonov, A. A. Dvorkin, A. P. Gulya, *et al.*, Dokl. Akad. Nauk SSSR **305** (3), 635 (1989).
3. Yu. A. Simonov, O. A. Bologa, A. A. Dvorkin, *et al.*, Koord. Khim. **20** (2), 106 (1994).

4. M. M. Botoshanskiĭ, Yu. A. Simonov, and T. I. Malinovsky, Kristallografiya **20** (1), 63 (1975) [Sov. Phys. Crystallogr. **20**, 34 (1975)].
5. S. Bruckner and L. Randaccio, J. Chem. Soc. Dalton Trans., 1017 (1974).
6. Yu. A. Simonov, P. N. Bourosh, O. A. Bologa, *et al.*, Zh. Strukt. Khim. **40** (1), 85 (1999).
7. V. M. Peshkova, V. M. Savostina, and E. K. Ivanova, *Oximes* (Nauka, Moscow, 1977).
8. G. M. Sheldrick, Acta Crystallogr., Sect. A: Found. Crystallogr. **46**, 467 (1990).
9. G. M. Sheldrick, *SHELXL93: Program for the Refinement of Crystal Structures* (University of Göttingen, Göttingen, 1993).
10. K. I. Turté, V. E. Zubareva, V. N. Shafranskiĭ, *et al.*, Koord. Khim. **13** (5), 634 (1987).
11. Yu. A. Simonov, N. V. Gérbéléu, M. Gdanets, *et al.*, Koord. Khim. (in press).

Translated by I. Polyakova

Crystallography Reports, Vol. 47, No. 1, 2002, pp. 55–57. Translated from Kristallografiya, Vol. 47, No. 1, 2002, pp. 62–64.

STRUCTURE OF COORDINATION COMPOUNDS

Crystal Structure of (3-Aminopropionato)*bis*(ethylenediamine)cobalt(III) *catena*-Di(μ-chloro)dichloroplumbate(II) Monohydrate

I. F. Burshteĭn* and A. L. Poznyak**

** Analytical X-ray Instrumentation Department, Siemens Energy and Automation Inc., 6300 Enterprise Lane, Madison, WI, USA*

*** Institute of Molecular and Atomic Physics, National Academy of Sciences of Belarus, pr. F. Skoriny 70, Minsk, 220072 Belarus*

Received January 30, 2001

Abstract—Crystals of $[Co(C_2H_8N_2)_2(C_3H_6NO_2)]PbCl_4 \cdot H_2O$ [a = 7.627(1) Å, b = 11.238(1) Å, c = 11.444(1) Å, α = 99.125(1)°, β = 103.80(1)°, γ = 94.739(1)°, V = 933.09(1) Å^3, Z = 2, and space group $P\bar{1}$] contain the octahedral $PbCl_6$ groups that share edges to form infinite $[Cl_2Pb(\mu\text{-}Cl)_2]_n^{2n-}$ chains, in which the terminal Cl atoms occupy the *cis* positions. The Pb–Cl bond lengths are 2.763(1)–3.180(3) Å. In the discrete cationic complexes, the Co atom is coordinated by two ethylenediamine molecules and the 3-aminopropionate anion. In the enantiomeric complex with the Δ absolute configuration, the ethylenediamine rings have the λ and δ configurations and the aminopropionate ring has the λ configuration. © *2002 MAIK "Nauka/Interperiodica".*

INTRODUCTION

X-ray diffraction studies of the crystal structure of lead complexes with halide ions have been reported in a large number of publications (see, for example, [1, 2] and references therein). In most of these crystals, the cationic part consists of protonated organic amines, and only some of them contain cationic complexes, namely, $[Co(NH_3)_6]^{3+}$, $[Co(En)_3]^{3+}$ (*En* is ethylenediamine), or $[Co(CH_3NHCH_2CH_2NH_2)_2C_2O_4]^+$ [3–5]. However, the use of other cationic complexes can provide a greater variety of anionic parts owing to the changes in the coordination sphere of the lead ion and the nonstereospecific nature of the halide ions as ligands.

For this purpose, we prepared crystals of $[Co(En)_2(Ala)]PbCl_4 \cdot H_2O$ (**I**) (*Ala* is the anion of β-alanine, i.e., 3-aminopropionate $NH_2CH_2CH_2CO_2^-$) and determined their structure.

EXPERIMENTAL

An aqueous solution of $[Co(En)_2(Ala)]Cl_2 \cdot 2H_2O$, which was synthesized according to the procedure

Table 1. Atomic coordinates (×10^4) and equivalent isotropic thermal parameters U_{eq} (Å^2, ×10^3)

Atom	x	y	z	U_{eq}	Atom	x	y	z	U_{eq}
Pb(1)	2375(1)	5653(1)	9393(1)	29(1)	N(3)	−4370(6)	−2475(4)	5648(4)	30(1)
Co(1)	−2512(1)	−1272(1)	6854(1)	20(1)	N(4)	−737(6)	−2345(4)	6428(5)	30(1)
Cl(1)	1522(2)	8158(1)	9839(1)	38(1)	N(5)	−538(6)	−142(4)	8030(4)	26(1)
Cl(2)	3715(2)	3389(1)	9084(2)	47(1)	C(1)	−3714(8)	−1252(5)	9004(5)	30(1)
Cl(3)	3034(2)	6087(1)	7217(1)	43(1)	C(2)	−5144(7)	−672(6)	8202(5)	32(1)
Cl(4)	−1350(2)	4954(2)	8212(2)	52(1)	C(3)	−3595(10)	−3623(6)	5403(7)	50(2)
O(1)	−2385(4)	−459(3)	5502(3)	27(1)	C(4)	−1664(9)	−3329(6)	5360(7)	50(2)
O(2)	−2163(5)	1155(4)	4626(3)	33(1)	C(5)	648(7)	628(5)	7520(5)	31(1)
O(1*w*)	−4277(8)	2482(5)	7051(5)	61(1)	C(6)	−448(9)	1375(6)	6704(6)	38(1)
N(1)	−2917(7)	−2094(4)	8178(4)	27(1)	C(7)	−1738(6)	652(5)	5548(4)	25(1)
N(2)	−4366(7)	−260(5)	7228(4)	27(1)					

Note: U_{eq} is defined as a one-third of the trace of the orthogonalized U_{ij} tensor.

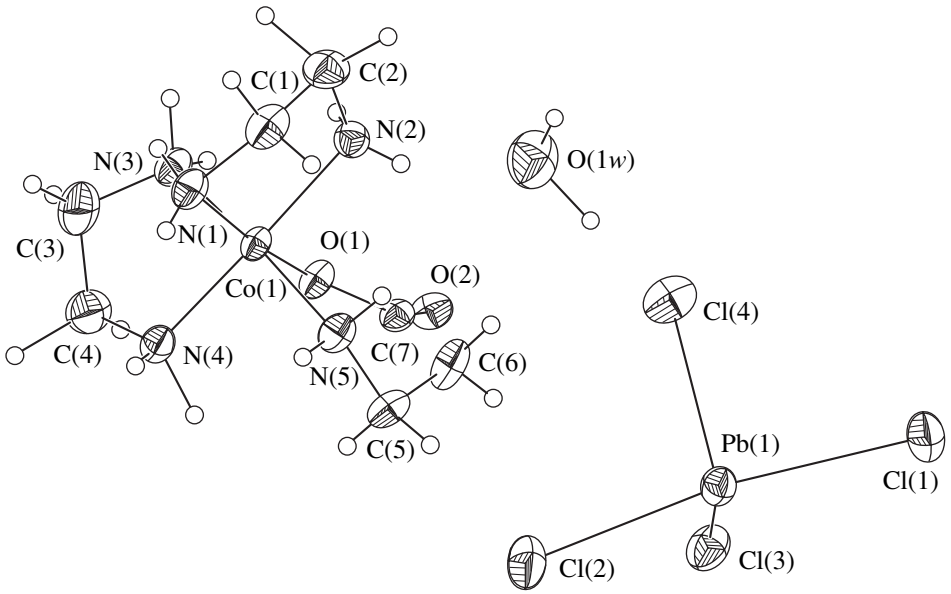

Fig. 1. Asymmetric part of the unit cell in the crystal structure of $[Co(En)_2(Ala)]PbCl_4 \cdot H_2O$.

described in [6], and equimolar amounts of HCl and $PbCl_2$ was allowed to evaporate slowly at room temperature until crystallization began. Dark red crystals of **I**, suitable for X-ray structure analysis, were chosen from their mixture with colorless crystals (apparently, $PbCl_2$). Crystals **I** are triclinic, $a = 7.627(1)$ Å, $b = 11.238(1)$ Å, $c = 11.444(1)$ Å, $\alpha = 99.125(1)°$, $\beta = 103.80(1)°$, $\gamma = 94.739(1)°$, $V = 933.09(1)$ Å^3, $Z = 2$ (the formula unit is $C_7H_{24}Cl_4CoN_5O_3Pb$), space group $P\bar{1}$, $d_{calcd} = 2.257$ g/cm^3, $\mu = 104.8$ cm^{-1}.

Table 2. Bond lengths (d, Å) in anionic chains

Bond	d
Pb–Cl(1)	2.935(1)
Pb–Cl(2)	2.821(2)
Pb–Cl(3)	2.762(1)
Pb–Cl(4)	2.825(2)
Pb–Cl(2')	3.080(2)
Pb–Cl(4')	3.180(3)

Table 3. Possible hydrogen bonds in the crystal structure of $[Co(En)_2(Ala)]PbCl_4 \cdot H_2O$

A···B	Distance, Å	Position of the B atom
O(1*w*)···Cl(2)	3.16(1)	$x-1, y, z$
O(1*w*)···Cl(4)	3.29(1)	x, y, z
N(2)···O(1*w*)	3.12(1)	x, y, z
N(3)···O(1*w*)	3.01(1)	$-1-x, -y, 1-z$
N(3)···O(2)	2.95(1)	$-1-x, -y, 1-z$
N(4)···O(2)	3.07(1)	$-x, -y, 1-z$
N(5)···Cl(1)	3.26(1)	$x, y-1, z$
N(5)···Cl(1)	3.30(1)	$-x, 1-y, 2-z$

The intensities of the reflections were measured on a Siemens *P*4 automated diffractometer (λMoK_α, graphite monochromator, $\omega/2\theta$ scan mode, $\theta_{max} = 28.3°$).

Absorption corrections were applied empirically (Ψ-scan technique). The structure was solved by the heavy-atom method and refined by the full-matrix least-squares procedure in the anisotropic approximation (the number of parameters was 281). The hydrogen atoms at the fixed calculated positions were included in the last cycle of the refinement.

The final estimates of the refinement are $R_1 = 0.0341$, $wR_2 = 0.0803$, and *GooF* = 1.007 for 4482 reflections with $I > 2\sigma(I)$. All the calculations were performed with the XP [7] and SHELXTL [8, 9] software packages. The atomic coordinates and equivalent thermal parameters are listed in Table 1.

RESULTS AND DISCUSSION

The asymmetric part of the unit cell of structure **I** contains the cobalt(III) cationic complex, the $PbCl_4^{2-}$ anionic group, and the crystallization water molecule (Fig. 1). The Co atom has the octahedral environment formed by five nitrogen atoms and the oxygen atom belonging to two ethylenediamine molecules and the alanine anion. The *En* ligands form two five-membered metallocycles, and the *Ala* ligand forms the six-membered ring. The latter ring has the λ configuration, and the *En* rings have different configurations (λ and δ). The mutual arrangement of the three metallocycles

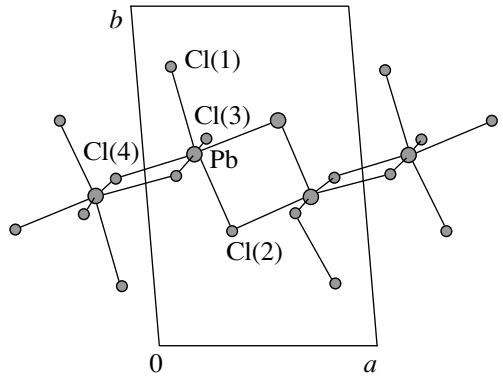

Fig. 2. Projection of the $[Cl_2Pb(\mu\text{-}Cl)_2]_n$ chain along the *z*-axis in structure **I**.

shown in Fig. 1 corresponds to the Δ absolute configuration. Since compound **I** crystallizes in the centrosymmetric space group $P\bar{1}$, the crystal contains the $[Co(En)_2(Ala)]^{2+}$ cationic complexes with the opposite configuration Λ(δ, λ, δ). The distances Co–N [1.966(4)–1.980(5) Å] and Co–O [1.935(3) Å] are typical of the Co(III) complexes. The coordination octahedron of the Co atom is slightly distorted: the endocyclic angles deviate from an ideal value of 90°. The cationic complexes are arranged in layers parallel to the *x*0*z* plane.

The $PbCl_4$ groups (Fig. 1) are linked into the $[Cl_2Pb(\mu\text{-}Cl)_2]_n^{2n-}$ infinite anionic chains, which are parallel to the *x*-axis and are located between the cationic layers (Fig. 2). Two pairs of atoms [Cl(2), Cl(2)' and Cl(4), Cl(4)'], each related by a center of symmetry, serve alternately as bridges in the chain. Thus, the Pb atom has the distorted octahedral environment. The Pb–Cl distances vary in the range from 2.76 to 3.18 Å (Table 2), which is close to the Pb–Cl distances in other polymeric chloroplumbate(II) complexes [3–5].

Several O–H···Cl, N–H···O, and N–H···Cl hydrogen bonds are likely formed in structure **I**. These bonds act within the cationic layers and link the layers to the anionic chains (Table 3).

ACKNOWLEDGMENTS

This study was supported in part by the Belarussian Foundation for Basic Research, project no. F98-243.

REFERENCES

1. M. Geselle and H. Fuess, Z. Kristallogr. **212** (2), 241 (1997).
2. A. Bonamartini Corradi, A. M. Ferrari, G. C. Pellacani, *et al.*, Inorg. Chem. **38** (4), 716 (1999).
3. H. J. Haupt and F. Huber, Z. Anorg. Allg. Chem. **442**, 31 (1978).
4. P. Mauersberger, H. J. Haupt, and F. Huber, Acta Crystallogr., Sect. B: Struct. Crystallogr. Cryst. Chem. **35** (2), 295 (1979).
5. J.-W. Cai, J. Myrczek, and I. Bernal, J. Chem. Soc., Chem. Commun., No. 16, 1147 (1992).
6. W. S. Keyes and J. I. Legg, J. Am. Chem. Soc. **98** (16), 4970 (1976).
7. *XP: Interactive Molecular Graphics Program, Version 5.03* (Siemens Analytical X-ray Instrumentation Inc., Madison, 1994).
8. G. M. Sheldrick, *Program for the Refinement of Crystal Structures* (University of Göttingen, Göttingen, 1993).
9. G. M. Sheldrick, *SHELXTL, Version 5.0: Reference Manual* (Siemens Analytical X-ray Instrumentation Inc., Madison, 1994).

Translated by I. Polyakova

Crystallography Reports, Vol. 47, No. 1, 2002, pp. 58–64. Translated from Kristallografiya, Vol. 47, No. 1, 2002, pp. 65–71.

STRUCTURE OF ORGANIC COMPOUNDS

Crystal Structures and Properties of Isomers of 3,5-Dinitro-(4-Acetylphenyl)aminobenzoyl (*p*-Bromophenyl)amide

A. P. Korobko, I. V. Levakova, S. V. Krasheninnikov, A. I. Stash, N. A. Kon'kova, V. V. Kuz'min, N. V. Kozlova, and T. A. Korobko

Karpov Research Institute of Physical Chemistry, Russian State Scientific Center, ul. Vorontsovo pole 10, Moscow, 103064 Russia

e-mail: korobko@cc.nifhi.ac.ru

Received June 19, 2001

Abstract—The *para* and *ortho* isomers of 3,5-dinitro-(4-acetylphenyl)aminobenzoyl (*p*-bromophenyl)amide (**I** and **II**, respectively) are synthesized, and their physicochemical properties and structure are investigated. The *para* isomer **I** has a higher melting temperature and is less soluble in organic solvents as compared to the *ortho* isomer **II**. The electronic absorption spectra indicate that absorption for molecule **I** occurs at longer wavelengths than for molecule **II**. A correlation between the physicochemical properties and the crystal structures of compounds **I** and **II** is revealed. Crystals $\mathbf{I} \cdot 0.5C_6H_6$ are triclinic; the unit cell parameters are $a = 11.760(2)$ Å, $b = 13.958(3)$ Å, $c = 15.012(3)$ Å, $\alpha = 108.01(2)°$, $\beta = 103.95(1)°$, $\gamma = 92.00(2)°$, $V = 2258.3(8)$ Å^3, space group $P\bar{1}$, and $Z = 4$. Crystals **II** are monoclinic; the unit cell parameters are $a = 9.302(2)$ Å, $b = 16.380(3)$ Å, $c = 13.480(3)$ Å, $\beta = 100.09(3)°$, $V = 2022.1(7)$ Å^3, space group $P2_1/c$, and $Z = 4$. Structures $\mathbf{I} \cdot 0.5C_6H_6$ and **II** are characterized by intramolecular and intermolecular hydrogen bonds. © *2002 MAIK "Nauka/Interperiodica".*

INTRODUCTION

Pigments based on dinitrobenzoic acid [1] are of practical interest as hydrophobic organic dyes with submicron particles. They can be used for preparation of transparent colored polymeric nanocomposites with improved mechanical and dielectric properties [2].

In order to choose a suitable pigment, it is important to know its properties (electronic absorption spectra, crystal structure, etc.). Earlier [3], we studied the structure and some properties of two derivatives of 3,5-dinitrobenzoic acid, namely, the *para* and *ortho* isomers of 3,5-dinitro-(4-methoxyphenyl)aminobenzoyl (*p*-bromophenyl)amide.

The purpose of the present work was to investigate the structure and properties of the *para* and *ortho* isomers of 3,5-dinitro-(4-acetylphenyl)aminobenzoyl (*p*-bromophenyl)amide.

SYNTHESIS AND PROPERTIES OF THE PIGMENTS

The synthesis of the *para* and *ortho* isomers of 3,5-dinitro-(4-acetylphenyl)aminobenzoyl (*p*-bromophenyl)amide was performed according to the procedure described in [3]. In order to prepare the target products, namely, 3,5-dinitro-4-(4-acetylphenyl)aminobenzoyl (*p*-bromophenyl)amide (**I**) and 3,5-dinitro-2-(4-acetylphenyl)aminobenzoyl (*p*-bromophenyl)amide (**II**)

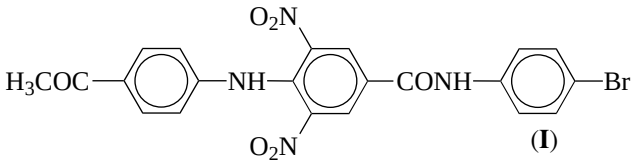

(**I**)

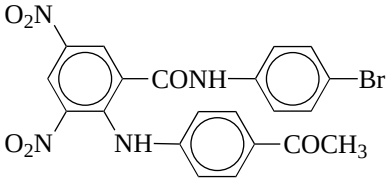

(**II**)

p-anisidine was replaced by *p*-aminoacetophenone at the second stage. The rest of the reagents and the synthesis conditions remained unchanged.

The results of the chemical analysis are as follows:

For $C_{21}H_{15}N_4O_6Br$, anal. calcd. (%): C, 50.51; H, 3.03; N, 11.22; Br, 16.01; O, 19.28.

Found for **I** (%): C, 50.4; H, 3.1; N, 11.3; Br, 15.3.

Found for **II** (%): C, 50.5; H, 3.0; N, 11.0; Br, 15.5.

Both isomers are insoluble in water and almost insoluble in hexane and CCl_4. Their solubility in toluene, benzene, ethanol, chloroform, ethyl acetate, and acetone is moderate. The solubility of **II** is slightly higher than that of **I**. The solubility in acetone is the highest (13.22 and 23.06 mmol/l for **I** and **II**, respec-

tively), whereas the solubility in ethanol is significantly less (1.00 and 1.69 mmol/l, respectively).

According to differential scanning calorimetry (TA-3000 equipped with a Mettler DSC-20 attachment; heating rate, 20 K/min), the melting temperatures T_m of the fine crystalline samples **I** and **II**, which were prepared in an ethanol solution, are equal to 219.4 and 134.1°C, respectively. The heats of melting ΔH_m for **I** and **II** are 100.7 and 96.9 J/g, respectively. Both compounds easily become amorphous upon cooling their melts at a rate higher than 20 K/min.

ELECTRONIC ABSORPTION SPECTRA

The electronic absorption spectra of compounds **I** and **II** in the UV and visible ranges were recorded on a Perkin-Elmer Model 402 spectrophotometer. The spectra of the samples prepared in the form of ethanol solutions and nujol (or petrolatum oil) pastes are shown in Fig. 1. The initial fine crystalline samples **I** and **II** were used in these measurements. The maxima of the absorption bands and the corresponding extinction coefficients are given in Table 1.

The data obtained indicate that the absorption of compound **I** occurs at longer wavelengths than that of compound **II**. The electronic absorption spectra of the synthesized compounds in the solid and dissolved states differ substantially. This is probably due to the difference in the interactions of the pigment molecules with their environment (i.e., with the pigment molecules in the solid state and the ethanol molecules in solutions [4, p. 57]). The shift of the long-wavelength bands (attributed to the particular color) toward the short-wavelength range upon dissolving the pigments in ethanol allows us to assign these bands to the n–π^* transitions [4, p. 60].

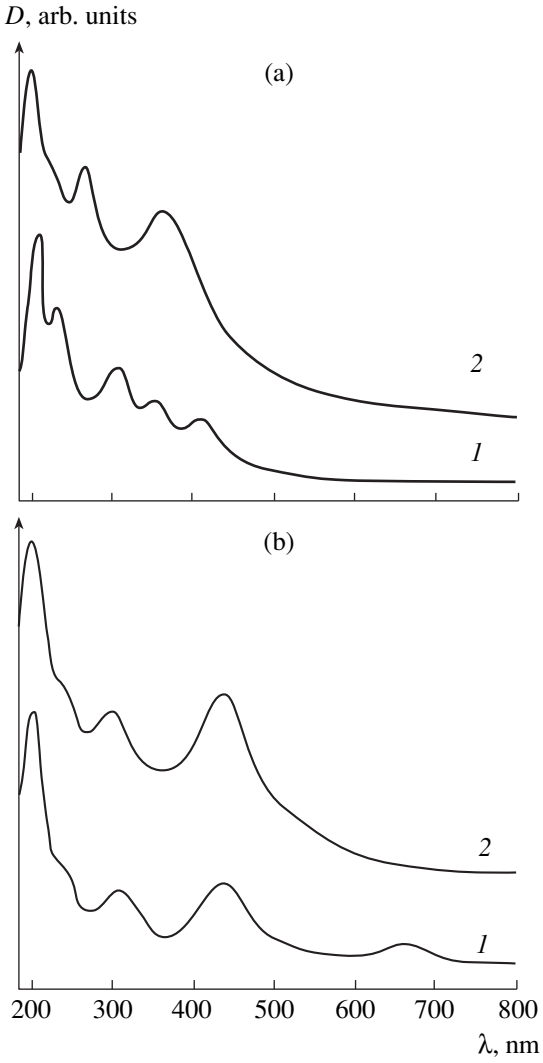

Fig. 1. Electronic absorption spectra of compounds (*1*) **I** and (*2*) **II** in (a) ethanol and (b) nujol.

X-RAY STRUCTURE ANALYSIS

Single crystals suitable for X-ray structure analysis were obtained by slow evaporation of saturated solutions of compound **I** in an acetone : benzene (1 : 1) mixture and compound **II** in acetone. Single crystals of both pigments have a yellowish color that is hardly distinguishable by eye. The linear dimensions of the single crystals chosen for X-ray diffraction analysis did not exceed 0.6 mm.

Growing single crystals of compound **I** involved the greatest difficulties. All our attempts to grow single crystals free of solvent molecules failed. When employing the individual solvents in the synthesis of the studied compounds, we observed the formation of concretions of thin flakes (chloroform), piles of thin needle crystals (acetone and ethanol), or dendrite-like concretions (toluene, ethyl acetate, and benzene) irrespective of the conditions of solvent evaporation. With the mixtures of acetone and ethanol or benzene, we obtained well-shaped crystals with dimensions large enough for X-ray diffraction analysis. It turned out that crystals of both types were crystal solvates. The crystals grown from the acetone : ethanol (1 : 1) mixture were unstable in air. For this reason, we failed to perform their complete X-ray structure analysis. Stable solvates between molecules of compound **I** and benzene in the 2 : 1 ratio

Table 1. Parameters of the electronic absorption spectra of pigments **I** and **II**

Pigment	λ, nm (ε, (l/mol cm) × 10^{-4})	
	Ethanol	Nujol
I	215 (3.37); 231 (2.17); 307 (0.98); 352 (0.34); 406 (0.14)	205; 240*; 310; 440; 660
II	199 (4.98); 228* (2.58); 263 (248); 360 (1.69)	200; 242*; 300; 442

* The band reveals itself as a shoulder.

Table 2. Main crystal data and parameters of data collection and structure refinement for pigments **I** and **II**

Parameter	Structure **I**	Structure **II**
Empirical formula	$C_{21}H_{15}BrN_4O_6 \cdot 1/2C_6H_6$	$C_{21}H_{15}BrN_4O_6$
Molecular weight	538.33	499.28
Crystal form	Plate	Prism
Crystal system	Triclinic	Monoclinic
Space group	$P\bar{1}$	$P2_1/c$
Unit cell parameters		
a, Å	11.760(2)	9.302(2)
b, Å	13.958(3)	16.380(3)
c, Å	15.012(3)	13.480(3)
α, deg	108.01(2)	90
β, deg	103.95(1)	100.09(3)
γ, deg	92.00(2)	90
V, Å^3	2258.3(8)	2022.1(7)
Z	4	4
ρ_{calcd}, g/cm^3	1.583	1.640
Radiation (λ, Å)	CuK_α (1.54178)	CuK_α (1.54178)
Absorption coefficient, mm^{-1}	2.920	3.207
Diffractometer	Syntex $P\bar{1}$	Enraf–Nonius CAD4
Scan mode	θ/2θ	θ/2θ
Number of reflections measured	4331	2193
Number of unique reflections with $I > 2\sigma(I)$	4146 (R_{int} = 0.018)	2017 (R_{int} = 0.063)
2θ range, deg	3.21 ⟶ 57.40	4.29 ⟶ 64.94
Refinement on	F^2	F^2
$R(F)$	0.041	0.033
$wR(F^2)$	0.102	0.088
S	1.02	1.09
Number of parameters refined	764	350
Extinction coefficient	0.00044(6)	0.0030(2)

(**I** · $0.5C_6H_6$) can be formed only from an acetone : benzene mixture. According to the data of differential scanning calorimetry, the crystal solvates grown are stable to rather high temperatures. The DSC curve exhibits three endothermal peaks: the first peak is observed at 144.6°C (ΔH = 32.3 J/g) and can be considered the limit of the range of the solvate existence; the second peak, at 220.0°C (ΔH = 3.5 J/g), corresponds apparently to a crystal–crystal phase transformation; and the third peak, at 271.2°C (ΔH = 107.7 J/g), characterizes melting of the crystallites formed. Note that the thermal properties of the initial fine crystalline sample **I** and the grown single crystals of the solvate are essentially different. At the same time, the DSC curves of the initial fine crystalline compound **II** and its single crystals grown from acetone coincide within the measurement error.

The main characteristics of the X-ray diffraction experiment and the crystal data are summarized in Table 2. The measurements were performed at room temperature.

The structures were solved by the direct method and refined in the anisotropic approximation for the non-hydrogen atoms and in the isotropic approximation for the hydrogen atoms using the SHELXL97 program package [5]. The sets of the observed data were corrected for absorption empirically (with allowance made for crystal habit) using the ABSCOR program, which is included in the CSD software package [6]. The parameters T_{max} and T_{min} were equal to 0.892 and 0.437 for

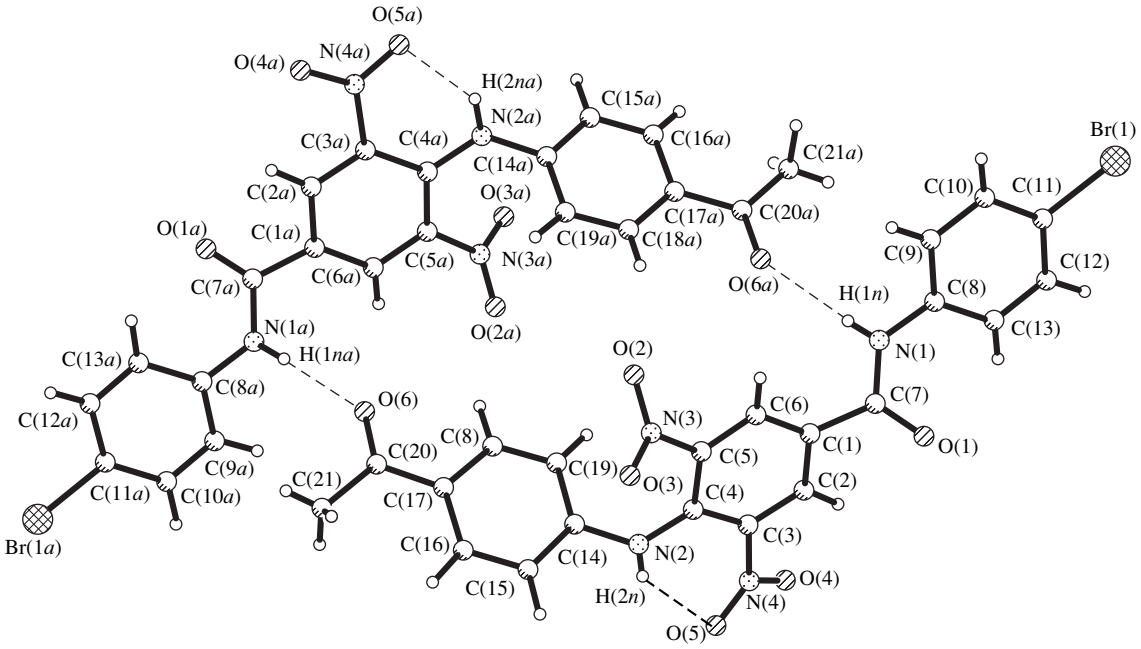

Fig. 2. Pseudocentrosymmetric dimer **I** and the atomic numbering.

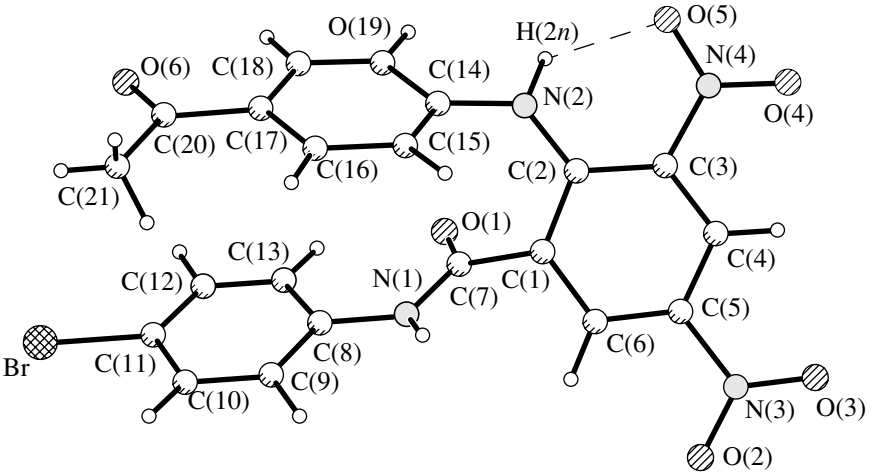

Fig. 3. Molecule **II** and the atomic numbering.

structure **I** · $0.5C_6H_6$ and 0.523 and 0.349 for structure **II**, respectively.

The structures of molecules **I** and **II** with the atomic numbering are shown in Figs. 2 and 3, respectively. The atomic coordinates and equivalent isotropic thermal parameters of the non-hydrogen atoms are listed in Table 3.

RESULTS AND DISCUSSION

Both independent molecules of structure **I** · $0.5C_6H_6$ (Fig. 2) involve the N–H···O(NO_2) intramolecular hydrogen bonds. These bonds are characterized by the following parameters: N···O, 2.68(1) and 2.64(1) Å; H···O, 2.18(5) and 2.03(5) Å; and the N–H···O angle, 131.9(4)° and 135.0(4)°.

The mean atomic deviation from the plane of the C(3)C(4)N(2)N(4)O(5)H(2*na*) fragment is 0.09 Å. The maximum deviations are observed for the O(5) and N(4) atoms (+0.13 and –0.17 Å, respectively). The mean deviation from the plane of the corresponding fragment in the second molecule is 0.05 Å; in this case, the maximum deviations are observed for the N(2*a*) and H(2*n*) atoms (+0.08 Å and –0.05 Å, respectively).

In addition to the intramolecular hydrogen bonds, the structures involve two intermolecular hydrogen bonds. One of them, N(1*a*)–H(1*na*)···O(6), is characterized by the following parameters: N(1*a*)···O(6), 2.88(1) Å;

Table 3. Coordinates ($\times 10^4$) and isotropic equivalent thermal parameters ($Å^2 \times 10^3$) of the non-hydrogen atoms in structures **I** · $0.5C_6H_6$ and **II**

Atom	*x*	*y*	*z*	U_{eq}, $Å^2$	Atom	*x*	*y*	*z*	U_{eq}, $Å^2$
Structure **I** · $1/2C_6H_6$									
Br(1)	159(1)	6740(1)	8921(1)	85(1)	O(3*a*)	2908(3)	2637(3)	733(3)	61(1)
O(1)	2533(4)	9148(3)	6259(3)	87(1)	O(4*a*)	6944(4)	−235(3)	1114(3)	87(1)
O(2)	5837(3)	6282(2)	4158(2)	56(1)	O(5*a*)	5537(3)	−3(2)	1787(3)	64(1)
O(3)	6985(3)	7639(3)	4432(2)	60(1)	O(6*a*)	3020(3)	5474(2)	4842(3)	61(1)
O(4)	2708(3)	10196(3)	3536(3)	70(1)	N(1*a*)	7193(3)	2815(3)	−985(3)	45(1)
O(5)	4456(3)	10296(2)	3329(2)	52(1)	N(2*a*)	4472(3)	1648(3)	1910(3)	45(1)
O(6)	7055(3)	4706(2)	445(3)	67(1)	N(3*a*)	3872(3)	3074(3)	838(3)	44(1)
N(1)	2639(3)	7484(3)	6048(3)	46(1)	N(4*a*)	6141(3)	225(3)	1311(3)	46(1)
N(2)	5487(3)	8587(2)	3172(3)	45(1)	C(1*a*)	6279(4)	1932(3)	−140(3)	39(1)
N(3)	6014(3)	7184(3)	4277(3)	45(1)	C(2*a*)	6446(4)	1166(3)	269(3)	44(1)
N(4)	3695(4)	9924(3)	3596(3)	47(1)	C(3*a*)	5872(4)	1074(3)	943(3)	38(1)
C(1)	3482(4)	8284(3)	5089(3)	42(1)	C(4*a*)	5039(4)	1729(3)	1237(3)	37(1)
C(2)	3325(4)	9029(3)	4649(3)	42(1)	C(5*a*)	4864(4)	2469(3)	770(3)	38(1)
C(3)	3965(4)	9119(3)	4021(3)	40(1)	C(6*a*)	5487(4)	2590(3)	138(3)	42(1)
C(4)	4855(4)	8497(3)	3798(3)	39(1)	C(7*a*)	6865(4)	1909(3)	−920(3)	42(1)
C(5)	5002(4)	7775(3)	4293(3)	38(1)	C(8*a*)	7776(4)	2978(3)	−1660(3)	43(1)
C(6)	4328(4)	7649(3)	4881(3)	42(1)	C(9*a*)	7700(4)	3883(4)	−1856(4)	49(1)
C(7)	2841(4)	8342(3)	5846(3)	50(1)	C(10*a*)	8286(5)	4095(4)	−2478(4)	56(1)
C(8)	2067(4)	7355(3)	6732(3)	42(1)	C(11*a*)	8954(4)	3402(4)	−2895(3)	52(1)
C(9)	2212(4)	6488(3)	7000(3)	48(1)	C(12*a*)	9032(5)	2498(4)	−2716(4)	56(1)
C(10)	1653(4)	6314(4)	7653(4)	55(1)	C(13*a*)	8460(4)	2283(4)	−2091(4)	52(1)
C(11)	944(4)	6988(4)	8032(3)	53(1)	C(14*a*)	3986(4)	2400(3)	2522(3)	38(1)
C(12)	816(4)	7854(4)	7799(4)	60(1)	C(15*a*)	3014(4)	2109(4)	2774(3)	44(1)
C(13)	1363(4)	8032(4)	7143(4)	55(1)	C(16*a*)	2533(4)	2818(3)	3399(4)	46(1)
C(14)	5997(4)	7835(3)	2581(3)	39(1)	C(17*a*)	3007(4)	3827(3)	3783(3)	38(1)
C(15)	6973(4)	8129(3)	2325(3)	44(1)	C(18*a*)	4010(4)	4104(4)	3534(3)	46(1)
C(16)	7478(4)	7399(3)	1727(3)	46(1)	C(19*a*)	4489(4)	3405(3)	2915(3)	45(1)
C(17)	7028(4)	6381(3)	1386(3)	41(1)	C(20*a*)	2529(4)	4609(4)	4480(3)	47(1)
C(18)	6026(4)	6114(3)	1641(3)	43(1)	C(21*a*)	1436(5)	4298(5)	4714(5)	60(2)
C(19)	5513(4)	6825(3)	2230(3)	42(1)	C(22)	9518(8)	−541(5)	466(8)	92(2)
C(20)	7542(4)	5572(4)	757(3)	46(1)	C(23)	10656(7)	−39(5)	871(6)	89(2)
C(21)	8660(4)	5839(4)	528(4)	61(1)	C(24)	8877(7)	−486(6)	−394(7)	90(2)
Br(1*a*)	9821(1)	3686(1)	−3722(1)	84(1)	C(25)	9302(10)	9183(8)	4572(12)	159(5)
O(1*a*)	7013(3)	1098(2)	−1461(2)	61(1)	C(26)	9574(14)	9371(16)	5443(12)	212(8)
O(2*a*)	4051(3)	3978(2)	946(3)	61(1)	C(27)	9744(8)	9705(7)	3773(13)	214(8)
Structure **II**									
Br(1)	2937(1)	2605(1)	2254(1)	74(1)	C(6)	−3031(6)	−111(2)	−2677(2)	41(1)
O(1)	−2616(3)	65(1)	−145(2)	45(1)	C(7)	−2411(4)	394(2)	−927(2)	37(1)
O(2)	−2209(6)	−849(2)	−4293(3)	103(1)	C(8)	−238(4)	1216(2)	−230(2)	35(1)
O(3)	−4441(4)	−1081(2)	−4997(2)	95(1)	C(9)	783(4)	1747(2)	−500(3)	44(1)
O(4)	−8325(4)	−395(3)	−3360(3)	135(2)	C(10)	1744(5)	2158(2)	234(3)	50(1)
O(5)	−8105(3)	362(2)	−2085(2)	66(1)	C(11)	1658(4)	2038(2)	1231(3)	47(1)
O(6)	−1923(3)	3168(2)	2164(2)	69(1)	C(12)	651(4)	1516(2)	1509(3)	45(1)
N(1)	−1248(3)	859(2)	1024(2)	38(1)	C(13)	−296(4)	1094(2)	778(2)	43(1)
N(2)	−5488(4)	811(2)	−1128(2)	43(1)	C(14)	−4662(4)	1431(2)	−547(2)	37(1)
N(3)	−3522(6)	−819(2)	−4303(2)	70(1)	C(15)	−3848(4)	1980(2)	−1008(2)	39(1)
N(4)	−7558(5)	−9(2)	−2687(3)	64(1)	C(16)	−2989(4)	2551(2)	−427(2)	39(1)
C(1)	−3505(5)	253(2)	−1872(2)	36(1)	C(17)	−2946(4)	2597(2)	605(2)	38(1)
C(2)	−5014(5)	373(2)	−1861(2)	38(1)	C(18)	−3835(4)	2075(2)	1037(2)	45(1)
C(3)	−5972(5)	−13(2)	−2663(2)	42(1)	C(19)	−4685(4)	1497(2)	473(2)	43(1)
C(4)	−5492(6)	−403(2)	−3439(3)	53(1)	C(20)	−1844(4)	3187(2)	1262(2)	42(1)
C(5)	−4042(6)	−427(2)	−3462(2)	48(1)	C(21)	−1005(6)	3732(3)	804(4)	65(1)

Note: The equivalent thermal parameter *U* is defined as a one-third of the sum of equivalent elements of the tensor of thermal vibrations. The parameters of the anisotropic thermal vibrations of the non-hydrogen atoms and the positional and thermal parameters of the hydrogen atoms are available from the authors.

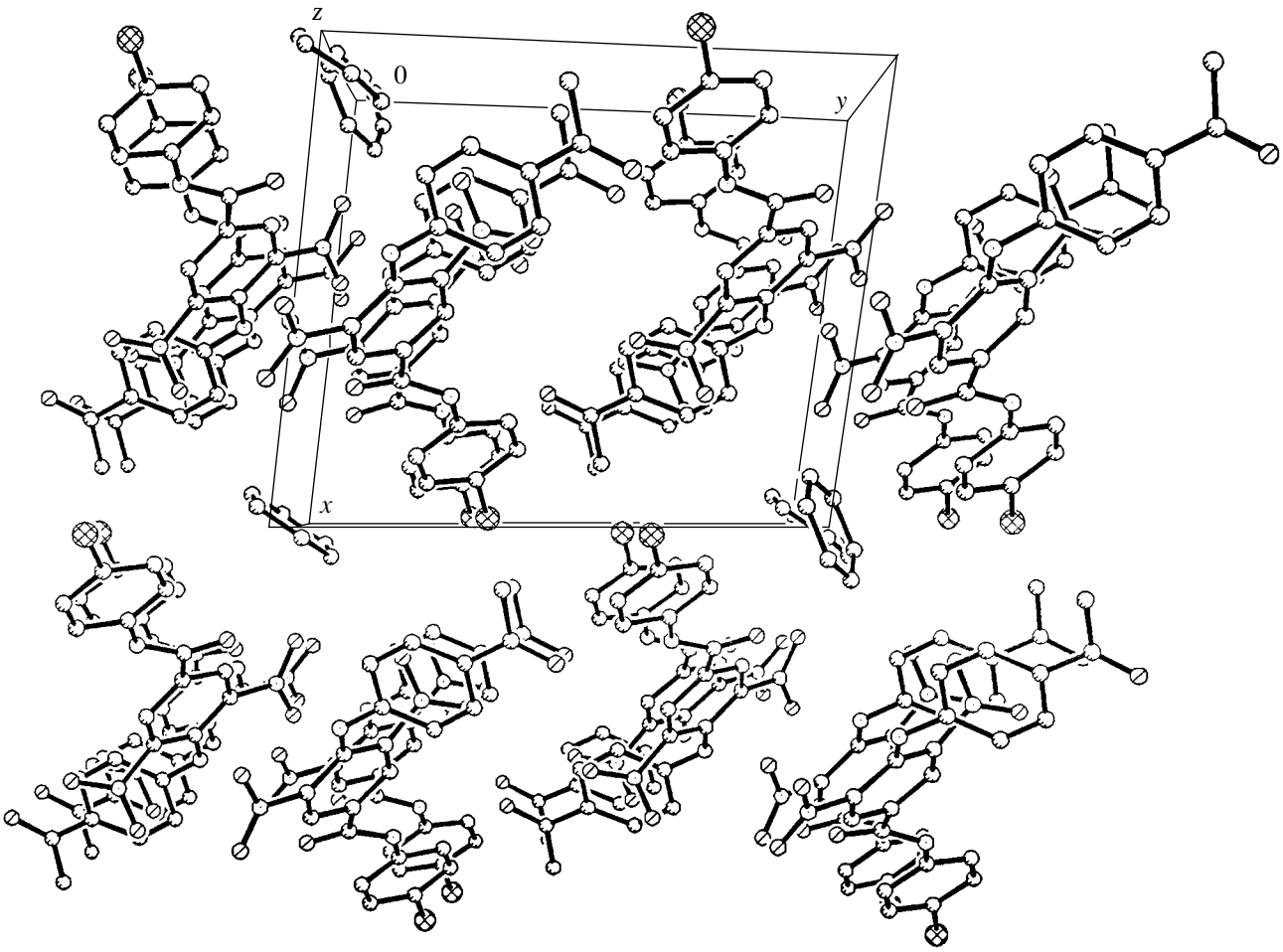

Fig. 4. Molecular packing in structure **I** · $0.5C_6H_6$.

H(1*na*)···O(6), 2.11(5) Å; and the N(1*a*)–H(1*na*)···O(6) angle, 177.2(4)°. The second intermolecular bond is symmetric with respect to the first bond, and its parameters are 2.95(1) Å, 2.20(5) Å, and 174.2(4)°, respectively.

These hydrogen bonds link independent molecules **I** into pseudocentrosymmetric dimers. The position of the pseudocenter of symmetry in the dimer is close to 1/2, 1/2, 1/4. It is interesting that both nitro groups (even the group involved in the intramolecular hydrogen bond) are rotated with respect to the phenylene ring through rather large angles. Actually, the O(5)N(4)C(3)C(4) and O(3)N(3)C(5)C(4) torsion angles are equal to 24.8(4)° and –46.0(4)°, respectively. The corresponding torsion angles in the other independent molecule **I** are 9.1(4)° and –44.1(4)°.

The molecular packing in structure **I** · $0.5C_6H_6$ is shown in Fig. 4. The pseudocentrosymmetric dimers are packed into stacks running along the *z*-axis. The stacks are separated by the channels, which accommodate the solvate benzene molecules. In the crystal studied, there are no specific interactions between molecules **I** and the solvate benzene molecules: the shortest distances C(23)···O(1*a*), C(27)···O(1), C(27)···H(1*a*), and C(27)···H(15) [3.23(3), 3.16(2), 2.70(2), and 3.00(4) Å, respectively] correspond to the van der Waals interactions.

In structure **II**, the N(2)–H(2*n*)···O(5) hydrogen bond is also formed. This bond is characterized by the N(2)···O(5) [2.65(1) Å] and H(2*n*)···O(5) [2.14(5) Å] distances and the N(2)–H(2*n*)···O(5) angle [116.5(4)°]. The O(5)N(4)C(3)C(2) and O(2)N(3)C(5)C(6) torsion angles [4.7(4)° and –0.7(4)°, respectively] are significantly smaller than those in structure **I** · $0.5C_6H_6$. The nitro group that is involved in the intramolecular hydrogen bond is rotated with respect to the phenylene ring to a larger degree as compared to the free group. The mean atomic deviation from the plane of the C(2)C(3)N(2)N(4)O(5)H(2n) fragment of the molecule is 0.08 Å, and the maximum deviations are observed for the N(2) (+0.15 Å) and H(2*n*) (–0.18 Å) atoms.

Two intermolecular contacts in structure **II**, namely, N(2)–H(2*n*)···O(1) (1 – *x*, –*y*, –*z*) and N(1)–H(1*n*)··· O(6) (*x*, 1/2 – *y*, *z* – 1/2) (Fig. 5), can be considered

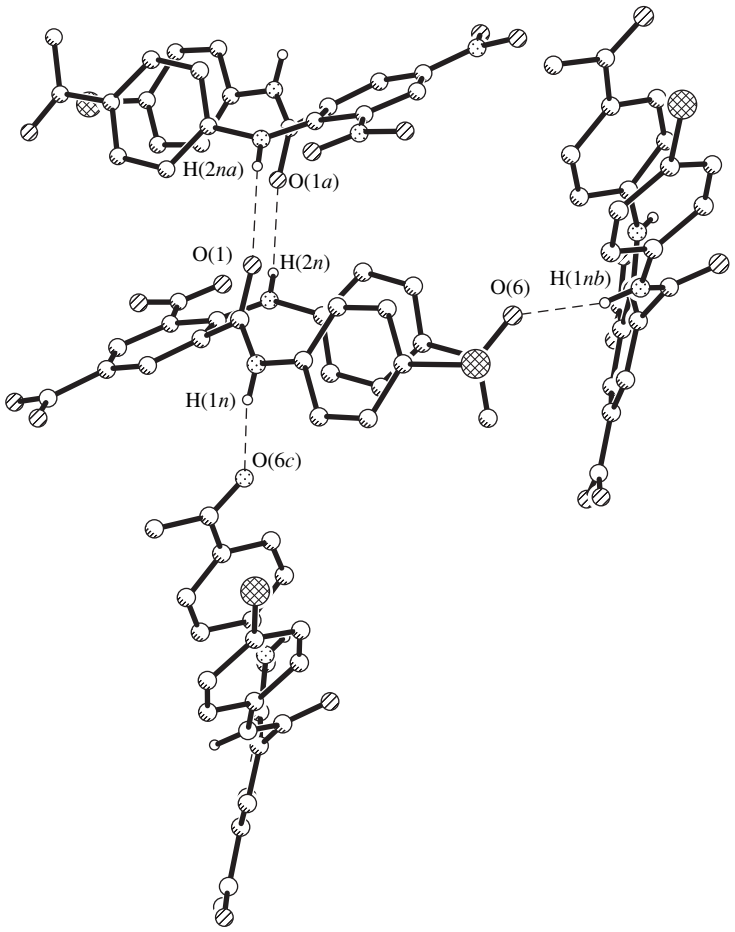

Fig. 5. A fragment of the molecular packing in crystal **II**.

rather strong intermolecular hydrogen bonds. Their parameters have the following values: N(2)···O(1), 3.03(1) Å; H(2*n*)···O(1), 2.25(5) Å; and the N(2)–H(2*n*)···O(1) angle, 146.9(4)°; and N(1)···O(6), 2.89(1) Å; H(1*n*)···O(6), 2.11(5) Å; and the N(1)–H(1*n*)···O(6) angle, 159.1(4)°. Bonds of the first type link the molecules into the centrosymmetric dimers, whereas bonds of the second type form a continuous network of intermolecular hydrogen bonds in the crystal structure.

CONCLUSION

Based on the data obtained, we can conclude that the isomerism has a profound effect not only on the crystal structure but also on the main physicochemical properties of the synthesized acetyl derivatives of 3,5-dinitrobenzoic acid. The crystals of the *para* isomer, which has elongated molecules, exhibit higher temperature and greater heat of melting and are less soluble in organic media in comparison with the crystals of the *ortho* isomer. The packing of molecules of the *para* isomer into stacks in the process of crystal growth is accompanied by the entrapment of solvent molecules (solvatation), which are located in the free space formed between the stacks (channels).

REFERENCES

1. N. N. Vorozhtsov, *Principles of Synthesis of Intermediate Products and Dyes* (Goskhimizdat, Moscow, 1955).
2. G. Carotenuto, Y.-S. Her, and E. Matijevic, Ind. Eng. Chem. Res. **35** (9), 2929 (1996).
3. A. P. Korobko, I. V. Levakova, S. V. Krasheninnikov, *et al.*, Kristallografiya **44** (2), 262 (1999) [Crystallogr. Rep. **44**, 229 (1999)].
4. E. Stern and C. Timmons, *Gillam and Stern's Introduction to Electronic Spectroscopy in Organic Chemistry* (Edward Arnold, London, 1970; Mir, Moscow, 1974).
5. G. M. Sheldrick, *SHELXL97: Program for the Refinement of Crystal Structures* (Univ. of Göttingen, Göttingen, 1997).
6. L. G. Aksel'rud, Yu. N. Grin', P. Yu. Zavaliĭ, and V. K. Pecharskiĭ, in *Proceedings of the All-Union Conference "Precision Structural Investigations of Crystals," Riga, 1990*, p. 158.

Translated by I. Polyakova

Crystallography Reports, Vol. 47, No. 1, 2002, pp. 65–68. Translated from Kristallografiya, Vol. 47, No. 1, 2002, pp. 72–75.

STRUCTURE OF ORGANIC COMPOUNDS

Molecular and Crystal Structures of 2,4,6-Trinitro-*N*-Methyl-*N*-Nitroaniline

N. E. Zhukhlistova*, W. W. Prezdo, and A. S. Bykova*****

** Shubnikov Institute of Crystallography, Russian Academy of Sciences, Leninskiĭ pr. 59, Moscow, 117333 Russia*

*** Institute of Chemistry, Pedagogical University, ul. Checinska 5, Kielce, 25-020 Poland*

**** Kharkov State Polytechnical University, ul. Frunze 21, Kharkov, 61-002 Ukraine*

e-mail: nez@ns.crys.ras.ru

Received July 5, 2000; in final form, April 23, 2001

Abstract—The structure of single crystals of 2,4,6-trinitro-*N*-methyl-*N*-nitroaniline $C_7H_5N_5O_8$ (**I**) is determined by X-ray diffraction analysis. The unit cell parameters are $a = 14.137(3)$ Å, $b = 10.621(2)$ Å, $c = 7.376(2)$ Å, $\gamma = 95.19\ (5)^\circ$, space group $P2_1/b$, and $Z = 4$. The structure is solved by the direct method and refined in the anisotropic approximation to $R = 0.051$ for 1917 reflections with $I > 2\sigma(I)$. All hydrogen atoms are located and refined in the isotropic approximation. The carbon skeleton of the aromatic nucleus of the molecule tends to adopt the C(2),C(5)-boat conformation. The angle of rotation of the planar NNO_2 group with respect to the plane of the six-membered ring is 123.1(2)°. The NO_2 groups that are bonded to the aromatic nucleus of the molecule are also rotated relative to this plane. *© 2002 MAIK "Nauka/Interperiodica".*

INTRODUCTION

Nitro compounds have attracted considerable interest due to the variety of their properties. In particular, these compounds are used as starting materials in the synthesis of dyes and explosives [1] (*N*-nitro compounds are active in photochemical reactions [2]). An interesting feature of *N*-methyl-*N*-phenylnitroamine and its derivatives is their ability to undergo a rearrangement under the effect of an acid medium and a high temperature [3]. In the present work, we performed X-ray diffraction investigation of the crystal and molecular structures of 2,4,6-trinitro-*N*-methyl-*N*-nitroaniline (**I**)

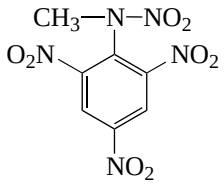

I

in order to refine the data obtained in [4] and to reveal the changes in the structure parameters of the molecule containing four nitro groups as compared to the parameters in other derivatives of *N*-methyl-*N*-nitroaniline [5–8].

EXPERIMENTAL

Single crystals **I** were grown from dichloroethane at room temperature. The compound is characterized by the following crystallographic data: $a = 14.137(3)$ Å, $b = 10.621(2)$ Å, $c = 7.376(2)$ Å, $\gamma = 95.19(5)^\circ$, space group $P2_1/b$, $Z = 4$, $V = 1103.0(10)$ Å^3, and $\rho_{calcd} = 1.729$ g/cm^3. A set of 3311 reflections was obtained at room temperature on a Syntex $P2_1$ diffractometer ($\theta/2\theta$ scan mode, graphite monochromator, MoK_α radiation). After the primary processing, we obtained a set of 2733 unique nonzero structure amplitudes. The structure was solved by the direct method and refined with the SHELX97 program [9]. The hydrogen atoms were located from the difference syntheses of electron density. The non-hydrogen atoms were refined in the anisotropic approximation, and the hydrogen atoms were refined isotropically. The final *R* factor was 0.051 for 1917 reflections with $I > 2\sigma(I)$ and 0.073 for 2733 reflections. The atomic coordinates are listed in Table 1.

RESULTS AND DISCUSSION

The structure of molecule **I** is shown in Fig. 1. In molecule **I**, unlike the molecules reported earlier in [5–7], the carbon skeleton of the aromatic nucleus is essentially nonplanar and tends to adopt the C(2),C(5)-boat conformation. The deviations of the C(2) and C(5) atoms from the plane of the remaining four atoms of the

Table 1. Atomic coordinates and thermal parameters in the structure

Atom	*x*/*a*	*y*/*b*	*z*/*c*	U_{eq}/U_{iso}, Å^2
C(1)	0.7633(1)	0.5763(2)	–0.0416(3)	0.0330(4)
C(2)	0.7756(1)	0.5272(2)	0.1312(3)	0.0349(4)
C(3)	0.7172(1)	0.4278(2)	0.2030(3)	0.0370(4)
C(4)	0.6399(1)	0.3832(2)	0.1013(3)	0.0345(4)
C(5)	0.6196(1)	0.4321(2)	–0.0673(3)	0.0366(4)
C(6)	0.6832(1)	0.5262(2)	–0.1371(2)	0.0341(4)
N(1)	0.8345(1)	0.6655(2)	–0.1128(3)	0.0426(4)
N(2)	0.8526(1)	0.5829(2)	0.2497(3)	0.0470(4)
N(4)	0.5767(1)	0.2761(2)	0.1720(3)	0.0428(4)
N(6)	0.6643(2)	0.5655(2)	–0.3250(3)	0.0478(5)
N(7)	0.8073(2)	0.7792(2)	–0.1644(3)	0.0483(5)
O(8)	0.7274(1)	0.8042(2)	–0.1201(3)	0.0553(5)
O(9)	0.8652(2)	0.8482(2)	–0.2491(4)	0.0789(7)
C(10)	0.9279(2)	0.6316(3)	–0.1688(5)	0.0605(7)
O(11)	0.8655(2)	0.6979(2)	0.2566(3)	0.0718(6)
O(12)	0.8956(2)	0.5104(2)	0.3381(3)	0.0719(6)
O(13)	0.6102(1)	0.2066(2)	0.2808(3)	0.0595(5)
O(14)	0.4959(2)	0.2629(2)	0.1162(4)	0.0753(7)
O(15)	0.5839(2)	0.5475(3)	–0.3785(3)	0.0924(9)
O(16)	0.7308(2)	0.6112(2)	–0.4158(3)	0.0662(6)
H(3)	0.728(2)	0.394(2)	0.314(4)	0.040(6)
H(5)	0.565(2)	0.405(3)	–0.138(4)	0.052(7)
H(101)	0.970(3)	0.687(4)	–0.120(6)	0.090(13)
H(102)	0.934(3)	0.552(4)	–0.129(5)	0.079(11)
H(103)	0.931(3)	0.633(4)	–0.308(7)	0.109(15)

Table 2. Short intramolecular contacts between the atoms (Å)

Contact	Length	Contact	Length
N(1)···O(11)	2.776(4)	O(8)···O(16)	2.997(3)
N(1)···O(16)	2.707(3)	H(3)···O(12)	2.58(2)
N(6)···N(7)	3.132(3)	H(3)···O(13)	2.49(2)
N(6)···O(8)	3.016(3)	H(5)···O(14)	2.54(3)
N(7)···O(16)	2.728(3)	H(5)···O(15)	2.33(3)

ring are –0.049(3) and –0.031(3) Å, respectively. The nitrogen atoms that are attached to the six-membered ring deviate differently from the plane passing through all the six atoms of the ring. The N(1) and N(6) atoms deviate by 0.157(3) and 0.122(3) Å in the same direction, whereas the N(2) atom deviates by –0.164(3) Å in the opposite direction. The N(4) atom, which is in the *para* position relative to the planar *N*-nitro group, shows the smallest deviation [0.079(3) Å] from this plane. Comparison of four C(N)–NO_2 fragments of the molecule reveals that the N(1)–N(7)O_2 and C(4)–N(4)O_2 fragments have the most planar structures: the deviations of the N atom from the planes passing through three adjacent atoms are 0.006(3) and 0.005(2) Å, respectively. The N(2) atom has the largest deviation from the plane through the adjacent atoms [0.020(2) Å], and the deviation of the N(6) atom is 0.010(2) Å.

In molecule **I**, the planar NNO_2 group is rotated relative to the plane of the six-membered ring. The C(2)–C(1)–N(1)–N(7) torsion angle is –123.1(2)°. For comparison, in the related compounds, the corresponding angle has the following values: –72.3° in *N*-nitro-*N*-methyl-4-nitroaniline [5]; –65.6(4)° in 4-chloro-*N*-methyl-*N*-nitroaniline [6]; 73.5° in *N*-methyl-*N*-2-chloroaniline [7]; and 42.6°, 63.9°, and 65.4° in three other nitro derivatives of *N*-methyl-*N*-nitroaniline [8]. The NO_2 groups that are attached to the aromatic nucleus of the molecule are also rotated relative to the six-membered ring. The C(3)–C(2)–N(2)–O(11) angle is –135.5(2)°. Two other nitro groups are rotated relative to the ring to a significantly lesser degree: the C(1)–C(6)–N(6)–O(15) and C(5)–C(4)–N(4)–O(13) angles are –159.3(2)° and –154.7(2)°, respectively. The C(10)–N(1)–N(7)–O(8) and C(10)–N(1)–N(7)–O(9) torsion angles are 178.0(3)° and –2.9(4)°, respectively; and the C(1)–N(1)–N(7)–O(9) and C(1)–N(1)–N(7)–O(8) angles are –169.7(2)° and 11.2(3)°, respectively. These values indicate that the conformation of the fragment discussed is noticeably distorted relative to similar fragments in the compounds with the substituents in the *para*-position [5, 6]. Similar changes are observed in the compound in which the Cl substituent is situated in the *ortho* position to the N(CH_3)–NO_2 group [7].

The bond lengths and angles agree with the corresponding values in *N*-nitro-*N*-methyl-4-nitroaniline [5]. The differences in bond lengths do not exceed 0.02 Å. The differences in bond angles are more significant: the N(1)–C(1)–C(6) [124.7(2)°], C(1)–C(2)–C(3) [123.4(2)°], and C(1)–C(6)–C(5) [122.6(2)°] bond angles increase by 4.8°, 4.0°, and 3.1°, respectively; and the C(2)–C(1)–C(6) angle [116.2(2)°] decreases by 5.5°. The increase in the endocyclic bond angles at the atoms of the aromatic ring that are bound to the nitro groups was also observed in other compounds [10]. The difference between the other bond angles is no more than 1.6°. In molecule **I**, the C(1)–N(1) bond is asymmetric with respect to the aromatic ring. The C(2)–C(1)–N(1) and C(6)–C(1)–N(1) angles are 118.9(2)° and 124.7(2)°, respectively. A similar situation is observed in other compounds in which nitro groups are in the *ortho* positions relative to the substituent at the C(1) atom, even if this substituent consists of one atom (Cl in picrylchloride [10]). The angle of rotation of the nitro group at the C(2) atom with respect to the aromatic ring [43.0(1)°] is larger than the rotation angles

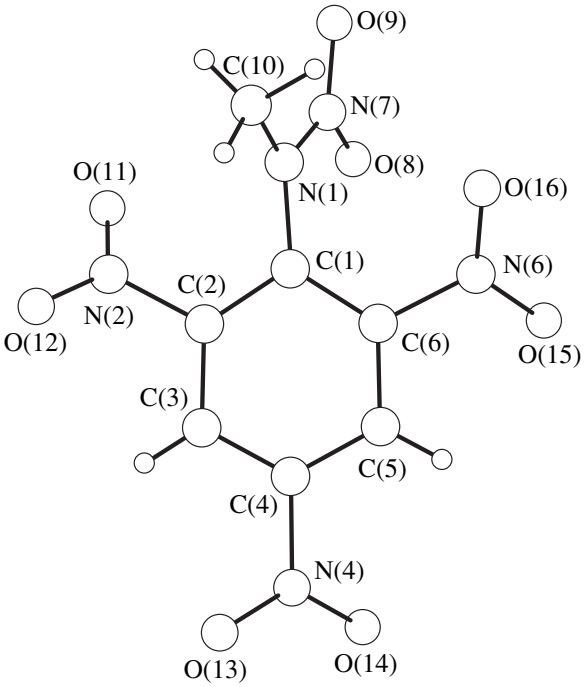

Fig. 1. Molecular structure of 2,4,6-trinitro-*N*-methyl-*N*-nitroaniline.

of the nitro groups at the C(6) [24.8(2)°] and C(4) [25.2(2)°] atoms. The adjoining angles at the C(4)–N(4) bond are equal to each other. The N–N bond in compound **I** [1.355(3) Å] is significantly longer than those in azo compounds (1.25 Å) [11] and shorter than the single N–N bond (1.48 Å) [12]. Its length agrees well with those of similar bonds in other *N*-nitro compounds (1.346(3) Å [5], 1.346(3) Å [6], 1.362(2) Å [7], and 1.352–1.360 Å [8]). The N–O bond lengths fall in the range from 1.202(3) to 1.228(3) Å, and the N(7)–O(8) bond in the $N–NO_2$ molecular fragment is the longest among them. The shortest C–N bond [1.419(2) Å] is observed in the nitroamino group, and the average length of the remaining C–N bonds is 1.477(3) Å, which is 0.06 Å longer than the similar bond between the aromatic ring and the nitroamino group. The same difference is also observed in other nitro derivatives of *N*-methyl-*N*-nitroaniline [8].

A number of short intramolecular contacts (Table 2), which are apparently due to both steric and electrostatic interactions, are observed in molecule **I**. The quantum-chemical calculations showed that the N(7) atom of the nitroamino group bears a large positive charge, whereas all its neighbors are charged negatively [7]. It was found [8] that the molecules of the nitro derivatives of

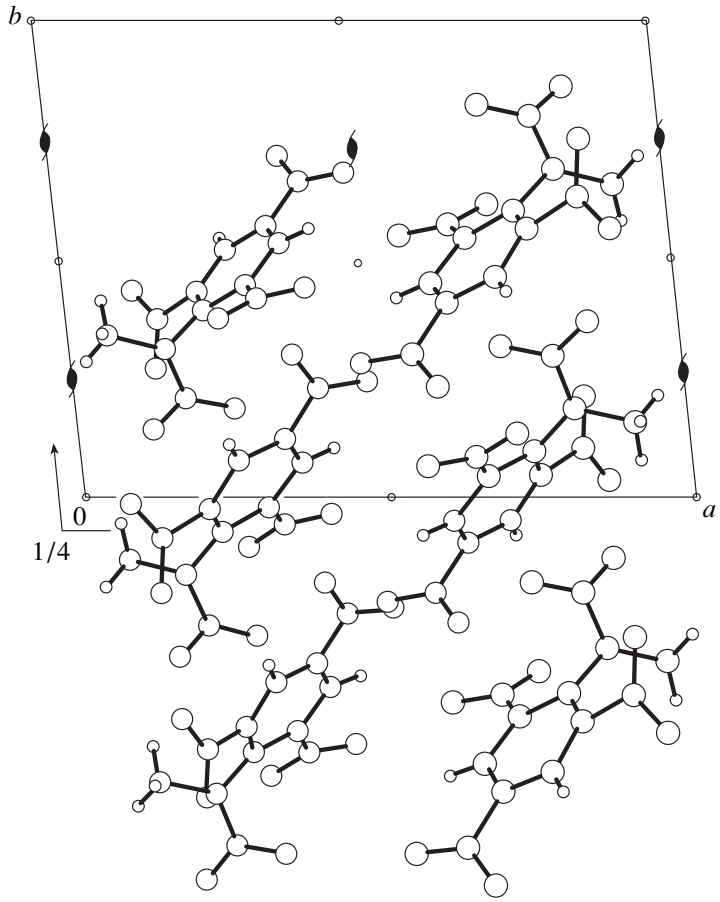

Fig. 2. Crystal structure of compound **I**.

N-methyl-*N*-nitroaniline are polar, and their dipole moments are equal to the vector sum of the dipole contributions of the substituted ring and the nitroamino group [13]. Undoubtedly, the dipole moments in the molecule affect the crystal structure. The packing of molecule **I** is shown in Fig. 2. In the crystal, the molecules are arranged in such a way that the nitro groups in the *para* position to the nitroamino group face each other and the oxygen atoms of the neighboring molecules form the short contacts O(13)···O(14) (1 – *x*, 0.5 – *y*, 0.5 + *z*) and O(14)···O(13) (1 – *x*, 0.5 – *y*, –0.5 + *z*), which are equal to 2.926(4) Å (the sum of the van der Waals radii of the O atoms is 3.04 Å [14]). Moreover, the N(2)···O(16) (*x*, *y*, 1 + *z*) and N(6)···O(8) (*x*, –0.5 + *y*, –0.5 – *z*) distances [3.040(3) and 3.018(3) Å, respectively] are slightly shorter than the sum of the van der Waals radii of the O and N atoms (3.10 Å [14]). As a result, the molecules form layers containing the methyl groups on each side. The thickness of each layer is equal to the *a* parameter of the unit cell of the crystal. The six-membered rings of the molecules that are related by the inversion center are approximately parallel to each other, and the molecules related by the *b* glide plane are inclined to each other at an angle of ~50°.

ACKNOWLEDGMENTS

We are grateful to Yu.V. Nekrasov for his aid in data collection and Z. Daszkiewicz for supplying the substance for studies.

REFERENCES

1. D. H. L. Williams, *The Chemistry of Amino, Nitroso, and Nitro Compounds and Their Derivatives* (Wiley, Chichester, 1982).
2. J. C. Mialocq and J. C. Stephenson, Chem. Phys. **106**, 281 (1986).
3. B. G. Growenlock, J. Pfab, and V. M. Young, J. Chem. Soc., Perkin Trans. **2**, 915 (1997).
4. H. H. Cady, Acta Crystallogr. **23**, 601 (1967).
5. R. Anulewicz, T. M. Krygowski, R. Gawinecki, *et al.*, J. Phys. Org. Chem. **6**, 257 (1993).
6. K. Ejsmont, J. Kyziol, Z. Daszkiewicz, *et al.*, Acta Crystallogr., Sect. C: Cryst. Struct. Commun. **54**, 672 (1998).
7. W. W. Prezdo, A. S. Bykova, T. Glowiak, *et al.*, Kristallografiya **46**, 439 (2001) [Crystallogr. Rep. **46**, 389 (2001)].
8. Z. Daszkiewicz, J. B. Kyziol, W. W. Prezdo, and J. Zaleski, J. Mol. Struct. **553**, 9 (2000).
9. G. M. Sheldrick, *SHELX97: Program for the Solution and Refinement of Crystal Structures* (Univ. of Göttingen, Göttingen, 1997).
10. J. S. Willis, J. M. Stewart, H. L. Ammon, and H. S. Preston, Acta Crystallogr., Sect. B: Struct. Crystallogr. Cryst. Chem. **27**, 786 (1971).
11. C. A. Ogle, K. A. van der Kooi, G. D. Mendenhall, *et al.*, J. Am. Chem. Soc. **105**, 5114 (1982).
12. A. F. Cameron, N. J. Hair, and D. G. Morris, J. Chem. Soc., Perkin Trans. **2**, 1071 (1972).
13. Z. Daszkiewicz, E. Nowakowska, W. W. Prezdo, and J. B. Kyziol, Pol. J. Chem. **69**, 437 (1995).
14. B. K. Vainshtein, V. M. Fridkin, and V. L. Indenbom, *Modern Crystallography*, Vol. 2: *Structure of Crystals*, Ed. by B. K. Vainshtein, A. A. Chernov, and L. A. Shuvalov (Nauka, Moscow, 1979; Springer-Verlag, Berlin, 1995).

Translated by I. Polyakova

Crystallography Reports, Vol. 47, No. 1, 2002, pp. 69–74. Translated from Kristallografiya, Vol. 47, No. 1, 2002, pp. 76–81.

STRUCTURE OF ORGANIC COMPOUNDS

X-ray Mapping in Heterocyclic Design: VI. X-ray Diffraction Study of 3-(Isonicotinoyl)-2-Oxooxazolo[3,2-*a*]pyridine and the Product of Its Hydrolysis

V. B. Rybakov*, E. V. Babaev*, K. Yu. Pasichnichenko*, and E. J. Sonneveld**

** Faculty of Chemistry, Moscow State University, Vorob'evy gory, Moscow, 119899 Russia*

*** Laboratory of Crystallography, Faculty of Chemistry, University of Amsterdam, Nieuwe Achtergracht 166, 1018 WV Amsterdam, The Netherlands*

e-mail: rybakov@biocryst.phys.msu.su

Received January 29, 2001

Abstract—The structure of 3-(isonicotinoyl)-2-oxooxazolo[3,2-*a*]pyridine, $C_{13}H_8N_2O_3$, (**I**) is determined by X-ray powder diffraction analysis. Crystals **I** are orthorhombic, $a = 16.610(2)$ Å, $b = 3.853(1)$ Å, $c = 16.431(2)$ Å, $Z = 4$, and space group $Pna2_1$. The structure is solved by the grid search procedure and refined by the Reitveld method ($R_p = 0.086$, $R_{wp} = 0.115$, $R_e = 0.030$, and $\chi^2 = 11.138$). The structure of the product of hydrolysis of compound **I**, $C_{12}H_{10}N_2O_2$, (**II**) is determined by the single-crystal X-ray diffraction technique. Crystals **II** are orthorhombic, $a = 8.755(4)$ Å, $b = 10.526(17)$ Å, $c = 23.088(6)$ Å, $Z = 8$, and space group $Pc2_1b$. The structure is solved by the direct method and refined by the full-matrix least-squares procedure to $R = 0.0464$. A fragment of two fused heterocycles in **I** is planar. The dihedral angle between the plane of the pyridine ring in the isonicotinoyl fragment and the plane of the bicyclic system is 51.2(2)°. Both exocyclic CO groups that are adjacent to the five-membered fragment contain double bonds. The structures of two crystallographically independent molecules **II** are almost identical to each other, and the isonicotinoyl fragment is nearly perpendicular to the plane of the pyridone fragment [84.3(1)° and 87.0(1)°]. *© 2002 MAIK "Nauka/Interperiodica".*

INTRODUCTION

This paper continues a series of our structural investigations of the heterocyclic compounds that are able to enter readily into various chemical rearrangements and reactions of ring transformations [1–12]. In the present work, we concentrated on the structures of 3-(isonicotinoyl)-2-oxooxazolo[3,2-*a*]pyridine, $C_{13}H_8N_2O_3$ (**I**), which belongs to the class of mesoionic heterocyclic compounds, and the product of its hydrolysis, $C_{12}H_{10}N_2O_2$ (**II**). Data on the structures of these molecules are unavailable in the Cambridge Structural Database [13].

Our interest in the structure and properties of the molecules belonging to mesoionic compounds, such as **I**, is due to, first, the unusual (ilide) structural type of their heterocycles [9] and, second, the possibility of ready opening of the oxazolone ring and its transformation into the oxazolium ring [14] according to the **I**–**IV** conversion:

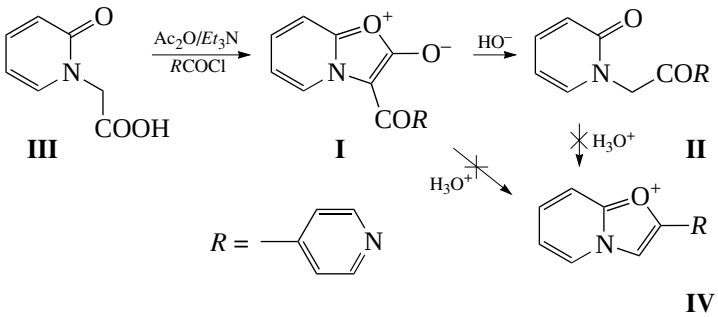

A number of representatives of the mesoionic heterocycles with the general formula $C_{13}H_8N_2O_3$ (**I**) and aliphatic or aromatic *R* residues have been described in the literature. We prepared the first representative of this series with a heterocyclic residue *R* (γ-pyridyl). Compound **I** was obtained from pyridonacetic acid **III** according to the procedure analogous to that used in [14] (*R* = *Ar*) with isonicotinoyl chloride as an acylating

Table 1. Atomic coordinates ($\times 10^4$) and isotropic thermal parameters B_{iso} (Å^2) for structure **I**

Atom	*x*	*y*	*z*	B_{iso}	Atom	*x*	*y*	*z*	B_{iso}
C(1)	1991(5)	5229(18)	−405	3.55	C(14)	439(4)	1779(21)	−1279(7)	5.70
C(2)	1456(5)	3740(18)	186(6)	3.55	N(1)	1947(4)	3072(16)	863(4)	3.55
C(3)	1744(5)	1900(21)	1618(6)	3.55	O(1)	2741(3)	5340(11)	−24(4)	3.55
C(4)	2349(5)	1259(22)	2183(5)	3.55	O(2)	1945(3)	6360(12)	−1082(4)	6.25
C(5)	3134(5)	2245(22)	1986(6)	3.55	O(3)	270(3)	1934(13)	833(4)	3.06
C(6)	3324(5)	3616(21)	1249(6)	3.55	H(3)	1222(27)	1036(159)	1758(36)	4.0
C(7)	2721(5)	4139(18)	699(6)	3.55	H(4)	2236(36)	335(135)	2691(31)	4.0
C(8)	612(4)	3033(22)	184(6)	3.55	H(5)	2540(31)	1951(175)	2378(30)	4.0
C(9)	191(5)	3327(22)	−533(6)	5.70	H(6)	3854(28)	4289(129)	1126(33)	4.0
C(10)	−576(6)	5040(21)	−491(6)	5.70	H(10)	−730(23)	5917(115)	10(35)	4.0
C(11)	−1022(4)	5424(27)	−1178(7)	5.70	H(11)	−1527(26)	6437(128)	−1144(35)	4.0
N(12)	−767(4)	3916(19)	−1938(5)	5.70	H(13)	157(31)	1329(145)	−2462(33)	4.0
C(13)	−10(6)	2390(28)	−1975(7)	5.70	H(14)	935(25)	666(138)	−1324(35)	4.0

agent. The yield of compound **I** was 47%, even though the reaction was accompanied by a substantial resinification. Heating of compound **I** with an aqueous solution of sodium carbonate resulted in the hydrolytic cleavage of the oxazolone ring and the formation of pyridone **II**. Note that it is impossible to prepare pyridone **II** by another procedure. For example, it would be difficult to follow the standard strategy for preparation of these compounds by the reaction of pyridone-2 with the corresponding bromoketone, because the suitable bromoketone, 4-bromoacetylpyridine, contains both the heteroatom of the pyridine ring and the alkylating fragment, and, therefore, it is capable of self-quaternization.

The transformation of α-amino acids into α-amino ketones under the effect of acid halides is usually called the Dakin–West reaction. The step-by-step transformation of pyridonacetic acid **III** (formally, an α-amino acid) into pyridone **II** (formally, an α-amino ketone) through the stage of formation of the stable mesoionic heterocycle **I**, which we have accomplished, should also be considered as a Dakin–West reaction.

Our attempts to carry out acid cyclodehydration of pyridone **II** into bicyclic cation **IV** were unsuccessful. Under standard conditions, which provide for an oxazolium ring closure with the other 1-phenacylpyridones (successive treatment with sulfuric and perchloric acids), pyridone **II** formed the stable perchlorate. In the latter compound, the nitrogen heteroatom of the isonicotinoyl fragment, apparently, served as a center of protonation. A similar perchlorate of pyridone **II** was also isolated in an attempt to perform recyclization of mesoionic oxazolopyridine **I** in the acid medium by analogy with the transformation revealed earlier for the case of *R* = *Ar* [14]. Thus, we have at least in part drawn the boundaries of applicability of the recyclization of mesoionic oxazolopyridines into cationoid systems.

Earlier, we characterized systems of types **I** and **II** with *Ar* = C_6H_5 [3, 9] and *para*-NO_2-C_6H_4 [8, 11] by the X-ray powder and single-crystal diffraction techniques. The present study of one more complementary pair of molecules supplements the data on the structures of mesoionic systems and the products of their hydrolysis and provides one more example of the X-ray mapping of chemical reactions [5–7, 11, 12].

EXPERIMENTAL

The X-ray diffraction experiment for **I** was performed in an evacuated Enraf–Nonius Guinier–Johansson FR552 camera ($\lambda CuK_{\alpha 1}$, quartz monochromator). The intensities and angle parameters of the X-ray spectrum were measured using an LS18 densitometer in 0.01° steps. The unit cell parameters were determined according to the ITO indexing program [15] in the 2θ angle range 4°–86° and the index ranges $0 \le h \le 13$; $0 \le k \le 3$, $0\ 0 \le l \le 13$. The space group was determined from the systematic absences of reflections. Crystals **I** are orthorhombic, $a = 16.610(2)$ Å, $b = 3.853(1)$ Å, $c = 16.431(2)$ Å, $V = 1051.6(3)$ Å^3, $d_{calcd} = 1.436$ g/cm^3, $\mu(\lambda Cu) = 8.89$ cm^{-1}, $Z = 4$, and space group $Pna2_1$.

Structure **I** was solved by the grid search procedure [16] using the given molecular fragments. The full-profile refinement of the structure was performed by the Reitveld method with the MRIA program [17]. The pseudo-Voigt function was used as a profile shape function, and the background was approximated by the Chebyshev polynomials of the fifth order. The parameters of the texture in the [010] direction were refined within the March–Dollase model [18]. The final refinement parameters are as follows: $R_p = 0.086$, $R_{wp} = 0.115$, $R_e = 0.030$, and $\chi^2 = 11.138$, where $R_p = \sum |I_o - I_c| / \sum I_o$, $R_{wp} = \sum w|I_o - I_c| / \sum wI_o$, $R_e = \sum \sigma I_o / \sum I_o$; I_o is

Table 2. Atomic coordinates ($\times 10^4$) and equivalent isotropic thermal parameters U_{eq} ($Å^2 \times 10^3$) for structure **II**

Atom	*x*	*y*	*z*	U_{eq}	Atom	*x*	*y*	*z*	U_{eq}
N(1*A*)	2515(2)	8000(2)	8031(1)	48(1)	C(9*B*)	3677(2)	10598(2)	1727(1)	49(1)
C(2*A*)	1987(3)	6861(2)	8234(1)	73(1)	C(10*B*)	4385(2)	9734(2)	1367(1)	53(1)
O(2*A*)	1588(2)	6042(2)	7876(1)	99(1)	C(11*B*)	4500(3)	10009(3)	792(1)	75(1)
C(3*A*)	1910(3)	6746(2)	8837(1)	87(1)	N(12*B*)	4008(2)	11056(2)	534(1)	86(1)
C(4*A*)	2353(3)	7668(3)	9192(1)	83(1)	C(13*B*)	3352(4)	11873(3)	892(1)	104(1)
C(5*A*)	2886(2)	8805(2)	8969(1)	66(1)	C(14*B*)	3157(3)	11706(2)	1472(1)	94(1)
C(6*A*)	2941(2)	8969(2)	8400(1)	59(1)	H(3*A*)	1452(16)	6081(17)	8983(6)	43(5)
C(7*A*)	2556(2)	8171(2)	7410(1)	52(1)	H(4*A*)	2360(20)	7600(20)	9573(9)	118(9)
C(8*A*)	1018(2)	8316(2)	7142(1)	44(1)	H(5*A*)	3320(20)	9570(20)	9262(8)	99(8)
O(8*A*)	−94(1)	8508(1)	7440(1)	64(1)	H(6*A*)	3310(30)	9750(20)	8165(9)	125(9)
C(9*A*)	860(2)	8207(2)	6511(1)	46(1)	H(7*A*1)	3105(17)	8840(20)	7319(7)	62(6)
C(10*A*)	−426(2)	8675(2)	6240(1)	72(1)	H(7*A*2)	3070(20)	7520(20)	7223(7)	81(7)
C(11*A*)	−541(3)	8557(3)	5654(1)	91(1)	H(10*A*)	−1249(19)	8970(20)	6485(7)	72(6)
N(12*A*)	483(2)	8031(2)	5308(1)	81(1)	H(11*A*)	−1415(19)	8860(10)	5453(7)	70(6)
C(13*A*)	1714(3)	7602(2)	5576(1)	67(1)	H(13*A*)	2474(18)	7325(18)	5314(7)	73(7)
C(14*A*)	1946(2)	7643(2)	6159(1)	58(1)	H(14*A*)	2790(20)	7330(20)	6319(8)	86(7)
N(1*B*)	2442(2)	10839(1)	3307(1)	46(1)	H(3*B*)	4471(17)	11115(19)	4465(7)	67(6)
C(2*B*)	3687(2)	11161(2)	3631(1)	47(1)	H(4*B*)	2344(15)	10235(15)	4846(6)	35(4)
O(2*B*)	4809(2)	11629(2)	3383(1)	62(1)	H(5*B*)	328(18)	9553(17)	4283(7)	55(6)
C(3*B*)	3611(2)	10883(2)	4226(1)	57(1)	H(6*B*)	365(18)	10010(18)	3314(7)	54(5)
C(4*B*)	2377(3)	10337(2)	4458(1)	62(1)	H(7*B*1)	1432(13)	11137(14)	2540(6)	23(4)
C(5*B*)	1169(3)	9984(2)	4110(1)	71(1)	H(7*B*2)	2890(20)	12030(20)	2672(8)	98(7)
C(6*B*)	1220(2)	10253(2)	3552(1)	63(1)	H(10*B*)	4680(20)	8880(30)	1554(8)	112(8)
C(7*B*)	2454(2)	11184(2)	2700(1)	52(1)	H(11*B*)	5040(20)	9540(20)	550(8)	82(7)
C(8*B*)	3423(2)	10284(2)	2346(1)	47(1)	H(13*B*)	2820(30)	12440(30)	706(12)	151(11)
O(8*B*)	3962(1)	9335(1)	2551(1)	59(1)	H(14*B*)	2690(20)	12230(20)	1716(8)	80(7)

the observed intensity, and I_c is the calculated intensity. The atomic coordinates and isotropic thermal parameters are listed in Table 1.

The unit cell parameters of **II** were determined and refined using 25 reflections in the θ range 14°–16° on a CAD4 automated diffractometer [19] (λMoK_α, graphite monochromator). Crystals **II** are orthorhombic, a = 8.755(4) Å, b = 10.526(17) Å, c = 23.088(6) Å, V = 2128(4) $Å^3$, d_{calcd} = 1.337 g/cm^3, μ(λMo) = 0.093 mm^{-1}, Z = 8, space group $Pc2_1b$. A set of 1266 reflections with $I \geq 2\sigma(I)$ was collected by the ω-scan technique in the range θ ≤ 21.96° on the same diffractometer. The preliminary processing of the diffraction data set was performed with the WinGX98 program [20]. The structure was solved by the direct method and refined by the least-squares procedure in the anisotropic approximation using the SHELX97 program package [21]. The hydrogen atoms were located from the electron-density difference synthesis and refined in the isotropic approximation. The final discrepancy factors are R_1 = 0.0461 and wR_2 = 0.0868. The residual electron density lies between $\Delta\rho_{max}$ = 0.139 and $\Delta\rho_{min}$ = –0.116 e/$Å^3$. The atomic coordinates and equivalent thermal parameters are listed in Table 2.

The spatial arrangements of atoms in molecules **I** and **II** with atomic numberings are shown in Figs. 1 and 2, respectively. The figures were drawn using the PLUTON96 graphical program package [22].

RESULTS AND DISCUSSION

The angle between the planes of oxazolo[3,2-*a*]pyridine bicycle and the six-membered pyridine ring in molecule **I** is equal to 51.2(2)°. The C(1)–C(2) bond (1.44 Å) appeared to be significantly longer than the expected double bond, whereas the exocyclic C(1)–O(2) bond is 1.20 Å. It follows from these bond lengths that the geometry of the C(2)–C(1)=O(2) fragment is similar to that of the exocyclic C(2)–C(8)=O(3) keto group. The parameters of the O(2)=C(1)–C(2)–C(8)=O(3) structural fragment correspond to a combination of two ordinary carbonyl groups linked through

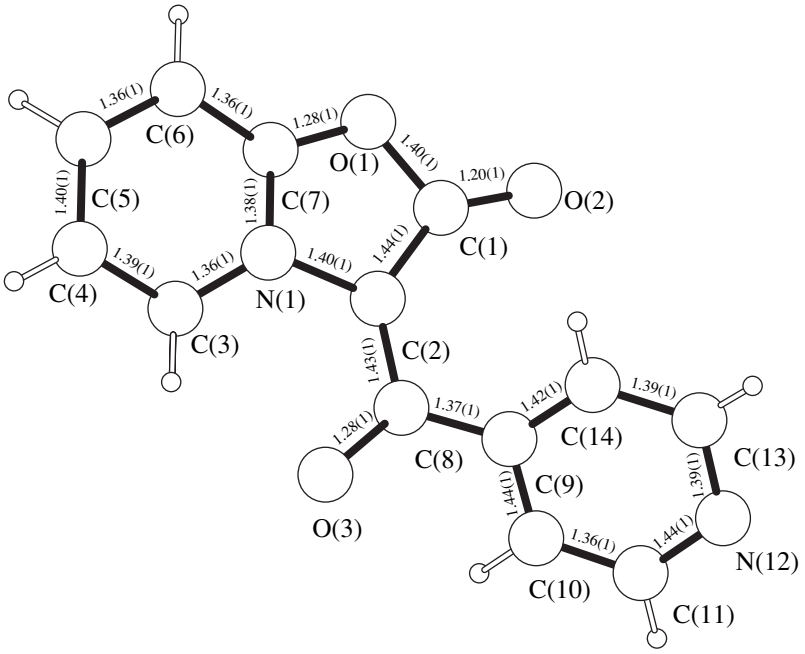

Fig. 1. Structure of molecule **I** with the atomic numbering and interatomic distances (*A*).

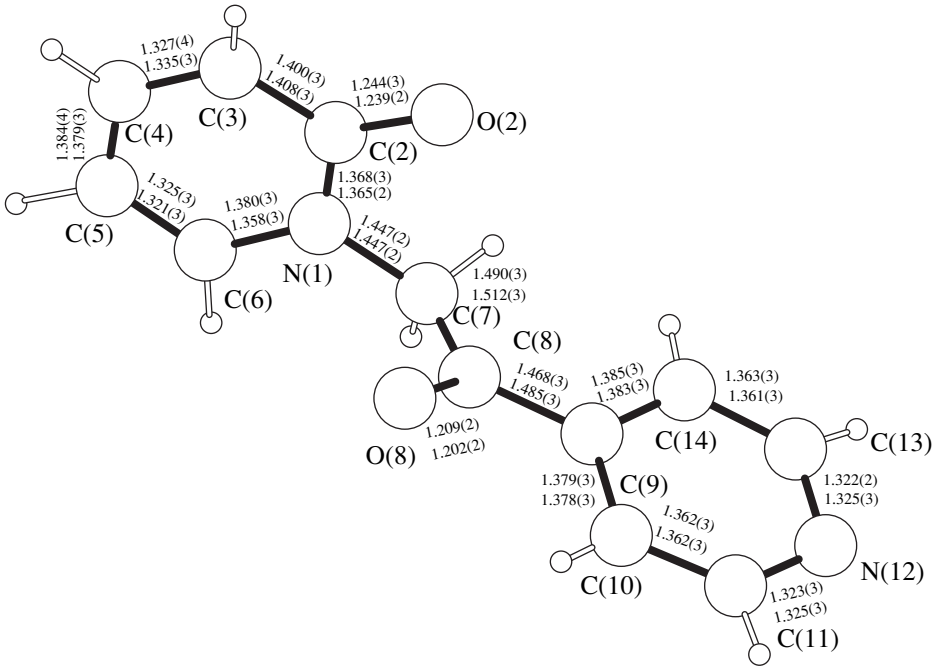

Fig. 2. Structure of molecule **II** with the atomic numbering and interatomic distances (*A*; the upper value refers to molecule *A*, and the lower value refers to molecule *B*).

the C(2) atom. This can be explained by the localization of the negative charge at the C(2) atom of the mesoionic molecule. The positive charge is delocalized in the N(1)–C(7)–O(1) chain and does not touch the pyridine fragment of the mesoionic bicycle. We revealed a similar but more pronounced delocalization of the positive charge in the molecule of the chemical analogue of **I**, which was described earlier in [9].

Earlier, we investigated the structures of *N*-substituted pyridones-2, in which the phenacyl [3] and *para*-nitrophenacyl groups are located at the nitrogen atom [8]. The structure of **II** agrees closely with the molecu-

Table 3. Parameters of the interatomic contacts* in structure **I**

D–H	*d*(*D*–H), Å	*d*(*D*···*A*), Å	*d*(H···*A*), Å	ω(*D*–H···A), deg	*A* [symmetry code]
C(3)–H(3)	0.96(5)	2.77(1)	2.22(5)	115(3)	O(3) [*x*, *y*, *z*]
C(10)–H(10)	0.93(6)	2.85(1)	2.64(5)	94(3)	O(3) [*x*, *y*, *z*]
C(14)–H(14)	0.93(5)	3.08(1)	2.79(5)	99(3)	O(2) [*x*, *y*, *z*]
C(4)–H(4)	0.93(5)	3.08(1)	2.46(5)	124(4)	O(2) [1/2 – *x*, *y* – 1/2, 1/2 + *z*]
C(5)–H(5)	0.94(5)	3.20(1)	2.67(5)	116(4)	O(2) [1/2 – *x*, *y* – 1/2, 1/2 + *z*]
C(14)–H(14)	0.93(5)	3.27(1)	2.39(5)	158(4)	O(2) [*x*, *y* – 1, *z*]

* *D* is a donor, *A* is an acceptor, and H is a hydrogen atom.

Table 4. Parameters of the interatomic contacts* in structure **II**

D–H	*d*(*D*–H), Å	*d*(*D*···*A*), Å	*d*(H···*A*), Å	ω(*D*–H···A), deg	*A* (symmetry code)
C(7*A*)–H(7*A*2)	0.93(2)	2.626(4)	2.52(2)	86(1)	O(2*A*) [*x*, *y*, *z*]
C(10*A*)–H(10*A*)	0.97(2)	2.791(3)	2.48(2)	99(1)	O(8*A*) [*x*, *y*, *z*]
C(5*B*)–H(5*B*)	0.95(2)	3.498(4)	2.86(2)	125(1)	N(12*A*) [*x*, *y*, *z*]
C(7*B*)–H(7*B*2)	0.97(2)	2.638(3)	2.39(2)	94(1)	O(2*B*) [*x*, *y*, *z*]
C(10*B*)–H(10*B*)	1.03(2)	2.790(3)	2.44(2)	99(1)	O(8*B*) [*x*, *y*, *z*]
C(3*B*)–H(3*B*)	0.97(2)	3.674(3)	2.81(2)	150(1)	N(12*B*) [1 – *x*, *y*, *z* + 1/2]
C(7*A*)–H(7*A*1)	0.88(2)	3.302(3)	2.68(2)	130(1)	O(8*B*) [1 – *x*, *y*, *z* + 1/2]
C(6*A*)–H(6*A*)	1.04(3)	3.424(5)	2.62(3)	134(2)	O(2*B*) [1 – *x*, *y*, *z* + 1/2]
C(6*A*)–H(6*A*)	1.04(3)	3.378(3)	2.81(2)	114(1)	O(8*B*) [1 – *x*, *y*, *z* + 1/2]
C(7*A*)–H(7*A*1)	0.88(2)	3.207(5)	2.71(2)	117(2)	O(2*A*) [*x*, *y* + 1/2, 3/2 + *z*]
C(7*A*)–H(7*A*2)	0.93(2)	3.363(3)	2.51(2)	153(2)	O(2*B*) [1 – *x*, *y* – 1/2,1 – *z*]
C(14*A*)–H(14*A*)	0.89(2)	3.213(3)	2.33(2)	171(2)	O(2*B*) [1 – *x*, *y* – 1/2,1 – *z*]
C(13*A*)–H(13*A*)	0.95(2)	3.640(3)	2.72(2)	163(1)	N(12*B*) [*x*, *y* – 1/2,1/2 – *z*]
C(10*B*)–H(10*B*)	1.03(2)	3.340(6)	2.38(3)	155(2)	O(2*B*) [*x*, *y* – 1/2,1/2 – *z*]
C(6*B*)–H(6*B*)	0.96(2)	3.307(3)	2.57(2)	133(1)	O(8*A*) [–*x*, *y*, *z* – 1/2]
C(7*B*)–H(7*B*2)	0.97(2)	3.218(4)	2.91(2)	100(1)	O(8*A*) [–*x*, *y* + 1/2,1 – *z*]
C(7*B*)–H(7*B*1)	0.97(1)	3.218(4)	2.76(2)	110(1)	O(8*A*) [–*x*, *y* + 1/2,1 – *z*]
C(7*B*)–H(7*B*1)	0.97(1)	3.783(3)	2.82(1)	177(1)	O(2*A*) [–*x*, *y* + 1/2,1 – *z*]
C(7*B*)–H(7*B*2)	0.97(2)	3.617(5)	2.66(2)	172(2)	O(8*B*) [*x*, *y* + 1/2,1/2 – *z*]

* *D* is a donor, *A* is an acceptor, and H is a hydrogen atom.

lar structures of these phenacylpyridones. For example, molecules *A* and *B* in structure **II** are almost identical to each other, and the O(2) and C(7) atoms (the pyridone fragment), as well as the C(8) and O(8) atoms (the acyl fragment), lie in the planes of the corresponding heterocycles.

In the pyridone fragment, the partially single and partially double bonds alternate with the formation of the quasi-diene C(3)=C(4)–C(5)=C(6) structural fragment.

The plane of the heterocycle of the acyl fragment is nearly perpendicular to the plane of the pyridone fragment; the dihedral angles are 84.34(8)° and 86.96(8)° for molecules *A* and *B*, respectively. The mutual arrangement of the six-membered rings in the molecule almost coincides with that in phenacylpyridone [87.55(6)°] [8]. In *para*-nitrophenacylpyridone [3], the corresponding dihedral angle [77.21(1)°] is, on average, 10° smaller than that in molecules *A* and *B*. Hence, we can conclude that the geometry of the molecule does not depend on the type of the acyl radical (phenyl, *para*-nitrophenyl, or γ-pyridyl).

In the crystal structures of compounds **I** and **II**, the systems of interatomic contacts involving hydrogen, nitrogen, and oxygen atoms are formed (Tables 3 and 4). These contacts were calculated with the PARST95 program [23].

ACKNOWLEDGMENTS

This study was supported by the Netherlands Society of Basic Research (NWO). The synthetic part of this work was supported by the Russian Foundation for Basic Research, project no. 99-03-33076. We are also grateful to this Foundation for the payment of the license for using the Cambridge Structural Database, project no. 99-07-90133.

REFERENCES

1. E. V. Babaev, A. V. Efimov, S. G. Zhukov, and V. B. Rybakov, Khim. Geterotsikl. Soedin., No. 7, 983 (1998).
2. E. V. Babaev, S. V. Bozhenko, D. A. Maiboroda, *et al.*, Bull. Soc. Chim. Belg. **106** (11), 631 (1997).
3. S. G. Zhukov, V. B. Rybakov, E. V. Babaev, *et al.*, Acta Crystallogr., Sect. C: Cryst. Struct. Commun. **53**, 1909 (1997).
4. E. V. Babaev, S. V. Bozhenko, S. G. Zhukov, and V. B. Rybakov, Khim. Geterotsikl. Soedin., No. 8, 1105 (1997).
5. V. B. Rybakov, S. G. Zhukov, E. V. Babaev, *et al.*, Kristallografiya **44** (6), 1067 (1999) [Crystallogr. Rep. **44**, 997 (1999)].
6. V. B. Rybakov, S. G. Zhukov, E. V. Babaev, *et al.*, Kristallografiya **45** (1), 108 (2000) [Crystallogr. Rep. **45**, 103 (2000)].
7. V. B. Rybakov, S. G. Zhukov, E. V. Babaev, *et al.*, Kristallografiya **45** (2), 292 (2000) [Crystallogr. Rep. **45**, 261 (2000)].
8. E. V. Babaev, V. B. Rybakov, S. G. Zhukov, and I. A. Orlova, Khim. Geterotsikl. Soedin., No. 4, 542 (1999).
9. S. G. Zhukov, E. V. Babaev, V. V. Chernyshev, *et al.*, Z. Kristallogr. **215**, 306 (2000).
10. V. B. Rybakov, S. G. Zhukov, K. Yu. Pasichnichenko, and E. V. Babaev, Koord. Khim. **26** (9), 714 (2000).
11. V. B. Rybakov, S. G. Zhukov, E. V. Babaev, and E. J. Sonneveld, Kristallografiya **46** (3), 435 (2001) [Crystallogr. Rep. **46**, 385 (2001)].
12. V. B. Rybakov, S. I. Troyanov, E. V. Babaev, *et al.*, Kristallografiya **46** (6), 1069 (2001) [Crystallogr. Rep. **46**, 986 (2001)].
13. F. H. Allen and O. Kennard, Chem. Design Automat. News **8** (1), 31 (1993).
14. E. V. Babaev and I. A. Orlova, Khim. Geterotsikl. Soedin., No. 4, 569 (1997).
15. J. W. Visser, J. Appl. Crystallogr. **2**, 89 (1969).
16. V. V. Chernyshev and Y. Schenk, Z. Kristallogr. **213**, 1 (1998).
17. V. B. Zlokazov and V. V. Chernyshev, J. Appl. Crystallogr. **25**, 447 (1992).
18. W. A. Dollase, J. Appl. Crystallogr. **19**, 267 (1986).
19. *Enraf–Nonius CAD4 Software: Version 5.0* (Enraf–Nonius, Delft, 1989).
20. L. J. Farrugia, *WinGX98: X-ray Crystallographic Programs for Windows* (Univ. of Glasgow, Glasgow, 1998).
21. G. M. Sheldrick, *SHELX97: Program for the Solution and Refinement of Crystal Structures* (Univ. of Göttingen, Göttingen, 1997).
22. A. L. Spek, *PLUTON96: Molecular Graphics Program* (Univ. of Utrecht, Utrecht, 1996).
23. M. Nardelli, J. Appl. Crystallogr. **28**, 659 (1995).

Translated by I. Polyakova

Crystallography Reports, Vol. 47, No. 1, 2002, pp. 75–79. From Kristallografiya, Vol. 47, No. 1, 2002, pp. 82–86.

STRUCTURE OF ORGANIC COMPOUNDS

Structure Determination of 3β-Acetoxy-Cholest-5-Ene-7-one—A Steroid*

Rajnikant[1], V. K. Gupta[1], E. H. Khan[2], S. Shafi[2], S. Hashmi[2], Shafiullah[2], B. Varghese[3], and Dinesh[1]**

[1] *X-ray Crystallography Laboratory, Post-Graduate Department of Physics, University of Jammu, Jammu Tawi, 180 006 India*

[2] *Steroid Research Laboratory, Department of Chemistry, Aligarh Muslim University, Aligarh, 202 002 India*

[3] *Regional Sophisticated Instrumentation Center, Indian Institute of Technology, Chennai, 600 036 India*

e-mail: rajni_kant_verma@hotmail.com

Received January 15, 2001; in final form, March 12, 2001

Abstract—The crystal structure of 3β-acetoxy-cholest-5-ene-7-one ($C_{29}H_{46}O_3$) has been determined by X-ray diffraction methods. The compound crystallizes in the monoclinic crystal system (space group $P2_1$) with the unit cell parameters a = 9.632(1) Å, b = 12.280(1) Å, c = 23.099(2) Å, β = 99.52(1)°, and Z = 4. The structure has been solved by direct methods and refined to an R-value of 0.065 for 3927 observed reflections [$F_0 > 4\sigma(F_0)$]. Two crystallographically independent molecules (**I** and **II**) in the asymmetric unit have been observed. In both molecules, rings *A* and *C* of the steroid nucleus exist in a *chair* conformation. Ring *B* of molecule **I** adopts a 5α,6β *half-chair* conformation, and ring *B* of molecule **II** shows a 6α *sofa* conformation. Ring *D* adopts a 13α,14β *half-chair* conformation in molecule **I** and a 13α,14β *half-chair* conformation in molecule **II**. The crystal structure is stabilized by the intramolecular and intermolecular C–H···O interactions. © *2002 MAIK "Nauka/Interperiodica".*

INTRODUCTION

Steroids are of considerable interest due to their biological properties [1–3]. Recent studies have shown some remarkable properties exhibited by a variety of steroids, and most notable among these have found place in *antiulcer* [4], *immunoassay* [5], and *dermatological* and *ophthalmological* activities [6]. The present work is a part of our systematic research on the synthesis and structure analysis of a variety of steroidal molecules [7–16].

EXPERIMENTAL

The title compound was synthesized by adding a solution of *t*-butyl chromate [from *t*-butyl alcohol (60 ml), CrO_3 (20 g), acetic acid (84 ml), and acetic anhydride (10 ml)] at 0°C to a solution of 3β-acetoxy-cholest-5-ene (8 g) in carbon tetrachloride (150 ml), acetic acid (30 ml), and acetic anhydride (10 ml). The contents were refluxed for 3 h and then were diluted with water. The organic layer was washed with a sodium bicarbonate solution (5%) and water and then were dried over anhydrous sodium sulfate. Evaporation of the solvent under reduced pressure yielded oil, which was crystallized in methanol to give the ketone.

Transparent rectangular platelike crystals of 3β-acetoxy-cholest-5-ene-7-one (the melting point is 436 K) were obtained. Three-dimensional intensity data were collected on an Enraf–Nonius CAD4 diffractometer (CuK_α radiation, λ = 1.5418 Å, ω/2θ scan mode). A total of 5306 reflections were measured, of which 4992 reflections were found to be unique ($0 \le h \le 11$, $0 \le k \le 14$, $-27 \le l \le 27$) and 3927 reflections were observed [$F_0 > 4\sigma(F_0)$]. Two standard reflections ($35\bar{4}$ and $31\bar{9}$) measured every 100 reflections showed no significant variation in the intensity data. The reflection data were corrected for Lorentz and polarization effects. Absorption and extinction corrections were not applied.

The structure was solved by the direct method using the SHELXS97 program [17]. Two crystallographically independent molecules were found in the asymmetric unit. All the non-hydrogen atoms of the mole-

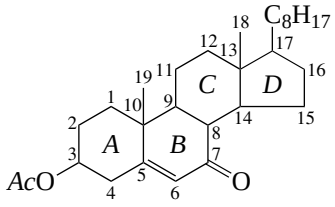

Fig. 1. Chemical structure of the molecule.

* This article was submitted by the authors in English.
** Author for correspondence.

Table 1. Crystal data and structure refinement details

Crystal habit	Rectangular plates
Empirical formula	$C_{29}H_{46}O_3$
Molecular weight	442.66
Crystal system, space group	Monoclinic, $P2_1$
Unit cell parameters:	a = 9.632(1) Å, b = 12.280(1) Å, c = 23.099(2) Å, β = 99.51(1)°
Volume	2694.4(4) Å^3
Z, density (calcd)	4, 1.091 Mg/m^3
F(000)	976
Crystal size	0.3 × 0.2 × 0.1 mm
Reflections collected/unique	5306/4992
Maximum and minimum transmission	0.99 and 0.95
Refinement method	Full-matrix least-squares on F^2
Data/restraints/parameters	4992/1/578
Goodness-of-fit on F^2	1.052
Final R factors	R = 0.065, wR = 0.169
R factors (all data)	R = 0.080, wR = 0.193
Absolute structure parameter	0.0(4)
Residual (maximum and minimum) electron densities	0.244 and –0.258 e Å^{-3}

cule were located from the *E*-map. The refinement of the structure was carried out by the full-matrix least-squares method using the SHELXL97 program [18]. The positional and thermal parameters of the non-hydrogen atoms were refined isotropically, and the *R*-factor converged at 12.7%. All the hydrogen atoms were fixed stereochemically. The anisotropic refinement in the final cycle brought down the *R*-factor of 0.065 with $wR(F^2)$ = 0.169. The maximum and minimum residual electron densities were equal to 0.24 and –0.26 e Å^{-3}, respectively. The atomic scattering factors were taken from the *International Tables for Crystallography* (1992, Vol. C Tables 4.2.6.8 and 6.1.1.4). The crystallographic data are listed in Table 1.

RESULTS AND DISCUSSION

The final atomic positions and equivalent isotropic displacement parameters for all the non-hydrogen atoms for both molecules are listed in Table 2. The endocyclic torsion angles are presented in Table 3. The chemical structure of the molecule is shown in Fig. 1. A general view of the molecule with the atomic numbering (thermal ellipsoid drawn at 50% probability) is shown in Fig. 2 [19]. The geometric calculations were performed using the PARST program [20].

In both crystallographically independent molecules, the bond distances and angles are in good agreement with analogous structures [7–16, 21]. The mean bond lengths, C(sp^3)–C(sp^3) = 1.530(8) Å [1.530(7) Å for mol-

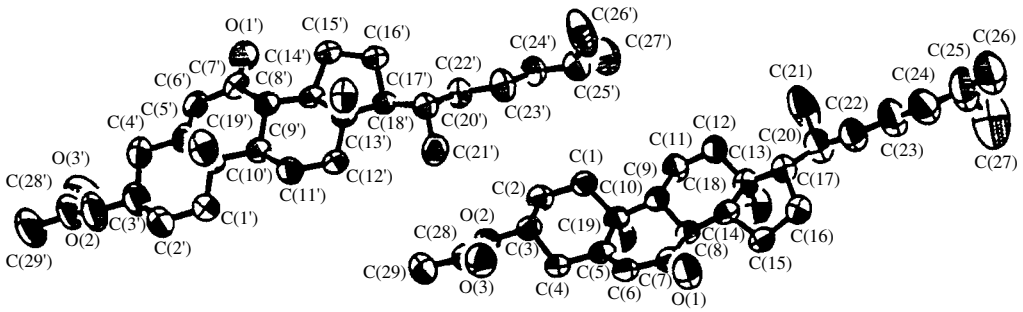

Fig. 2. A general view of the molecule with the atomic numbering.

Table 2. Atomic coordinates and equivalent isotropic thermal parameters (Å^2) for non-hydrogen atoms (e.s.d.'s are given in parentheses)

Atom	*x*	*y*	*z*	U_{eq}^*	Atom	*x*	*y*	*z*	U_{eq}^*
Molecule **I**					Molecule **II**				
O(1)	1.0099(6)	0.8092(3)	−0.2028(2)	0.111(2)	O(1')	0.3850(5)	0.0156(3)	0.2612(2)	0.101(2)
O(2)	0.9641(1)	0.5080(3)	0.0516(1)	0.072(1)	O(2')	0.5100(6)	0.3041(5)	0.5321(2)	0.132(2)
O(3)	0.8432(5)	0.6622(3)	0.0559(2)	0.102(2)	O(3')	0.6241(13)	0.1498(9)	0.5585(3)	0.221(5)
C(1)	0.9598(4)	0.4191(3)	−0.1030(2)	0.064(1)	C(1')	0.5533(6)	0.3877(5)	0.3812(2)	0.083(2)
C(2)	0.9728(5)	0.4092(4)	−0.0363(2)	0.069(1)	C(2')	0.5349(7)	0.3996(5)	0.4461(2)	0.096(2)
C(3)	0.9518(4)	0.5199(3)	−0.0115(2)	0.063(1)	C(3')	0.5344(7)	0.2891(6)	0.4724(2)	0.100(2)
C(4)	1.0621(4)	0.6003(4)	−0.0260(2)	0.067(1)	C(4')	0.4172(7)	0.2195(5)	0.4396(2)	0.094(2)
C(5)	1.0567(4)	0.6078(3)	−0.0922(2)	0.058(1)	C(5')	0.4228(5)	0.2132(4)	0.3740(2)	0.073(2)
C(6)	1.0457(4)	0.7057(4)	−0.1174(2)	0.067(1)	C(6')	0.4087(5)	0.1191(4)	0.3460(2)	0.077(2)
C(7)	1.0433(5)	0.7209(3)	−0.1807(2)	0.068(2)	C(7')	0.3983(5)	0.1058(4)	0.2829(2)	0.069(1)
C(8)	1.0784(4)	0.6221(3)	−0.2152(2)	0.061(1)	C(8')	0.3987(4)	0.2087(3)	0.2464(2)	0.059(1)
C(9)	1.0103(4)	0.5202(3)	−0.1920(2)	0.059(1)	C(9')	0.4870(4)	0.2966(4)	0.2831(2)	0.063(1)
C(10)	1.0620(4)	0.5014(3)	−0.1249(2)	0.056(1)	C(10')	0.4379(4)	0.3188(4)	0.3432(2)	0.066(1)
C(11)	1.0251(6)	0.4203(4)	−0.2293(2)	0.075(1)	C(11')	0.4984(6)	0.3994(4)	0.2472(2)	0.081(2)
C(12)	0.9744(6)	0.4402(4)	−0.2955(2)	0.078(2)	C(12')	0.5504(5)	0.3778(4)	0.1897(2)	0.072(1)
C(13)	1.0532(5)	0.5357(4)	−0.3180(2)	0.068(1)	C(13')	0.4584(3)	0.2953(3)	0.1518(2)	0.055(1)
C(14)	1.0277(4)	0.6356(3)	−0.2809(2)	0.062(1)	C(14')	0.4534(4)	0.1911(3)	0.1890(2)	0.055(1)
C(15)	1.0812(5)	0.7321(4)	−0.3135(2)	0.080(2)	C(15')	0.3805(5)	0.1081(4)	0.1442(2)	0.073(2)
C(16)	1.0438(6)	0.6984(5)	−0.3788(2)	0.084(2)	C(16')	0.4371(5)	0.1377(4)	0.0877(2)	0.071(1)
C(17)	0.9911(5)	0.5779(4)	−0.3801(2)	0.071(1)	C(17')	0.5167(4)	0.2472(3)	0.0986(2)	0.054(1)
C(18)	1.2111(6)	0.5092(6)	−0.3138(3)	0.096(2)	C(18')	0.3110(5)	0.3435(4)	0.1308(2)	0.080(2)
C(19)	1.2126(4)	0.4569(5)	−0.1119(2)	0.081(2)	C(19')	0.2954(6)	0.3798(6)	0.3352(2)	0.096(2)
C(20)	1.0161(7)	0.5178(5)	−0.4356(2)	0.097(2)	C(20')	0.5098(4)	0.3140(3)	0.0418(2)	0.060(1)
C(21)	0.9707(14)	0.4005(6)	−0.4360(3)	0.168(5)	C(21')	0.5844(7)	0.4232(4)	0.0522(2)	0.096(2)
C(22)	0.9420(7)	0.5762(5)	−0.4901(2)	0.098(2)	C(22')	0.5794(4)	0.2479(4)	−0.0020(2)	0.067(1)
C(23)	0.9742(9)	0.5371(7)	−0.5485(2)	0.124(3)	C(23')	0.5557(5)	0.2918(5)	−0.0647(2)	0.078(2)
C(24)	0.8874(9)	0.5991(6)	−0.5993(3)	0.121(3)	C(24')	0.6225(5)	0.2222(4)	−0.1066(2)	0.074(2)
C(25)	0.9099(14)	0.5655(8)	−0.6590(3)	0.160(5)	C(25')	0.6086(5)	0.2656(5)	−0.1684(2)	0.083(2)
C(26)	0.8000(12)	0.6222(14)	−0.7045(4)	0.201(7)	C(26')	0.4617(7)	0.2736(11)	−0.1994(2)	0.159(5)
C(27)	1.0486(12)	0.5967(12)	−0.6738(4)	0.203(7)	C(27')	0.4955(7)	0.1960(7)	−0.2036(3)	0.117(3)
C(28)	0.9050(6)	0.5857(5)	0.0802(2)	0.083(2)	C(28')	0.5668(16)	0.2367(11)	0.5718(3)	0.171(3)
C(29)	0.9203(8)	0.5653(6)	0.1439(2)	0.114(3)	C(29')	0.5348(14)	0.2653(10)	0.6324(3)	0.203(6)

* $U_{eq} = (1/3)\sum_i \sum_j U_{ij} a_i^* a_j^* (\mathbf{a}_i \mathbf{a}_j)$.

ecule **II**], [C(sp^3)–C(sp^2)] = 1.508(6) Å [1.517(8) Å], [C(sp^2)–C(sp^2)] = 1.401(6) Å [1.387(7) Å], [C(sp^2)=O] = 1.210(6) Å [1.238(12) Å], [C(sp^2)–O] = 1.340(7) Å [1.288(12) Å], [Csp^3–O] = 1.450(5) Å [1.448(7) Å] are quite close to their theoretical values [22, 23].

In molecule **I**, the endocyclic bond angles in the steroid nucleus fall in the range from 106.7(4)° to 124.6(4)° [the average value is 112.9(4)°] for the six-membered rings and from 100.1(4)° to 107.1(4)° [the average value is 103.5(4)°] for the five-membered ring [the corresponding average values for both kinds of rings in the case of molecule **II** are 113.2(4)° and 103.4(3)°, respectively]. In both molecules, the ring *A* adopts a *chair* conformation, the asymmetry parameters are ΔC_2 [C(2)–C(3)] = 2.19 and ΔC_s [C(3)] = 3.85 [for molecule **II**, the corresponding values are ΔC_2 [C(2)–C(3)] = 3.07 and ΔC_s [C(2)] = 3.07] [24]. Ring *B*

Table 3. Endocyclic torsion angles (deg) for non-hydrogen atoms (e.s.d.'s are given in parentheses)

Molecule **I**		Molecule **II**	
C(2)–C(1)–C(10)–C(5)	−48.3(5)	C(2')–C(1')–C(10')–C(5')	−50.5(6)
C(10)–C(1)–C(2)–C(3)	56.8(5)	C(10')–C(1')–C(2')–C(3')	58.6(6)
C(1)–C(2)–C(3)–C(4)	−60.0(5)	C(1')–C(2')–C(3')–C(4')	−58.7(6)
C(2)–C(3)–C(4)–C(5)	57.6(5)	C(2')–C(3')–C(4')–C(5')	−54.6(7)
C(3)–C(4)–C(5)–C(10)	−51.3(5)	C(3')–C(4')–C(5')–C(10')	−48.8(6)
C(4)–C(5)–C(10)–C(1)	45.4(5)	C(4')–C(5')–C(10')–C(1')	45.4(6)
C(6)–C(5)–C(10)–C(9)	−16.0(6)	C(6')–C(5')–C(10')–C(9')	−19.9(6)
C(10)–C(5)–C(6)–C(7)	−2.6(7)	C(10')–C(5')–C(6')–C(7')	−3.5(8)
C(5)–C(6)–C(7)–C(8)	−9.9(8)	C(5')–C(6')–C(7')–C(8')	−2.2(7)
C(6)–C(7)–C(8)–C(9)	39.4(5)	C(6')–C(7')–C(8')–C(9')	30.7(5)
C(7)–C(8)–C(9)–C(10)	−58.3(4)	C(7')–C(8')–C(9')–C(10')	−54.4(5)
C(9)–C(8)–C(14)–C(13)	−55.8(5)	C(9')–C(8')–C(14')–C(13')	−55.9(5)
C(14)–C(8)–C(9)–C(11)	49.8(5)	C(14')–C(8')–C(9')–C(11')	51.3(5)
C(8)–C(9)–C(10)–C(5)	46.5(4)	C(8')–C(9')–C(10')–C(5')	49.2(5)
C(8)–C(9)–C(11)–C(12)	−51.5(5)	C(8')–C(9')–C(11')–C(12')	−52.9(5)
C(9)–C(11)–C(12)–C(13)	56.9(5)	C(9')–C(11')–C(12')–C(13')	56.2(5)
C(11)–C(12)–C(13)–C(14)	−57.8(5)	C(11')–C(12')–C(13')–C(14')	−55.7(5)
C(12)–C(13)–C(14)–C(8)	59.4(5)	C(12')–C(13')–C(14')–C(8')	57.5(4)
C(14)–C(13)–C(17)–C(16)	41.0(4)	C(14')–C(13')–C(17')–C(16')	40.7(4)
C(17)–C(13)–C(14)–C(15)	−47.5(4)	C(17')–C(13')–C(14')–C(15')	−48.1(4)
C(13)–C(14)–C(15)–C(16)	34.5(4)	C(13')–C(14')–C(15')–C(16')	36.1(4)
C(14)–C(15)–C(16)–C(17)	−8.1(5)	C(14')–C(15')–C(16')–C(17')	−10.1(5)
C(15)–C(16)–C(17)–C(13)	−20.8(5)	C(15')–C(16')–C(17')–C(13')	−19.3(5)

Table 4. Torsion angles about the bonds in the C_8H_{17} side chain

Torsion bond	Molecule **I** (torsion angle)	Molecule **II** (torsion angle)	Molecule **I** (conformation)	Molecule **II** (conformation)
C(13)–C(17)–C(20)–C(21)	55.5(7)	57.7(5)	+*sc*	+*sc*
C(21)–C(20)–C(22)–C(23)	−64.1(8)	−69.0(5)	−*sc*	−*sc*
C(20)–C(22)–C(23)–C(24)	177.2(6)	−178.3(4)	*ap*	*ap*
C(22)–C(23)–C(24)–C(25)	−179.2(7)	−176.8(4)	*ap*	*ap*
C(23)–C(24)–C(25)–C(26)	−70.7(11)	−62.9(7)	−*sc*	−*sc*

Note: The designations *sc* and *ap* refer to *syn-clinal* and *anti-periplanar*, respectively.

of molecule **I** exists in a 5α,6β *half-chair* conformation [ΔC_2 [C(5)–C(6)] = 6.62], while the same ring assumes a 6α *sofa* conformation [ΔC_s [C(6)] = 6.96] in molecule **II**. Ring *C* adopts a *chair* conformation for both molecules [ΔC_2 [C(8)–C(9)] = 3.52 (2.31) and ΔC_s [C(9)] = 1.49(1.40)]. The five-membered ring *D* occurs in a *distorted* 13α,14β *half-chair* conformation [ΔC_2 [C(13)–C(14)] = 10.09] in molecule **I**, while it exists in a 13β,14α *half-chair* [ΔC_2 [C(13)–C(14)] = 7.27] in molecule **II**, the phase angle of pseudorotation Δ = –4.86° (–3.56° for molecule **II**), and the maximum angle of torsion φ_m = –47.5° (–48.1° in molecule **II**) [25].

Table 5. Geometry of intra- and intermolecular C–H···O interactions (e.s.d.'s are given in parentheses)

C–H···O	H···O (Å)	C···O (Å)	C–H···O (deg)
C(3)–H(3)···O(3)	2.418	2.667	93.7
C(4)–H(4A)···O3	2.670	3.150	111.0
C(15)–H(15B)···O(1)	2.436	2.913	110.0
C(3')–H(3')···O(3')	2.362	2.657	96.5
C(4')–H)4'2)···O(3')	2.796	3.230	108.0
C(15')–H(15D)···O(1')	2.472	2.925	108.3
C(2')–H2'2···O3'	2.704	2.427	131.6

Note: Symmetry code: (*i*) $-x + 1, y + 1/2, -z + 1$.

For both crystallographically independent molecules, the conformational designations of the single bond at the C(17) position are presented in Table 4 [26–27]. There exists intra- and intermolecular C–H··O interactions (see Table 5), which contribute to the stability of the crystal structure.

ACKNOWLEDGMENTS

Rajnikant acknowledges the support of the University Grant Commission and the Council of Scientific and Industrial Research, New Delhi, Government of India for research funding.

REFERENCES

1. H. G. Williams-Ashman and H. Reddi, Annu. Rev. Physiol. **33**, 31 (1971).
2. E. V. Jensen and E. R. Desombre, Annu. Rev. Biochem. **41**, 203 (1972).
3. W. L. Duax, C. M. Weeks, and D. C. Rohrer, in *Topics in Stereochemistry,* Ed. by N. L. Allinger and E. L. Eliel (Wiley, New York, 1976), Vol. 9, p. 271.
4. M. R. Bell, R. Oesterlin, K. O. Geolotte, *et al.*, J. Heterocycl. Chem. **14**, 1059 (1977).
5. M. Kimto, H. Tsuji, T. Ogawa, and K. Sasaoka, Arch. Biochem. Biophys. **300**, 657 (1993).
6. J. M. Bernardon, Chem. Abstr. **118**, 191364j (1993).
7. V. K. Gupta, Rajnikant, K. N. Goswami, and K. K. Bhutani, Cryst. Res. Technol. **29**, 77 (1994).
8. V. K. Gupta, K. N. Goswami, K. K. Bhutani, and R. M. Vaid, Mol. Mater. **4**, 303 (1994).
9. V. K. Gupta, Rajnikant, K. N. Goswami, *et al.*, Acta Crystallogr., Sect. C: Cryst. Struct. Commun. **50**, 798 (1994).
10. A. Singh, V. K. Gupta, Rajnikant, and K. N. Goswami, Cryst. Res. Technol. **29**, 837 (1994).
11. A. Singh, V. K. Gupta, Rajnikant, *et al.*, Mol. Mater. **4**, 295 (1994).
12. A. Singh, V. K. Gupta, K. N. Goswami, *et al.*, Mol. Mater. **6**, 53 (1996).
13. Rajnikant, V. K. Gupta, J. Firoz, *et al.*, Kristallografiya **46** (3), 465 (2001) [Crystallogr. Rep. **46**, 415 (2001)].
14. Rajnikant, V. K. Gupta, J. Firoz, *et al.*, Kristallografiya **45**, 857 (2000) [Crystallogr. Rep. **45**, 785 (2000)].
15. Rajnikant, V. K. Gupta, J. Firoz, *et al.*, Cryst. Res. Technol. (in press).
16. Rajnikant, V. K. Gupta, J. Firoz, *et al.*, Cryst. Res. Technol. (in press).
17. G. M. Sheldrick, *SHELXS97: Program for the Solution of Crystal Structures* (Univ. of Göttingen, Göttingen, 1997).
18. G. M. Sheldrick, *SHELXL97: Program for the Refinement of Crystal Structures* (Univ. of Göttingen, Göttingen, 1997).
19. M. N. Burnett and C. K. Johnson, ORTEP-III. Report ORNL-5138 (Oak Ridge National Laboratory, Tennessee, 1996).
20. M. Nardelli, Comput. Chem. **7**, 95 (1993).
21. R. Radhakrishnan, M. A. Viswamitra, K. K. Bhutani, and R. M. Vaid, Acta Crystallogr., Sect. C: Cryst. Struct. Commun. **44**, 1820 (1988).
22. L. E. Sutton, *Tables of Interatomic Distances and Configuration in Molecules and Ions,* Spec. Publ. No. 18 (The Chemical Society, London, 1965).
23. L. S. Bartell and R. A. Bonhan, J. Chem. Phys. **32**, 824 (1960).
24. W. L. Duax and D. A. Norton, *Atlas of Steroid Structures* (Plenum, New York, 1975), Vol. 1.
25. C. Altona, H. J. Geise, and C. Romers, Tetrahedron **24**, 13 (1968).
26. W. Klyne and V. Prelog, Experientia **12**, 521 (1960).
27. R. S. Cahn, C. K. Ingold, and V. Prelog, Experientia **12**, 81 (1956).

Crystallography Reports, Vol. 47, No. 1, 2002, pp. 80–85. Translated from Kristallografiya, Vol. 47, No. 1, 2002, pp. 87–92.

STRUCTURE OF ORGANIC COMPOUNDS

Crystal and Molecular Structures of Dimethyl 4-Phenylthiosemicarbazidediacetate and Its Adduct with Rhodium(II) Acetate

V. Ch. Kravtsov*, Yu. A. Simonov*, J. Lipkowski, O. A. Bologa***, N. V. Gérbéléu***, and V. I. Lozan*****

** Institute of Applied Physics, Academy of Sciences of Moldova, ul. Academiei 5, Chisinau, MD-2028 Moldova*

*** Institute of Physical Chemistry, Polish Academy of Sciences, Kasprzaka 44/52, Warsaw, 01-224 Poland*

**** Institute of Chemistry, Academy of Sciences of Moldova, ul. Academiei 3, Chisinau, MD-2028 Moldova*

e-mail: kravtsov.xray@phys.asm.md

Received March 27, 2001

Abstract—The crystal structures of dimethyl 4-phenylthiosemicarbazidediacetate $C_{13}H_{17}N_3O_4S$ (**I**) and its adduct $[C_8H_{12}O_8Rh_2\ (C_{13}H_{17}N_3O_4S)_2]$ (**II**) with rhodium(II) acetate are determined by X-ray diffraction analysis. The unit cell parameters of crystals **I** are as follows: a = 8.066(6) Å, b = 15.812(6) Å, c = 24.977(8) Å, β = 94.88(3)°, space group $P2_1/n$, and Z = 8. The unit cell parameters of crystals **II** are a = 8.513(1) Å, b = 16.055(1) Å, c = 16.071(3) Å, β = 104.99(1)°, space group $P2_1/c$, and Z = 2. In structure **I**, two crystallographically independent molecules considerably differ from each other in the mutual orientation of the structural fragments containing the ester groups. In the centrosymmetric dimeric complex **II**, the organic molecule **I** acts as a monodentate thio ligand and adopts only one conformation. © *2002 MAIK "Nauka/Interperiodica".*

INTRODUCTION

Thiosemicarbazidediacetic acid [1] is a polydentate multifunctional ligand that forms different complexes with transition and post-transition metals, depending on the synthesis conditions. The data on structures of 24 coordination compounds with this ligand are available in the Cambridge Structural Database (version 5.20, October 2000) [2]. Analysis of these data demonstrates that the tetradentate tripodal ligand coordination with the metal chelation through a group of the S, N, O, and O donor atoms occurs most frequently. 4-Phenylthiosemicarbazidediacetic acid participates in the coordination in a similar manner [3]. For the purpose of changing the donor properties of these ligands and increasing their selectivity, we synthesized dimethyl 4-phenylthiosemicarbazidediacetate (*Es*, **I**). In our earlier work [4], we succeeded in preparing the copper(II) complex with this compound. It should be noted that, in the $[CuCl_2Es]$ compound, the ester adds through a group of the S, N, O, and O donor atoms in a tripodal manner.

The aim of the present work was to determine the crystal and molecular structures of dimethyl 4-phenylthiosemicarbazidediacetate (**I**) and its adduct (**II**) with rhodium(II) acetate.

EXPERIMENTAL

Synthesis of the complex. The reaction between warm methanol solutions of $[Rh_2(CH_3COO)_4(H_2O)_2]$ and *Es* resulted in the formation of a dark violet solution. Upon cooling of this solution, dark brown crystals precipitated. The yield was 40%.

For $C_{34}H_{46}Rh_2N_6O_{16}S_2$, anal. calcd. (%): C, 38.36; H, 4.32; N, 7.89.

Found (%): C, 38.40; H, 4.50; N, 8.02.

X-ray diffraction analysis. Transparent, colorless, prismatic single crystals of compound **I** belong to the monoclinic crystal system (space group $P2_1/n$). A sample 0.2 × 0.3 × 0.7 mm in size was chosen for X-ray structure analysis. The intensities of experimental reflections were collected at room temperature on a DAR-UMB automated inclined diffractometer (MoK_α radiation, graphite monochromator). The unit cell parameters refined from 15 reflections in the θ range 9.3°–16.4° are as follows: a = 8.066(6) Å, b = 15.812(6) Å, c = 24.977(8) Å, β = 94.88(3)°, V = 3174(5) Å^3, d_{calcd} = 1.303 g/cm^3, and Z = 8 ($C_{13}H_{17}N_3O_4S$). The intensities of 1728 unique reflections with $I \geq 2\sigma(I)$ were measured in the ω-$\theta/2\theta$ scan mode. The structure was solved by the direct method and refined by the least-squares procedure in the anisotropic approximation for the non-hydrogen atoms. The

Table 1. Atomic coordinates ($\times 10^4$) and equivalent thermal parameters in structure **I**

Atom	Molecule **Ia**				Molecule **Ib**			
	x/*a*	*y*/*b*	*z*/*c*	B_{eq}, Å^2	*x*/*a*	*y*/*b*	*z*/*c*	B_{eq}, Å^2
S(1)	1877(2)	1509(2)	1422(1)	4.37(7)	408(2)	1939(2)	5553(1)	4.17(7)
O(21)	6584(11)	1331(6)	2650(3)	9.6(3)	−4435(7)	2939(5)	4224(3)	6.8(2)
O(31)	7532(8)	2642(5)	2577(3)	7.1(3)	−6364(8)	3738(4)	4571(3)	7.2(3)
O(22)	5938(8)	−524(4)	1133(3)	6.3(2)	−5514(7)	1672(4)	6134(2)	5.4(2)
O(32)	6960(8)	−196(4)	364(2)	5.7(2)	−6207(7)	319(4)	5956(3)	6.4(2)
N(1)	5050(7)	1391(5)	1395(3)	4.1(2)	−2841(7)	1992(4)	5397(3)	3.5(2)
N(2)	6681(6)	1088(4)	1546(3)	3.6(2)	−4380(7)	1836(4)	5095(3)	3.5(2)
N(3)	4017(8)	396(5)	1935(3)	4.2(2)	−1537(7)	1592(5)	4671(3)	4.4(2)
C(1)	3721(9)	1048(6)	1608(3)	3.3(3)	−1416(9)	1834(6)	5178(3)	3.4(2)
C(2)	2987(10)	−153(6)	2213(3)	4.5(3)	−127(9)	1406(7)	4346(4)	4.5(3)
C(3)	3643(13)	−919(7)	2366(5)	7.0(4)	326(11)	560(7)	4299(4)	5.5(4)
C(4)	2750(20)	−1476(9)	2653(6)	9.2(5)	1623(14)	389(9)	3975(5)	7.5(5)
C(5)	1210(20)	−1253(12)	2800(6)	10.0(6)	2373(14)	1026(12)	3723(6)	8.3(6)
C(6)	56(20)	−480(12)	2645(6)	9.8(6)	1890(14)	1847(10)	3776(5)	7.9(5)
C(7)	1428(11)	87(8)	2356(4)	7.0(4)	610(11)	2040(7)	4101(4)	6.2(4)
C(21)	7641(9)	1765(6)	1819(3)	4.2(3)	−5440(9)	2577(6)	5070(4)	4.1(3)
C(31)	7168(9)	1880(7)	2386(4)	5.2(3)	−5325(9)	3096(6)	4570(4)	4.5(3)
C(41)	7110(20)	2799(10)	3130(5)	10.3(6)	−6404(15)	4319(9)	4123(6)	10.9(6)
C(22)	7411(9)	792(6)	1069(4)	4.0(3)	−5133(9)	1053(6)	5266(4)	4.0(3)
C(32)	6678(9)	−40(6)	871(4)	4.4(3)	−5604(9)	1074(6)	5839(3)	3.9(3)
C(42)	6301(13)	−986(7)	134(4)	7.2(4)	−6754(14)	218(9)	6501(5)	8.9(5)

hydrogen atoms were located from the electron-density difference synthesis and refined in the isotropic approximation. The final *R* factor was equal to 0.0548 (elementary weighting scheme). The calculations were performed according to the CSD program package [5].

Dark brown, nontransparent, needle-shaped single crystals of compound **II** belong to the monoclinic crystal system (space group $P2_1/c$). The unit cell parameters and reflection intensities were measured on a KM-4 automated four-circle diffractometer (KUMA Diffraction, Poland) (CuK_α radiation, graphite monochromator) for a single-crystal sample $0.04 \times 0.06 \times 0.4$ mm in size. The unit cell parameters refined from 32 reflections in the θ range 12.8°–32.2° are as follows: a = 8.513(1) Å, b = 16.055(1) Å, c = 16.071(3) Å, β = 104.99(1)°, V = 2121.8(5) Å^3, d_{calcd} = 1.667 g/cm^3, and Z = 2 ($C_{34}H_{46}N_6O_{16}Rh_2S_2$). The intensities of 4052 reflections [3906 unique reflections with R_{int} = 0.0292 and 2377 reflections with $I \geq 2\sigma(I)$] were measured using the θ/2θ scan mode in the range 3.96° ≤ θ ≤ 70.10°.

The structure was solved by the direct method and refined on F^2 in the full-matrix anisotropic approximation for the non-hydrogen atoms according to the SHELX97 software package [6]. All the hydrogen atoms were located from the difference synthesis calculated at this stage. In further structure refinements of the methyl groups, only the orientation of the hydrogen atoms for an ideal CH_3 group was determined from the difference Fourier synthesis and then was refined by the least-squares procedure. The remaining hydrogen atoms were placed at calculated ideal positions and refined as if they were rigidly bound to the relevant carbon atoms. The isotropic thermal parameters for the hydrogen atoms were taken equal to $1.2U_{eq}$ (or $1.5U_{eq}$ for the methyl groups), where U_{eq} is the equivalent isotropic thermal parameter for the non-hydrogen atom bonded to the refined hydrogen atom. The final discrepancy factors are R = 0.044, R_w = 0.120, and S = 1.028. The atomic coordinates and equivalent isotropic thermal parameters for structures **I** and **II** are listed in Tables 1 and 2, respectively. The selected torsion angles are given in Table 3.

RESULTS AND DISCUSSION

In crystal **I**, the asymmetric part of the unit cell involves two crystallographically independent molecules **Ia** and **Ib**. The structures of these molecules are shown in Figs. 1a and 1b, respectively. Three structural fragments can be distinguished in molecule **I**: a 4-phe-

Table 2. Atomic coordinates ($\times 10^4$) and equivalent thermal parameters ($Å^2 \times 10^4$) in complex **II**

Atom	*x*/*a*	*y*/*b*	*z*/*c*	U_{eq}
S(1)	−100(2)	7693(1)	197(1)	28(1)
O(21)	3633(5)	6818(3)	−1286(3)	38(1)
O(31)	4359(5)	7944(3)	−1894(3)	36(1)
O(22)	−1785(6)	8283(3)	−3105(3)	38(1)
O(32)	−3620(6)	7268(4)	−3547(3)	50(1)
N(1)	40(6)	7532(3)	−1402(3)	24(1)
N(2)	403(6)	7099(3)	−2111(3)	22(1)
N(3)	880(6)	6389(3)	−587(3)	23(1)
C(1)	309(6)	7165(3)	−626(3)	21(1)
C(2)	1489(7)	5862(3)	125(3)	23(1)
C(3)	880(8)	5832(4)	848(4)	29(1)
C(4)	1556(9)	5288(4)	1509(4)	35(2)
C(5)	2774(8)	4743(4)	1442(4)	36(2)
C(6)	3350(8)	4751(4)	716(5)	37(2)
C(7)	2687(8)	5303(4)	58(4)	32(1)
C(21)	1650(7)	7524(4)	−2405(4)	28(1)
C(31)	3283(7)	7377(4)	−1790(4)	27(1)
C(41)	5982(8)	7855(5)	−1348(6)	51(2)
C(22)	−1055(7)	6857(4)	−2750(4)	25(1)
C(32)	−2157(7)	7562(4)	−3147(3)	30(1)
C(42)	−4811(1)	7871(6)	−3988(6)	67(3)
Ph(1)	−43(1)	9249(1)	1(1)	22(1)
O(1*a*)	−1425(5)	9313(2)	−1238(3)	29(1)
O(2*a*)	1397(5)	9285(2)	1237(3)	30(1)
C(1*a*)	−1807(7)	10014(4)	−1577(4)	28(1)
C(2*a*)	−2875(9)	10040(4)	−2484(4)	43(2)
O(1,)	−2049(5)	9354(3)	470(3)	31(1)
O(2,)	1952(5)	9248(3)	−484(3)	32(1)
C(1,)	−2522(8)	10064(4)	636(4)	32(1)
C(2,)	−3933(8)	10095(5)	1048(5)	40(2)

Table 3. Selected torsion angles (deg)

Atoms	**Ia**	**Ib**	**II**
S(1)–C(1)–N(3)–C(2)	4(1)	−2(1)	−9.8(9)
C(1)–N(3)–C(2)–C(3)	158(1)	97(1)	36.4(9)
S(1)–C(1)–N(1)–N(2)	176.4(6)	−174.8(6)	179.0(4)
C(1)–N(1)–N(2)–C(21)	−115.9(8)	−126.0(8)	−117.1(5)
N(1)–N(2)–C(21)–C(31)	76.2(8)	95.8(8)	75.6(6)
N(2)–C(21)–C(31)–O(21)	26(1)	−1(1)	21.2(8)
C(1)–N(1)–N(2)–C(22)	121.1(1)	102.6(8)	109.2(6)
N(1)–N(2)–C(22)–C(32)	−74.0(9)	64.1(9)	59.6(6)
N(2)–C(22)–C(32)–O(22)	−19(1)	5(1)	15.3(8)

nylthiosemicarbazide fragment and two methyl diacetate groups. Their mutual arrangement is characterized by the torsion angles about the N(1)–N(2), N(2)–C(21), and N(2)–C(22) bonds. The torsion angles about the first two bonds are responsible for the mutual arrangement of the thiosemicarbazide fragment and one of the ester groups. These angles in molecules **Ia** and **Ib** differ from each other by no more than 20° (Table 3). The main conformational difference between the crystallographically independent molecules resides in the orientation of the second ester group. The N(1)–N(2)–C(22)–C(32) torsion angles in two molecules are close in magnitude but opposite in sign. In molecule **Ia**, the oxygen and carbon atoms of both ester groups are located in virtually the same plane (the out-of-plane deviation is no more than 0.145 Å). In this case, the ester groups are symmetrically arranged with respect to the thiosemicarbazide fragment. A similar conformation of these ester groups in the molecule was observed in the structures of its adduct with copper(II) chloride [4] and the closest analogues of compound **I**, namely, dimethyl 4-phenyl-*S*-methylisothiosemicarbazidediacetate [7] and 4-phenylthiosemicarbazidediacetic acid [8]. In molecule **Ib**, the ester groups are noncoplanar: the angle between the root-mean-square planes is equal to 52.1°. The mutual arrangement of the ester groups with respect to the thiosemicarbazide fragment is asymmetric and similar to those revealed in the structure of thiosemicarbazidediacetic acid [1] and in one of two different conformers in the structure of 4-phenylthio-semicarbazidediacetic acid dihydrazide [9].

Analysis of the mutual arrangement of the molecular fragments in the aforementioned compounds shows that, in all the structures, the thio or semicarbazide fragment and one of the side group retain their orientation, even though they undergo a substantial modification [10]. At the same time, the third group is conformationally mobile. Different conformation mobilities of two side groups were also noted by Burshteĭn *et al.* [11], who compared the molecular structure of dimethyl semicarbazidediacetate in the crystalline state and the theoretical structure calculated by the molecular mechanics method.

In both molecules, the thiosemicarbazide fragment has a conventional conformation with the N(2) and N(3) nitrogen atoms in the *cis* positions with respect to the C(1)–N(1) bond, which is stabilized by the N(3)–H···N(2) intramolecular hydrogen bond. In molecules **Ia** and **Ib**, the N(3)···N(2) distances are equal to 2.67 and 2.64 Å, the N(3)–H distances are 1.08 and 0.90 Å, the H···N(2) distances are 2.15 and 2.21 Å, and the N(3)–H···N(2) angles are 106° and 108°, respectively. A similar hydrogen bond in the thiosemicarbazide fragment was observed earlier in [9, 12].

The phenyl rings in both crystallographically nonequivalent molecules **Ia** and **Ib** exhibit different orientations and form dihedral angles with the thiosemicarbazide fragment planes (21.4° and 95.8°, respectively).

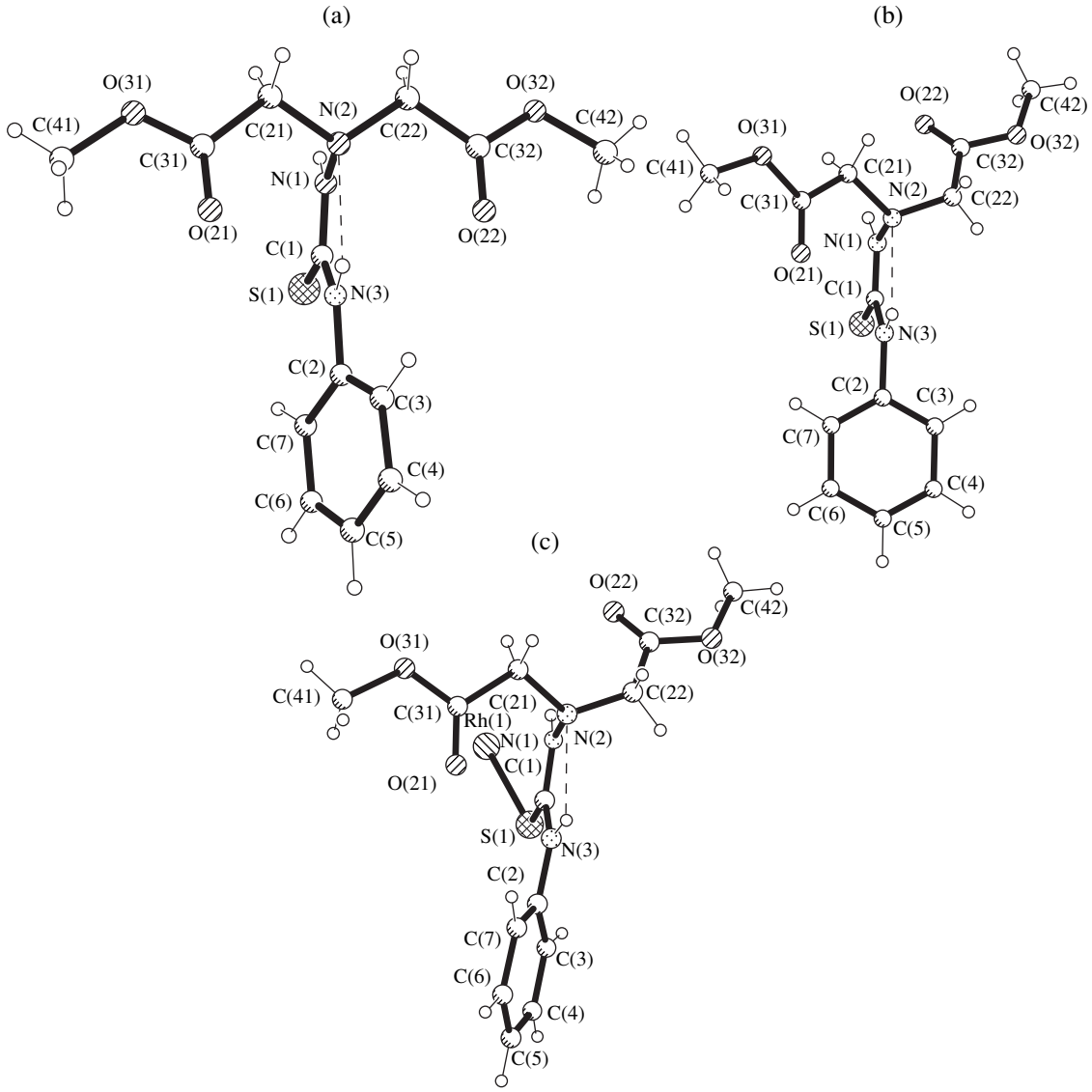

Fig. 1. Structures of the conformers in compound **I**: (a) molecule **Ia** and (b) molecule **Ib**. (c) Structure of the organic ligand in complex **II**.

These orientations are responsible for different degrees of the π-conjugation of these fragments and, correspondingly, for different N(3)–C(2) bond lengths, which, in molecules **Ia** and **Ib**, are equal to 1.42(1) and 1.48(1) Å, respectively. The other interatomic distances in both molecules coincide to within the experimental error. They have normal values for compounds of this class.

Compound **I** enters into the reaction with rhodium(II) acetate to form the centrosymmetric dimeric complex **II**, whose structure is depicted in Fig. 2. In this complex, the organic molecule acts as a monodentate thio ligand and adds to the rhodium atom at the apical position through the sulfur atom. The structural data for two binuclear rhodium(II) acetates of the composition $[Rh_2(O_2CMe)_4 \cdot 2L]$ (where *L* is *N*,*N*-dimethylthioformamide or *N*,*N*-dimethyl-*O*-ethylthiocarbamide) are available in the literature [13]. In these compounds, the Rh–Rh distances are equal to 2.409 and 2.418 Å and the Rh–S distances are 2.614 and 2.546 Å, respectively. In complex **II**, the bond lengths Rh(1)–Rh(1)' [2.413(1) Å] and S(1)–Rh(1) [2.519(2) Å] agree and the Rh(1)–S(1)–C(1) angle (112.8°) is slightly larger than the corresponding parameters observed for two rhodium dimers with the S=C grouping at the apical position [13]. In the aforementioned dimers, the Rh–S=C angles are 98.3° and 103.6° [13]. An increase in the Rh–S=C angle in structure **II** is most likely caused by steric factors. The mutual arrangement of the organic ligand and the rhodium(II) acetate dimer is stabilized by the N(1)–H···O(1*a*) intramolecular hydrogen bond. The N(1)–H···O(1*a*) intramolecular hydrogen bond [3.158(6) Å]

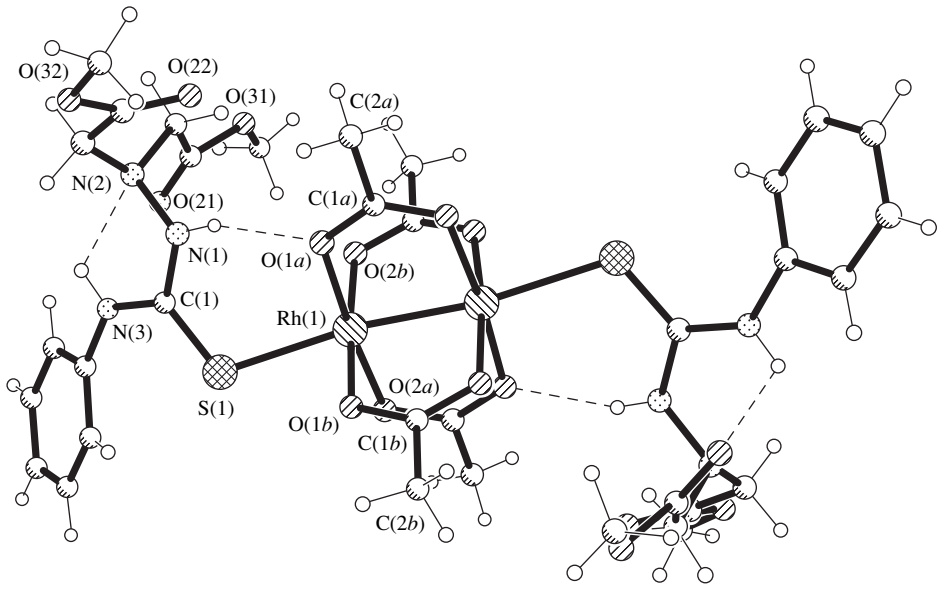

Fig. 2. Structure of complex **II**.

is characterized by the following parameters: H···O(1*a*), 2.33 Å; N(1)–H, 0.86 Å; and the N(1)–H···O(1*a*) angle, 162.7°.

Figure 1c shows the structure of the organic thio ligand in complex **II**. The thio ligand adopts a conformation with an asymmetric arrangement of the ester groups, which almost coincides with the conformation of molecule **Ib** in structure **I** (Table 3). The asymmetric arrangement of the acetate groups was also observed in a related compound, namely, thiosemicarbazidediacetic acid coordinated as a monodentate thio ligand in the complexes with rhodium [14] and cobalt [15, 16].

In complex **II**, the dihedral angle between the phenyl ring and the thiosemicarbazide fragment plane is equal to 27.8°. The N(3)–C(2) bond length is 1.410(7) Å and corresponds to a greater degree of the π-conjugation of these fragments, as is the case with molecule **Ia** in compound **I**. The other interatomic distances in the ligand and uncoordinated molecules coincide to within two or three standard deviations. The N(3)–H···N(2) intramolecular hydrogen bond [N(3)···N(2), 2.635(6) Å; N(3)–H, 0.86 Å; H···N(2), 2.18 Å; and the N(3)–H···N(2) angle, 112°] is retained in the ligand. It is interesting to note that the participation of the sulfur atom in the coordination of the rhodium atom does not affect the S–C bond length, which is equal to 1.682(5) Å in complex **II** and 1.686(8) [1.684(8)] Å in molecule **Ia** (**Ib**) in compound **I**.

The structure investigation revealed that the dimethyl 4-phenylthiosemicarbazidediacetate molecule exhibits sufficiently stable conformations with respect to the mutual (symmetric and asymmetric) orientation of the ester groups. Upon the complex formation, one of the conformations is retained independently of the structural (tetradentate tripodal or monodentate) function of the ligand. A similar behavior is observed for structural analogues of compound **I**.

The methylation of the carboxyl groups in compound **I** leads to a decrease in its complexation ability as compared to that of 4-phenylthiosemicarbazidediacetic acid. As was noted above, the structural data are available only for the copper(II) complex with dimethyl 4-phenylthiosemicarbazidediacetate [4]. The formation of this complex is favored by the ability of copper(II) to form the coordination environment of the 4 + 2 and 4 + 1 + 1 types. As a result, the oxygen atoms of the ester groups can act as weakly bound ligands located at apical positions [4, 7]. Moreover, the substitution of the methyl groups for the hydrogen atoms in the acetate fragments makes impossible the deprotonation of the ligand through the carboxyl groups upon coordination. In this situation, molecule **I** universally acts as a neutral ligand.

The monodentate coordination of molecule **I** and other sulfur-containing ligands with rhodium(II) acetate should be governed primarily by the stability of the $Rh_2(O_2CMe)_4$ lantern fragment; as a result, the coordination should occur only through the apical positions. In two rhodium(II) acetate complexes described earlier in [13], all the donor atoms in the sulfur-containing multifunctional ligands, except the sulfur atom of the C=S group, cannot be involved in the coordination. As a consequence, the *L* ligand can be coordinated to the central atom only through the sulfur atom. On the other hand, it uniquely follows from the structure of the $[CuCl_2Ef]$ copper complex that at least four donor centers in molecule **I** can participate in the coordination. Note that, according to the hard–soft–acid–base principle [17–19], the coordination of the sulfur-containing ligands through the sulfur atom in the rhodium com-

plexes can also be associated with the fact that rhodium acts as a weak acid with respect to the sulfur atom (a weak base).

ACKNOWLEDGMENTS

The authors from Chisinau acknowledge the support of the Russian Foundation for Basic Research (project no. 99-07-90133) in the payment of the license to use the Cambridge Structural Database in analyzing the results obtained in this work.

REFERENCES

1. I. F. Burshteĭn, G. A. Kiosse, N. V. Gérbéléu, *et al.*, Dokl. Akad. Nauk SSSR **266** (1), 109 (1982) [Sov. Phys. Dokl. **27**, 673 (1982)].
2. F. N. Allen and O. Kennard, Chem. Design Automat. News **8**, 131 (1993).
3. V. Kh. Kravtsov, J. Lipkowski, O. A. Bologa, *et al.*, Koord. Khim. **21** (4), 341 (1995).
4. V. Kh. Kravtsov, V. I. Lozan, Yu. A. Simonov, *et al.*, Kristallografiya **37** (2), 391 (1992) [Sov. Phys. Crystallogr. **37**, 199 (1992)].
5. L. G. Aksel'rud, Yu. N. Grin', P. Yu. Zavaliĭ, *et al.*, *CSD Program Package for Structure Analysis of Crystals* (Lvovskiĭ Gos. Univ., Lvov, 1990).
6. G. M. Sheldrick, *SHELX97: Program for the Solution and Refinement of Crystal Structures* (Univ. of Göttingen, Göttingen, 1997).
7. V. Kh. Kravtsov, Yu. A. Simonov, O. A. Bologa, *et al.*, Zh. Strukt. Khim. **39** (2), 310 (1998).
8. V. Kh. Kravtsov, Yu. A. Simonov, N. V. Gérbéléu, *et al.*, Zh. Strukt. Khim. **35** (3), 154 (1994).
9. V. Kh. Kravtsov, V. K. Bel'skiĭ, O. A. Bologa, *et al.*, Izv. Akad. Nauk Resp. Mold., Fiz. Tekh., No. 3, 22 (1994).
10. Yu. A. Simonov, J. Lipkowski, V. Kh. Kravtsov, *et al.*, Kristallografiya **38** (5), 105 (1993) [Crystallogr. Rep. **38**, 640 (1993)].
11. I. F. Burshteĭn, S. S. Sotman, N. V. Gérbéléu, *et al.*, Kristallografiya **35** (1), 68 (1990) [Sov. Phys. Crystallogr. **35**, 40 (1990)].
12. M. D. Revenko, V. Kh. Kravtsov, and Yu. A. Simonov, Kristallografiya **39** (1), 50 (1994) [Crystallogr. Rep. **39**, 42 (1994)].
13. G. Faraglia, R. Graziani, L. Volponi, and U. Casellato, Inorg. Chim. Acta **148** (2), 159 (1988).
14. I. F. Burshteĭn, N. V. Gérbéléu, V. I. Lozan, *et al.*, Dokl. Akad. Nauk SSSR **316** (2), 368 (1991) [Sov. Phys. Dokl. **36**, 4 (1991)].
15. N. V. Gérbéléu, I. F. Burshteĭn, O. A. Bologa, *et al.*, Zh. Neorg. Khim. **31** (6), 1432 (1986).
16. A. V. Ablov, L. I. Petukhov, G. F. Volodina, *et al.*, Dokl. Akad. Nauk SSSR **237** (1), 94 (1977).
17. R. G. Pearson, Usp. Khim. **40** (7), 1259 (1971).
18. K. B. Yatsimirskiĭ, Teor. Éksp. Khim. **6**, 462 (1970).
19. A. D. Garnovskiĭ, A. P. Sadimenko, O. A. Osipov, and G. V. Tsintsadze, *Hard–Soft Interactions in Coordination Chemistry* (Rostovskiĭ Univ., Rostov-on-Don, 1986).

Translated by O. Borovik-Romanova

Crystallography Reports, Vol. 47, No. 1, 2002, pp. 86–93. Translated from Kristallografiya, Vol. 47, No. 1, 2002, pp. 93–100.

STRUCTURE OF ORGANIC COMPOUNDS

Crystal Structures of Molecular Complexes of 18-Crown-6 with 2-Aminobenzoic and 5-Amino-1-Benzyl-1,2,3-Triazole-4-Carboxylic Acid Hydrazides

Yu. A. Simonov*, M. S. Fonar'*, V. Ch. Kravtsov*, J. Lipkowski, É. V. Ganin***, and A. A. Yavolovskiĭ*****

** Institute of Applied Physics, Academy of Sciences of Moldova, ul. Academiei 5, Chisinau, MD-2028 Moldova*

*** Institute of Physical Chemistry, Polish Academy of Sciences, Kasprzaka 44/52, Warsaw, 01-224 Poland*

**** Physicochemical Institute for Human and Environmental Protection, Education Department, National Academy of Sciences of Ukraine, Odessa State University, Odessa, Ukraine*

e-mail: simonov.xray@phys.asm.md

Received April 12, 2001

Abstract—The crystal structures of two host–guest molecular complexes of 18-crown-6 with 2-aminobenzoic acid hydrazide monohydrate (the ratio host : guest : H_2O = 1 : 2 : 2) (complex **I**) and 5-amino-1-benzyl-1,2,3-triazole-4-carboxylic acid hydrazide (the host : guest ratio = 1 : 2) (complex **II**) are determined by X-ray diffraction analysis. Crystals **I** are monoclinic, a = 8.468(2) Å, b = 17.378(3) Å, c = 10.517(2) Å, β = 96.88(3)°, space group $P2_1/n$, and R = 0.0393 for 6692 reflections. Crystals **II** are orthorhombic, a = 18.489(1) Å, b = 10.192(3) Å, c = 20.412(2) Å, space group *Pbca*, and R = 0.0540 for 3513 reflections. In both complexes, the centrosymmetric 18-crown-6 and guest molecules are joined together through the NH··O(crown) hydrogen bonds, which involve all the hydrogen atoms of the hydrazine group. The NH··O=C intramolecular hydrogen bond is observed in the guest molecule. In structure **I**, the water molecule serves as a bridge between the guest molecules related by the glide-reflection plane and combines the guest–host–guest complexes into layers. In structure **II**, the guest molecules are linked into chains through hydrogen bonds of the NH··O=C type; in turn, the chains composed of guest molecules and the crown ether molecules bonded to these chains form a layered structure. © *2002 MAIK "Nauka/Interperiodica".*

INTRODUCTION

A considerable amount of structural information on the host–guest complexes of 18-crown-6 with neutral proton-donating molecules has been accumulated to date. This makes it possible to draw certain inferences concerning the guest coordination and the structure (monomeric, dimeric, or chain) of these complexes [1]. Both hydrogen atoms of a particular amino group in the guest, as a rule, are coordinated to the first and third oxygen atoms of the macrocycle, and the guest–host–guest centrosymmetric complex is stabilized through four NH··O hydrogen bonds [2]. One hydrogen atom each of two amino groups in an urea molecule in the complex with a ratio of 1 : 5 [3] (or in a thiourea molecule in the complex with a ratio of 1 : 4 [4]) is involved in the interaction with the neighboring oxygen atoms in the crown ether ring. In the 1 : 2 complex of 18-crown-6 with thiourea, three hydrogen atoms of two amino groups form the NH··O hydrogen bonds with three crystallographically independent oxygen atoms of the crown ether [5]. Therefore, the cooperative system of interactions involves all oxygen atoms of the crown ether. In the 1 : 1 complex of 18-crown-6 with hypothiazide, two NH groups separated by the methylene group in the guest form short contacts with the oxygen atoms also separated by the hydroxyethylene fragment, and the crown ether molecule adopts an unusual conformation [6]. The hydrogen atoms of the adjacent chemically equivalent amino groups in the diaminooxadiazole molecule are asymmetrically distributed among the two nearest-neighbor crown ether molecules in the guest molecule; as a result, the coordination numbers of oxygen in the 15-crown-5 and 18-crown-6 molecules are equal to three and four, respectively [7, 8]. All three hydrogen atoms of the $–NH–NH_2$ hydrazine group in molecules of 2,4-dinitrophenylhydrazine [9] and 4-(2-chloroethylamino)-1,2,5-oxadiazole-3-carboxylic acid hydrazide [10] participate in the interaction with 18-crown-6, and all six oxygen atoms of the centrosymmetric host molecule are involved in the coordination.

It is of interest to elucidate how the proton-donating group adjacent to the hydrazine group in the ring of the guest molecule affects the ability of the hydrazine group to participate in coordination with the crown

Table 1. Crystal data, data collection, and refinement parameters for the crystal structure of complexes **I** and **II**

Complex	**I**	**II**
Empirical formula	$C_{13}H_{23}N_3O_5$	$C_{32}H_{48}N_{12}O_8$
Molecular weight	301.34	728.82
Crystal system	Monoclinic	Orthorhombic
Space group	$P2_1/n$	*Pbca*
Unit cell parameters:		
a, Å	8.468(2)	18.489(1)
b, Å	17.378(3)	10.192(3)
c, Å	10.517(2)	20.412(2)
β, deg	96.88(3)	
V, Å^3	1536.5(5)	3846.4(1)
Z	4	4
d_{calcd}, g/cm^3	1.303	1.259
μ, mm^{-1}	0.100	0.093
F(000)	648	1552
Crystal size, mm	0.2 × 0.20 × 0.30	0.10 × 0.30 × 0.30
θ range, deg	2.69–34.95	2.00–25.69
Index ranges	$0 < h < 13$, $-27 < k < 27$, $-16 < l < 16$	$0 < h < 22$, $0 < k < 12$, $-24 < l < 0$
Scan mode	ω	ω/2θ
Number of reflections measured	12981	3513
Number of unique reflections [*R*(int)]	6692 [0.017]	3513 [0.000]
Refinement technique	Full-matrix, based on F^2	
Goodness-of-fit *S* on F^2	1.024	0.967
Final *R* factors for reflections with $I > 2\sigma(I)$	$R_1 = 0.0393$, $wR_2 = 0.1067$	$R_1 = 0.0540$, $wR_2 = 0.1457$
Final *R* factors for all reflections	$R_1 = 0.0502$, $wR_2 = 0.1128$	$R_1 = 0.1139$, $wR_2 = 0.1722$
	$w = 1/[\sigma^2(F_o)^2 + (ap)^2 + bp]$, $p = (F_o^2 + 2F_c^2)/3$	
	$a = 0.0592$	$a = 0.1050$
	$b = 0.24$	$b = 0.0$
Residual (maximum and minimum) electron densities $\Delta\rho_{max}$, $\Delta\rho_{min}$, e Å^{-3}	0.397 and –0.216	0.220 and –0.220

ether and to analyze the molecular architecture in the complexes with bulk guest molecules.

In the present work, we investigated the crystal structures of two novel complexes of 18-crown-6 with 2-aminobenzoic acid hydrazide (complex **I**) and 5-amino-1-benzyl-1,2,3-triazole-4-carboxylic acid hydrazide (complex **II**).

EXPERIMENTAL

Synthesis of complex I. 2-Aminobenzoic acid hydrazide (15 mg, 0.1 mmol) and 18-crown-6 (26 mg, 0.1 mmol) were dissolved in methanol (1 ml) at a temperature of 64°C. Then, benzene (2.5 ml) was added to the solution, and the resultant solution was allowed to stand for some time for spontaneous evaporation of the solvents. Colorless prismatic crystals precipitated. The melting temperature was 57–58°C.

The results of elemental analysis are as follows.

For $C_{26}H_{46}N_6O_{10}$ (complex **I**), anal. calcd. (%): C, 51.82; H, 7.69; N, 13.94.

Found (%): C, 51.90; H, 7.65; N, 14.00.

Synthesis of complex II. 5-Amino-1-benzyl-1,2,3-triazole-4-carboxylic acid hydrazide was synthesized according to the procedure described in [11]. The product obtained was the colorless compound with a melting temperature of ~212–214°C. 5-Amino-1-benzyl-1,2,3-triazole-4-carboxylic acid hydrazide (23 mg, 0.1 mmol) and 18-crown-6 (26 mg, 0.1 mmol) were dissolved in methanol (1 ml) at a temperature of 64°C. Then, benzene (2.5 ml) was added to the solution, and the resultant solution was allowed to stand for some

Table 2. Coordinates of non-hydrogen atoms ($\times 10^4$) and equivalent isotropic thermal parameters U_{eq} ($Å^2 \times 10^3$) for complex **I**

Atom	*x*	*y*	*z*	U_{eq}
C(1*g*)	6154(1)	1088(1)	4971(1)	17(1)
C(2*g*)	5183(1)	1244(1)	3715(1)	16(1)
C(3*g*)	4692(1)	2003(1)	3382(1)	17(1)
C(4*g*)	3807(1)	2129(1)	2180(1)	21(1)
C(5*g*)	3402(1)	1525(1)	1350(1)	24(1)
C(6*g*)	3852(1)	773(1)	1687(1)	24(1)
C(7*g*)	4735(1)	642(1)	2866(1)	20(1)
O(1*g*)	5949(1)	1447(1)	5959(1)	25(1)
N(1*g*)	7254(1)	533(1)	4930(1)	19(1)
N(2*g*)	8293(1)	340(1)	6041(1)	20(1)
N(3*g*)	5106(1)	2624(1)	4181(1)	24(1)
O(1*w*)	7679(1)	1067(1)	8442(1)	32(1)
O(1)	11183(1)	1347(1)	6298(1)	25(1)
C(2)	12405(1)	1212(1)	7325(1)	28(1)
C(3)	11857(1)	610(1)	8193(1)	29(1)
O(4)	11574(1)	−92(1)	7510(1)	23(1)
C(5)	10917(1)	−663(1)	8267(1)	29(1)
C(6)	10804(1)	−1410(1)	7542(1)	28(1)
O(7)	9721(1)	−1325(1)	6411(1)	25(1)
C(8)	9645(1)	−2005(1)	5659(1)	29(1)
C(9)	8372(1)	−1923(1)	4547(1)	29(1)

Table 3. Coordinates of non-hydrogen atoms ($\times 10^4$) and equivalent isotropic thermal parameters U_{eq} ($Å^2 \times 10^3$) for complex **II**

Atom	*x*	*y*	*z*	U_{eq}
O(1*g*)	181(1)	3310(2)	2080(1)	60(1)
N(1*g*)	−155(1)	3519(2)	1019(1)	63(1)
N(2*g*)	331(2)	4574(2)	899(1)	67(1)
N(3*g*)	−537(2)	1253(3)	2839(1)	69(1)
N(4*g*)	−1372(1)	350(2)	2070(1)	59(1)
N(5*g*)	−1595(1)	575(2)	1442(1)	73(1)
N(6*g*)	−1203(1)	1538(2)	1213(1)	68(1)
C(1*g*)	−199(1)	2987(2)	1611(1)	51(1)
C(2*g*)	−731(1)	1933(2)	1682(1)	52(1)
C(3*g*)	−836(1)	1182(2)	2241(1)	52(1)
C(4*g*)	−1743(2)	−639(3)	2467(1)	69(1)
C(5*g*)	−2440(1)	−129(2)	2752(1)	58(1)
C(6*g*)	−2447(2)	939(3)	3156(2)	82(1)
C(7*g*)	−3081(2)	1393(2)	3428(2)	95(1)
C(8*g*)	−3717(2)	773(4)	3294(2)	95(1)
C(9*g*)	−3720(2)	−965(4)	2880(2)	106(1)
C(10*g*)	−3090(2)	−703(3)	2612(2)	88(1)
O(1)	1432(1)	4235(3)	−313(1)	114(1)
C(2)	1876(2)	5351(6)	−444(3)	135(2)
C(3)	1792(2)	6288(5)	90(2)	130(2)
O(4)	1088(1)	6763(2)	113(1)	89(1)
C(5)	1000(3)	7838(4)	551(2)	125(2)
C(6)	253(3)	8344(4)	481(2)	124(2)
O(7)	−239(2)	7377(2)	667(1)	107(1)
C(8)	−977(3)	7779(5)	626(3)	153(2)
C(9)	1457(3)	3319(7)	−818(3)	153(2)

time for spontaneous evaporation of the solvents. Colorless needle-shaped crystals precipitated. The melting temperature was 138–140°C.

The results of elemental analysis are as follows.

For $C_{32}H_{48}N_{12}O_8$ (complex **II**), anal. calcd. (%): C, 52.74; H, 6.64; N, 23.06.

Found (%): C, 52.67; H, 6.70; N, 23.14.

X-ray diffraction analysis. The main crystal data, data collection, and refinement parameters for the studied compounds are presented in Table 1. X-ray diffraction analysis of compound **I** was performed on a Nonius CCD diffractometer (MoK_α radiation, graphite monochromator). The experimental data were processed using the DENZO program [12]. The experimental data for compound **II** were collected on a KUMA KM-4 diffractometer (CuK_α radiation). The unit cell parameters were refined by the least-squares method for 35 reflections in the θ range 13.7° < θ < 19.8°. Both structures were solved by the direct methods and refined according to the SHELX97 software package [13]. The hydrogen atoms of the CH_2 and CH groups were placed at calculated ideal positions and refined as if they were rigidly bound to the corresponding carbon atoms. The isotropic thermal parameters for the hydrogen atoms were taken equal to $1.2U_{eq}$, where U_{eq} is the equivalent isotropic thermal parameter for the corresponding carbon atom. The hydrogen atoms of the hydrazine groups and water molecule were located from the electron-density difference synthesis and refined in the isotropic approximation. The refinement was carried out by the full-matrix least-squares procedure on F^2 with the use of the weighting scheme given in Table 1. The final coordinates of the non-hydrogen atoms are listed in Tables 2 and 3. The geometric parameters of the hydrogen bonds are presented in Table 4. The crystal data (*cif* files) for structures **I** and

Table 4. Geometric parameters for hydrogen bonds in complexes **I** and **II**

D–H···*A*, Å	*d*(*D*–H), Å	*d*(H···*A*), Å	*d*(*D*···*A*), Å	∠(*DHA*)°
Complex **I**				
N(1*g*)–H(1N1)···O(4)^{i}	0.88(1)	2.08(1)	2.961(1)	174(1)
N(2*g*)–H(1N2)···O(1)	0.89(1)	2.16(1)	2.995(1)	158(1)
N(2*g*)–H(2N2)···O(7)	0.90(1)	2.29(1)	3.141(1)	157(1)
N(3*g*)–H(1N3)···O(1*g*)	0.89(1)	2.11(1)	2.806(9)	134(1)
N(3*g*)–H(2N3)···O(1*w*)^{ii}	0.88(1)	2.24(1)	3.102(1)	169(1)
O(1*w*)–H(1*w*1)···N(2*g*)	0.86(1)	2.07(2)	2.925(1)	174(2)
O(1*w*)–H(2*w*1)···O(1*g*)	0.87(2)	2.30(2)	2.913(1)	128(2)
Complex **II**				
N(1*g*)–H(1N1)···O(4)^{iii}	0.90(3)	2.01(3)	2.897(3)	170(3)
N(2*g*)–H(1N2)···O(1)	0.88(4)	2.39(4)	3.223(4)	159(3)
N(2*g*)–H(2N2)···O(7)	1.08(4)	2.09(4)	3.082(4)	151(3)
N(3*g*)–H(1N3)···O(1*g*)	0.88(3)	2.35(3)	2.925(3)	123(2)
N(3*g*)–H(2N3)···N(1*g*)^{iv}	0.78(3)	2.37(3)	3.116(4)	160(3)
N(3*g*)–H(2N3)···O(1*g*)^{iv}	0.78(3)	2.55(3)	3.075(3)	126(2)

Note: Symmetry codes: (*i*) $-x+2, -y, -z+1$; (*ii*) $x-1/2, -y+1/2, z-1/2$; (*iii*) $-x, -y+1, -z$; (*iv*) $-x, y-1/2, -z+1/2$.

II have been deposited with the Cambridge Structural Database (CCDC, nos. 160249 and 160250).

RESULTS AND DISCUSSION

Complex I. The guest–host–guest centrosymmetric complex (Fig. 1) is stabilized by six NH··O hydrogen bonds. These bonds involve three hydrogen atoms of the hydrazine fragment in the guest molecule and all oxygen atoms of the macrocycle. The N··O distances fall in the range 2.961(1)–3.141(1) Å (Table 4). The hydrazide group of the guest is arranged with respect to the 18-crown-6 molecule in such a manner that the deviations of the N(1*g*) and N(2*g*) nitrogen atoms from the plane passing through the oxygen atoms of the macrocycle are equal to 2.352(1) and 1.920(1) Å, respectively. The hydrogen atoms of the hydrazine group are located at the *cis* positions with respect to the N–N bond due to their participation in the coordination with the crown ether molecule. In phenylhydrazide monohydrate [14], unlike complex **I**, the hydrogen atoms at the neighboring nitrogen atoms exhibit a *trans* orientation relative to the N–N bond, because they are involved in the hydrogen bonds with different molecules. The dihedral angle between the aromatic ring of the guest molecule and the plane passing through the oxygen atoms of the crown ether molecule is equal to 23.5(4)°.

The hydrogen atoms of the water molecule form the hydrogen bonds with a lone electron pair of the nitrogen atom of the NH_2 group and the carbonyl oxygen atom of the 2-aminobenzoic acid hydrazide molecule [O(1*w*)··N(2*g*), 2.925(1) Å and O(1*w*)··O(1*g*), 2.913(1) Å], thus closing the seven-membered heterocycle H(1*w*1)O(1*w*)H(2*w*1)O(1*g*)C(2*g*)N(1*g*)N(2*g*). This cycle is virtually planar: the out-of-plane deviations of atoms do not exceed 0.043 Å. In complex **I**, the electron pair (as a proton acceptor) of the water molecule is involved in the formation of a weak hydrogen bond with the amino group of the guest molecule related by the basal glide-reflection plane [N(3*g*)··O(1*w*)($x-1/2, -y+1/2, z-1/2$) 3.102(1) Å]. The guest–host–guest complexes and water molecules are linked by the hydrogen bonds into layers bound to one another through only the van der Waals contacts (Fig. 2). Each layer is composed of the centrosymmetric associates, which, in turn, consist of four crown ether molecules, six guest molecules, and four water molecules. Each associate is stabilized by 32 NNH··O hydrogen bonds, which can be identified as the NH··O(crown) and NH··O(water) contacts.

In complex **I**, the bond lengths and angles in the 2-aminobenzoic acid hydrazide molecule have standard values [15]. The amino group in the *ortho* position with respect to the hydrazide fragment participates in the formation of the intramolecular hydrogen bond with the O(1*g*) carbonyl oxygen atom [N(3*g*)··O(1*g*), 2.806(9) Å] (Fig. 1). This leads to the formation of the six-membered ring H(1N3)N(3*g*)C(3*g*)C(2*g*)C(1*g*)O(1*g*), which is fused with the aromatic ring through the C(2*g*)–C(3*g*) bond. The aromatic and hydrogen-containing rings (with mean atomic deviations of 0.072 and 0.054 Å, respectively) form a nearly planar bicyclic system in which the dihedral angle between the rings is 1.50(3)°. Similar hydrogen-containing rings with *ortho* hydroxyl oxygen atoms were also observed in other derivatives of aromatic acids, for example, in the structures of *o*-hydroxybenzoic acid [16] and 2,5-diacetyl-

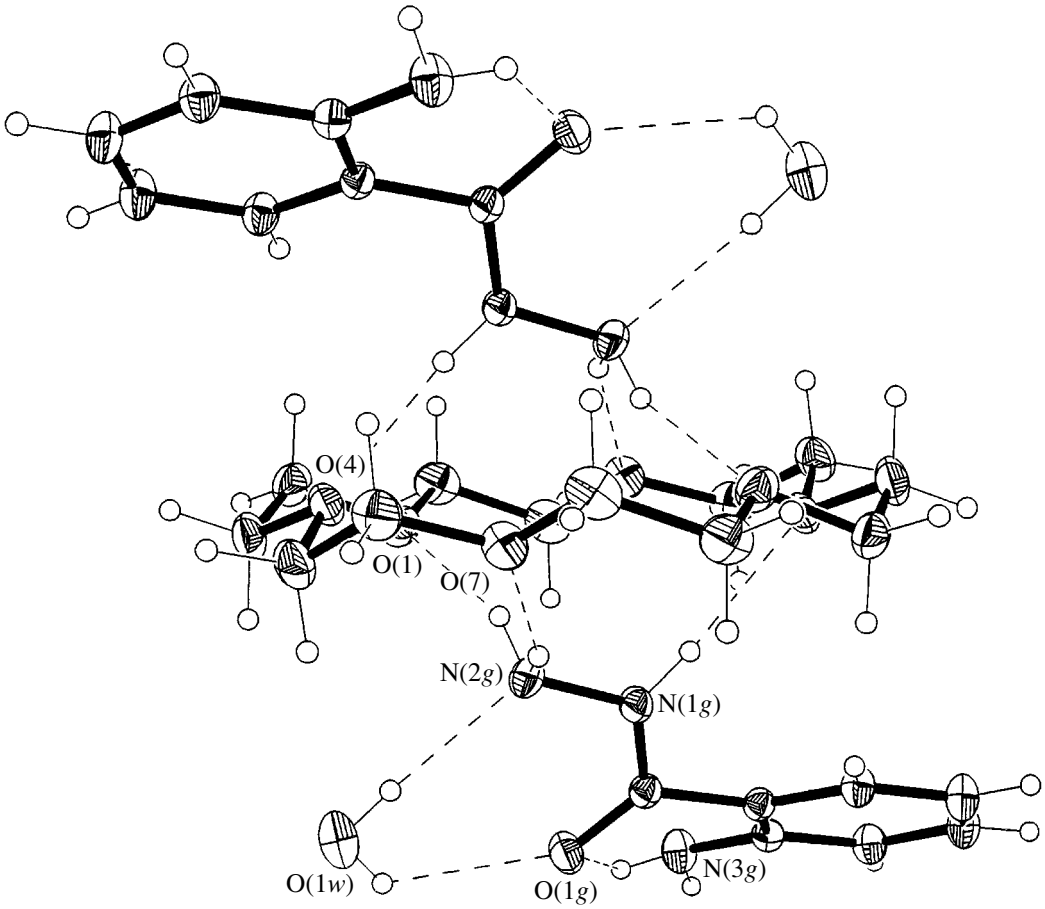

Fig. 1. Profile projection of the structure of complex **I**.

hydroquinone [17] with close parameters of the hydrogen bonds (O··O, 2.533 and 2.58 Å).

The crown ether molecule in complex **I** is centrosymmetric and can be described in terms of a conventional geometry [15] with the following mean interatomic distances and the mean bond angles: C–O, 1.421(1) Å; C–C, 1.500(1) Å; C–C–0, 109.4(5)°; and C–O–C, 111.5(6)°. The molecular conformation exhibits a symmetry similar to D_{3d}. The *gauche* torsion angles about the C–C bonds fall in the range 62.8(1)°–71.5(2)°, and the maximum difference between the *trans* torsion angles about the C–O bonds and the straight angle is equal to 11°. The O···O transannular distances lie in the range from 5.536(5) to 5.716(5) Å. The oxygen atoms deviate from their mean plane in opposite directions by 0.22 Å.

Complex II. In centrosymmetric complex **II**, as in complex **I**, two guest molecules identically interact with the crown ether molecule (Fig. 3). These contacts involve all hydrogen atoms of the hydrazine group. The primary amino group forms two NH··O hydrogen bonds with the O(1) and O(7) oxygen atoms separated by one hydroxyethylene fragment in the crown ether [N(2*g*)··O(1), 3.223(4) Å and N(2*g*)··O(7), 3.082(4) Å]. The secondary amino group forms the NH··O hydrogen bond with the O(4) oxygen atom [N(1*g*)··O(4)(–*x*, –*y* + 1, –*z*), 2.897(3) Å]. The N(1*g*) and N(2*g*) nitrogen atoms deviate from the plane passing through all the oxygen atoms of the macrocycle by 2.433(2) and 1.929 Å, respectively.

The 18-crown-6 molecules are oriented with respect to the guest molecules in such a manner that the dihedral angle between the plane passing through six oxygen atoms of the macrocycle and the triazole ring of the guest is equal to 76.8(1)°. This arrangement is typical of the host–guest complexes of eighteen-membered crown ethers (for example, 18-crown-6 and the *A* and *B* isomers of dicyclohexyl-18-crown-6) with amino derivatives of benzene and five-membered heterocycles. In the majority of these complexes, the dihedral angle between the cyclic fragment of the guest and the mean plane of crown ether heteroatoms is close to 90° [2, 15].

Figure 4 shows a fragment of the packing of complex **II**. The guest molecules related by a twofold screw axis form chains through the NH··O and NH··N hydrogen bonds [N(3*g*)··O(1*g*)(–*x*, *y* – 1/2, –*z* + 1.2) 3.075(3) Å and N(3*g*)··N(2*g*)(–*x*, *y* – 1/2, –*z* + 1/2)

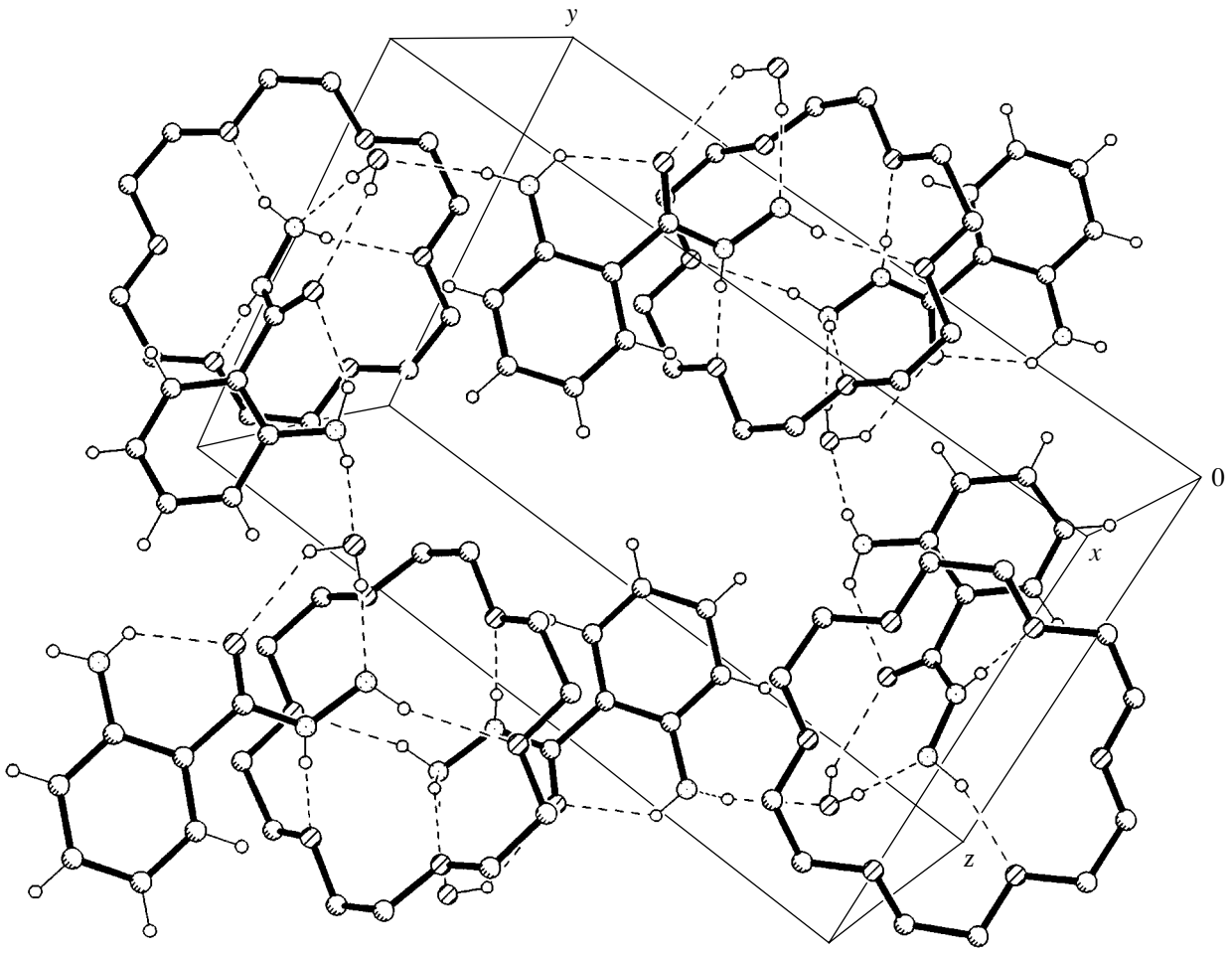

Fig. 2. A fragment of the packing of complex **I** (the hydrogen atoms of the crown ether molecule are omitted for the benefit of clarity).

3.075(3) Å]. Six guest and two 18-crown-6 ether molecules are joined into the centrosymmetric associate (–guest–guest–guest–host–)$_2$, which is stabilized by 16 intermolecular hydrogen bonds of the NH··O(crown) and NH··O=C types. These associates are combined into a layer.

In the guest molecule of complex **II**, both (triazole and aromatic) rings are almost planar: the non-hydrogen atoms in these rings are coplanar to within 0.009 and 0.003 Å, respectively. The geometry of the triazole ring is similar to that described for related compounds containing the benzotriazole fragment [18, 19]. The C(4*g*) methylene bridging atom deviates from the triazole ring plane by 0.026(3) Å. The N(4*g*) atom involved in a slightly pyramidal conformation deviates from the N(5*g*)C(3*g*)C(4*g*) plane by 0.065 Å. The C(4*g*)–C(5*g*) and C(4*g*)–N(4*g*) bonds are almost mutually perpendicular as judged from the corresponding torsion angles: N(5*g*)–N(4*g*)–C(4*g*)–C(5*g*), –80.09°; C(3*g*)–N(4*g*)–C(4*g*)–C(5*g*), 95.90°; N(4*g*)–C(4*g*)–C(5*g*)–C(6*g*), –59.29°; and N(4*g*)–C(4*g*)–C(5*g*)–C(10*g*), 119.92°. The dihedral angle between the aromatic and triazole rings is 76.76°, which is characteristic of compounds of this class [18–20]. The NH··O=C intramolecular hydrogen bond [N(3*g*)···O(1*g*), 2.925 Å] is observed in the molecule (Fig. 3). The geometric parameters of this bond are close to those of the hydrogen bonds found in 2-aminobenzoic acid hydrazide (complex **I**), 4-(2-chloroethylamino)-1,2,5-oxadiazole-3-carboxylic acid hydrazide, and 4-amino-1,2,5-oxadiazole-3-carboxylic acid amide [10]. In the six-membered virtually planar hydrogen-containing ring, the H(2N3), N(3*g*), C(3*g*), C(2*g*), C(1*g*), and O(1*g*) atoms are coplanar to within 0.054 Å. The triazole heterocycle and six-membered hydrogen-containing ring form a planar system in which the dihedral angle between these rings is equal to 1.06°.

The molecular conformation of 18-crown-6 has a symmetry similar to D_{3d}. The *gauche* torsion angles about the C–C bonds fall in the range 63.1(1)–71.8(2)°, and the maximum difference between the *trans* torsion angles about the C–O bonds and the straight angle is 10°. The O···O transannular distances lie in the range from 5.413(5) to 5.666(5) Å. The oxygen atoms

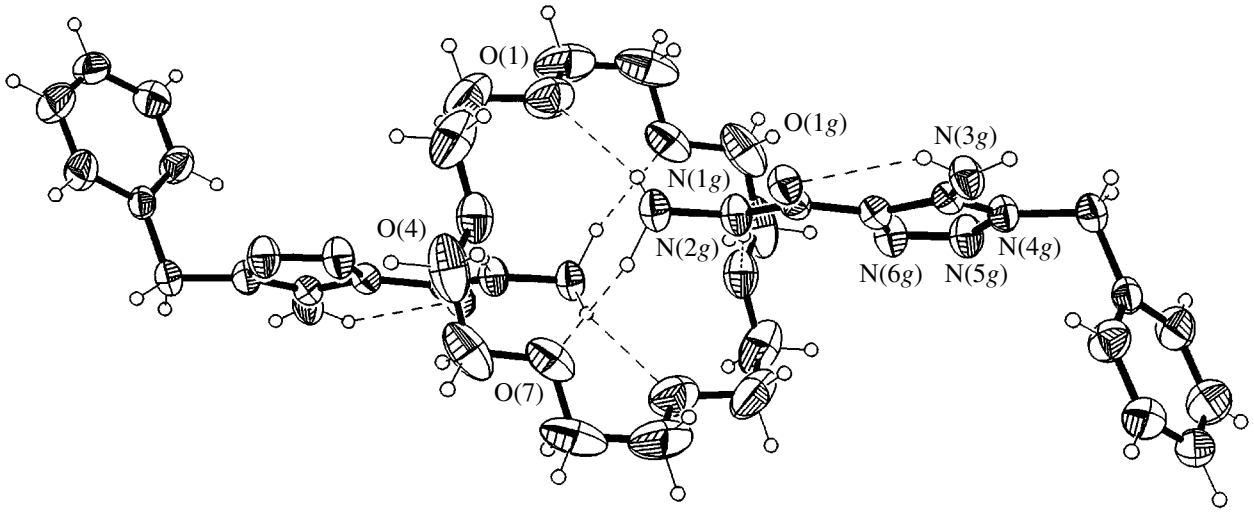

Fig. 3. Projection of the structure of molecular complex **II** onto the plane passing through the oxygen atoms of the macrocycle.

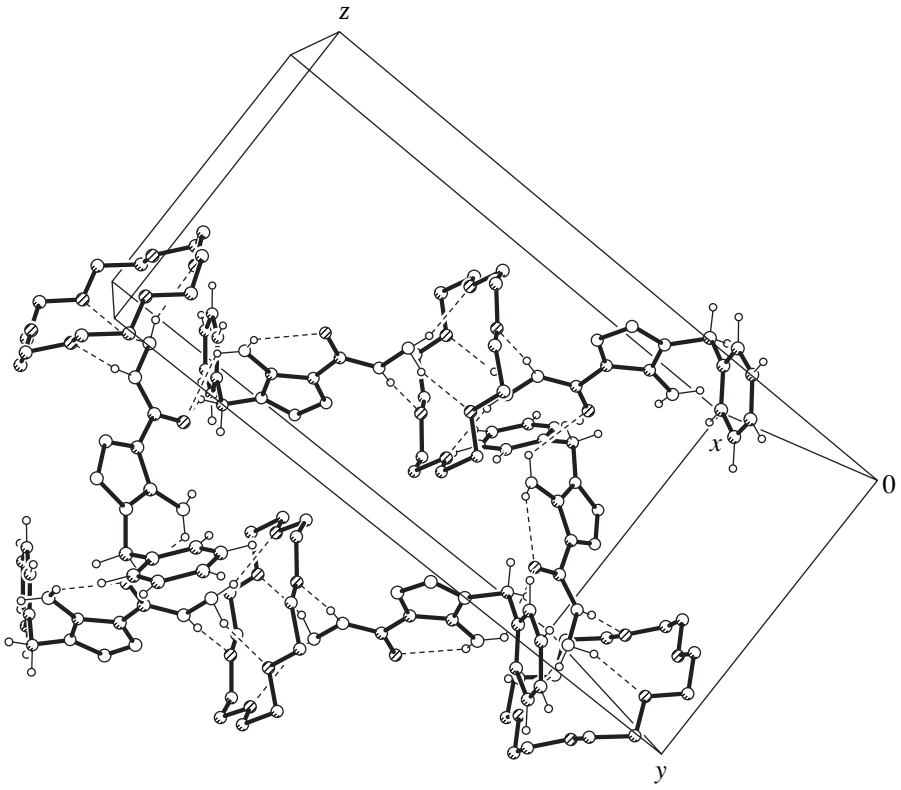

Fig. 4. A fragment of the packing of complex **II** (the hydrogen atoms of the crown ether molecule are omitted for the benefit of clarity).

involved in a crownlike conformation deviate from their mean plane by ±0.179 Å.

Complexes **I** and **II** can be considered prototypes of organic sieves, which can be used, for example, for fixation of small-sized organic molecules (methanol, chloroform, etc.). In these compounds, the size of meshes in the organic layer can be increased by modifying the skeleton of the guest molecule, for example, by increasing the length of the substituent chain.

REFERENCES

1. R. D. Rogers and C. B. Bauer, in *Comprehensive Supramolecular Chemistry,* Ed. by J. L. Atwood, J. E. D. Da-

vies, and F. Vögtle (Pergamon, New York, 1996), Vol. 1, p. 315.

2. Yu. A. Simonov, M. S. Fonar', A. A. Dvorkin, and T. I. Malinovskiĭ, in *Modern Problems of Crystallography* (Nauka, Moscow, 1992), p. 221.
3. S. Harkema, G. J. van Hummel, K. Daasvatn, and D. N. Reinhoudt, J. Chem. Soc., Chem. Commun., No. 8, 368 (1981).
4. G. Weber, J. Inclusion Phenom. **1**, 339 (1984).
5. M. G. B. Drew and D. G. Nicholson, Acta Crystallogr., Sect. C: Cryst. Struct. Commun. **41**, 1358 (1985).
6. A. A. Dvorkin, Yu. A. Simonov, J. Lipkowski, *et al.*, Kristallografiya **35**, 682 (1990) [Sov. Phys. Crystallogr. **35**, 396 (1990)].
7. R. Luboradzki, J. Lipkowski, Yu. Simonov, *et al.*, J. Inclusion Phenom. **23**, 181 (1995).
8. R. Luboradzki, J. Lipkowski, Yu. Simonov, *et al.*, J. Inclusion Phenom. (in press).
9. R. Hilgenfeld and W. Saenger, Z. Naturforsch. B **36**, 242 (1981).
10. M. S. Fonar', Yu. A. Simonov, V. Kh. Kravtsov, *et al.*, Zh. Strukt. Khim. (in press).
11. É. I. Ivanov, G. D. Kaloyanov, and I. M. Yaroshchenko, Zh. Org. Khim. **25** (9), 1975 (1989).
12. Z. Otwinowski and W. Minor, Methods Enzymol. **276**, 307 (1997).
13. G. M. Sheldrick, *SHELX97: Program for the Solution and Refinement of Crystal Structures* (Univ. of Göttingen, Göttingen, 1997).
14. I. A. Krol', V. M. Agre, and V. S. Pangani, Zh. Strukt. Khim. **29**, 194 (1988).
15. E. Wajsman, M. G. Grabowski, A. Stepein, and M. Cugler, Cryst. Struct. Commun. **7**, 232 (1978).
16. A. Sundheim and R. Mattes, Z. Naturforsch. B **48**, 125 (1993).
17. F. N. Allen and O. Kennard, Chem. Design Automat. News **8**, 31 (1993).
18. A. Dunand, Acta Crystallogr., Sect. B: Struct. Crystallogr. Cryst. Chem. **38**, 2299 (1982).
19. A. Albert and A. Dunand, Angew. Chem., Int. Ed. Engl. **19**, 310 (1980).
20. P. R. Ashton, P. T. Glink, J. F. Stoddart, *et al.*, Tetrahedron Lett. **37**, 6217 (1996).

Translated by O. Borovik-Romanova

Crystallography Reports, Vol. 47, No. 1, 2002, pp. 94–100. Translated from Kristallografiya, Vol. 47, No. 1, 2002, pp. 101–107.

PHASE TRANSITIONS

System of Hydrogen Bonds in High-Pressure Phases of $CsHSO_4$ Crystals

A. I. Beskrovnĭ and V. S. Shakhmatov

Joint Institute for Nuclear Research, p/ya 79, Dubna, Moscow oblast, 141980 Russia

e-mail: beskr@nf.jinr.ru

Received April 11, 2001

Abstract—The system of hydrogen bonds in the high-pressure phases of $CsHSO_4$ crystals has been constructed on the basis of the group-theoretical analysis of the systems of hydrogen bonds in the $CsHSO_4$ phases with the known symmetry. *© 2002 MAIK "Nauka/Interperiodica".*

INTRODUCTION

The compounds described by the general formula $MXAO_4$ with M = Cs and Rb, X = H and D, and A = S and Se are characterized by the phase transition into the superionic phase accompanied by an increase in the ionic-conductivity value by several orders of magnitude [1].

In addition to high conductivity with respect to hydrogen (deuterium) ions, the superionic phases also possess superplasticity. The mechanical and polarization–optical studies showed that, similar to clay and modeling clay, a $CsHSO_4$ crystal can readily change its shape [2].

The transition into the superionic phase is still actively studied [3] but the microscopic nature of this transition is still not clear. The reorientation of SO_4-tetrahedra in the superionic phase results in the dynamic disordering of the network of hydrogen bonds, which, in turn, leads to high plasticity [2] and ionic conductivity in $CsHSO_4$ crystals.

Thus, it is assumed that the microscopic mechanism of the transition into the phase with high conductivity is associated either with the disordering of hydrogen ions or with the orientational disordering of SO_4-tetrahedra, with both phenomena being closely related.

The variation of temperature and pressure can give rise to some other phase transitions in a $CsHSO_4$ crystal including the transitions into the phases with high protonic conductivity (phases I, VI, and VII [4, 5], Fig. 1). To understand the microscopic nature of these phase transitions, one has to know the crystal structure and, most importantly, the structure of the system of hydrogen bonds in various phases. The crystal structure of the phases under the atmospheric pressure (phases I, II, and III) was determined by the neutron [7–9] and X-ray [10, 11] diffraction methods. Despite experimental difficulties, the first neutron diffraction studies of high-pressure $CsHSO_4$ phases [12, 13] provided the determination of the symmetry groups of phases IV and V, but, the crystal structures of the high-pressure phases have not been determined. The preliminary theoretical analysis of a possible symmetry of high-pressure phases [14] and the experimental data obtained in [12, 13] provided the determination of the symmetry of all the high-pressure phases [6] and the development of the phenomenological theory of possible phase transitions between these phases [15]. Moreover, the systems of hydrogen bonds in phases II and III under atmospheric pressure suggested in [15] were confirmed by the experimental observations [8, 10].

Below, we constructed the systems of hydrogen bonds in high-pressure phases of $CsHSO_4$ crystals by the approach suggested in [15].

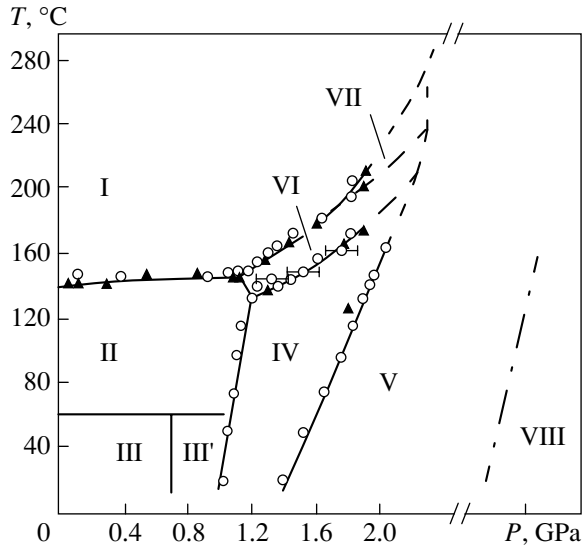

Fig. 1. Phase diagram of a $CsHSO_4$ crystal in the pressure–temperature coordinates. The phases are denoted by Roman numerals from I to VIII. The continuous lines show the experimentally determined phase boundaries [4, 5]. The dashed lines indicate possible extrapolation of the phase boundaries. The dash-dotted line shows schematically the boundary of possible new phase VIII [6].

1063-7745/02/4701-0094$22.00 © 2002 MAIK "Nauka/Interperiodica"

SYMMETRY OF HIGH-PRESSURE PHASES

The crystal structure of the superionic $CsHSO_4$ phase (I) having the symmetry D_{4h}^{19} (Fig. 2) was determined by the diffraction methods [9, 11]. The primitive unit cell of the lattice with the translation vectors $\mathbf{a}_1 = (-\tau, \tau, \tau_z)$, $\mathbf{a}_2 = (\tau, -\tau, \tau_z)$, and $\mathbf{a}_3 = (\tau, \tau, -\tau_z)$ (the zeroth primitive unit cell) contains two $CsHSO_4$ formula units, where $\tau = a/2$, $\tau_z = c/2$, and $a = 0.5729(9)$, $c = 1.421(1)$ nm [11].

The transition of phase I into phase II results in the doubling of the unit-cell volume and the lowering of the symmetry from $D_{4h}^{19} \longrightarrow C_{2h}^{5}$. The twofold axis of the monoclinic phase (C_{2h}^{5}) is directed along the [110] or the $[1\bar{1}0]$ crystallographic direction of the tetragonal phase (D_{4h}^{19}). Being compared to phase I, phase III has the same monoclinic symmetry C_{2h}^{5} and a double unit-cell volume; however, the twofold axis in phase III is directed either along the [100] or the [010] direction of tetragonal phase I [10].

To explain a double increase of the unit-cell volume upon the phase transition $D_{4h}^{19} \longrightarrow C_{2h}^{5}$, one has to consider the wave vectors $\mathbf{k}_1 = \pi(1/2, 1/2, 0)$, $\mathbf{k}_2 = \pi(1/2, -1/2, 0)$, and $\mathbf{k}_3 = \pi(0, 0, 1)$ at the boundary of the Brillouin zone. The phase transition with the wave vector $\mathbf{k}_1$ (or $\mathbf{k}_2$) leads to the monoclinic symmetry C_{2h}^{5} with the twofold axis coinciding with the [110] direction (phase II). The phenomenological theory of this phase transition was developed in [16]. The monoclinic phase with the symmetry C_{2h}^{5} and the twofold axis coinciding with the [100] direction (phase III) arises as a result of the phase transition with the wave vector $\mathbf{k}_3$ [14].

The table indicates all possible phase transitions undergone by phase I associated with the wave vector $\mathbf{k}_3$. It is seen that the phase transition according to the irreducible representation τ_2 results in the sp. gr. D_{2h}^{16} with the monoclinic subgroup $C_{2h}^{5}(x)$ and the twofold symmetry axis directed along the crystallographic *x*-axis. The analogous monoclinic subgroup $C_{2h}^{5}(y)$ with the twofold symmetry axis directed along the crystallographic *y*-axis is possessed by the group D_{2h}^{6} (irreducible representation τ_4). Thus, phase III with the monoclinic symmetry C_{2h}^{5} and the twofold axis along the crystallographic [100] or [010] direction can arise as a result of the following chain of phase transformations: $D_{4h}^{19} \longrightarrow D_{2h}^{16} \longrightarrow C_{2h}^{5}(x)$ or $D_{4h}^{19} \longrightarrow D_{2h}^{6} \longrightarrow C_{2h}^{5}(y)$.

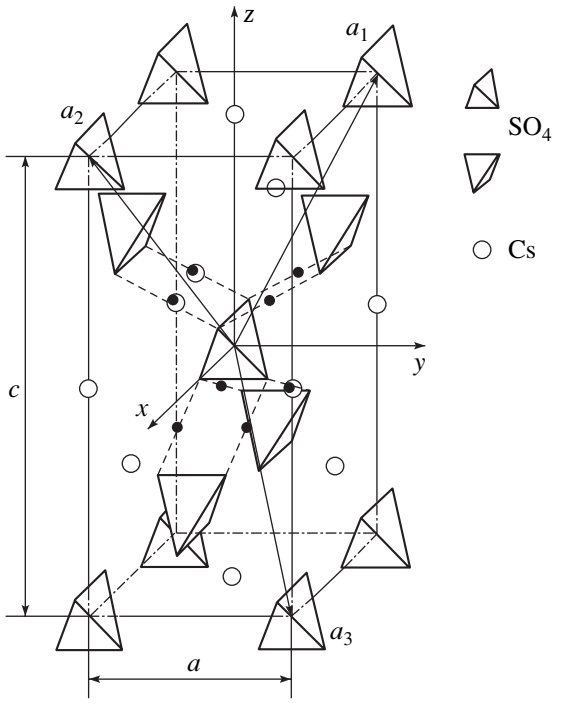

Fig. 2. The unit cell of superionic phase I of a $CsHSO_4$ crystal. The dashed lines show possible hydrogen bonds only for one central SO_4-tetrahedron. Filled circles indicate eight possible positions of two hydrogen ions in the primitive unit cell of the crystal.

In fact, two order parameters describing the phase transformation of the orthorhombic phase D_{2h}^{16} to the monoclinic phases $C_{2h}^{5}(x)$ and $C_{2h}^{2}(y)$ (table, irreducible representation τ_2) form a two-component order parameter of the tetragonal phase D_{4h}^{19}. A similar situation also takes place for two phase transitions from the phase D_{2h}^{6} to the monoclinic phases $C_{2h}^{4}(x)$ and $C_{2h}^{5}(y)$ (irreducible representation τ_4). Thus, the variations of

Possible phase transformations from phase I associated with the wave vector $\mathbf{k_3} = \pi(001)$ at the Brillouin-zone boundary

Phase I	Irreducible representation	Low-symmetry phases
D_{4h}^{19}	τ_1	$D_{2h}^{7}\{C_{2h}^{1}(x), C_{2h}^{4}(y), C_{2h}^{5}(z)\}$
	τ_2	$D_{2h}^{16}\{C_{2h}^{5}(x), C_{2h}^{2}(y), C_{2h}^{5}(z)\}$
	τ_3	$D_{2h}^{5}\{C_{2h}^{1}(x), C_{2h}^{2}(y), C_{2h}^{4}(z)\}$
	τ_4	$D_{2h}^{6}\{C_{2h}^{4}(x), C_{2h}^{5}(y), C_{2h}^{4}(z)\}$

Note: The monoclinic subgroups with the highest symmetry are indicated in braces. The directions of the twofold symmetry axes in monoclinic subgroups are indicated in parentheses.

temperature, pressure, or some other parameter determining the state of a $CsHSO_4$ crystal can give rise to phase transitions $D_{2h}^{16} \longrightarrow C_{2h}^{2}(y)$ or $D_{2h}^{6} \longrightarrow C_{2h}^{4}(x)$. The experimental studies [12, 13] showed that high-pressure phase IV has the symmetry C_{2h}^{2}, whence we can draw the conclusion that the following chain of phase transitions occur in $CsHSO_4$ crystals: $D_{4h}^{19} \longrightarrow D_{2h}^{16} \longrightarrow C_{2h}^{5}(x)$. Thus, phase VI has the symmetry D_{2h}^{16} [6].

It should be indicated that, in fact, the order parameter in the $D_{4h}^{19} \longrightarrow D_{2h}^{16}$ phase transition (the transition between phases I and VI) and the order parameter in the $D_{4h}^{19} \longrightarrow C_{2h}^{5}$ phase transition (the transitions between phases I and II) form the order parameter for the parental phase O_h^7 of a $CsHSO_4$ crystal [17]. This leads to the conclusion [14] that of two possible sequences of phases transitions ($D_{4h}^{19} \longrightarrow D_{2h}^{16} \longrightarrow C_{2h}^{5}(x)$ and $D_{4h}^{19} \longrightarrow D_{2h}^{6} \longrightarrow C_{2h}^{5}(y)$), the former sequence is more probable.

According to experimental data [12, 13], phase V has either the symmetry C_{2h}^{2} or C_2^2, with the unit-cell volume being equal to double the volume of the primitive unit cell of phase I. Let us analyze the possible formation of the phase with the symmetry C_{2h}^{2} or C_2^2. The analysis of the table shows that the monoclinic phase C_{2h}^{2} can be formed only as a result of the chain of phase transitions $D_{4h}^{19} \longrightarrow D_{2h}^{5} \longrightarrow C_{2h}^{2}(y)$ (irreducible representation τ_3). Upon the analysis similar to that made for the phase transitions I $\longrightarrow$ VI $\longrightarrow$ IV ($D_{4h}^{19} \longrightarrow D_{2h}^{16} \longrightarrow C_{2h}^{2}(y)$) with the irreducible representation τ_2), we draw the conclusion that phase VII has the symmetry D_{2h}^{5} and that the $D_{2h}^{5} \longrightarrow C_{2h}^{1}(x)$ phase transition is also possible [6]. The boundary of possible new phase VIII with the symmetry C_{2h}^{1} is schematically shown by the dash-dotted line in Fig. 1.

Now, consider the case where phase V has the symmetry C_2^2. The group–theoretical analysis of the high-pressure phase [14] shows that the phase with the symmetry C_2^2 can arise as an intermediate one between the nonconducting phase II (sp. gr. C_{2h}^{5}, the twofold axis coincides with the [110] direction) and a certain new phase with the symmetry D_2^5. In this case, it can be assumed that phase VIII has the symmetry D_2^5.

This variant of the symmetry analysis does not allow the determination of the symmetry of phase VII. The fact that phase V is not adjacent to phase II (Fig. 1) leads to the conclusion that the most probable symmetry group of phase V is C_{2h}^{2}. It should also be indicated that only experimental determination of the direction of the twofold symmetry axis in phase V could confirm the symmetry of phase V. Thus, in the C_{2h}^{2} group, the twofold symmetry axis is directed either along the [100] or the [010] direction, whereas in the group C_2^2, it is directed along [110].

Now, discuss the symmetry of phase III' established in [5, 18–20]. The position of this phase on the phase diagram lead to the assumption that phase III' is an intermediate phase between phases III and IV. Then, the symmetry group of phase III' is C_i^1 [6]. Phase III' can also appear as a result of the phase transition II $\longrightarrow$ III'. The above symmetry analysis of the phase transition shows that $CsHSO_4$ crystals have at least two order parameters that differ by their symmetries. Thus, for the wave vector $\mathbf{k}_3$, these are two order parameters with the symmetries τ_2 and τ_3. The conditions of compatibility of irreducible representations [14] shows that these order parameters for the wave vector $\mathbf{k}_1$ have the symmetries τ_1 and τ_2, respectively. The condensation of the order parameter with the symmetry τ_2 (the wave vector $\mathbf{k}_1$) results in the phase transition I $\longrightarrow$ II. The further condensation of the order parameter of symmetry τ_1 can result in the phase transition II $\longrightarrow$ III'. In this case, phase III' has the symmetry C_2^2.

In the next section, we construct the system of hydrogen bonds in high-pressure phases of $CsHSO_4$ crystals using the approach developed in [15].

SYSTEMS OF HYDROGEN BONDS IN HIGH-PRESSURE PHASES

Now, construct the systems of hydrogen bonds in phases II and III determined in diffraction experiments [8, 10]. Figure 2 shows eight possible positions of hydrogen ions in the zeroth primitive unit cell of phase I with two $CsHSO_4$ formula units. These positions are randomly occupied by two hydrogen ions but with the same probabilities. Therefore, phase I is characterized by a random dynamically disordered network of hydrogen bonds. It is convenient to attribute eight proton positions to one central SO_4-tetrahedron (Fig. 2) and not to two tetrahedra contained in the zeroth primitive unit cell of phase I [21]. Then, the positions in other primitive unit cells are obtained from the positions shown in Fig. 2 with the aid of lattice translations (with due regard for the phase factor, see below). It should also be noted that a hydrogen ion in the hydrogen bond

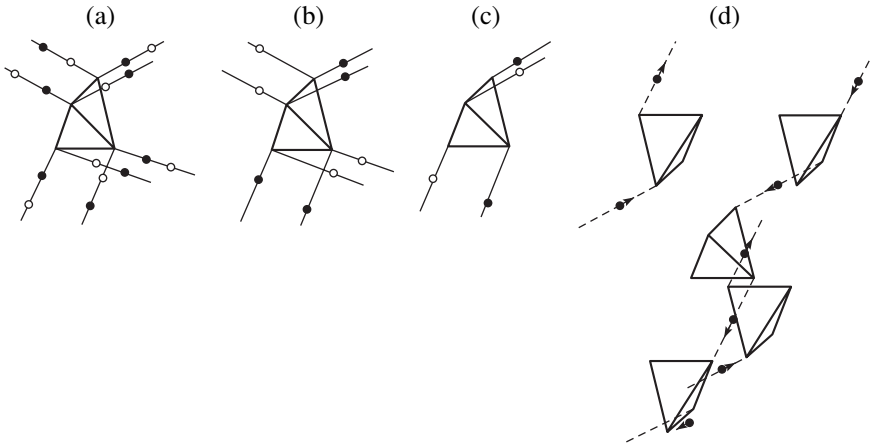

Fig. 3. System of hydrogen bonds in phase II: (a) partial ordering of hydrogen ions due to condensation of the secondary order parameter with the symmetry B_{2g} and the wave vector $\mathbf{k} = 0$. Filled circles indicate the positions occupied by hydrogen ions, light circles indicate free positions; (b) further ordering of hydrogen ions due to condensation of the secondary order parameter with symmetry E_{2g} and the wave vector $\mathbf{k} = 0$; (c) complete ordering of two hydrogen ions due to condensation of the primary parameter of symmetry τ_2 and the wave vector $\mathbf{k}_1 = \pi(1/2, 1/2, 0)$; and (d) the system of hydrogen bonds of the central and four nearest SO_4-tetrahedra (see Fig. 2). The arrows indicate the displacements of hydrogen ions to one of the two positions of the two-well potential of the hydrogen bond.

can be located in a two-well potential, then the number of positions is doubled.

Figure 3 illustrates the process of ordering of hydrogen ions in the zeroth primitive unit cell due to condensation of the primary and two secondary order parameters [15]. Two secondary order parameters have the wave vector $\mathbf{k} = 0$ and, therefore, hydrogen ions are ordered in the similar way in all the primitive unit cells. Condensation of the secondary order parameter with the symmetry B_{2g} results in ordering of hydrogen ions in one of the two possible positions in the two-well potential (Fig. 3a). Another secondary order parameter with the symmetry E_g (Fig. 3b) lead to further partial ordering of hydrogen ions. Condensation of the primary order parameter with the wave vector $\mathbf{k}_1 = \pi(1/2, 1/2, 0)$ results in complete ordering of two hydrogen ions in the zeroth primitive unit cell (Fig. 3c). Since the wave vector has the nonzero value $\mathbf{k}_1 \neq 0$, the occupied and the free positions in an arbitrary primitive unit cell with the radius-vector $\mathbf{R}_n = n_1\mathbf{a}_1 + n_2\mathbf{a}_2 + n_3\mathbf{a}_3$ (where n_i are integers) (Fig. 3c) exchange their positions depending on the phase factor $\exp(-i\mathbf{k}_1\mathbf{R}_n) = \pm 1$. The system of hydrogen bonds in phase II of a $CsHSO_4$ crystal is shown in Fig. 3d, where hydrogen bonds are oriented along the $[\bar{1}11]$ direction (in low-symmetric phase II, four domains with different orientations of hydrogen bonds with respect to the [111] direction can be formed), which is consistent with the experimental results obtained in [9].

Now, construct the system of hydrogen bonds in phase III. According to the above symmetry analysis, phase III arises as a result of the following phase transformations I $\longrightarrow$ VI $\longrightarrow$ III. Figure 4a shows partial ordering of two hydrogen ions in the zeroth primitive unit cell occurring due to condensation of the secondary order parameter with the symmetry B_{1g} and the wave vector $\mathbf{k} = 0$. The further partial ordering of two hydrogen ions due to condensation of the primary order parameter with the symmetry τ_2 and the wave vector $\mathbf{k}_3 = \pi(0, 0, 1)$ is shown in Fig. 4b. The final system of hydrogen bonds in superionic phase VI is shown in Fig. 4c. This system can be formed only if a hydrogen bond is characterized by a two-well potential. The further condensation of the order parameter with the symmetry B_{3g} and the wave vector $\mathbf{k} = 0$ results in the VI $\longrightarrow$ III phase transition (the corresponding system of hydrogen bonds is shown in Fig. 4d), whereas the condensation of the order parameters with the symmetry B_{2g}, to the VI $\longrightarrow$ IV transition (Fig. 4e). As is seen from Fig. 4d, hydrogen bonds in phase III are oriented along the crystallographic *x*-axis (Fig. 2). The twofold symmetry axis of monoclinic phase III is also directed along the *x*-axis, which is confirmed by the experimental observations [10].

It was shown above that phase III' (Fig. 1) can be an intermediate phase between phases III and IV. In this case, the system of hydrogen bonds in phase III' should be similar to the system shown in Fig. 4d but with the break of some hydrogen bonds and the formation of dimers by the nearest SO_4 tetrahedra at the sites of bond breaks (Fig. 4e). If phase III' is formed due to the II $\longrightarrow$ III' transition, the system of hydrogen bonds is similar to the system shown in Fig. 3d.

Now, construct the system of hydrogen bonds in phases V, VII, and VIII. These phases are formed as a result of the following transitions: I $\longrightarrow$ VII, VII $\longrightarrow$ V, and VII $\longrightarrow$ VIII. Partial ordering of two hydrogen ions in the zeroth primitive unit cell due to the conden-

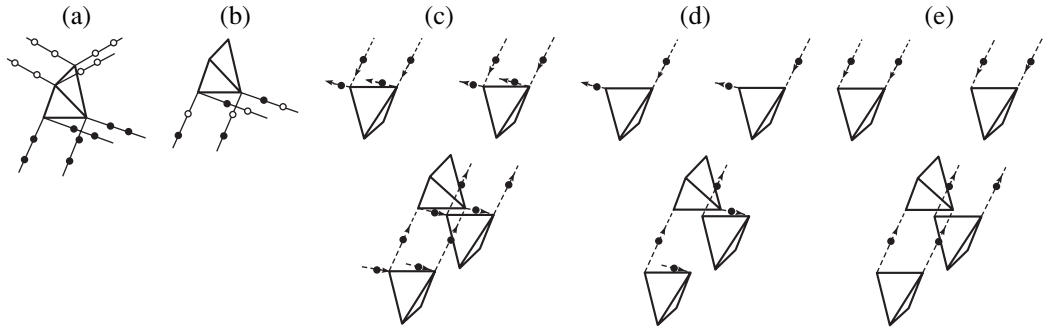

Fig. 4. System of hydrogen bonds in phases VI, III, and IV: (a) partial ordering of two hydrogen ions in the primitive unit cell due to condensation of the secondary order parameter with the symmetry B_{1g} and the wave vector $\mathbf{k} = 0$; (b) further partial ordering of hydrogen ions due to condensation of the primary order parameter with the symmetry τ_2 and the wave vector $\mathbf{k}_3$; (c) dynamically disordered network of hydrogen bonds in superionic phase VI constructed based on the distribution (b); the arrow indicates the displacement of a hydrogen ion to one of two positions of the two-well potential of the hydrogen bond; (d) a system of hydrogen bonds in phase III; (e) dimers formed by hydrogen bonds in phase IV.

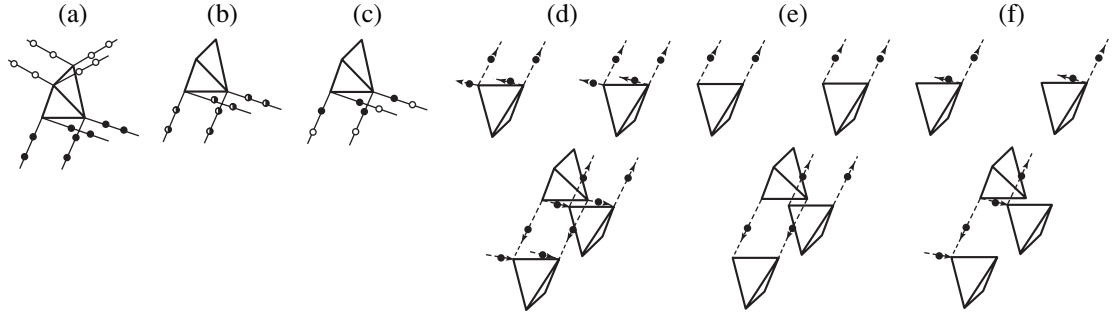

Fig. 5. Systems of hydrogen bonds in phases VII, V, and VIII: (a) partial ordering of two hydrogen ions in the zeroth primitive unit cell due to condensation of the secondary order parameter with the symmetry B_{1g} and the wave vector $\mathbf{k} = 0$; (b and c) two variants of possible partial ordering of hydrogen ions due to condensation of the primary order parameter with the symmetry τ_3 and the wave vector $\mathbf{k}_3$; (d) dynamically disordered network of hydrogen bonds in superionic phase VII constructed based on the distribution (c); (e) the system of hydrogen bonds in phase V; (f) system of hydrogen bonds in phase VIII.

sation of the secondary order parameter with the symmetry B_{1g} and the wave vector $\mathbf{k} = 0$ is shown in Fig. 5a. The condensation of the primary order parameter with the symmetry τ_3 and the wave vector k_3 can lead to two variants of partial ordering of hydrogen ions (Figs. 5b and 5c). Figure 5d shows the system of hydrogen bonds in superionic phase VII constructed on the basis of ordering of hydrogen ions shown in Fig. 5c. It should be indicated that ordering shown in Fig. 5b is less probable because of the generation of the charge-density wave associated with hydrogen ions. In this case, all the positions (shown by half-filled circles) in the primitive unit cell are either occupied by four hydrogen ions (with probability 1/2) or are empty depending on the phase factor $\exp(-i\mathbf{k}_3\mathbf{R}_n) = \pm 1$. Figures 5e and 5f show the systems of hydrogen bonds in phases V and VIII, which represent two different types of complete ordering of hydrogen ions arising from the configuration shown in Fig. 5d.

Concluding this Section, consider a network of hydrogen bonds in phase VIII for the case where this phase has the symmetry D_2^5. The condensation of three secondary order parameters with the symmetries A_{1u}, B_{2g}, and B_{2u} and the wave vector $\mathbf{k} = 0$ results in partial ordering of two hydrogen ions in the zeroth primitive unit cell shown in Fig. 6a. It should be indicated that a configuration is possible in which either the positions closest to the SO_4-tetrahedron or the distant positions are occupied (the filled and the empty circles in Fig. 6a). The condensation of the primary order parameter with the symmetry τ_2 and the wave vector $\mathbf{k}_1 = \pi(1/2, 1/2, 0)$ results in complete ordering of hydrogen ions in the zeroth primitive unit cell. The symmetry analysis admits two configurations shown in Figs. 6b and 6c. These two types of ordering can take place for both closest and distant positions and, therefore, Figures 6b and 6c show only one position on the hydrogen bond. Figure 6d shows the system of hydrogen bonds constructed on the basis of the configuration shown in Fig. 6b, with the use of only the closest positions. For the distant positions, the directions of the arrows in Fig. 6 should be changed to opposite ones. It should

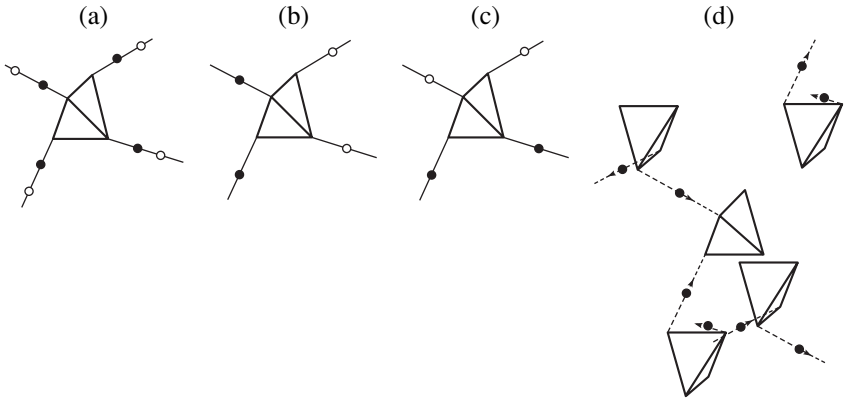

Fig. 6. System of hydrogen bonds in phase VIII with the symmetry D_2^5: (a) partial ordering of two hydrogen ions in the zeroth primitive unit cell due to condensation of three secondary order parameters with the symmetries A_{1u}, B_{2g}, and B_{2u} and the wave vector $\mathbf{k} = 0$; (b and c) two possible types of complete ordering of hydrogen ions in the primitive unit cell due to condensation of primary parameter of the symmetry τ_2 with the wave vector $\mathbf{k}_1 = \pi(1/2, 1/2, 0)$; (d) system of hydrogen bonds in phase VIII constructed based on the configuration corresponding to (c).

also be indicated that the displacement of the origin of the coordinate system by the vector $(0, \tau, \tau_z/2)$ (Fig. 2) results in the formation of the system of hydrogen bonds that can be constructed based on the configuration shown in Fig. 6c. As is seen from Fig. 6d, the hydrogen bonds are directed along the [111] directions. Intermediate phase V in this variant of the analysis has the system of hydrogen bonds shown in Fig. 3d, with the breaks and restructuring of bonds in the sites of these breaks (Fig. 6d).

DISCUSSION OF RESULTS AND CONCLUSIONS

Using the group–theoretical methods, we constructed the systems of hydrogen bonds in all of the high-pressure phases of $CsHSO_4$ crystals. The systems of hydrogen bonds in phases II and III are consistent with the experimental data determined by the diffraction methods [7–11]. In superionic phases VI (the symmetry D_{2h}^{16}) and VII (the symmetry D_{2h}^{5}), the hydrogen bonds are partly ordered. The fully ordered systems of hydrogen bonds should be formed in phases IV (C_{2h}^2), V (C_{2h}^2), and VIII (C_{2h}^1). The system of hydrogen bonds in the intermediate phase III' (C_i^1) is characterized by a break of hydrogen bonds and the formation of dimers in the sites of these breaks.

The system of hydrogen bonds in this study was constructed with the use of the 16*h* positions located between the closest SO_4 tetrahedra (Fig. 2). Moreover, we took into account the two-well potential of the hydrogen bond, which resulted in a doubling of the total number of positions (denoted as $16h \oplus 16h$ in [15]). The symmetry analysis shows that only the use of doubled positions allows the construction of the network of hydrogen bonds in superionic phase VI with the symmetry D_{2h}^{16}. Thus, in this high-pressure phase, the anharmonic effects in the dynamics of hydrogen ions should take place. Since the experimental studies [13] revealed only the harmonic behavior of hydrogen ions in the nonconducting high-pressure phase V adjacent to phase VI in the phase diagram (Fig. 1), one can assume that the anharmonic effects in superionic phase VI would be less noticeable than the anharmonic effects revealed in phases II and III [13].

It is also of interest to study experimentally the effect of other possible types of proton positions (e.g., 8*e* positions [22]) on the static and dynamic properties of the system of hydrogen bonds. Possibly, the 8*e* position can play a certain role in high protonic conductivity [22] and therefore the effect of the 8*e* positions on proton diffusion can be studied on superionic phases VI and VII.

ACKNOWLEDGMENTS

We are grateful to L.A. Shuvalov, A.V. Belushkin, and V.P. Dmitriev for fruitful discussion of the results. The study was supported by the Russian Foundation for Basic Research, projects no. 99-02-17389 and 00-15-96797).

REFERENCES

1. A. I. Baranov, L. A. Shuvalov, and N. M. Shchagina, Pis'ma Zh. Éksp. Teor. Fiz. **36**, 381 (1982) [JETP Lett. **36**, 459 (1982)].
2. L. F. Kirpichnikova, A. A. Urusovskaya, and V. I. Mozgovoĭ, Pis'ma Zh. Éksp. Teor. Fiz. **62**, 616 (1995) [JETP Lett. **62**, 638 (1995)].

3. L. F. Kirpichnikova, M. Polomska, Ya. Volyak, and B. Hilczher, Pis'ma Zh. Éksp. Teor. Fiz. **63**, 871 (1996) [JETP Lett. **63**, 912 (1996)].
4. E. G. Ponyatovskiĭ, V. I. Rashchupkin, V. V. Sinitsyn, *et al.*, Pis'ma Zh. Éksp. Teor. Fiz. **41**, 114 (1985) [JETP Lett. **41**, 139 (1985)].
5. V. V. Sinitsyn, E. G. Ponyatovskiĭ, A. I. Baranov, *et al.*, Zh. Éksp. Teor. Fiz. **100**, 693 (1991) [Sov. Phys. JETP **73**, 386 (1991)].
6. V. S. Shakhmatov, High Press. Res. **14**, 67 (1995).
7. A. M. Balagurov, A. V. Belushkin, A. I. Beskrovnyĭ, *et al.*, Kratk. Soobshch. Ob'edin. Inst. Yad. Issled., No. 13-85, 18 (1985).
8. A. M. Balagurov, A. I. Beskrovnyi, and B. N. Savenko, Phys. Status Solidi A **100**, K3 (1987).
9. Z. Jirak, M. Dlouha, S. Vratislav, *et al.*, Phys. Status Solidi A **100**, K117 (1987).
10. B. V. Merinov, A. I. Baranov, B. A. Maksimov, and L. A. Shuvalov, Kristallografiya **31**, 450 (1986) [Sov. Phys. Crystallogr. **31**, 264 (1986)].
11. V. B. Merinov, A. I. Baranov, and L. A. Shuvalov, Kristallografiya **32**, 86 (1987) [Sov. Phys. Crystallogr. **32**, 47 (1987)].
12. A. V. Belushkin, L. A. Shuvalov, and S. Hull, Annual Report ISIS (Rutherford Appleton Laboratory) **2**, A33 (1993).
13. A. V. Belushkin, M. A. Adams, S. Hull, *et al.*, Physica B (Amsterdam) **213/214**, 1034 (1995).
14. V. S. Shakhmatov, Kristallografiya **38** (6), 176 (1993) [Crystallogr. Rep. **38**, 805 (1993)].
15. N. M. Plakida and V. S. Shakhmatov, Ferroelectrics **167**, 73 (1995).
16. N. M. Plakida and V. S. Shakhmatov, Izv. Akad. Nauk SSSR, Ser. Fiz. **51**, 2107 (1987).
17. V. S. Shakhmatov, Kristallografiya **36**, 1021 (1991).
18. B. Baranowski, M. Friesel, and A. Lunden, Z. Naturforsch. A **41**, 733 (1986).
19. B. Baranowski, M. Friesel, and A. Lunden, Physica A (Amsterdam) **156**, 353 (1989).
20. A. Lunden, B. Baranowski, and M. Friesel, Ferroelectrics **167**, 33 (1995).
21. N. A. Dzhavadov and K. A. Rustamov, Phys. Status Solidi B **170**, 67 (1992).
22. A. V. Belushkin, W. I. F. David, R. M. Ibberson, and L. A. Shuvalov, Acta Crystallogr., Sect. B: Struct. Sci. **47**, 161 (1991).

Translated by L. Man